

INFORMATION TO USERS

This manuscript has been reproduced from the microfilm master. UMI films the text directly from the original or copy submitted. Thus, some thesis and dissertation copies are in typewriter face, while others may be from any type of computer printer.

The quality of this reproduction is dependent upon the quality of the copy submitted. Broken or indistinct print, colored or poor quality illustrations and photographs, print bleedthrough, substandard margins, and improper alignment can adversely affect reproduction.

In the unlikely event that the author did not send UMI a complete manuscript and there are missing pages, these will be noted. Also, if unauthorized copyright material had to be removed, a note will indicate the deletion.

Oversize materials (e.g., maps, drawings, charts) are reproduced by sectioning the original, beginning at the upper left-hand corner and continuing from left to right in equal sections with small overlaps.

Photographs included in the original manuscript have been reproduced xerographically in this copy. Higher quality 6" x 9" black and white photographic prints are available for any photographs or illustrations appearing in this copy for an additional charge. Contact UMI directly to order.

Bell & Howell Information and Learning
300 North Zeeb Road, Ann Arbor, MI 48106-1346 USA
800-521-0600

UMI[®]

UNIVERSITY OF OKLAHOMA
GRADUATE COLLEGE

**SURFACE THERMODYNAMIC
CHARACTERISTICS OF HOOK ECHOES AND
REAR-FLANK DOWNDRAFTS, WITH
IMPLICATIONS FOR TORNADO GENESIS
AND MAINTENANCE**

A Dissertation
SUBMITTED TO THE GRADUATE FACULTY
in partial fulfillment of the requirements for the
degree of
Doctor of Philosophy

By
PAUL MICHAEL MARKOWSKI
Norman, Oklahoma
2000

UMI Number: 9988306

UMI[®]

UMI Microform 9988306

Copyright 2001 by Bell & Howell Information and Learning Company.

All rights reserved. This microform edition is protected against
unauthorized copying under Title 17, United States Code.

Bell & Howell Information and Learning Company

300 North Zeeb Road

P.O. Box 1346

Ann Arbor, MI 48106-1346

© by PAUL MICHAEL MARKOWSKI 2000
All Rights Reserved.

SURFACE THERMODYNAMIC
CHARACTERISTICS OF HOOK ECHOES AND
REAR-FLANK DOWNDRAFTS, WITH
IMPLICATIONS FOR TORNADO GENESIS
AND MAINTENANCE

A Dissertation APPROVED FOR THE
SCHOOL OF METEOROLOGY

By

J. McAnake

Delwood G. White

Fredrick H. Carr

Brian Fredler

Bob Davis-John

Dedication

This dissertation is dedicated to Naomi Greaser and all whose lives were changed by the tornado outbreak in central Oklahoma on 3 May 1999, especially David Greaser and the Squires Family.

Acknowledgments

I am grateful to all VORTEX volunteers (too numerous to mention). I thank my committee members for their thoughtful criticisms and dedication: Dr. Jerry Straka, Dr. Erik Rasmussen, Dr. Frederick Carr, Dr. Brian Fiedler, Dr. Robert Davies-Jones, and Dr. Deborah Watson. I also thank Dr. Erik Rasmussen for his leadership and nowcasting during field operations, and for the use of his software, and Dr. Jerry Straka for his invaluable technical expertise with the mobile mesonet. Furthermore, I could not have completed the numerical simulations without the generous support of Dr. Lou Wicker, who provided me with his axisymmetric model and advice on many occasions.

Special thanks also go to the staff of the School of Meteorology. I am indebted to Rob Carver for his extensive computing assistance (too often to mention), and Al Pietrycha for running quality-control checks on the 1998 mobile mesonet data. Tom Shepherd, Mike Magsig, and Scott Stephens also are acknowledged for helping to obtain hard-to-find radar data, and I thank Mark Shafer for speedy fulfillment of Oklahoma Mesonet data requests. Lastly, I thank Dr. Bill Winn for providing 8 June 1995 turtle data and Dr. Dave Blanchard for providing some needed FORTRAN code.

I could not have finished without the support of my family (Michael, Patricia, and Andy) and fiancée, Marisa. They provided encouragement when needed, without fail.

Contents

Dedication	iv
Acknowledgments	v
List Of Tables	ix
List Of Figures	x
Abstract	xiii
1 Observations of hook echoes and rear-flank downdrafts	1
1.1 Early observations	1
1.1.1 Hook echoes	1
1.1.2 Rear-flank downdrafts	9
1.2 Doppler radar studies	12
1.2.1 Early single and multiple Doppler radar observations	12
1.2.2 Brandes' work	18
1.2.3 Obstacle appearance	24
1.2.4 Collapse of overshooting tops	25
1.3 Visual and surface observations of RFDs	25
1.4 Recent findings	29
2 Theoretical and numerical modeling studies pertaining to rear-flank downdrafts	31
2.1 Research prior to 1990	31
2.1.1 Numerical modeling efforts	31
2.1.2 Theoretical studies	36
2.2 Recent studies	38
3 Motivation for investigating RFD surface thermodynamics	43
3.1 Documentation of surface thermodynamic fields	45
3.2 Differences between tornadic and non-tornadic supercells	46

4	Data description and analysis techniques	52
4.1	Mobile mesonet data	55
4.1.1	Instrument specifications and quality control procedures . . .	55
4.1.2	Time-to-space conversion	57
4.1.3	Density of mobile mesonet observations	58
4.2	Radar data	61
4.3	Thermodynamic variables analyzed	62
4.3.1	Virtual potential temperature	62
4.3.2	Equivalent potential temperature	64
4.3.3	Parcel origin	65
4.3.4	CAPE and CIN	65
4.3.5	Pressure	67
4.4	Specification of the base state	67
4.5	Limitations	70
5	Surface observations in hook echoes and RFDs	72
5.1	RFDs associated with non-tornadic supercells	72
5.2	RFDs associated with tornadic supercells	78
5.3	Miscellaneous new observations	85
5.4	Summary	103
5.5	Reconciliation of findings with past observations	117
6	Anticipation of surface RFD characteristics from sounding data	119
7	Idealized numerical simulations	129
7.1	Rationale and experiment design	129
7.2	Methods	131
7.2.1	Model and domain description	131
7.2.2	Initial conditions	137
7.2.3	Downdraft generation	142
7.3	Results	146
7.3.1	Experiments HCHL and HCLL	147
7.3.2	Experiments LCHL and LCLL	148
7.4	Discussion	157
7.5	Extension to three dimensions	159
7.6	Sensitivity studies	164
8	Implications for tornado genesis and maintenance	166
8.1	RFD forcing mechanisms	166
8.2	Effects of low-level stability	167
8.3	A new hypothesis	168
8.4	Additional implications for operational meteorology	177

9 Summary and conclusions	180
References	183
Appendix A	
Error analysis	200
A.1 Reduced pressure errors	200
A.2 Virtual potential temperature fluctuation errors	203
A.3 Errors associated with other derived quantities	206
Appendix B	
Buoyancy formulation	209
Appendix C	
Axisymmetric model validation	215

List Of Tables

2.1	Summary of findings pertaining to hook echoes and RFDs	42
4.1	Cases of mobile mesonet observations obtained within the hook echoes of non-tornadic supercells	53
4.2	Cases of mobile mesonet observations obtained within the hook echoes of tornadic supercells	54
4.3	Characteristics of the mobile mesonet	57
4.4	Sampling densities for the mobile mesonet cases	60
5.1	Summary of RFD observations	105
5.2	Mean thermodynamic variables in RFDs	107
6.1	Summary of environmental data obtained from "best" proximity sound- ings	121
7.1	Model sounding parameters	138
7.2	Summary of idealized simulation results	156
7.3	Surface thermodynamic data at tornadogenesis and demise	156
8.1	Description of Ψ , Λ , and Υ	174

List Of Figures

1.1	The first documented hook echo	3
1.2	Fujita's analysis of the 9 April 1953 Champaign, IL hook echo	4
1.3	Evolution of the hook echo studied by Browning	5
1.4	Fujita's (1965) hypothesis for hook formation	6
1.5	Various types of hook echoes	7
1.6	Cyclonic and anticyclonic tornadoes on 3 June 1980	8
1.7	Pressure field near the 20 June 1957 Fargo tornado, as inferred by Fujita	11
1.8	Lemon and Doswell (1979) conceptual model	15
1.9	Thermodynamic retrieval from the Del City storm by Hane and Ray (1985)	17
1.10	Dual-Doppler analysis of the Del City storm by Brandes (1981)	20
1.11	Thermodynamic retrieval from the Del City storm by Brandes (1984a)	22
1.12	Dual-Doppler analysis of the Del City storm by Klemp et al. (1981)	26
1.13	Photograph of the 2 June 1995 Dimmitt, TX tornado	27
2.1	Near-ground occlusion downdraft forcings in the numerical simulation by Klemp and Rotunno (1983)	35
3.1	Sample of some of the hook echoes in which mobile mesonet observations have been collected	44
3.2	Brandes' (1978) conceptual model of low-level mesocyclone characteristics during the tornadic phase	47
3.3	Vertical velocity and trajectories in the Wicker and Wilhelmson (1995) simulation	48
3.4	Schematic diagram showing how cyclonic vorticity may be generated from tilting of baroclinic horizontal vorticity in a downdraft	49
3.5	Comparison of a non-tornadic and tornadic supercell by Trapp (1999)	51
4.1	Mobile mesonet unit	55
4.2	Schematic showing method of quantification of observation density	59
5.1	Analysis of θ'_v at 0028:32 UTC 30 April 1995	73
5.2	Analysis of θ'_v at 0205:12 UTC 20 May 1998	74

5.3	Analysis of θ'_c at 0028:32 UTC 30 April 1995	75
5.4	Analysis of θ'_c at 0205:12 UTC 20 May 1998	76
5.5	Analysis of z_o at 0028:32 UTC 30 April 1995	77
5.6	Analysis of CAPE at 0028:32 UTC 30 April 1995	79
5.7	Analysis of CIN at 0028:32 UTC 30 April 1995	80
5.8	Analysis of θ'_v at 2014:43 UTC 8 June 1995	81
5.9	Analysis of CAPE at 2014:43 UTC 8 June 1995	82
5.10	Analysis of θ'_v at 2349:30 UTC 6 May 1994	83
5.11	Analysis of θ'_v at 0028:13 UTC 3 June 1999	84
5.12	Analysis of θ'_v at 0138:00 UTC 17 May 1995	86
5.13	Analysis of θ'_v at 2345:12 UTC 2 June 1995	87
5.14	Analysis of θ'_c at 2345:12 UTC 2 June 1995	88
5.15	Analysis of θ'_v at 0106:00 UTC 3 June 1995	89
5.16	Analysis of θ'_v at 0022:00 UTC 9 June 1995	90
5.17	Analysis of θ'_c at 0052:04 UTC 4 May 1999	91
5.18	Analysis of θ'_c at 0052:04 UTC 4 May 1999	92
5.19	Analysis of z_o at 2345:12 UTC 2 June 1995	93
5.20	Analysis of CAPE at 0022:00 UTC 9 June 1995	94
5.21	Analysis of CAPE at 0052:04 UTC 4 May 1999	95
5.22	Analysis of θ'_c at 0101:00 UTC 9 June 1995	96
5.23	Analysis of CAPE at 0101:00 UTC 9 June 1995	97
5.24	Analysis of p' at 0205:12 UTC 20 May 1998	99
5.25	Analysis of p' at 2345:12 UTC 2 June 1995	100
5.26	Analysis of p' at 0101:00 UTC 9 June 1995	101
5.27	Analysis of p' at 0028:13 UTC 3 June 1999	102
5.28	Scatter plot of maximum θ'_v versus minimum θ'_v	108
5.29	Scatter plot of maximum θ'_c versus minimum θ'_c	109
5.30	Scatter plot of maximum z_o versus minimum z_o	110
5.31	Scatter plot of maximum θ'_v versus maximum CAPE	111
5.32	Scatter plot of maximum θ'_v versus minimum CIN	112
5.33	Scatter plot of maximum $\nabla_h \theta'_v$ values	113
5.34	Scatter plot of maximum p' values	113
5.35	Mean thermodynamic variables by quadrant	115
5.36	Composite diagram illustrating the general characteristics of RFDs	116
6.1	Scatter plots of environmental conditions as determined by soundings	123
6.2	Scatter plot of θ'_v versus surface T_{dd}	128
7.1	Idealized axisymmetric simulations design	132
7.2	Model soundings	139
7.3	Steady-state updrafts in the control simulations	143
7.4	Experiment HCHL results	149
7.5	Experiment HCLL results	151

7.6	Experiment LCHL results	153
7.7	Experiment LCLL results	154
7.8	Time series of θ'_v and ζ	155
7.9	Vorticity forcing terms in Experiment HCHL	160
7.10	Vorticity forcing terms in Experiment HCLL	161
7.11	Circulation in Experiments HCHL and HCLL	162
8.1	Tornadogenesis conceptual model	170
8.2	Schematic illustrating what controls surface θ_e values in the RFD . .	175
8.3	Schematic illustrating what controls surface θ_v values in the RFD . .	176
C.1	Steady-state vortex as in Howells et al. (1988)	217

Abstract

Since its first documentation in 1953, the “hook echo” has been perhaps the best-recognized radar feature of supercell storms. Hook echoes have been associated with a region of subsiding air to the rear of both tornadic and non-tornadic supercells. Today this feature usually is referred to as the “rear-flank downdraft” (RFD). For over twenty years, the RFD has been hypothesized to play an important role in the final concentration of vorticity at the surface that gives rise to tornadoes.

Despite the long-surmised importance of the hook echo and RFD in tornadogenesis, only a paucity of direct observations have been obtained at the surface within hook echoes and RFDs. In this dissertation, *in situ* surface observations within hook echoes and RFDs are analyzed. These “mobile mesonet” data have unprecedented horizontal spatial resolution, and were obtained from the Verifications of the Origins of Rotation in Tornadoes Experiment (VORTEX) and additional field experiments conducted since the conclusion of VORTEX. The surface thermodynamic characteristics of hook echoes and RFDs associated with tornadic and non-tornadic supercells are investigated to address whether certain types of hook echoes and RFDs are favorable (or unfavorable) for tornadogenesis.

Evidence will be presented that evaporative cooling and entrainment of midlevel potentially cold air play a smaller role in the forcing of RFDs associated with tornadic supercells compared to non-tornadic supercells. Tornadogenesis is more likely and tornado intensity and longevity increase as the surface buoyancy, potential buoyancy, and equivalent potential temperature in the RFD increase, and as the convective inhibition associated with RFD parcels at the surface decreases. Furthermore, baroclinity at the surface within the hook echo is not a necessary condition for tornadogenesis. It also will be shown that environments characterized by high boundary layer relative humidity (and low cloud base) are more conducive to RFDs

associated with relatively high buoyancy than environments characterized by low boundary layer relative humidity (and high cloud base).

Chapter 1

Observations of hook echoes and rear-flank downdrafts

1.1 Early observations

1.1.1 Hook echoes

Perhaps the best-recognized radar feature associated with supercells is the extension of low-level echo on the right-rear flank of these storms—first documented by Stout and Huff (1953: Fig. 1.1) in an Illinois tornado outbreak on 9 April 1953—called the “hook echo” by van Tassell (1955). This reflectivity appendage usually is oriented roughly perpendicular to storm motion. Hook echoes have been found to be associated with the small-scale circulation common in supercell thunderstorms [called the “tornado cyclone” by Brooks (1949)]. Furthermore, these low-level reflectivity features are typically downward extensions of the rear side of an elevated reflectivity region (Forbes 1981) called the “echo overhang” (Browning 1964; Marwitz 1972a; Lemon 1982), with the region beneath the echo overhang termed a “weak echo region” (Chisholm 1973; Lemon 1977) or vault (Browning and Donaldson 1963; Browning 1964, 1965a).

In Stout and Huff’s report, the evidence was inconclusive as to whether the hook echo preceded tornadogenesis, or vice versa. In van Tassell’s (1955) documentation of a hook echo near Scottsbluff, Nebraska on 27 June 1955 (it moved directly over the radar), it was not mentioned whether the hook echo developed before or after tornadogenesis. Furthermore, van Tassell’s images suggested the possible presence

of a faint anticyclonic protrusion from the tip of the hook, extending outward in a direction opposite that of the cyclonic protrusion.

Sadowski (1958) documented a tornado that occurred *after* the hook echo became visible (in fact, the hook echo was becoming less discernible on radar at the time of the reported tornado touchdown). Sadowski might have been the first to speculate that if hook echoes generally precede tornadogenesis [later shown not always to be true, at least in the radar studies using Weather Surveillance Radar (WSR)-57], then it may be possible to issue tornado warnings in advance.

Garrett and Rockney (1962) were the first to relate a circular echo on the tip of a hook echo to the tornado or tornado cyclone. They called this “ball-shaped” echo an “asc” (annular section of the cylinder of the vortex), but the authors did not offer an explanation of the exact cause for the appearance of the asc. Stout and Huff (1953) also observed an echo hole, but little was discussed of it. Donaldson (1970) noted an echo hole in the tornado he studied, and found that it was co-located with a tornado vortex. Forbes (1981) also observed similar reflectivity features during the tornado outbreak of 3-4 April 1974.

The tornado studied by Garrett and Rockney (1962) apparently touched down *before* the hook echo became prominent, unless a narrow hook echo went undetected by the WSR-3 (4 beamwidth) prior to tornadogenesis. The tornado dissipated when the hook “closed off” or merged with the forward-flank echo. The hook echo was approximately 0.5 mi (800 m) wide.

Fujita (1958a) documented in unprecedented (and since unparalleled) detail the evolution of several hook echoes observed in the outbreak of tornadoes on 9 April 1953 (Fig. 1.2; this is the same day on which Stout and Huff made their observations). He inferred the concept of thunderstorm rotation from the photographs of Stout and Huff. Fujita attributed hook echo formation essentially to the advection of precipitation from the rear of the main echo around the region of rotation associated with the tornado cyclone. Browning (1964, 1965b) also documented hook echoes and attributed their evolution (Fig. 1.3) to essentially the same process described by Fujita (1958a). Browning and Donaldson (1963) and Browning (1965b) also noted that the southern edge of the hook formed a wall of echo “which was often very sharp and sometimes rather upright.”

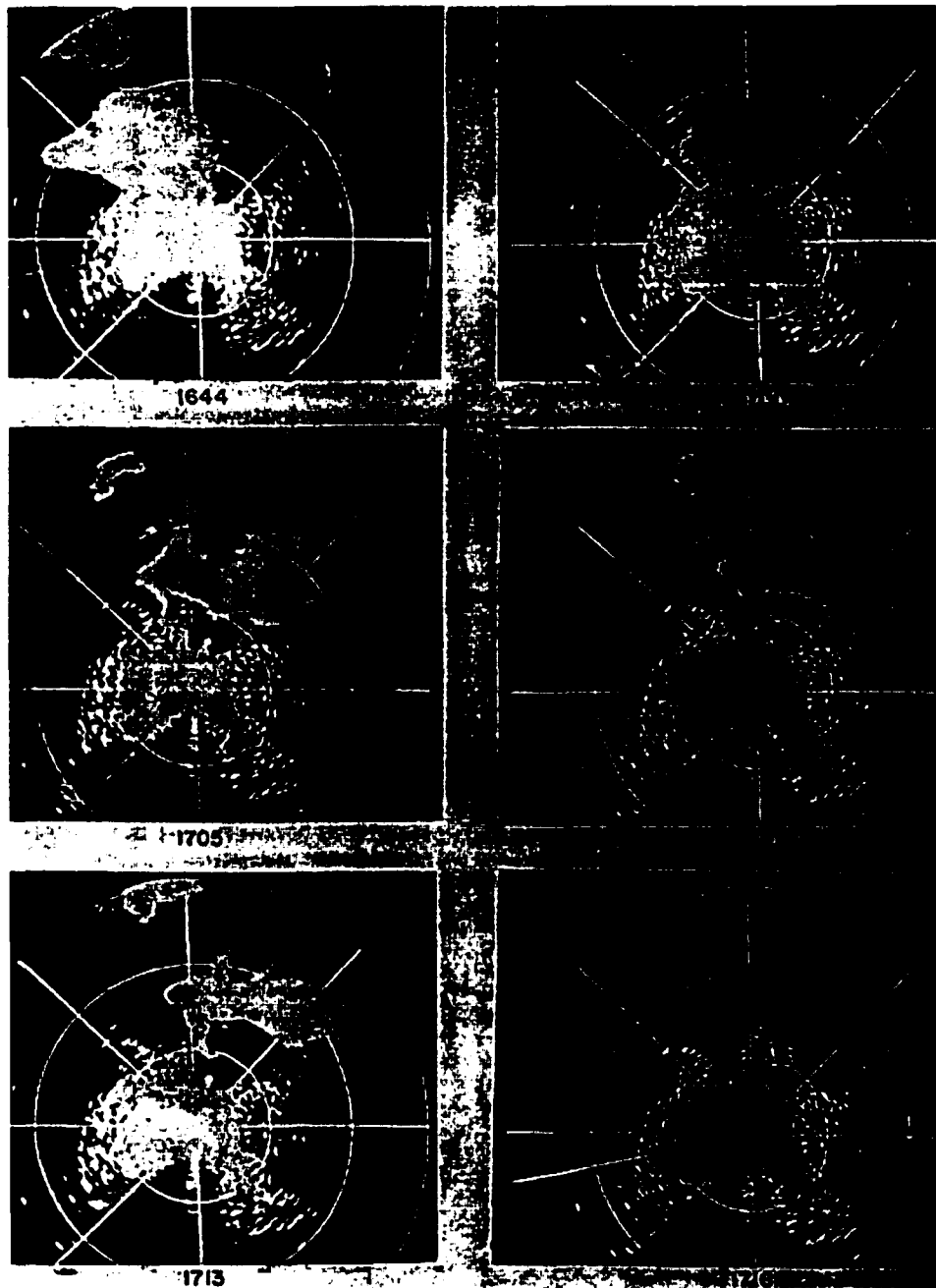


Figure 1.1: Radar images from the first documentation of a hook echo. The hook echo was associated with a tornadic supercell on 9 April 1953. [From Stout and Huff (1953).]

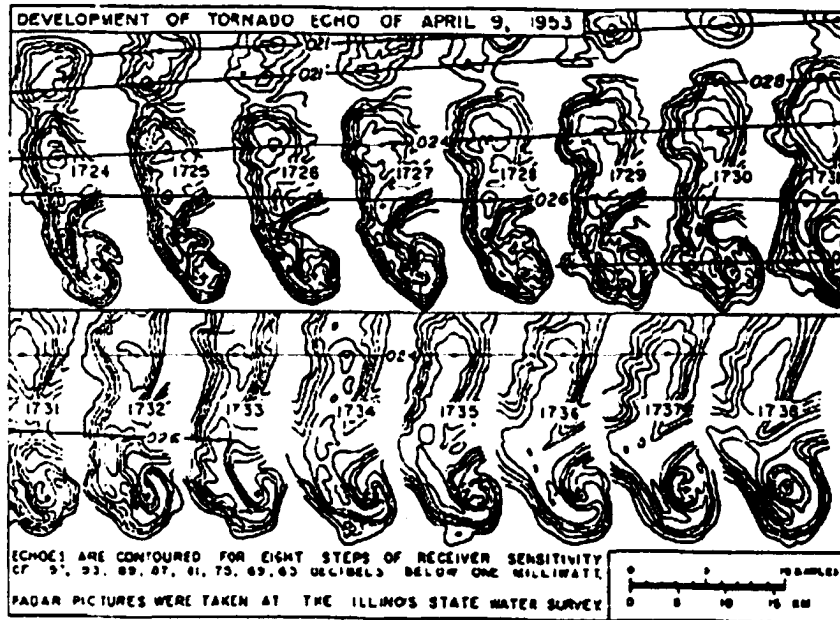


Figure 1.2: Development of the hook echo associated with the Champaign, Illinois tornado on 9 April 1953 from 1724-1738 CST, as analyzed by Fujita. [From Fujita (1958a).]

Fulks (1962) hypothesized that hook echo formation was due to a large convective tower extending into the levels of strong vertical wind shear, which produced cyclonic and anticyclonic flows at opposite ends of the tower—the cyclonic flow to the southwest gave rise to hook echo development. No mention was made of the possibility of an anticyclonic hook echo forming on the north side of the tower from the same mechanism.

Fujita (1965) later attributed hook echo formation to the Magnus force. He explained that this force “pulled” the spiraling updraft out of the main echo, resulting in the hook echo commonly observed on radar displays (Fig. 1.4). Furthermore, Fujita (1973) presented models of the variety of forms that the hook echo may take (Fig. 1.5).¹

¹Relatively recent radar observations of hook echoes (with greater spatial and temporal resolution than available in the 1960s and 1970s) suggest that hook echo formation may not result from any of these processes posed in the past, including solely advection of precipitation (Rasmussen and Straka 2001; L. Lemon 2000, personal communication). A thorough study of hook echo formation is beyond the scope of this dissertation.

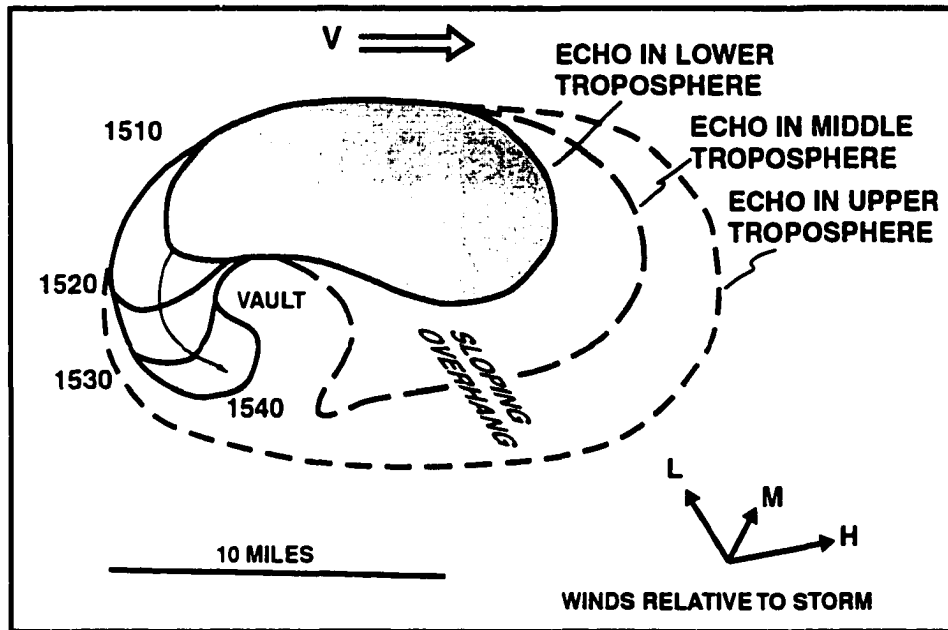


Figure 1.3: Evolution of the hook echo in an Oklahoma supercell on 26 May 1963 studied by Browning. [From Browning (1965b).]

The forecasting potential of hook echo detection began to be explored in the mid-1960s. Freund (1966) found that 6 of 13 tornadic storms near the National Severe Storms Laboratory (NSSL) in 1964 were associated with hook echoes. Furthermore, Sadowski (1969) documented a large amount of success using hook echoes to detect tornadoes within thunderstorms; he computed a false alarm rate of only 12% in a 1953-1966 study. On the other hand, Golden (1974) found that only 10% of waterspouts were associated with well-defined hook echoes.

The "Super Outbreak" of tornadoes on 3-4 April 1974 (Fujita 1975a,b) provided a large sample of a variety of "distinctive echoes" that were studied by Forbes (1975, 1981). Forbes (1975) found that (1) a majority of hook echoes were associated with tornadoes, (2) hook echoes often were associated with tornado families, and (3) tornadoes associated with hook echoes tended to be stronger than those from other echoes. Forbes (1975) also found that, on average, hook echoes appeared 25 min prior to tornado touchdown; however, much variance was present in his sample—10 of 27 (37%) of the hook echoes associated with the first tornado produced by a supercell

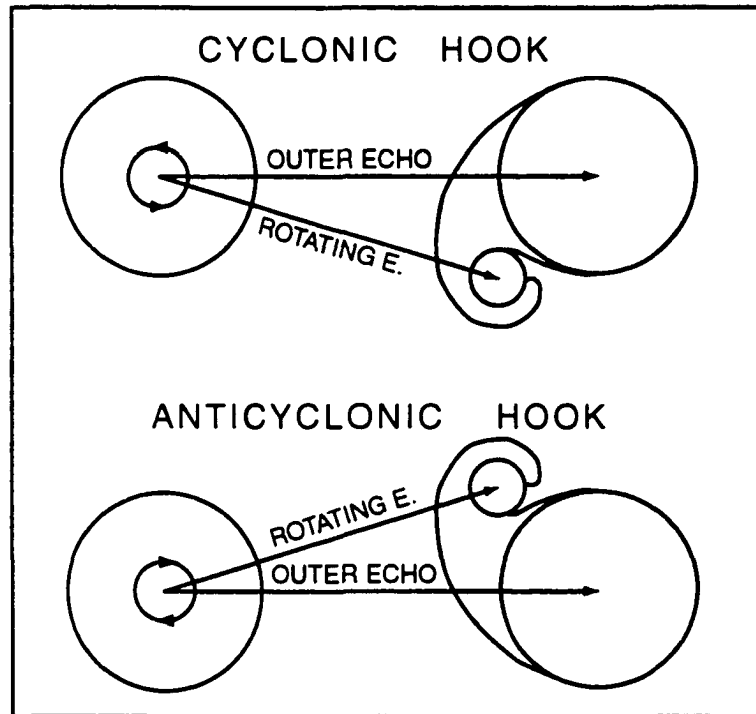


Figure 1.4: Fujita once hypothesized that the Magnus force led to the formation of hook echoes. [From Fujita (1965).]

were detected *after* the reported² tornado touchdowns. [Sadowski (1969) found an average time of 15 min between hook echo appearance and tornado touchdown in a sample of 13 cases in which hook echoes appeared before tornadoes were reported.]

Forbes (1981) found a false alarm rate of only 16% when using hook echoes to detect tornadoes. But because hook echoes were relatively rare (as he defined them), a less restrictive shape [a “distinctive echo,” e.g., appendages, line-echo wave patterns, etc.] also was considered. Distinctive echoes were associated with a probability of detection of tornadoes of 65%. Forbes (1975, 1981) did raise concern about the generality of his findings, since his statistics were based on the events of a single day. Finally, Forbes (1981) noted that “the hook represents a band of precipitation accompanied by downdraft and outflow, surrounding a WER (a region of inflow and updraft).” and that 1–10 min prior to tornadogenesis, a sharp reflectivity gradient

²The accuracy of the reported tornado times may be questionable for some of the tornadoes studied.

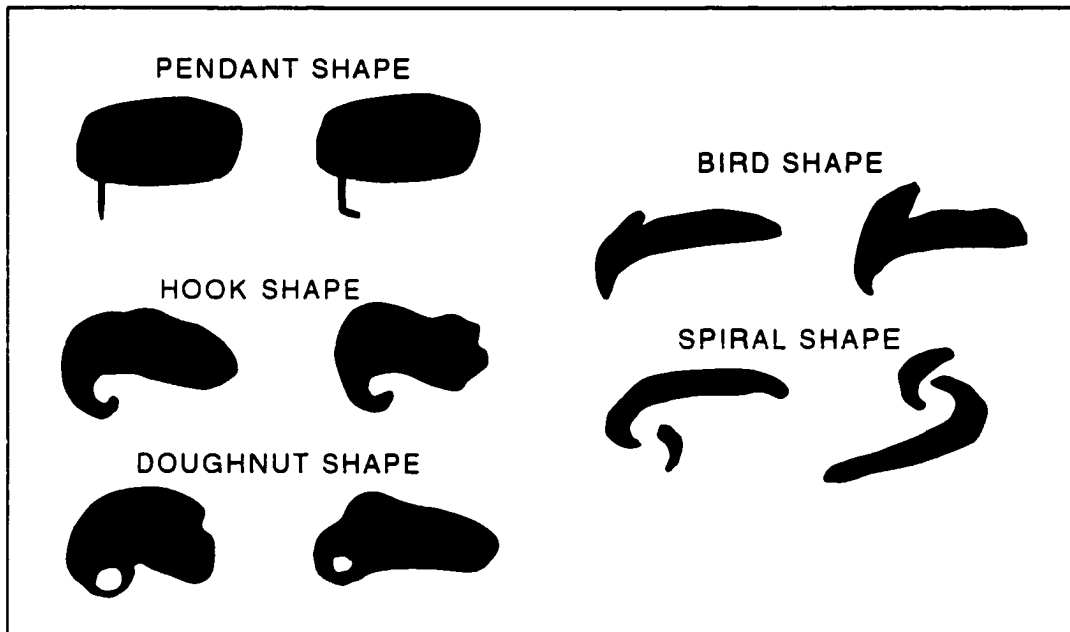


Figure 1.5: Fujita introduced five variations on the shapes of hook echoes. [From Fujita (1973).]

along the upshear side of the updraft (and occasionally a small echo mass several km to the right of the right-rear edge of the main echo) may appear.

Fujita and Wakimoto (1982) studied the Grand Island, Nebraska tornadoes of 3 June 1980, and not only documented an echo hole associated with a cyclonic tornado and a region of negative vertical vorticity on the opposite side of the hook echo, but the authors also documented an anticyclonic tornado on the side of the hook echo opposite that of the cyclonic tornado (Fig. 1.6). This anticyclonic vorticity region has been observed often (Brandes 1977b, 1981, 1984a; Ray 1976; Ray et al. 1975, 1981; Heymsfield 1978; Klemp et al. 1981), but its ubiquity largely has been ignored, with the exception of Fujita and his collaborators. Fujita (1981) proclaimed “*Mesoscale modelers should be attracted by such a pair of cyclonic and anticyclonic tornadoes which were evidenced in the Grand Island storm on 3 June 1980 and in the central Iowa storm on 13 June 1977.*” However, it was unclear why such attention should be given to the vortex couplet, and the couplet’s origin was not well understood.

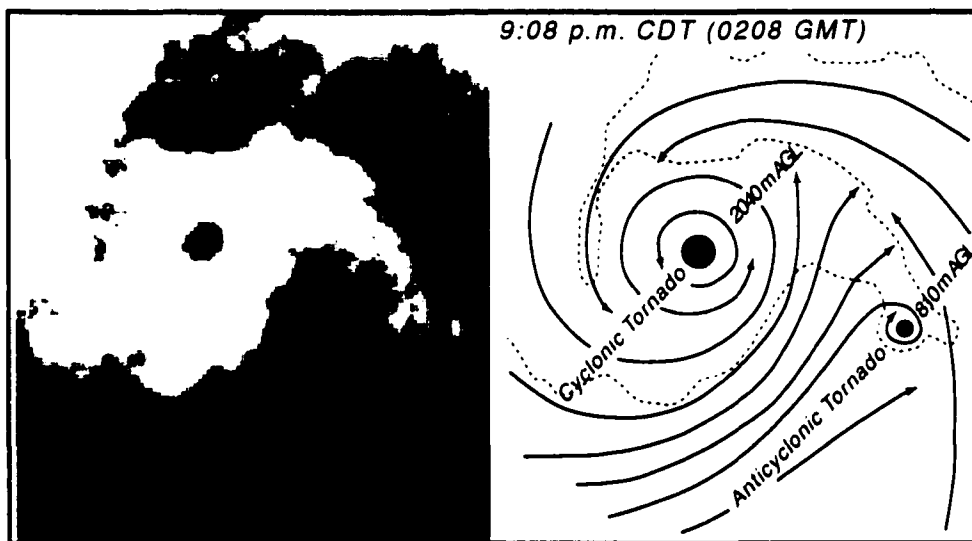


Figure 1.6: Radar image and analysis from Grand Island, Nebraska at 0208 UTC 4 June 1980 showing a vortex couplet straddling a hook echo, with tornadic circulations associated with *both* members of the vortex couplet. [From Fujita (1981) and Fujita and Wakimoto (1982).]

1.1.2 Rear-flank downdrafts

The first documentation of a rear-flank downdraft (RFD), although not recognized as such, was probably by van Tassell (1955). In that case study and in another by Beebe (1959) on the same storm complex, three “reliable” reports of severe downdrafts on the south side of the Scottsbluff tornado were made. One observer, located a few hundred meters south of the tornado, reported that the downdrafts felt “cold.”

Browning and Ludlam (1962) and Browning and Donaldson (1963) also were among the first to mention the presence of a downdraft in the vicinity of the strongest low-level rotation (behind the wall cloud). Both papers suggested that this downdraft may have been thermodynamically forced via evaporation. Browning and Donaldson (1963) also noted that the hook echo itself may be associated with this downdraft region. Browning (1964) surmised that the rightward propagation of “supercells” (a term that he coined to refer to steady, intense, large cells that appeared to propagate continuously to the right of the mean wind) increased their midlevel storm-relative flow so as to increase evaporative cooling, and ultimately aid in the genesis of downdrafts (both on the rear and forward storm flanks). These hypotheses were proposed at least partly because of findings by Browning and Ludlam (1962) and Browning and Donaldson (1963) of low wet-bulb potential temperature (θ_w) air in the wakes of the Wokingham, England and Geary, Oklahoma supercells, which apparently had midlevel origins. [Ward (1961) observed “cooler northwest winds a couple miles southwest of the (Geary) tornado.”]

In contrast to the findings of van Tassell (1955) and Beebe (1959), Browning and Ludlam (1962), and Browning and Donaldson (1963), Garrett and Rockney (1962) reported that a *warm* downdraft was observed about 12–15 km south of a tornado near Topeka, Kansas on 19 May 1960. The observer described the air as “suddenly becoming noticeably hot, similar to a blast of heat from a stove.” Furthermore, Williams (1963) also showed that RFD air can arrive at the surface warmer than the surrounding air. He noted that when such an event occurs, it may be south of the hook echo or wherever forced descent is less likely to encounter sufficient liquid water to maintain negative buoyancy.

Haglund (1969), Fujita (1973, 1979), Lemon et al. (1975), Burgess et al. (1977), Brandes (1977a), and Lemon (1977) also noted an association between hook echoes

and downdrafts. Haglund (1969) concluded that the hook echo trails the surface wind shift slightly, and is associated with the boundary between updraft and downdraft. Furthermore, surface analyses and aircraft penetrations have revealed that the hook echo is located in a region of large vertical velocity (w) and temperature (T) gradients, and somewhat behind the surface windshift line associated with the RFD (Burgess et al. 1977; Marwitz 1972a,c).

A few surface observations within RFDs were acquired prior to the more organized, scientific storm intercept programs conducted in the 1980s and 1990s. Tepper and Eggert (1956) analyzed traces of thermodynamic data within 25 km of tornadoes in more than 50 cases. Many of the thermograph traces measured minor fluctuations during the passage of the tornadoes (and associated RFDs, which were detected by the barograph traces), and other traces revealed cooling and moistening near the tornadoes. Only a few observations were available within 5 km of the tornadoes. Fujita (1958b) inferred the presence of a surface high pressure annulus encircling the Fargo, North Dakota, tornado cyclone (20 June 1957) from pressure traces in the vicinity of the tornadoes (Fig. 1.7). Although speculated, Fujita was unable to verify that the high pressure was associated with a ring of subsiding air surrounding the tornado. Ward (1964, 1972) and Snow et al. (1980) have found high pressure rings surrounding laboratory and numerically simulated vortices, but it is not clear whether these are the same phenomena inferred by Fujita, which appeared to be of a slightly larger scale.

Fujita (1975) was one of the first to mention the possible importance of downdrafts, especially those associated with hook echoes, in tornadogenesis, in terms of his "Recycling Hypothesis:" (1) downdraft air is recirculated into the (developing) tornado; (2) this process results in an appreciable convergence on the back side of the (developing) tornado; (3) the downward transport of the angular momentum by precipitation and the recycling of air into the tornado will create a tangential acceleration required for the intensification of the tornado. Research conducted with the aid of coherent radars in the ensuing years would lead others [e.g., Burgess et al. (1977), Barnes (1978a), Lemon and Doswell (1979), Brandes (1981)] to make the same general speculation.

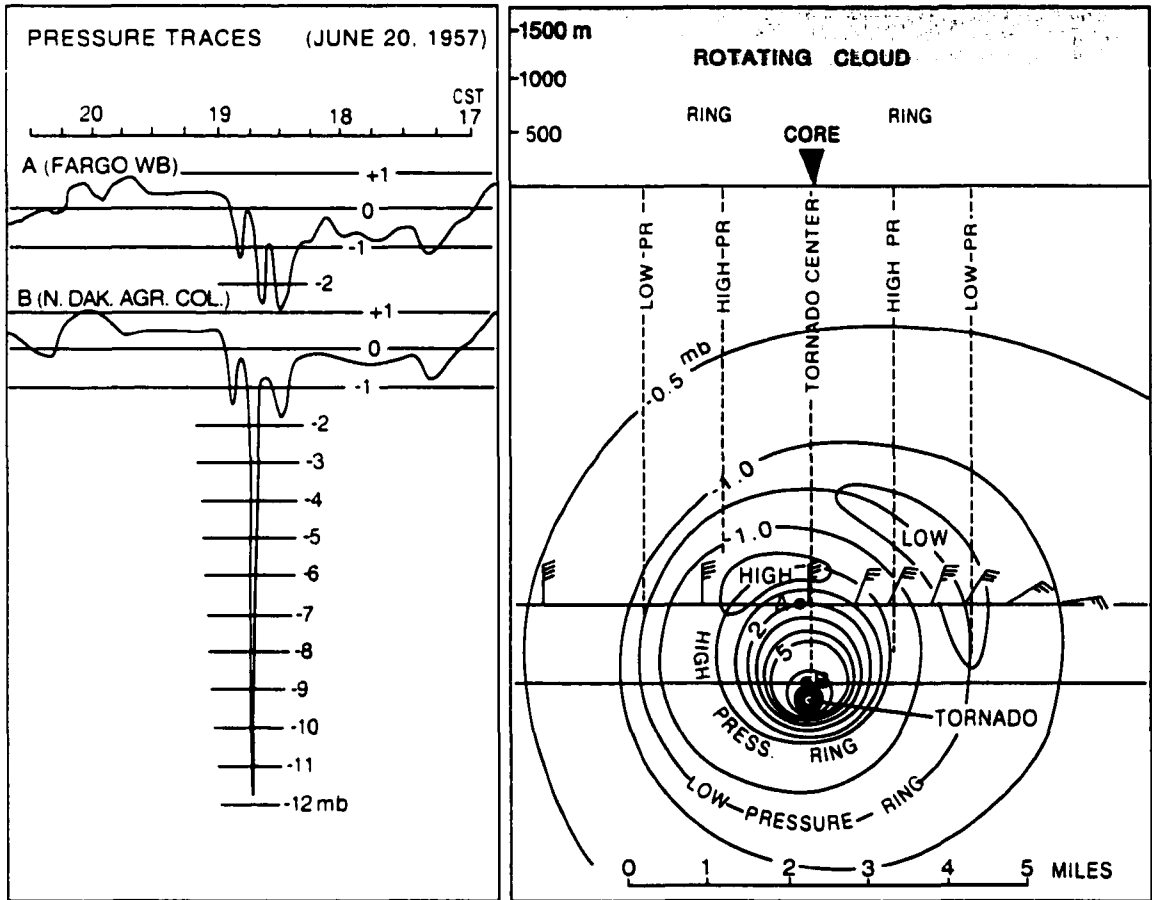


Figure 1.7: Pressure field near the center of the Fargo tornado cyclone (20 June 1957); A and B represent barograph stations. [Adapted from Fujita (1958b).]

1.2 Doppler radar studies

The installation of Doppler radars in central Oklahoma in the late 1960s allowed for the sampling of the three-dimensional wind structures of several supercells in the 1970s using dual- or multiple-Doppler radar techniques [Brandes (1993) provided a thorough review]. Some of these storms studied were the Harrah, Oklahoma (all storms listed hereafter occurred in Oklahoma) storm (8 June 1974; Ray 1976; Hevmsfield 1978), the Oklahoma City storm (20 April 1974; Ray et al. 1975), the Spencer-Luther storm (8 June 1974; Brandes 1978), the Del City storm (20 May 1977; Brandes 1981; Ray et al. 1981; Johnson et al. 1987), the Fort Cobb storm (20 May 1977; Johnson et al. 1987), the Lahoma storm (2 May 1979; Brandes et al. 1988), the Orienta storm (2 May 1979; Brandes et al. 1988), and the Lindsay storm (19 June 1980; Vasiloff et al. 1986).

1.2.1 Early single and multiple Doppler radar observations

Velocity data from the Doppler radar datasets mentioned above confirmed the previously believed association between hook echoes and strong horizontal shear zones associated with tornadoes (e.g., Donaldson 1970; Brown et al. 1973; Lemon et al. 1975; Ray et al. 1975; Ray 1976; Brandes 1977a; Burgess et al. 1977; Lemon 1977; Barnes 1978a,b). Burgess et al. (1977) believed that the RFD, hook echo, and tornadogenesis were intimately connected: *“The formation and evolution of the RFD is judged extremely important to tornado formation...the severe tornado [the Oklahoma City tornado of 8 June 1974] appears related to the increased vorticity source provided by presumed downdraft intensification and gust front acceleration along the right flank.”*

Lemon et al. (1978) suggested that the RFD formed above 7 km, based on analysis of the 24 May 1973 Union City, Oklahoma tornadic supercell. They analyzed a persistent diffluent flow region in the 7–10 km layer northwest (upshear) of the mesocyclone that they believed was associated with a downdraft.

Nelson (1977) found an erosion of the hydrometeor field at and below 7 km, as well as a sharp reflectivity gradient on the west flank of an Oklahoma multicell storm that evolved into a supercell on 25 May 1974—these radar observations were

believed to have been a manifestation of RFD formation that apparently occurred at the start of the transition from multicell to supercell. The lowest θ_w values were observed at the surface beneath the RFD (~ 6 K lower than than the “ambient” θ_w values. Complete separation of the forward-flank downdraft (FFD) and RFD was evidenced by separate temperature minima. Nelson noted two mechanisms suggestive of RFD formation – evaporative cooling and/or hydrodynamic pressure perturbations. Nelson believed that the evaporation-driven effect was more likely because of the echo erosion aloft: he also cited strong storm-relative winds (16 m s^{-1} at 7–9 km; 7 m s^{-1} at 4.5 km) and a large dewpoint depression (~ 21 K) at the level of apparent RFD formation.

Barnes (1978a) also concluded that the RFD originates at middle to upper levels (6.0–7.5 km) based on his study of the 29–30 April 1970 Oklahoma tornadic thunderstorms. He surmised that the storm-relative midlevel flow ($20\text{--}25 \text{ m s}^{-1}$) approaching the cyclonically rotating updraft was decelerated and deflected on the upwind (south) side while the relative upwind stagnation point shifted to the left of the intercepting wind vector: i.e., toward the southwest flank. Here “stagnating” air experienced the longest contact with the adjacent updraft while mixing only slightly with it – both cloud and small precipitation drops chilled this air by evaporation and begin its downward acceleration before saturation can occur. Barnes added “*We emphasize that the high horizontal momentum and proximity to the updraft make the RFD a potentially important interactant with the gust front and updraft’s surface roots . . . We also note that the location and extent of such a downdraft probably depends upon the ambient flow relative to the storm, which very likely requires a specific vertical shear profile to place it on the rear flank of a storm where it attains an influential position.*” Barnes interpreted the large reflectivity gradient on the midlevel upwind (southwest) flank as indicating dry ambient air adjacent to a precipitation-laden updraft [Bonesteel and Lin (1978) made a similar inference].

Based largely on the work by Barnes (1978a,b), Lemon and Doswell (1979) inferred that the RFD originated between 7–10 km on the relative upwind side of the updraft [note that they did not say *upshear* side; Rotunno and Klemp (1982) showed that the linear forcing for pressure fluctuations depends on the vertical shear, and numerical results confirmed this theoretical prediction, as did some later dual-Doppler radar findings (e.g., Hane and Ray 1985)]. They explained the evolution of

the RFD and tornadogenesis as follows: (1) air decelerates at the upwind stagnation point, is forced downward, and mixes with air below which then reaches the surface through evaporative cooling and precipitation drag; (2) the initially rotating updraft is then transformed into a new mesocyclone with a divided structure, in which the circulation center lies along the zone separating the RFD from the updraft (this process appears to result, in part, from tilting of horizontal vorticity); (3) “descent of the mesocyclone circulation occurs simultaneously (within the limits of temporal resolution) with the descent of the RFD.” The authors cited the observation of an echo-free hole at 7.5 km, directly above a notch behind the low-level hook echo - they believed this to be the signature of the RFD. Lemon and Doswell cited storm-relative midlevel inflow impingement as the RFD source, because Darkow and McCann (1977) showed that the relative flow at these levels is much stronger than the storm-relative minimum they found at 4 km, and because of the Barnes (1978a,b) and Nelson (1977) evidence. Lemon and Doswell also hypothesized that the RFD initially is dynamically forced, and then enhanced and maintained by precipitation drag and evaporative cooling.

Lemon and Doswell noted that just before tornadogenesis, the mesocyclone center shifted from near the updraft center to the zone of high vertical velocity gradient. The early mesocyclone was apparently a rotating updraft, whereas the transformed mesocyclone had a divided structure, with strong cyclonically curved updrafts to the east in the “warm inflow sector” and strong cyclonically curved downdrafts to the west in the “cold outflow sector.” And while the tornado was apparently found in a strong vertical velocity gradient, Lemon and Doswell noted that it was probably located on the updraft side of that gradient.

One last significant aspect of the review and conceptual model in Lemon and Doswell (1979; Fig. 1.8) was the absence of the anticyclonic vorticity commonly observed on the side of the hook and RFD opposite from the intense cyclonic vorticity (e.g., Ray et al. 1975; Ray 1976; Brandes 1977b, 1978). Understandably, greater attention historically has been given to the more intense cyclonic vorticity.

Klemp et al. (1981) attributed the RFD in the 20 May 1977 Del City, Oklahoma storm to water loading and evaporation based on precipitation trajectories crudely approximated using estimated terminal fall speeds. Moreover, midlevel flow approaching the storm from the east flowed through the FFD—not through the RFD

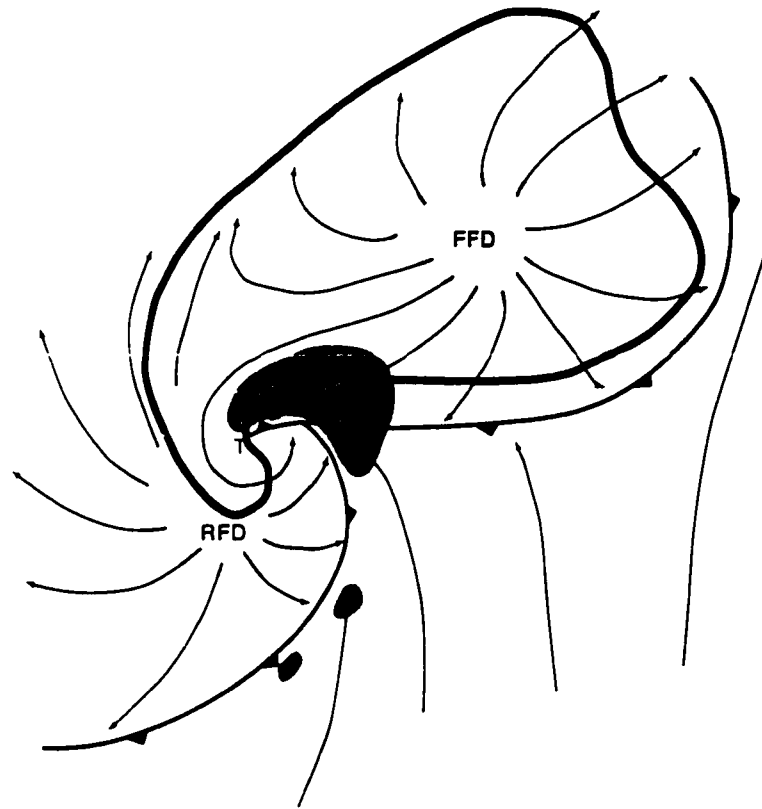


Figure 1.8: Conceptual model of a tornadic supercell at the surface based on observations and radar studies. [From Lemon and Doswell (1979).]

as Browning (1964) had conceptualized. RFD air at the surface appeared (from trajectory analyses in their numerical simulation and in the observations of the storm) to have come from 1–2 km above the ground (directly behind the gust front; air from higher levels reached the surface farther behind the storm).

Hane and Ray (1985) retrieved pressure and buoyancy fields in the Del City storm. In the pre-tornadic stage, the pressure distribution included at each level a high-low couplet across the updraft with the maximum horizontal pressure gradient ($\nabla_h p$) generally oriented along the environmental shear vector at that altitude, in agreement with linear theory predictions (Rotunno and Klemp 1982). In the tornadic stage the pressure field contained a pronounced minimum at low levels coincident with the mesocyclone, probably owing to strong low-level vertical vorticity (ζ). While the orientation of $\nabla_h p$ agreed relatively well with linear theory, the

strength of $\nabla_h p$ did not agree as well ($|\nabla_h p|$ depends on $|\partial \mathbf{v} / \partial z| |\nabla w| \cos \theta$, where \mathbf{v} is the horizontal wind velocity and θ is the angle between $\partial \mathbf{v} / \partial z$ and ∇w)—the authors stated that possibly the orientation and magnitude of the shear vector were not known exactly [owing to proximity issues for the “composite” sounding (e.g., Brooks et al. 1994b)]— $\nabla_h p$ is quite sensitive to $|\partial \mathbf{v} / \partial z| |\nabla w|$ —also, ∇w probably had significant errors]. Agreement of the locations of vorticity maxima with respect to $\partial \mathbf{v} / \partial z$ also appeared reasonable (in terms of linear theory; e.g., Rotunno 1981). Hane and Ray found weak high perturbation pressure ($p' \sim 1$ mb) in the RFD behind the gust front during the time of the tornado. An inflow low was retrieved (p' as low as -3 mb) east of the mesocyclone. Pressure excesses of 2–3 mb were retrieved in the precipitation core.

Hane and Ray (1985) attributed “occlusion downdraft formation” (reviewed in the next chapter) to increasing low-level rotation, but they, like others, did not discuss the asymmetry of the downdraft with respect to the vortex axis. Their Fig. 12 (Fig. 1.9) showed that the vorticity maximum was south of the buoyancy maximum at 1 km, but the authors used considerable smoothing on the buoyancy field to eliminate noise [Brandes (1984a) showed low-level buoyancy fields that contained considerable noise—the details in the low-level buoyancy fields retrieved by Hane and Ray (1985) and Brandes (1984a) probably are suspect]. The buoyancy and vorticity fields displayed in the figure would allow for the possibility of an off-vortex-axis occlusion downdraft that could be driven by low-level rotation, because the maximum vertical vorticity was not co-located with the maximum buoyancy (it should also be reminded that vertical pressure gradients associated with vertical vorticity gradients give rise to vertical accelerations, not vertical velocity itself). It also might be noteworthy that the tornado was situated in the buoyancy gradient between updraft and downdraft, and that the RFD contained significant negative buoyancy in Hane and Ray’s analysis (temperature deficit as low as -4.5 K).

Ray et al. (1981) showed evidence of a vorticity couplet straddling the hook echo (and downdraft maximum) of the Del City storm; the anticyclonic vorticity was small in magnitude, however. As with previous studies, little discussion was provided pertaining to the negative vorticity region, although the authors briefly mentioned that downward vortex tilting might have been the cause. The Doppler analyses by Klemp et al. (1981) of the same storm depicted a downdraft region that

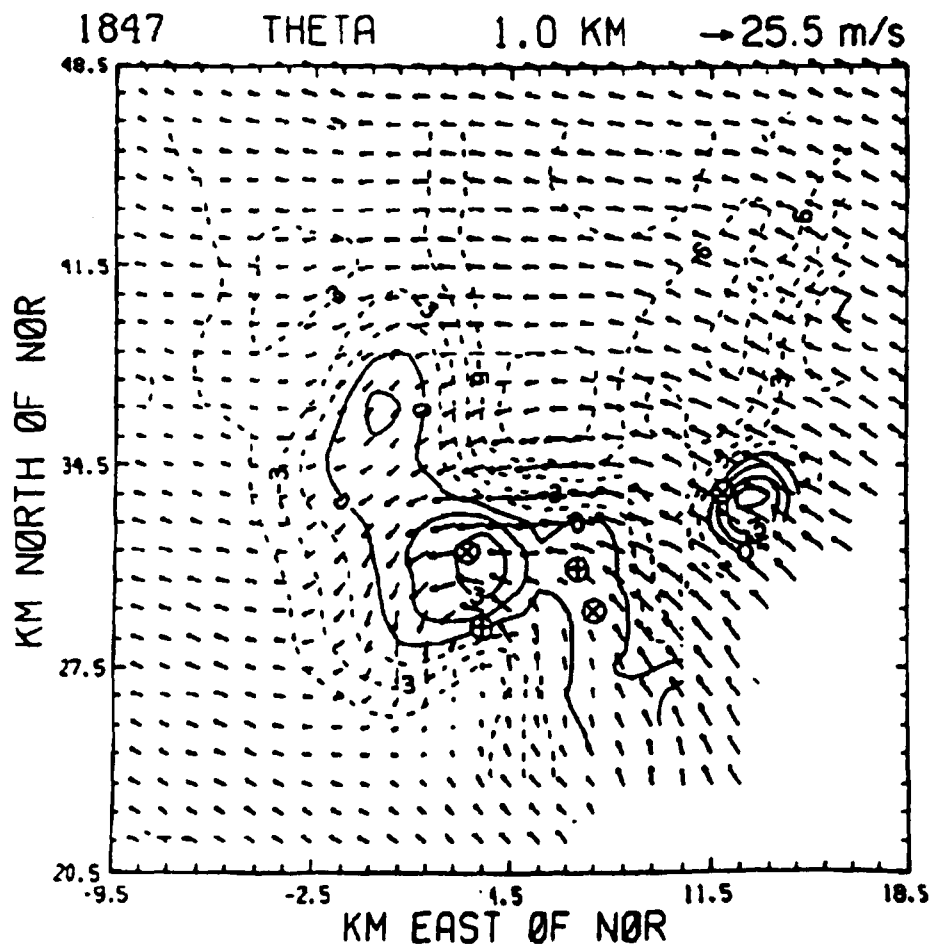


Figure 1.9: Horizontal distribution of buoyancy and vector horizontal wind at 1 km AGL at 1847 CST 20 May 1977 in the Del City storm. Buoyancy has been filtered to remove noise, and is contoured at 1.5°C intervals (negative values dashed). Updraft maxima are denoted by \oplus and vorticity maxima are denoted by \otimes . [From Hane and Ray (1985).]

turned counterclockwise (i.e., spiraled) around the updraft as it descended. The analyses by Klemp et al. also depicted anticyclonic vorticity at the surface on the opposite side of the RFD as the cyclonic vorticity; an anticyclonic reflectivity flare also was discernible. Maximum positive and negative vorticity (in their analysis and in their simulation results) were nearly equal in magnitude above approximately 2 km. But near the time of tornadogenesis, low-level (<2 km) maximum positive vorticity became twice as large as the negative vorticity.

Johnson et al. (1987) used observations of the 20 May 1977 tornadic storms to evaluate theories on the initiation of midlevel and low-level rotation and to verify thermodynamic retrievals. Johnson et al. found that the thermodynamic retrieval results by Brandes (1984a) and Hane and Ray (1985) were in good agreement with independent measurements where available; however, *“noticeable differences in the region of the RFD suggested that there was room for improvement in the retrieval methods.”* The vertical pressure gradients in the vicinity of the main updraft during the tornadic phase could not be verified by direct observation.

1.2.2 Brandes' work

Probably no one presented as many detailed Doppler radar analyses of supercells as Brandes [1977a, 1977b, 1978, 1981, 1984a, 1984b; Brandes et al. (1988)]. Brandes (1977a) looked at a non-tornadic supercell on 6 June 1974. Hook echo formation was attributed to the horizontal acceleration of low-level droplet-laden air as the downdrafts intensified and the outflow interacted with the inward-spiraling updraft (apparently this hypothesis was essentially that precipitation advection was responsible for hook formation). Moreover, Brandes hypothesized that the hook echo reflected downdraft intensification, and the hook shape was produced by “interaction between outflow and inflow.”

In addition to his study of the hook echo, Brandes (1977a) found low θ_w air ($\leq 18^\circ\text{C}$) on the southwest flank of the storm—this presumably was RFD air, and it was observed <6 km from the mesocyclone. Relatively high surface θ_w values ($\geq 20^\circ\text{C}$) were found in the central part of the reflectivity core (suggesting some mixing in the heavy rain areas with air originating at low levels). The rainfall maxima matched the hook echo locations, in contrast to Browning (1964), who

found the heaviest rainfall beneath left-hand parts of severe right-moving storms (i.e., in the main core).³

Brandes (1977b, 1978) analyzed the Oklahoma City and Harrah tornadic supercells of 8 June 1974. Observations again were made of vortex couplets that straddled the RFD and hook echo. With regard to the surface gust front, Brandes remarked that the wave-like gust front structure was remarkably similar to the roll-up of a perturbed vortex sheet into individual vortices. Furthermore, Brandes found that mesocyclones were occluded during the tornadogenesis stage and the parcels of air that entered the tornado came through the hook echo and RFD. Numerical simulation results (e.g., Wicker and Wilhelmson 1995) and more recent Doppler analyses (e.g., Dowell and Bluestein 1997) also have shown that the parcels entering the tornado pass through the RFD.

Brandes (1981) also showed evidence of anticyclonic vorticity on the opposite side of the hook echo as the cyclonic vorticity maximum in the Del City-Edmond tornadic storm of 20 May 1977 (his Figs. 2, 4, 5, 7, 8); however, no discussion of the feature was provided (Fig. 1.10). Brandes' Figs. 4a and 10 also depicted an anticyclonic reflectivity flare on the hook echo. As for RFD-genesis, Brandes stated "presumably the initiating downdraft (associated with the rear-flank gust front) is formed by precipitation falling from the sloping updraft ... we suppose the intruding flow has low θ_w , and when chilled by evaporation, becomes negatively buoyant ... because the entrained air penetrates well into the storm, evaporative cooling rather than perturbation pressure forces may initiate the downdraft." Intrusion of the hook south of the tornado was thought to result from increased entrainment and possible downdraft descent on the rear of the storm.

The tornado resided within the large vertical velocity gradient between the main updraft and RFD. Radial inflow accelerated to 35 m s^{-1} just prior to tornadogenesis. Brandes mentioned that the RFD appeared *prior* to tornadogenesis, in contrast to the Harrah tornado, in which, according to Brandes (1978), the RFD did not become prominent until after tornado formation. Maximum descent in the RFD was near 1.5–2.0 km. Brandes (1981) also stated "...the sudden appearance of

³The RFD may have been too cold/strong in this non-tornadic case—winds gusted to 42 m s^{-1} in the cold RFD.

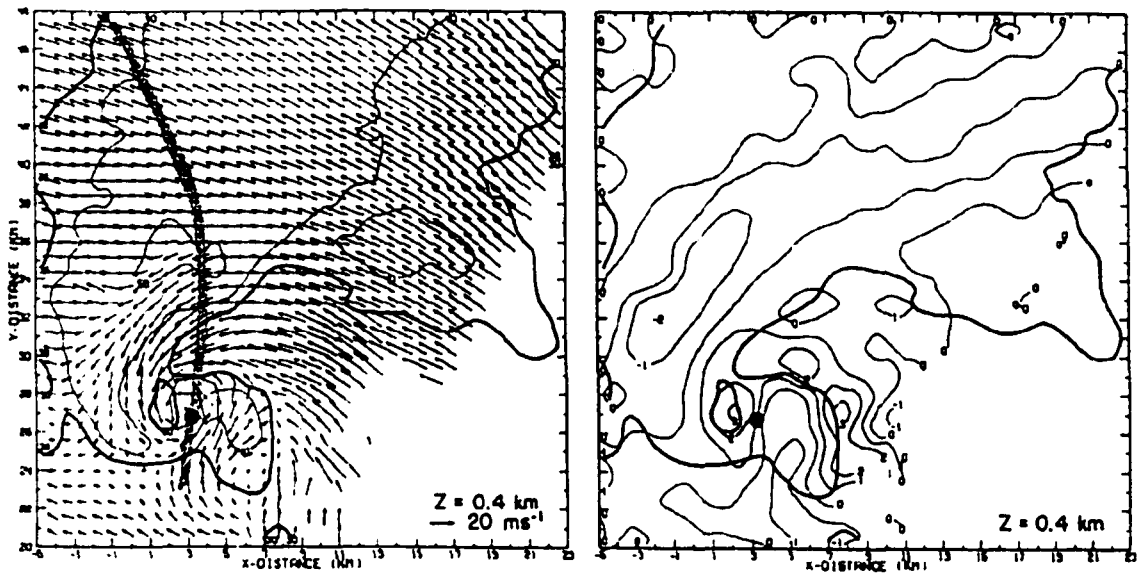


Figure 1.10: Three-dimensional wind field relative to the Del City storm at 1845 CST 20 May 1977 at 400 m AGL. Left panel shows horizontal wind vectors with reflectivity superposed. The right panel depicts vertical velocity (m s^{-1}), with the 30 dBZ contour accentuated on both panels. Tornado path is stippled. [From Brandes (1981).]

strong rear downdrafts in storms persisting for hours may also relate to the intensity and distribution of updrafts and vorticity.”

Blocking of midlevel environmental flow was most noticeable near the elevated vortex (5.4 km); the location of the vortex and the considerable entrainment to the right might have accounted for the apparent erosion of the radar reflectivity pattern [Brandes' (1981) Fig. 2]. The data also indicated that strong anomalous shears aloft *did not* build down to the surface prior to tornadogenesis, in contrast to radar observations of the Union City tornado (Lemon et al. 1978). Brandes suggested that stretching/conservation of angular momentum was most important for tornadogenesis, in contrast to the Lemon and Doswell (1979) model in which vorticity tilting by the RFD assumed a larger role. Brandes proposed that the RFD was important, but he did not state how or why—he also speculated more about the role that a shearing instability might play in tornadogenesis.

Brandes (1984a) retrieved the pressure and buoyancy fields in the Del City (20 May 1977) and Harrah (8 June 1974) tornadic storms (Fig. 1.11). [Hane and Ray (1985) also performed a thermodynamic retrieval on the Del City storm, but used a slightly different approach.] He found that upward-directed perturbation pressure gradient forces near the mesocyclone were reduced and could be reversed as the low-level vorticity amplifies; Brandes attributed the sudden formation of “concentrated rear downdrafts” to vertical, non-hydrostatic pressure gradient reversal. Furthermore, qualitative examination of the retrieved buoyancy distributions suggested that horizontal vorticity generation by buoyancy gradients in the inflow was not essential for mesocyclone intensification or tornadogenesis. [Johnson et al. (1987) also found weak forward-flank baroclinity in the Del City storm ($\Delta T < 2$ K over 15 km): the authors acknowledged that the baroclinity was too weak for it to be important.]

Brandes (1984a) also retrieved high p' on the rear of the Del City storm (as in Bonesteel and Lin 1978), but the data did not extend sufficiently far upwind so that vertical pressure gradients in the stagnation region could be examined. Some evidence was found of warm temperatures behind the gust front (Del City storm), which Brandes attributed to subsidence in the RFD.

Brandes (1984a) found cloud base temperature to be relatively cool ($T' < 0$), but an upward-directed non-hydrostatic vertical pressure gradient existed (Del City

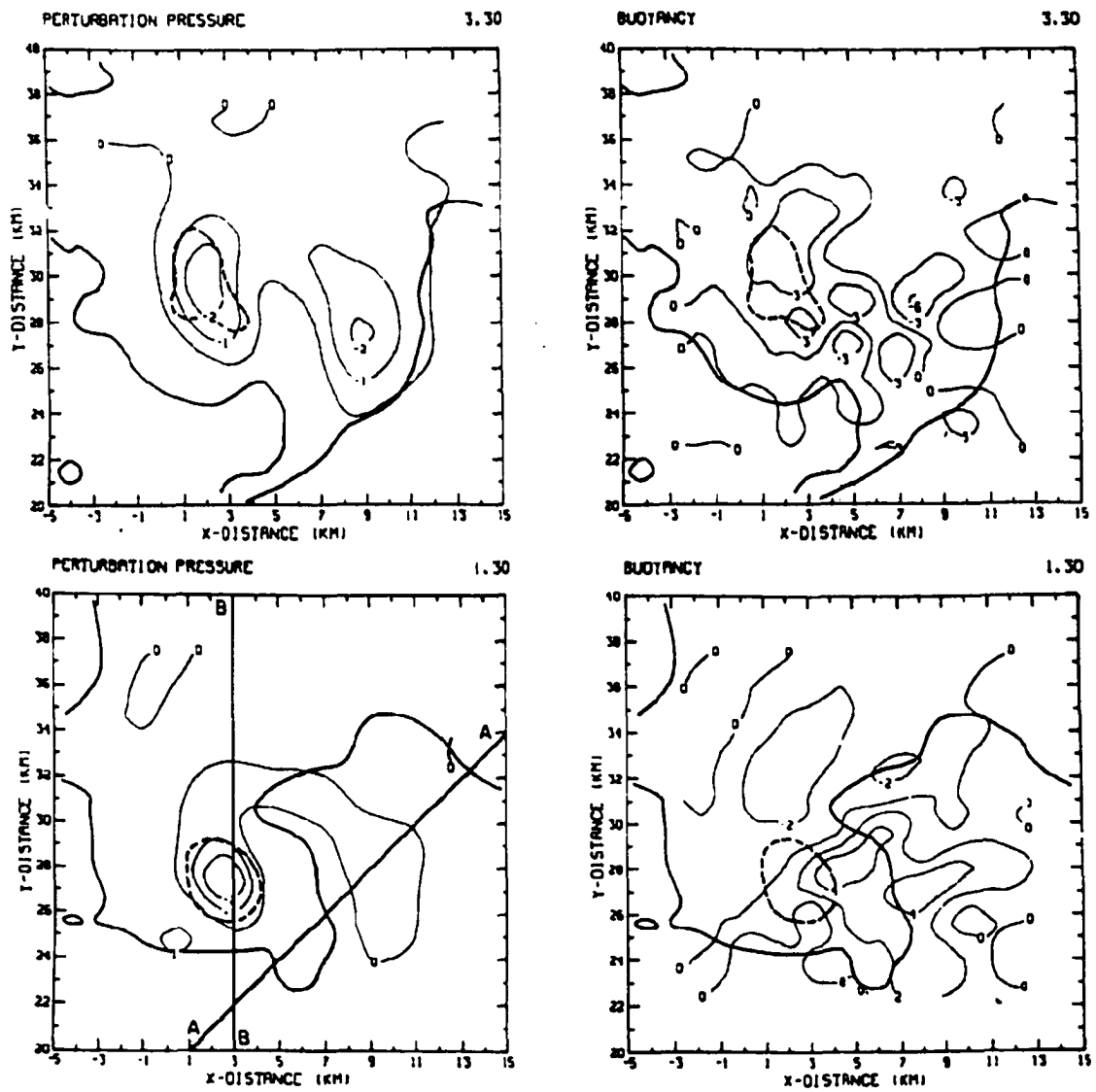


Figure 1.11: Retrieved perturbation pressure (mb; volume mean removed) and buoyancy ($^{\circ}\text{C}$) at 1.3 and 3.3 km AGL at 1845 CST 20 May 1977 in the Del City storm. Heavy line denotes the 30 dBZ reflectivity contour and heavy dashed line the mesocyclone. [From Brandes (1984a).]

storm). At 3.3 km, cool temperatures on the southern fringe of the storm were suggestive of evaporative cooling as environmental air mixed with storm air. Also at 3.3 km, cold temperatures were retrieved in the RFD—radar reflectivity was a minimum here, possibly implying that evaporation was occurring. In the Harrah storm, Brandes (1984a) also retrieved negative buoyancy in the RFD above the surface; no mention was made of the buoyancy immediately behind the gust front (in the Del City storm, Brandes stated that warm air was found near the surface behind the RFD gust front).

Brandes (1984a) attributed sudden “occlusion downdraft” formation to the vertical pressure gradient owing to the explosive growth of low-level vorticity as Klemp and Rotunno (1983) found. (Klemp and Rotunno defined the “occlusion downdraft” as a smaller-scale downdraft within the larger-scale RFD. A review of the origin of this term is presented in chapter 2.) However, Brandes’ data showed that the occlusion downdraft was not axisymmetric; this matter was not discussed. He argued that “previous explanations for rear downdrafts, such as evaporative cooling and downward pressure forces caused by strong upper tropospheric winds impinging upon storms, involved enduring processes which were inconsistent with the abrupt and concentrated nature of these phenomena.”

Brandes (1984b) claimed that the occlusion downdraft formed after the incipient tornado had been detected and roughly coincided with tornado touchdown. Brandes (1984b) concluded that (1) vertical vorticity amplification during tornadogenesis was largely by increased convergence that resulted from rainy downdraft-updraft interaction, and (2) rear downdrafts were not important for mesocyclone sustenance or intensification, although they figured prominently in the declining stages, when they pervaded the mesocyclone and vertical vorticity was reduced rapidly by divergence. He also stated that “. . . no compelling observational evidence was uncovered that related mesocyclone intensification to a vertical vorticity transport in either rainy or rear downdrafts.”

Brandes et al. (1988) hypothesized that because RFDs possessed weak positive or negative helicity (i.e., they straddled vortex couplets), the decline of storm circulation might be hastened by turbulent dissipation when the downdraft air eventually mixes into supercell updrafts. As in Brandes (1984a,b) and Klemp and Rotunno (1983), Brandes et al. claimed that “the updraft minimum in the Lahoma storm

and rear downdraft in the Orienta storm apparently owed their existence to the build-up of low-level vorticity and related downward vertical pressure gradients.” Large downward pressure forces existed within the rear downdraft and lefthand portions of the persistent updraft region in the Orienta storm, and to the rear of the persistent updraft in the Lahoma storm. Brandes et al. (1988) probably presented the most comprehensive analyses, discussion, and insight into the pressure distribution in supercells to date, but the RFD initiation mechanism remained unclear.

1.2.3 Obstacle appearance

Many have suggested that supercells act like obstacles in the flow (e.g., Newton and Newton 1959; Fujita 1965; Fujita and Grandoso 1968; Alberty 1969; Fankhauser 1971; Charba and Sasaki 1971; Lemon 1976b; Barnes 1978a; Klemp and Wilhelmson 1978a; Lemon et al. 1978; Lemon and Doswell 1979; Brandes 1981). Theoretical studies followed that refuted the obstacle analogy as a viable explanation for deviant storm propagation (e.g., Rotunno 1981; Rotunno and Klemp 1982), and these studies also showed that the pressure distribution around an updraft also was not what would be expected if the updraft was behaving as an obstacle [except at storm top (Davies-Jones 1985)]. Nonetheless, some studies have shown that updrafts can display behavior that appears similar to how a solid obstacle might be expected to behave.

Lemon (1976b) found evidence (five cases) of anticyclonic vortices being shed from severe right-moving storms. None of the eddies documented were cyclonic. Lemon offered two hypotheses: (1) von Karman vortices⁴ (do not require a rotating obstacle) — the cyclonic vortices were suppressed by enhanced subsidence on the right flanks that did not allow the vortices to persist and be advected downstream by the free stream velocity; (2) starting vortices (require a rotating obstacle)—the vortices were generated when a solid cylinder began rotating, with the vortices being shed with circulation of the opposite sign of the rotating cylinder. The second hypothesis might be more plausible, since it would explain why only anticyclonic eddies were

⁴Von Karman vortices have been shown in fluid dynamics laboratory experiments to develop when flow moves past a cylindrical solid object in intermediate Reynolds number (80–200) regimes (e.g., Kundu 1990)

observed. Furthermore, the second hypothesis was supported by the fact that the eddies were only observed in severe storms (assuming rotating updrafts are the most intense), and also because the vortices were seen shortly after the storms made right turns and hook echoes formed, suggesting that the eddy shedding occurred as a non-rotating obstacle first began to rotate. These observations suggested that updrafts might possess at least some blocking characteristics (or at least that updrafts were not entirely porous and did share similarities with solid, rotating obstacles).

Klemp et al. (1981) found in the Del City storm that flow around the storm at upper levels (7-10 km) resembled obstacle flow with strong outflow from the updraft being diverted downstream (Fig. 1.12). They noted, however, that this environmental air flow differed significantly from two-dimensional flow around an obstacle because flow approaching the storm just to the left of the "stagnation point" descended into downdraft regions while air immediately to the right entered the updraft and ascended to high levels. Below the 7-10 km layer (where flow was "obstacle-like"), the direction of flow within the updraft was strongly biased by the environmental wind direction at that level: this appeared to result partly from entrainment of environmental air into the updraft (Fig. 1.12).

1.2.4 Collapse of overshooting tops

Some evidence has suggested updraft weakening just prior to tornadogenesis. Burgess et al. (1977) and Lemon and Burgess (1976) documented tornadogenesis occurring during the collapse of the overshooting storm top. Fujita (1974a,b) also found visual and satellite evidence of an association between the collapse of overshooting tops and the onset of tornadogenesis, and hypothesized that tornadogenesis occurs when the overshooting top collapses (Fujita 1973).

1.3 Visual and surface observations of RFDs

Visual and surface observations of supercells increased during the 1970s largely because of organized storm intercept programs at NSSL (Golden and Morgan 1972; Davies-Jones 1986; Bluestein and Golden 1993). Many of these observations have

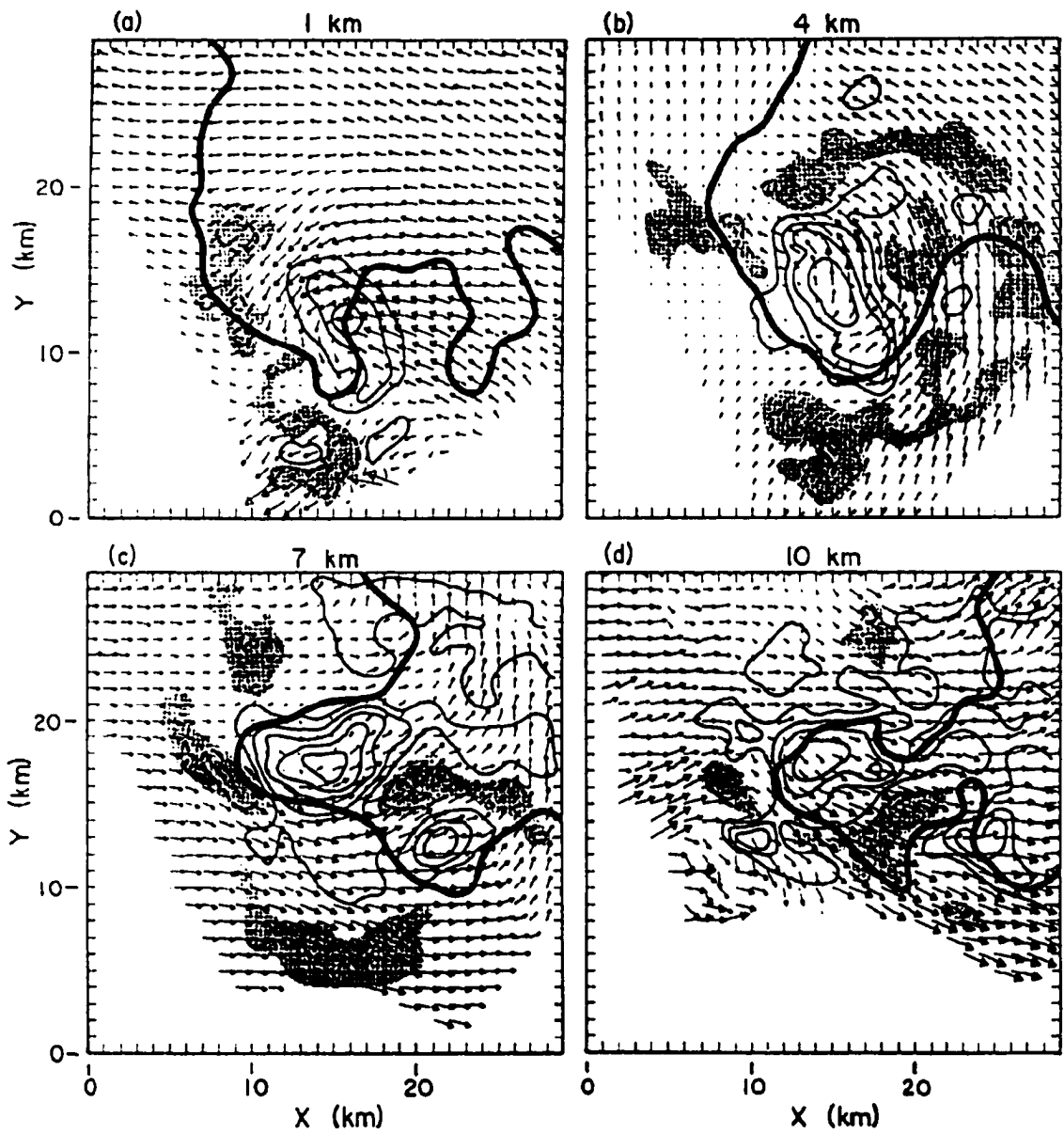


Figure 1.12: Horizontal cross sections of the Del City storm at 1833 CST 20 May 1977 at 1, 4, 7, and 10 km AGL. Updraft velocities (solid lines) and downdraft velocities (dashed lines) are contoured at 5 m s^{-1} increments. Shaded regions designate areas of negative vertical velocity ($w < -1 \text{ m s}^{-1}$). Wind vectors are scaled such that one grid interval represents 20 m s^{-1} . The heavy solid line corresponds to the 30 dBZ contour. [From Klemp et al. (1981).]

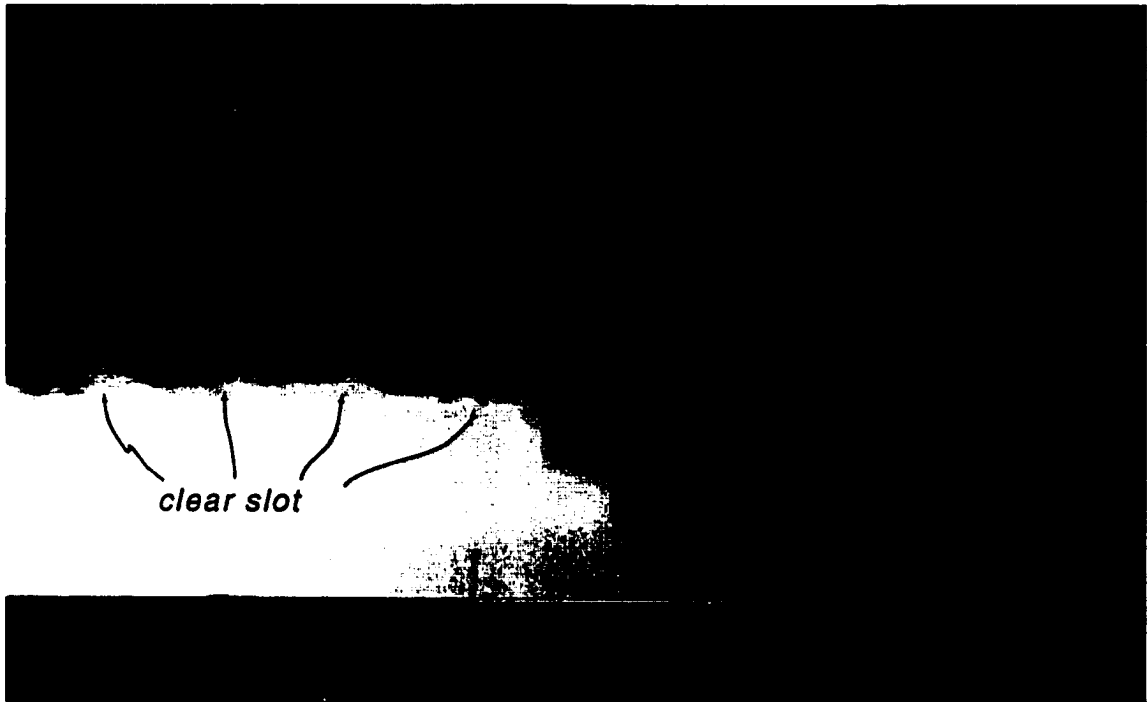


Figure 1.13: Photograph of the 2 June 1995 Dimmitt, TX tornado showing a typical clear slot associated with an RFD. Photograph by P. Markowski.

advanced our understanding of the basic structures of tornadoes and their parent storms.

Golden and Purcell (1978) photogrammetrically documented subsiding air on the south side of the Union City tornado, apparently a visual manifestation of the RFD and also evidence that the tornado occurred in a strong vertical velocity gradient. Moreover, a clear slot was seen to wrap itself at least two-thirds of the way around the tornado. Other observations of clear slots, which are probably always visual manifestations of subsiding air in an RFD, have been presented by Beebe (1959; this was probably the first documentation), Peterson (1976), Stanford (1977), Burgess et al. (1977), Lemon and Doswell (1979), Marshall and Rasmussen (1982), and Rasmussen et al. (1982) and Jensen et al. (1983), who also noted near total occlusion of the low-level mesocyclone prior to tornadogenesis (Fig. 1.13).

Burgess et al. (1977) also found that the clear slot could be associated with a hook echo: "Perhaps large droplets are present in the downdraft and are brought

down from the echo overhang, even though the air contains only ragged clouds or is visibly cloudless at low levels. If so, since radar reflectivity is more strongly dependent on the size rather than on the number of droplets, radar may show substantial echo in the 'clear' slot." [Analysis of the 2 June 1995 Dimmitt, TX tornadic supercell also indicated an association between the hook echo and clear slot, based on photogrammetrically determined cloud positions (Rasmussen and Straka 2001).]

Although a relatively small number of supercells were analyzed with Doppler radar, direct surface observations within supercells were even less common. Barnes (1978a,b) found that θ_w decreased by 2–3 K directly behind the RFD gust front in a tornadic storm on 29 April 1970; farther northwest, θ_w decreased by ≥ 5 K. Nelson (1977) also showed evidence of low θ_w at the surface in the divergent area behind the main updraft in his 25 May 1974 case. Furthermore, Lemon (1976) and Charba and Sasaki (1971) observed θ_w values compatible with midlevel (3–5 km) environmental air, as well as large pressure excesses and divergence on the right-rear flanks of supercells on 3 April 1964, immediately behind the echoes. Klemp et al. (1981) referred to "cold downdraft (rear-flank) outflow" in the Del City storm, but no evidence was presented proving that this was actually cold—observations by Brandes (1984a) and Johnson et al. (1987) suggested that at least parts of the Del City rear-flank outflow were warm, although θ_w values may not have been as large as in the inflow. Brown and Knupp (1980) documented nearly constant θ_w 3 km east of the Jordan, Iowa F3 and F5 tornado pair, and those observations probably were in the RFD air mass, based on the pressure trace, which measured a pressure excess of a few mb.

In his summary of Tobile Tornado Observatory (TOTO) observations, Bluestein (1983) documented a warm RFD and pressure rise of >2 mb in a non-tornadic supercell on 17 May 1981. Bluestein also presented evidence of a 1.5 K temperature rise in an RFD approximately 1.3 km south of the Cordell, Oklahoma tornado on 22 May 1981. Similar to what Fujita (1958b) first inferred, Bluestein also showed data that suggested high pressure at least partly encircling a tornado (his Fig. 7). In the violent Binger, Oklahoma tornado on 22 May 1981, small temperature fluctuations (<1 K) were observed as the tornado passed within a few 100 m north of TOTO.

Johnson et al. (1987) presented observations of the RFD and FFD of the Del City storm collected by a 444-m tower as the storm passed overhead. The RFD

was associated with equivalent potential temperature (θ_e) values approximately 4 K lower than the ambient conditions; however, the temperature increased 1.5 K and the dewpoint temperature decreased 2.5 K—if θ_e was nearly conserved, then air had subsided from approximately 1 km. Although the RFD was not sampled well by the tower, the data that were available suggested an apparent mesolow beneath the RFD. Also associated with the mesolow was a downward-directed perturbation pressure gradient force within the lowest half kilometer.

Lemon and Doswell (1979) proposed that RFD air can be distinguished from FFD air because it is drier, denser, and usually cooler. Other evidence of these differences appeared in Lemon (1974) and Nelson (1977), although Lemon and Doswell also noted the finding of Williams (1963) that RFD air can arrive at the surface warmer than its surroundings if insufficient condensate is present in the descending parcels to maintain negative buoyancy.

1.4 Recent findings

In contrast to the major observational, theoretical, and numerical simulation advancements of the previous decades, the last ten years have brought relatively few new revelations. The Verification of the Origins of Rotation in Tornadoes Experiment (VORTEX; Rasmussen et al. 1994) and smaller, post-VORTEX field experiments have collected surface data of unprecedented spatial and temporal resolution; however, these data have not yet been fully explored.

Rasmussen and Straka (1996) documented a warm RFD south of the Dimmitt tornado on 2 June 1995. In the same case, the hook echo was co-located with the surface divergence maximum, implying an association between the hook echo and (at least) a low-level downdraft [as also had been suggested by, e.g., Fujita (1973, 1975, 1979), Lemon (1977), Lemon et al. (1975), Brandes (1977), and Burgess et al. (1977)].

Additional evidence has come forth of vortex couplets straddling the hook echoes of tornadic storms (Rasmussen and Straka 1996; Wurman et al. 1996; Straka et al. 1996; Bluestein et al. 1997b; Dowell and Bluestein 1997; Wakimoto et al. 1998a,b; Rasmussen and Straka 2001) as well as in at least one non-tornadic storm (Gaddy and Bluestein 1998).

Wakimoto et al. (1998a) concluded that the occlusion downdraft was largely driven by the reversal of the vertical gradient of dynamic pressure, owing to increasing vorticity at low levels. They found that precipitation loading forcing of the occlusion downdraft was an order of magnitude less than the forcing provided by the non-hydrostatic vertical pressure gradient. [Carbone (1983) had suggested that precipitation loading may contribute to occlusion downdraft genesis.] Wakimoto et al. stated that “agreement between the occlusion downdraft and the (vertical) pressure gradient force provides convincing evidence that the negative vertical velocities are dynamically driven by the strong low-level rotation” (it is the author’s opinion that because pressure is retrieved from the 3D wind velocity field, the vertical pressure gradient force and vertical velocity fields should be expected to agree generally regardless of how realistic either field is). Wakimoto et al. did not discuss why the occlusion downdraft hypothesized to have been driven by low-level rotation was not coincident with the low-level vertical vorticity maximum (their Fig. 5f).

Other recent supercell studies by Blanchard and Straka (1998), Trapp (1999), and Wakimoto and Cai (2000) have presented evidence that the differences between tornadic and non-tornadic supercells may be subtle, if even distinguishable, in pseudo-dual-Doppler radar analyses of the wind fields. These observations partly have been a motivation for the present work. It is the author’s belief that the thermodynamic differences between these tornadic and non-tornadic supercells at the surface within their RFDs may not be so subtle. More discussion on this subject appears in future chapters.

Finally, at least one documentation has been made of hook echoes *not* associated with rotating updrafts and RFDs. Houze et al. (1993) showed examples of hook-shaped (in a cyclonic sense, with the hooks pointing toward the right with respect to storm motion) reflectivity structures in left-moving severe storms in Switzerland. These features, termed “false hooks” by the authors, apparently were associated with the cyclonic downdraft regions on the right (southern) flanks of the anticyclonically rotating storms [in which the updrafts would have been on the left (northern) flanks].

Chapter 2

Theoretical and numerical modeling studies pertaining to rear-flank downdrafts

2.1 Research prior to 1990

2.1.1 Numerical modeling efforts

At around the same time that the technological advance of Doppler radar allowed for a three-dimensional view of the air flow in a supercell, computer power had advanced to the point where three-dimensional cloud models could be contemplated (Rotunno 1993).

The first simulation was carried out by Schlesinger (1975), but a vortex pair at midlevels was the only feature that resembled a supercell. Later simulations, carried out for much longer than Schlesinger's original simulation, began to show features that were qualitatively similar in appearance to those observed in Doppler radar studies (e.g., Klemp and Wilhelmson 1978a,b; Wilhelmson and Klemp 1978).

Klemp et al. (1981) simulated a supercell with a composite sounding derived from three "proximity" soundings on 20 May 1977, and compared the simulated storm characteristics to those observed in the Del City storm (which was sampled by four Doppler radars). "Trajectory" analysis (these were not true trajectories, but rather streamlines if the storm was assumed to be quasi-steady, then the streamlines would be similar to trajectories) in the simulated supercell showed obstacle-like flow at 7–10 km. Parcels at 7 km that impinged upon the upshear side of the updraft did not appear to sink [in contrast to the hypotheses of Barnes (1978a), Nelson

(1977), and Lemon and Doswell (1979) which proposed that the RFD had an origin above 7 km], but those at 4 km did: i.e., the RFD was 4-7 km deep (parcels from 4-7 km did not reach the surface, but negative vertical velocities extended to 4-7 km). Surface RFD air appeared to come from 1-2 km aloft, directly behind the gust front: farther behind the gust front, air from higher levels reached the surface. Furthermore, the RFD air at the surface had θ_e values as much as 8 K lower than the surface inflow θ_e value. Lastly, the positive and negative vorticity maxima above 2 km were nearly equal in magnitude in the simulation by Klemp et al. But near the time of tornadogenesis, low-level positive vorticity became twice as large as the negative vorticity.

Klemp and Rotunno (1983) investigated the transition of a supercell into its tornadic phase through use of a high resolution (250 m grid spacing) model initiated within the interior of the domain of the Del City supercell simulation performed by Klemp et al. (1981). With the enhanced resolution, Klemp and Rotunno found that the low-level cyclonic vorticity increased dramatically and the gust front rapidly occluded as small-scale downdrafts developed in the vicinity of the low-level circulation center. They concluded that the intensification of the RFD during the occlusion process was dynamically driven by the strong low-level circulation. This was the first study to propose such a mechanism for downdraft genesis and intensification. Later, Brandes (1984a,b) and Brandes et al. (1988) would make the same conclusion based on Doppler radar analyses of tornadic storms.

Klemp and Rotunno (1983) defined the RFD as that "which supports the storm outflow behind the convergence line on the right flank." They stated that since non-tornadic storms often were observed to persist for long periods of time with a well-defined gust front, these storm-scale downdrafts (RFDs) were not uniquely linked to tornadogenesis within a storm. On the other hand, noted Klemp and Rotunno, if a storm progressed into a tornadic phase, the gust front became occluded and a strong downdraft formed directly behind the gust front at low levels and also might divide the updraft at midlevels. Klemp and Rotunno referred to this smaller-scale downdraft as the "occlusion downdraft." Klemp and Rotunno proposed that this occlusion process and its associated downdraft were dynamically induced by the strong low-level rotation that evolved along the convergence line. The rotation induced low pressure coincident with the center of circulation and dynamically forced

air down from above – the downdraft formed first at low levels and then extended upward as the flow adjusted to the non-hydrostatic vertical pressure gradient force. Rotunno (1986) also hypothesized that the occlusion downdraft was initiated by the explosive growth of vertical vorticity at low levels.

The finding of Klemp and Rotunno that the occlusion downdraft is *driven by low-level rotation* sometimes has been implied as being in conflict (e.g., Klemp 1987) with their predecessors' early hypotheses that the RFD is *driven from aloft* thermodynamically or dynamically and *is responsible for* increasing low-level rotation (e.g., Fujita 1975; Burgess et al. 1977; Barnes 1978a; Lemon and Doswell 1979). However, it is my opinion that the issue is one of semantics: I do not believe that a conflict exists at all. The occlusion downdraft and RFD are two distinct entities, as defined by Klemp and Rotunno; thus, the formation mechanisms and roles of the occlusion downdraft and RFD should not be anticipated to be necessarily identical. Observations of RFD formation preceding the increase of low-level vorticity are plentiful (e.g., Lemon and Doswell 1979; Brandes 1984a,b; Rasmussen and Straka 2001). Once a downdraft forms, the vertical distribution of angular momentum invariably must be affected, and feedbacks on the downdraft by the new angular momentum distribution would be probable (e.g., when low-level rotation becomes substantial, a downward-directed vertical pressure gradient could become established, accelerating air downward). Early hypotheses that the RFD is responsible for bringing rotation to low-levels never asserted that once low-level rotation began to intensify, that dynamic effects could not feed back on the downdraft. Therefore, I feel that the occlusion downdraft may be viewed as a rapid, small-scale intensification of the RFD that occurs after the RFD transports higher angular momentum air to low levels (i.e., the occlusion downdraft is a *byproduct* of the low-level vorticity increase); I stipulate that this evolution is not at odds with early proposals that the RFD is initiated at middle to upper levels and is responsible for initiating rotation near the ground (and I also speculate that the clear slot may be a visual manifestation of an intensifying RFD or "occlusion downdraft").

It should also be noted that although the occlusion downdraft in the Klemp and Rotunno (1983) simulation was found to be driven by low-level vorticity amplification, the occlusion downdraft *did not descend along the axis of low-level rotation*. No explanation was offered (one might expect that the vertical pressure gradient

associated with the vertical gradient of vertical vorticity would lead to a maximum acceleration along the rotation axis). Two reasons might account for the asymmetry: (1) the vertical pressure gradient associated with the vertical gradient of vertical vorticity ($\partial\zeta/\partial z$) does not contribute to vertical velocity directly, but rather to vertical accelerations (dw/dt)—thus, dw/dt might be a minimum in the vorticity maximum center, but if this occurs within the updraft (where $w \gg 0$), then a downdraft ($w < 0$) may first appear on the periphery of the updraft (away from the center of rotation), where w is less positive; (2) other terms in the vertical momentum equation, when combined with the vertical pressure gradient force ($\partial p'_D/\partial z$ —a dynamic perturbation pressure gradient) owing to $\partial\zeta/\partial z$, may force the strongest downward acceleration away from the axis of largest ζ —e.g., buoyancy or pressure gradients owing to buoyancy ($\partial p'_B/\partial z$ —a hydrostatic perturbation pressure gradient) may favor ascent in the updraft center, so that the net effect of buoyancy, $\partial p'_B/\partial z$, and $\partial p'_D/\partial z$ may yield the strongest downward acceleration on the updraft periphery. In fact, superposition of the fields of the vertical momentum equation forcing terms in Klemp and Rotunno's (1983) simulation leads to the strongest downward acceleration being a significant distance to the *south* of the maximum low-level rotation (Fig. 2.1). Thus, it is entirely possible for an occlusion downdraft to be "driven" by low-level rotation even if the occlusion downdraft is not co-located with the low-level rotation.¹

Rotunno and Klemp (1985) used simulations to investigate the origins of low-level rotation in supercells (being different from that responsible for midlevel rotation), and they were among the first [in addition to Davies-Jones (1984)] to use the property of near-conservation of equivalent potential vorticity to illustrate why linear theory appeared to be more accurate than one would expect in the presence of large amplitude perturbations. They also demonstrated how Bjerknes circulation theorem could be used to explore the origins of low-level rotation in a supercell. Though their work was important, the findings probably were not relevant to the subject of RFDs and hook echoes.

¹If a mesocyclone is vertically tilted, then it also may be possible for an occlusion downdraft to reach the surface away from the center of strongest surface vorticity, as found by Wakimoto and Cai (2000).

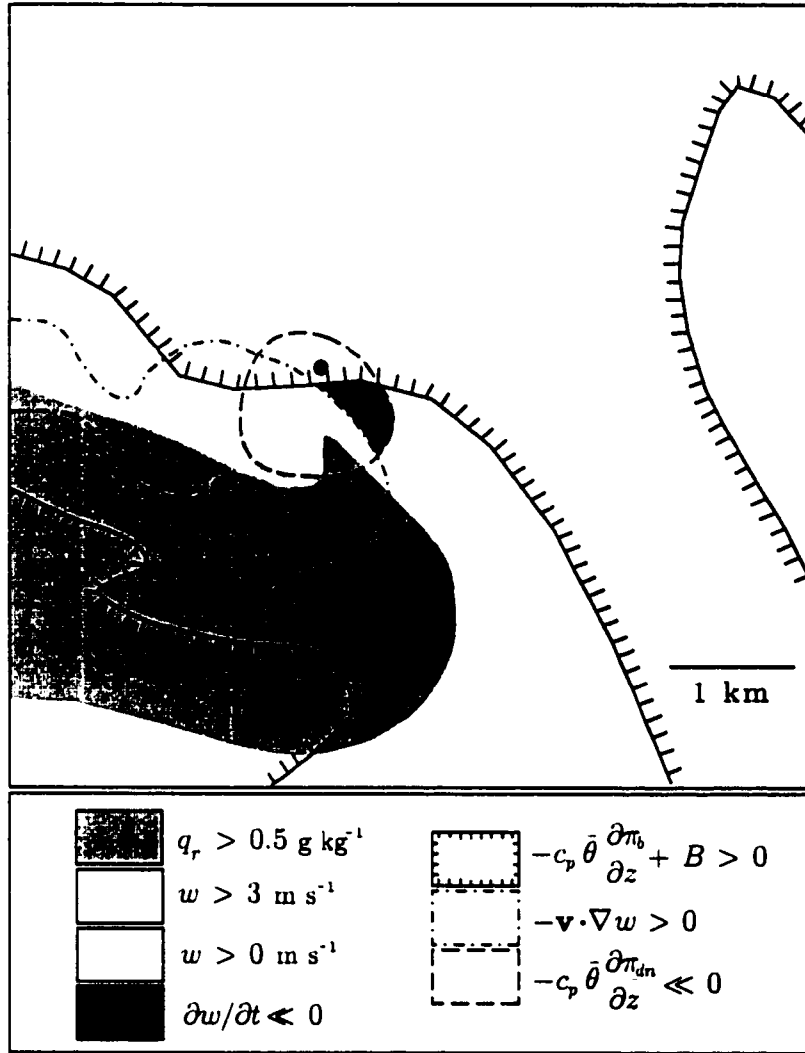


Figure 2.1: A composite of the forcing terms in the vertical momentum equation in the nested, high resolution simulation by Klemp and Rotunno (1983) at $t = 2$ min and $z = 250$ m. The figure has been adapted from Fig. 12 of Klemp and Rotunno's manuscript. The hook echo and regions where w exceeds 0 and 3 m s^{-1} are shaded according to the legend. The region where downward local vertical velocity accelerations ($\partial w / \partial t$) are largest also is shaded. This region is located where the superposition of the buoyancy forcing, advection, and dynamic pressure forcing leads to the strongest downward local vertical velocity changes ($\partial w / \partial t$). The regions where the buoyancy forcing ($-c_p \bar{\theta} \partial \pi_b / \partial z + B$, where π_b is the perturbation pressure owing to buoyancy, B is buoyancy, and all other terms have their conventional meanings) and advection of vertical velocity ($-\mathbf{v} \cdot \nabla w$) are positive, and where the dynamic vertical pressure gradient ($-c_p \bar{\theta} \partial \pi_{dn} / \partial z$, where π_{dn} is the perturbation pressure owing to nonhydrostatic effects) is most largely negative (downward), are indicated in the legend. The circulation center is indicated by the bold dot. Note that the largest downward acceleration occurs southeast of the low-level circulation center; a downdraft driven by increasing low-level rotation need not be co-located with the axis of strongest rotation.

Most three-dimensional numerical simulations of supercells have produced cold, negatively buoyant FFDs and RFDs. However, some idealized simulations have suggested that tornadogenesis may be favorable if downdrafts are not too cold. Eskridge and Das (1976) proposed that a warm, unsaturated downdraft could be important for tornadogenesis, although they did not specify whether the downdraft could also be cold, nor what the advantages of a warm downdraft over a cold downdraft were. Perhaps more importantly, Leslie and Smith (1978) found that some vortices could not establish contact with the ground when low-level stable air was present, even if very shallow. Remarkably, Ludlam (1963) many years earlier had argued that *“at least a proportion of the air that ascends in the tornado must be derived from the cold outflow; if this contains the potentially cold air from middle levels its ascent might be expected soon to impede if not destroy the tornado . . . it may be particularly important for the intensification and persistence of a tornado that some of the downdraft air may be derived from potentially warm air which enters the left flank of the storm at low-levels.”* Ludlam’s hypothesis may have been incredibly far-sighted, and it serves as a major motivation for this dissertation.

2.1.2 Theoretical studies

Although tilting of horizontal vorticity to produce a rotating updraft was first hypothesized by Barnes (1968, 1970) and demonstrated numerically by Schlesinger (1975), Klemp and Wilhelmson (1978a,b), and Wilhelmson and Klemp (1978), the first extensive theoretical study of the tilting process in supercells was provided by Rotunno (1981). Rotunno used a system of linearized momentum equations to show that linear theory can account for a pair of counter-rotating vortices straddling an updraft, such as those previously observed (Ray 1976; Ray et al. 1975; Ray et al. 1981) and numerically simulated (Klemp and Wilhelmson 1978a,b; Wilhelmson and Klemp 1978; Klemp et al. 1981) in supercells. Rotunno (1981) mentioned the alternative view that counter-rotating vortices are due to an effective obstacle formed by fluid of less horizontal momentum being transported upward, partially (at least) conserving that momentum, and so, at the higher level there is, relative to the surrounding flow, a deficit of horizontal momentum. Rotunno said “of course, these phenomena (tilting versus the process just described) are essentially the same.”

Rotunno and Klemp (1982) showed that linear theory predicts high and low pressure perturbations to be aligned with the environmental *shear* vector across the updraft, as opposed to the storm-relative wind. Rotunno and Klemp also commented on the obstacle flow analogy, which had been invoked numerous times to explain observations of midlevel rotation and stagnation high pressure, which could ultimately dynamically force an RFD (e.g., Alberty 1969; Lemon 1976b; Barnes 1978a; Klemp and Wilhelmson 1978a; Brown 1992): (1) significant entrainment of momentum occurs within the updraft “cylinder,” making it quite porous; (2) storm-relative flow impinging on the cylinder varies considerably with height; (3) the prediction of high and low pressure perturbations aligned with the environmental shear is consistent with the equations of motion. An important implication of their finding was that the prediction of the non-hydrostatic vertical pressure gradient is independent of any *a priori* estimate of storm motion.

While most of the theoretical studies pertaining to supercell storms investigated the development of midlevel rotation (e.g., Rotunno 1981; Rotunno and Klemp 1982; Lilly 1982, 1986a,b; Davies-Jones 1984), Rotunno and Klemp (1985) explored the source of low-level (1–3 km AGL) rotation in supercells and found the source (baroclinic horizontal vorticity generation in the forward-flank buoyancy gradient) to differ from the source of midlevel rotation (horizontal vorticity associated with the mean vertical shear). However, it was Davies-Jones (1982a,b) who first noted that in order to obtain large vertical vorticity at the ground (i.e., a tornado) in an environment in which vortex lines are initially quasi-horizontal, a *downdraft* would be necessary.

Davies-Jones (1982a,b) concluded that in a sheared environment *with negligible background* vertical vorticity, an “in, up, and out” circulation driven by forces primarily aloft would fail to produce vertical vorticity close to the ground [this conclusion depends on eddies being too weak to transport vertical vorticity downward against the flow: this was verified by Rotunno and Klemp (1985) and Walko (1993)]. If a Beltrami model is crudely assumed to represent the flow in a supercell (Davies-Jones and Brooks 1993), then vortex lines are coincident with streamlines and parcels flowing into the updraft at very low levels do not have significant vertical vorticity until they have ascended a few kilometers. Otherwise, abrupt upward

turning of streamlines, strong pressure gradients, and large vertical velocities would be required next to the ground.

Davies-Jones (1982a,b) neglected baroclinic vorticity and suggested that the downdraft had the following roles in near-ground mesocyclogenesis: (1) tilting of horizontal vorticity by a downdraft produces vertical vorticity; (2) subsidence transports air containing vertical vorticity closer to the surface; (3) this air flows out from the downdraft and enters the updraft where it is stretched vertically; (4) convergence beneath the updraft is enhanced by the outflow. Davies-Jones also showed kinematically that the flow responsible for tilting and concentrating vortex lines also tilts and packs isentropic surfaces, thus explaining observations of strong entropy gradients across mesocyclones near the ground.

2.2 Recent studies

In this section a short summary is presented of numerical and theoretical studies conducted in the last ten years.

Davies-Jones and Brooks (1993) showed that the vertical vorticity of air parcels descending in an RFD can be reversed during descent (from anticyclonic initially to less anticyclonic to cyclonic in the lowest 50-125 m of their descent):

1. Strong storm-relative inflow restrains the outflow beneath the updraft (Brooks et al. 1993)
2. As air subsides in the downdraft, vortex lines turn downward due to the barotropic "frozen fluid lines" effect, but with less inclination than the trajectories because horizontal southward vorticity is being generated continuously by baroclinity
3. Because the downdraft subsides "feet first" and the vortex lines now cross the streamlines from lower to higher ones, the barotropic effect acts to turn the vortex lines upward even during descent (tilting)
4. The baroclinic effect acts to increase horizontal vorticity further but does not control the sign of the vertical vorticity

5. Thus, air with cyclonic vertical vorticity appears close to the ground; as this air passes from the downdraft into the updraft, its cyclonic spin is substantially amplified by vertical stretching

Wicker and Wilhelmson (1995) used a two-way interactive grid to study tornadogenesis. During a 40-min period, two tornadoes grew and decayed within the mesocyclone. Maximum ground-relative surface winds exceeded 60 m s^{-1} during the tornadoes, which lasted approximately 10 min. Tornadogenesis was initiated when the mesocyclone rotation increased above cloud base; the increased rotation generated lower pressure in the mesocyclone, increasing the upward-directed dynamic vertical pressure gradient force. The upward-directed pressure gradient force accelerated the vertical motions near cloud base (to $20\text{-}30 \text{ m s}^{-1}$); as the updraft at cloud base intensified, the convergence in the subcloud layer increased rapidly and stretched vorticity sufficiently to form a tornado. No hypothesis was put forth of what caused rotation to suddenly increase above cloud base. Tornado decay began when the vertical pressure gradient decreased or reversed at cloud base, weakening the updraft above the tornado (apparently the vertical pressure gradient was upward-directed, not downward-directed just prior to tornadogenesis, when others found it to be downward-directed at the time of occlusion downdraft initiation). As the updraft weakened, the low-level flow advected the occlusion downdraft completely around the tornado, surrounding it with downdraft and low-level divergence. Cut off from its source of positive vorticity, the tornado dissipated, leaving a broad low-level circulation behind.

Wicker and Wilhelmson's Fig. 9 showed a spiraling, asymmetric RFD associated with tornadogenesis. Their figure also indicated anticyclonic vertical vorticity on the opposite side of the RFD as the cyclonic vertical vorticity. Furthermore, the RFD contained low θ_e values (θ_e' was as low as -15 K ; θ_e' was approximately -5 to -8 K in the hook echo).

In contrast to Davies-Jones and Brooks (1993), Trapp and Fiedler (1995), and Adlerman et al. (1999), Wicker and Wilhelmson claimed that "cyclonic vorticity found in the mesocyclone near the ground appears to be generated primarily from inflow air, which originates east of the forward flank downdraft and very close to the

ground.” Wicker and Wilhelmson also found that parcels that entered the mesocyclone from the RFD descend from ~ 500 m (like Davies-Jones and Brooks found) and initially contained negative vertical vorticity; however, vertical vorticity increased to only weakly negative values, not large positive values as Davies-Jones and Brooks had found. Trajectories into the tornado from the RFD revealed that positive vertical vorticity was acquired only after parcels began to ascend, not while they were still descending (Davies-Jones and Brooks 1993; Trapp and Fiedler 1995; Adlerman et al. 1999).

Trapp and Fiedler (1995) used an idealized thunderstorm representation (a “pseudostorm”) that emulated the storm-relative flow, into an updraft, of the horizontal streamwise vorticity that is baroclinically generated in cold air outflow. They concluded that the occlusion-like downdraft was an *effect* of the strong vortex flow on the vertical velocity and pressure fields rather than a cause of the final vortex spin-up. (Again, as iterated in the previous section, I do not believe that these findings are in conflict with the hypothesis that the RFD transports vorticity to low levels.)

Brooks et al. (1994a) found that the formation of persistent near-ground rotation was sensitive to the strength of the storm-relative midlevel winds. When storm-relative midlevel flow was too weak, outflow undercut the updrafts and associated mesocyclones. When storm-relative midlevel flow was too strong, the cold pool was not oriented suitably for vorticity generation in the baroclinic zone immediately behind the updraft, which was found to be needed for the development of near-ground rotation in their simulations.

Davies-Jones (1996) showed that low-level pressure had been incorrectly diagnosed by Rotunno and Klemp (1982) and a few others because they used their heuristic pressure solution (which assumes $\nabla^2 p \sim -p$, which is only approximately correct away from boundaries) to deduce pressure near the ground. This paper probably does not have much relevance for RFD formation; however, Davies-Jones showed how Rotunno and Klemp’s assumption did not allow pressure gradients to exist at the surface (since the linear forcing, $\partial \mathbf{v} / \partial z \cdot \nabla w$, is zero at the ground). Davies-Jones demonstrated that consideration of the proper lower boundary condition allowed for correct prediction of inflow lows. Davies-Jones also mentioned that the obstacle analogy predicts the direction of the horizontal pressure gradient force

correctly only near the equilibrium level, where the flow resembles a source in a uniform stream.

Shapiro and Markowski (1999) investigated the formation of downdrafts in simple two-layer (three-layer) vortices using an analytic (numerical) model. Applicability of the idealized model to real atmospheric vortices, in which buoyancy, buoyancy gradients, precipitation, and asymmetries probably are important, is questionable. Their results demonstrated how the "vortex-valve" effect (Lemon et al. 1975; Davies-Jones 1986) can transport vorticity from the top of a homogeneous, axisymmetric, rotating fluid to low levels via an annular downdraft and secondary circulation, when the top layer of fluid rotates with an angular velocity larger than that of the bottom layer of fluid.

Observation/Conclusion	References
RFD originates at or above 7 km	Nelson (1977), Lemon et al. (1978), Barnes (1978a), Lemon and Doswell (1979)
RFD originates below 7 km	Klemp et al. (1981)
Low θ_w at surface in RFD	van Tassell (1955), Beebe (1959), Ward (1961), Browning and Ludlam (1962), Browning and Donaldson (1963), Charba and Sasaki (1971), Lemon (1976a), Nelson (1977), Brandes (1977a), Barnes (1978a,b), Klemp et al. (1981), Wicker and Wilhelmson (1995)
Warm air (but not necessarily high θ_w) at surface in RFD	Tepper and Eggert (1956), Garrett and Rockney (1962), Williams (1963), Brown and Knupp (1980), Bluestein (1983), Brandes (1984a), Johnson et al. (1987), Rasmussen and Straka (1996), Rasmussen and Straka (2001)
Hypothesized that the occlusion downdraft is driven by low level ζ	Klemp and Rotunno (1983), Brandes (1984a,b), Hane and Ray (1985), Rotunno (1986), Brandes et al. (1988), Trapp and Fiedler (1995), Wakimoto et al. (1998a)
Hypothesized the RFD is forced mainly thermodynamically from aloft, which may result from stagnated	Browning and Ludlam (1962), Browning and Donaldson (1963), Browning (1964), Nelson (1977), Barnes (1978a), Brandes (1981), Klemp et al. (1981)
Hypothesized the RFD is initiated by dynamic p aloft but maintained thermodynamically	Lemon and Doswell (1979), Bonesteel and Lin (1978) mentioned vertical pressure gradients but did not necessarily discuss thermodynamic aspects
Reflectivity gradients found on the upshear side of storms	Nelson (1977), Bonesteel and Lin (1978), Barnes (1978a), Forbes (1981)
Tornadogenesis observed before hook formation	Garrett and Rockney (1962), Sadowski (1969), Forbes (1975)
Tornadogenesis observed at the time of overshooting top collapse	Fujita (1973,1974a,b), Lemon and Burgess (1976), Burgess et al. (1977)
Visual observations of clear slots accompanying tornadoes	Beebe (1959), Garrett and Rockney (1962), Moller et al. (1974), Peterson (1976), Stanford (1977), Burgess et al. (1977), Lemon and Doswell (1979), Marshall and Rasmussen (1982), Rasmussen et al. (1982), Jensen et al. (1983), Wakimoto et al. (1998b), Rasmussen and Straka (2001)
ζ couplets associated with hook echoes	Ray (1978), Ray et al. (1975,1981), Brandes (1977b,1978,1981,1984a), Heymsfield (1978), Klemp et al. (1981), Fujita (1981), Fujita and Wakimoto (1982), Klemp and Rotunno (1983), Wicker and Wilhelmson (1995), Wurman et al. (1996), Straka et al. (1996), Bluestein et al. (1997b), Dowell and Bluestein (1997), Gaddy and Bluestein (1998), Wakimoto et al. (1998a,b)
Anticyclonic reflectivity flares on the hook echoes	van Tassell (1955), Brandes (1981), Fujita (1981), Fujita and Wakimoto (1982), Wurman et al. (1996), Rasmussen and Straka (2001)
Hook echo formation attributed to rotation (but not necessarily the same mechanisms)	Fujita (1958a), Fulks (1962), Browning (1964,1965b), Fujita (1965), Brandes (1977a)
Hook echoes associated with strong horizontal shears at tornadoes	Stout and Huff (1953), van Tassell (1955), Fujita (1958a,1965), Garrett and Rockney (1962), Browning (1964,1965b), Freund (1966), Sadowski (1958,1969), Donaldson (1970), Forbes (1975,1981), Ray et al. (1975), Lemon et al. (1975), Ray (1976), Brown et al. (1978), Lemon (1977), Burgess et al. (1977), Brandes (1977a), Barnes (1978a,b)
Hook echoes associated with downdrafts	Browning and Donaldson (1963), Haglund (1969), Fujita (1973,1975,1979), Lemon et al. (1975), Lemon (1977), Brandes (1977a), Burgess et al. (1977), Forbes (1981), Rasmussen and Straka (1996)
Hook echoes located in strong u and T gradients, somewhat behind the surface windshift associated with the RFD	Marwitz (1972a,c), Burgess et al. (1977), Lemon and Doswell (1979), Brandes (1981)
Air parcels that enter the tornado pass through the RFD	Brandes (1978), Davies-Jones and Brooks (1993), Wicker and Wilhelmson (1995), Dowell and Bluestein (1997) [implied by findings of Lemon and Doswell (1979), Rasmussen et al. (1982), Jensen et al. (1983)]
Hypothesized that the RFD is important for tornadogenesis	Fujita (1975), Burgess et al. (1977), Barnes (1978a), Lemon and Doswell (1979), Brandes (1981), Davies-Jones (1982)

Table 2.1: Summary of findings pertaining to hook echoes and RFDs.

Chapter 3

Motivation for investigating RFD surface thermodynamics

The association between hook echoes and RFDs and tornadoes is well-established; however, direct observations within hook echoes and RFDs have been scarce [a few observations were mentioned by van Tassell (1955), Beebe (1959), Garrett and Rockney (1962) Browning and Ludlam (1962), Charba and Sasaki (1971), Lemon (1976), Barnes (1978a,b), and Brown and Knupp (1980)]. Thermodynamic retrievals have been performed (e.g., Brandes 1984a; Hane and Ray 1985), but small-scale details cannot be resolved, and buoyancy fields often are noisy.

Fig. 3.1 presents a sample of some of the hook echoes in which mobile mesonet data have been collected. No obvious characteristics capable of discriminating between hook echoes associated with tornadic and non-tornadic supercells are apparent in the radar data. The primary goal of this dissertation research is to determine if surface data collected by a mobile mesonet within hook echoes and RFDs can discriminate between hook echoes and RFDs associated with supercells that produce tornadoes and those that do not. Despite the well-documented association of hook echoes and RFDs with tornadoes, the dynamical relationship is not yet understood.

This dissertation has two main objectives: (1) document the surface thermodynamic fields in the proximity of tornadic and non-tornadic low-level mesocyclones in resolution not previously possible; (2) determine if differences exist at the surface in the hook echoes and RFDs of tornadic and non-tornadic supercells.

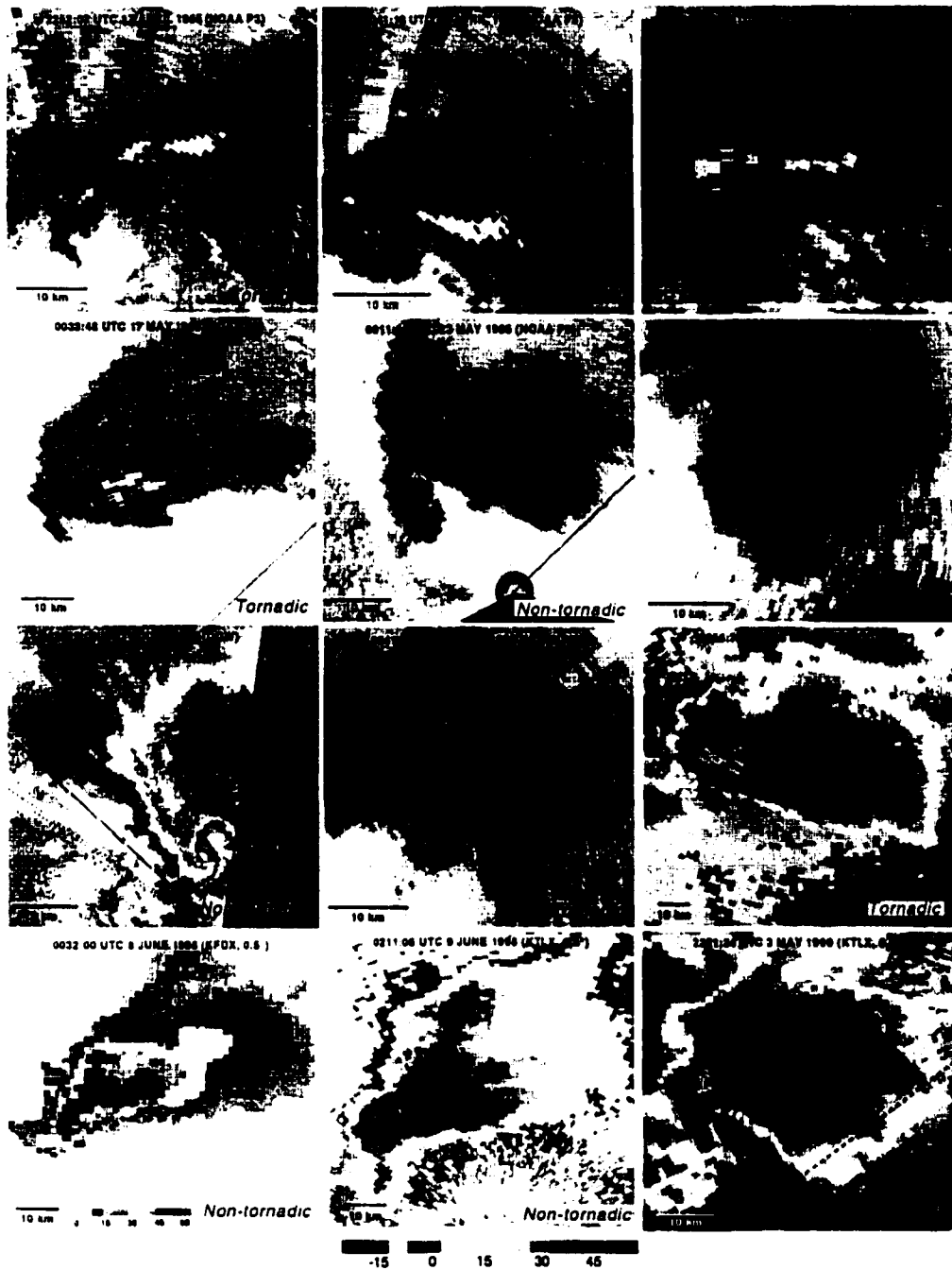


Figure 3.1: A sample of some of the hook echoes associated with both tornadic and non-tornadic supercells from which mobile mesonet observations have been collected. The hook echoes associated with tornadic supercells are as they appeared 5 min or less prior to tornadogenesis.

3.1 Documentation of surface thermodynamic fields

Brandes (1984a) and Hane and Ray (1985) were among the first to use the pioneering methods proposed by Gal-Chen (1978) and Hane et al. (1981) to retrieve thermodynamic (buoyancy and pressure) fields in supercells from multiple-Doppler-radar-synthesized three-dimensional wind fields. However, the computation of buoyancy requires assumptions about lateral and surface boundary conditions and the forcing for buoyancy involves one more derivative than the forcing for pressure; thus, buoyancy fields retrieved in past studies may contain significant uncertainties and almost invariably contain greater noise than retrieved pressure fields.

The spatial resolution of retrieval results is limited by the resolution of the dual-Doppler radar data. Usually horizontal resolution is limited to 1–3 km. Furthermore, ground clutter contaminates Doppler velocities; therefore, thermodynamic variables typically cannot be reliably retrieved at altitudes less than about 500 m above ground level (AGL).

In some cases, a height of 500 m AGL may be within the cloud. By definition, a tornado is a phenomenon *rooted in the surface layer*. Although radars can provide three-dimensional observations of entire storms (something that an observing system of vehicle-borne instruments cannot do), they cannot sample the most critical surface layer. Consequently, I contend that direct measurement of surface conditions may be some of the most important observations for a researcher attempting to address questions pertaining to tornadogenesis. In this dissertation, surface data obtained from an armada of instrumented automobiles (a “mobile mesonet”) will be analyzed. The system is described in detail in the next chapter.

Some might argue that observations are unnecessary because computing power has now increased to the level such that three-dimensional numerical simulations of supercells can be conducted with a horizontal and vertical resolution of less than 250 m (especially if grid nesting is employed). However, important processes must unavoidably be parameterized (e.g., microphysics and subgrid-scale mixing). Microphysics plays a critical role in dictating the degree of evaporational cooling within simulated storms: thus, surface thermodynamic fields are sensitive to microphysics parameterizations. Numerical simulations invariably have produced cold RFDs (e.g., Klemp and Rotunno 1983; Wicker and Wilhelmson 1995; Adlerman et al. 1999),

largely because the exclusion of ice leads to more concentrated downdrafts; the inclusion of ice leads to distribution of hydrometeors over a larger horizontal region and a reduction of the outflow intensity in close proximity to the updraft. Some past observations (e.g., Brown and Knupp 1980; Bluestein 1983; Rasmussen and Straka 1996) as well as those that will be presented in chapter 5, will reveal that the RFDs associated with many strong tornadoes are relatively warm, both in terms of temperature and equivalent potential temperature. Thus, observations apparently will continue to be of great benefit in this era of advancing computational capability. The author shares the view expressed by Doswell (1985): *“The RFD’s role remains confusing with respect to tornadogenesis. Truly confirming evidence about the various aspects of the numerical simulations awaits better observations, despite the compelling similarities between simulations and real storms.”*

3.2 Differences between tornadic and non-tornadic supercells

This aspect of the research addresses whether there is something thermodynamically “special” about RFDs associated with tornadoes compared to other thunderstorm downdrafts and RFDs associated with non-tornadic supercells.

Many studies have found that the air parcels that enter the tornado pass through the RFD. For example, observations by Brandes (1978; Fig. 3.2), Lemon and Doswell (1979), Rasmussen et al. (1982), and Jensen et al. (1983) have shown or implied a near total occlusion of the low-level mesocyclone by the RFD prior to tornadogenesis. Furthermore, Wicker and Wilhelmson (1995) found that trajectories entering their simulated tornado-like vortex passed through the hook echo and RFD (Fig. 3.3). Recent tornadogenesis hypotheses [e.g., those appearing in Davies-Jones and Brooks (1993) and Rasmussen and Straka (1997)] also have depended on air entering the tornado from the RFD. Davies-Jones and Brooks (1993) hypothesized that baroclinic generation of vorticity and reorientation of vortex lines in the RFD and hook echo were prerequisites for tornadogenesis (Fig. 3.4).

Given the prior emphasis on the RFD in the tornadogenesis process and the apparent consensus that RFD air parcels enter the tornado, the buoyancy and buoyancy

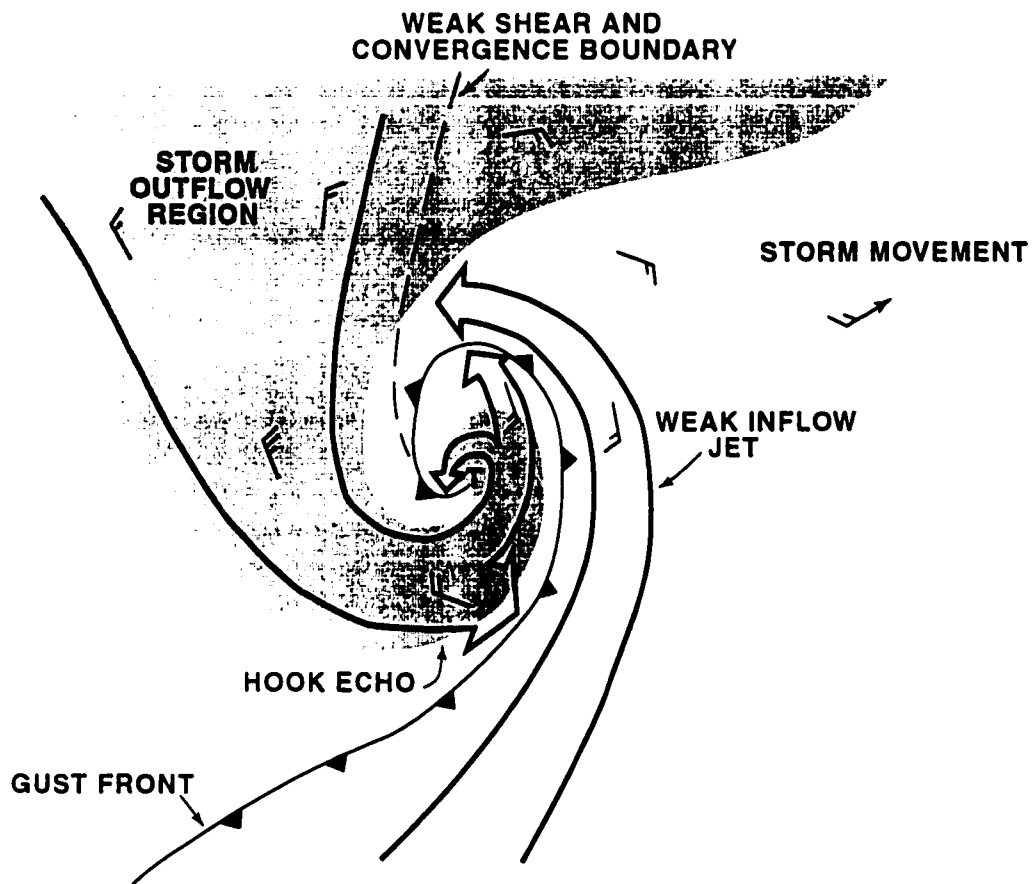


Figure 3.2: Brandes' (1978) conceptual model of low-level mesocyclone characteristics during the tornadic phase included an occluded mesocyclone with air parcels from the RFD feeding the tornado. Winds are relative to the storm. [Adapted from Brandes (1978).]

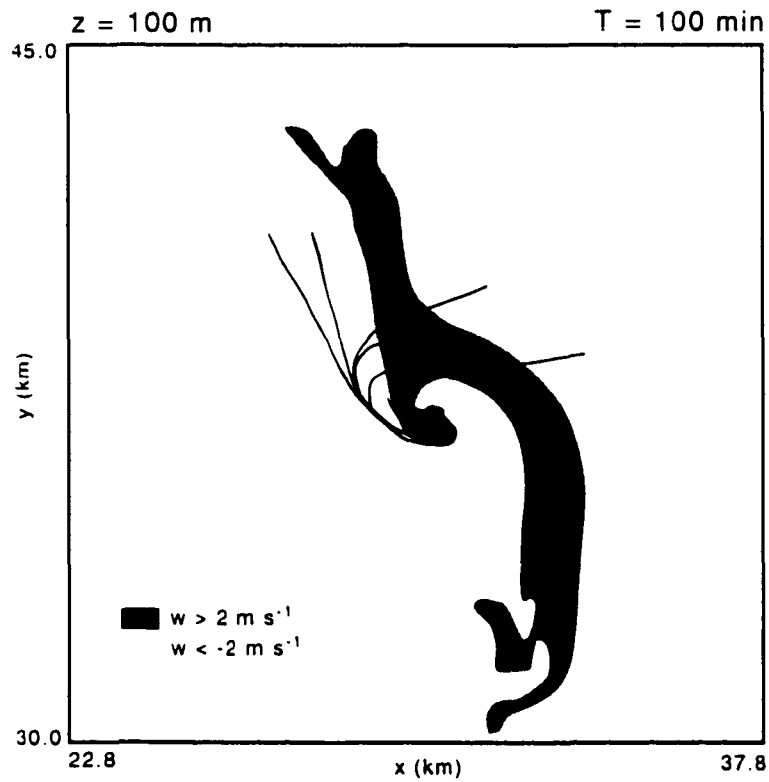


Figure 3.3: Vertical velocity and trajectories at 100 min (tornado-like vortex present in simulated storm at this time) for $z = 100 \text{ m}$ in the 120 m resolution simulation by Wicker and Wilhelmson (1995). The trajectories entering the vortex have come from the hook echo and RFD region. [Adapted from Wicker and Wilhelmson (1995).]

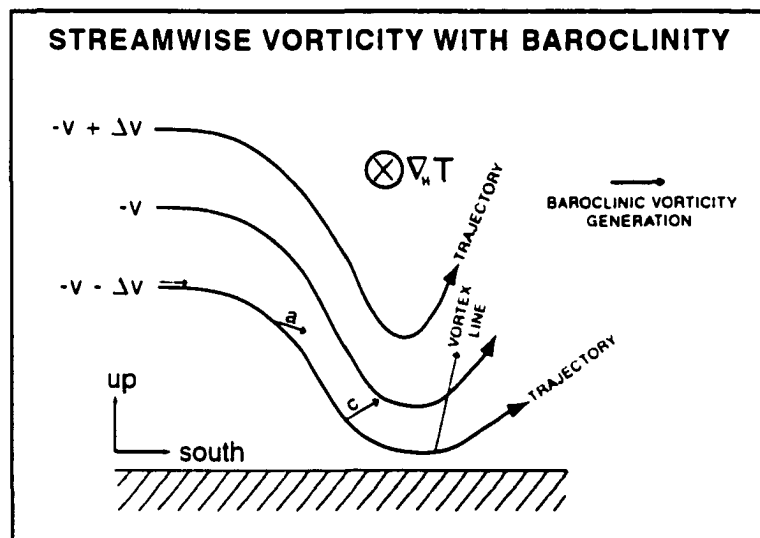


Figure 3.1: Schematic diagram showing how cyclonic vorticity may be generated from tilting of baroclinic horizontal vorticity in a downdraft. In the case of streamwise vorticity with flow to the right of the horizontal buoyancy gradient and a southerly shear component, a combination of tilting and baroclinic generation causes the vorticity of parcels to change from anticyclonic (a) to cyclonic (c) while still descending. [Adapted from Davies-Jones and Brooks (1993).]

gradients in hook echoes and RFDs naturally assume importance. Can tornadogenesis occur only for special ranges of buoyancy and/or buoyancy gradients in hook echoes and RFDs?¹ Leslie and Smith (1978) presented results from idealized numerical simulations that indicated the generation of intense surface vorticity could be precluded if low-level stability was too strong. And it is worth reiterating Ludlam's (1963) hypothesis: "if (the RFD) contains the potentially cold air from middle levels its ascent (into the tornado and parent updraft) might be expected to impede if not destroy the tornado . . . *it may be particularly important for the intensification and persistence of a tornado that some of the downdraft air be derived from potentially warm air . . .*" Furthermore, Brooks et al. (1993,1994a) showed that the cold air to the rear of numerically simulated supercell updrafts could undercut the mesocyclone and preclude generation of strong low-level rotation in some "failure cases."

Recent dual-Doppler radar observations from VORTEX have shown that, at least kinematically, the differences between tornadic and non-tornadic supercells are subtle, if even distinguishable in three-dimensional velocity data (Blanchard and Straka 1998; Wakimoto et al. 1998a,b; Trapp 1999; Wakimoto and Cai 2000; Fig. 3.5). Would surface observations collected in the RFDs of the storms analyzed by Blanchard and Straka, Wakimoto et al., and Trapp reveal significant differences?

¹Virtual potential temperature fluctuations (which are proportional to the density fluctuations that give rise to the "buoyancy force") are analyzed in the ensuing chapters, and not strictly buoyancy itself.

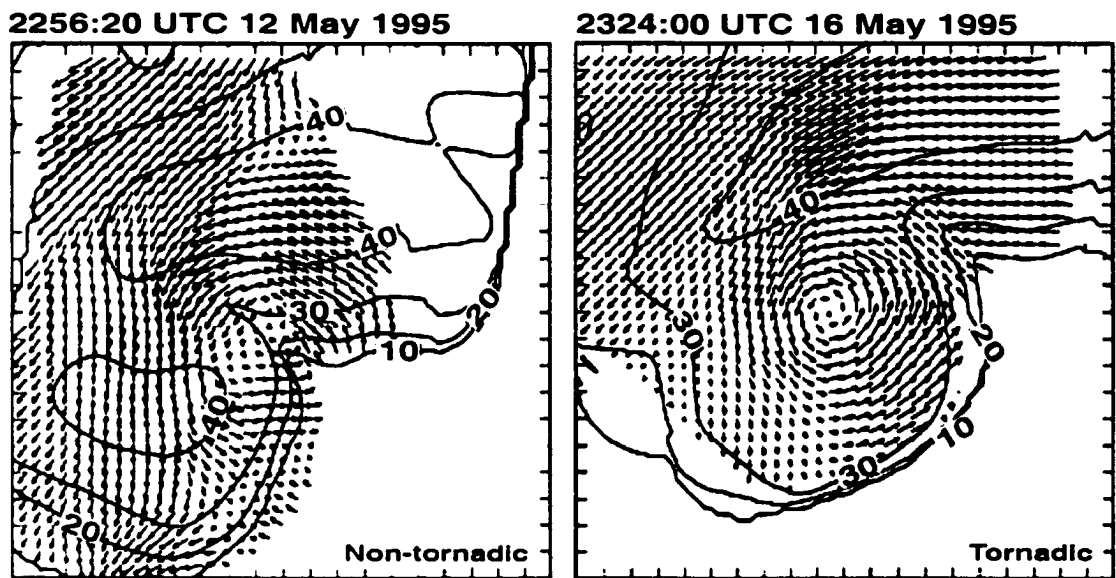


Figure 3.5: Comparison of a non-tornadic and tornadic supercell [adapted from Trapp (1999)]. The wind fields of the two storms (at 1 km AGL) are indistinguishable in the dual-Doppler analyses, for all practical purposes.

Chapter 4

Data description and analysis techniques

Mobile mesonet data were analyzed on 24 days from 1994–1999, which included the sampling of 30 hook echoes¹ in tornadic and non-tornadic supercells [Tables 4.1 and 4.2: hook echoes associated with more than one tornado (or at least in the radar data, only a single hook echo evolution was observed to be associated with multiple tornadoes) were counted as single cases]. Tornadoes were associated with the hook echoes and RFDs in 18 cases, and of the 12 non-tornadic cases, mesocyclones were observed at the surface in all but 1 case [8 June 1998—a mesocyclone was detected by the WSR-88D at an elevation of 300 m above radar level (ARL)]. The tornadic cases included tornadoes of all intensities, ranging from F0–F5. The 1994 and 1995 cases were from VORTEX operations days: on these days, radar data from the NOAA-P3 lower fuselage and tail radars, and occasionally mobile Doppler radar were used in the analyses. For the cases during 1997–1999, WSR-88D data were used in the analyses.

Throughout this dissertation, I will refer to the RFD as *the contiguous downdraft region that surrounds the low-level mesocyclone or tornado*. While it is probable that different parts of the RFD may have different dominant forcings at different times, in the mobile mesonet observations and visual observations in the field, the downdraft has the appearance of a single entity (e.g., only one “clear slot” is visible). I will not attempt to discriminate between what Klemp and Rotunno (1983) called an “occlusion downdraft” and what Browning and Donaldson called an “RFD.”

¹The following criteria for classification of an echo as a “hook echo” have been adopted from Forbes (1981): an appendage with echo protrusion oriented at least 60° to the right (south) of the main echo movement.

Case	Date	Location	Time of maximum rotational velocity (maximum rotational velocity) on WSR-88D 0.5° tilt	Height of 0.5° tilt (km ARL)	WSR-88D data available
1	5/29/94	Loving, TX	2252:07 (32 m s ⁻¹)	2.4	KFWS
2	4/29/95	Sherman, TX	0028:32 (25 m s ⁻¹)	2.4	KFWS
3	5/12/95	Hays, KS	2311:39 (42 m s ⁻¹)	3.5	KDDC
4	5/22/95	Shamrock, TX	0013:20 (21 m s ⁻¹)	2.3	KAMA
5	6/8/95	Elmwood, OK	2014:43 (14 m s ⁻¹)	2.3	KDDC
6	5/19/98	Sidney, NE	0205:12 (12 m s ⁻¹)	2.9	KCYS
7	5/20/98	Yuma, CO	0145:33 (15 m s ⁻¹)	1.5	KGLD
8	5/21/98	Medicine Lodge, KS	0126:05 (29 m s ⁻¹)	1.6	KICT
9	6/8/98	Oklahoma City, OK	0211:06 (19 m s ⁻¹)	0.3	KTLX
10	6/9/98	Seymour, TX	2134:00 (19 m s ⁻¹)	0.7	KFDR
11	5/26/99	Carlsbad, NM	2151:08 (18 m s ⁻¹)	4.8	KMAF
12	5/26/99	Mentone, TX	0056:00 (20 m s ⁻¹)	2.5	KMAF

Table 4.1: Cases of mobile mesonet observations obtained within the hook echoes and RFDs of non-tornadic supercells. All times are UTC. The date given for each case is with respect to local, not UTC time.

Case	Date	Location	Tornado times	Duration (min)	Fujita rating	Estimated maximum diameter (m)	TVS type	WSR-88D data available
13	5-6-94	Kaw Lake, OK	0012-0023	11	F1	100	D	KINX
14	5-25-94	Northfield, TX	2230-2300	30	F3	500	D	KLBB
15	4-17-95	Temple, OK	2256-2300	4	F1	50	N/A	KTLX
16	5-16-95	Jetmore, KS	0049-0054	5	F0	<50	N/A	KDDC
17	5-16-95	Hanston, KS	0138-0230	44	F3	500	ND	KDDC
18	6-2-95	Frona, TX	2343-0015	32	F4	500	N/A	KLBB
19	6-2-95	Dimmitt, TX	0057-0118	21	F4	275	N/A	KLBB
20	6-8-95	Wheeler, TX	2335-0030	55	F5	500	N/A	KFDR
21	6-8-95	Allison, TX	0045-0131	46	F4	2000	N/A	KFDR
22	5-25-97	South Haven, KS	0135-0155	20	F2	1500	D	KICT
23	6-7-98	Farwell, TX	0042	<1	F0	<50	N/A	KFDX
24	5-3-99	Apache, OK	2220-2235	15	F3	100	D	KTLX
25	5-3-99	Musco, OK	0047-0100	13	F1	60	D	KTLX
26	5-20-99	Jericho, TX	2313-2315	2	F0	<50	D	KAMA
27	5-25-99	Roswell, NM	2125-2132	7	F1	<50	N/A	KLBB
28	5-31-99	Sitka, KS	0029-0039	10	F1	150	D	KDDC
29	6-1-99	Coleman, OK	0006	<1	F0	<50	N/A	KTLX
30	6-2-99	Nazareth, TX	0045	<1	F0	<50	D	KLBB

Table 4.2: Cases of mobile mesonet observations obtained within the hook echoes and RFDs of tornadic supercells. All times are UTC. For TVS types, “ND” (“D”) indicates non-descending (descending) TVS, following the criteria of Trapp et al. (1999) (“N/A” means that either no TVS was detected or Level II WSR-88D data were unavailable). The date given for each case is with respect to local, not UTC time.



Figure 4.1: A photograph of a mobile mesonet unit similar to the ones used to collect surface data from 1994–1999.

4.1 Mobile mesonet data

The mobile mesonet is a system of vehicle-borne weather sensors that was developed for VORTEX and also was deployed in field research from 1997–1999 (Straka et al. 1996; Fig. 4.1). The observing system samples storms with high spatial (100–1000 m) and temporal (10–60 s) resolutions.

4.1.1 Instrument specifications and quality control procedures

The mobile mesonet records time and position [both using a Global Positioning System (GPS) receiver]. “fast” temperature (measured by a short-response thermistor), “slow” temperature (measured with a slower response time, comparable to the response time of the relative humidity sensor, and sheltered in the same manner as the relative humidity sensor, so that derived quantities that are functions of temperature and moisture can be accurately computed, e.g., dewpoint temperature),

relative humidity, pressure, and wind velocity. Data were recorded at 2-s intervals during the years of this study. Additional specifications are provided in Table 4.3.

Numerous quality control tests were performed on the data prior to analysis:

Radio Frequency interference Field operations required fairly frequent use of a 40 W VHF transceiver, as well as other communication equipment. Use of these transmitters caused large errors in several meteorological quantities. The source for these errors was believed to be radio frequency (RF) interference—when large RF energy was present, the flux-gate compass produced large voltages that overwhelmed the datalogger and corrupted the data. Data collected when RF interference was detected (the flux gate compass output was used as a detector of this interference) were not included in the analyses.

Position Occasionally vehicle positions became frozen for short intervals, causing erroneous latitude, longitude, and wind velocity. These data were not included in the analyses.

Vehicle heading Vehicle heading (used to determine wind velocity) was measured by a flux-gate compass when stationary and by GPS when moving. The flux-gate compass measures direction with respect to magnetic north, while GPS directions are relative to true north. Moreover, the magnetic fields induced by the vehicles are an additional error source for the flux-gate compasses. Both sources of errors in vehicle heading were removed prior to analysis.

Wind velocity Vehicle accelerations (determined using the GPS heading and speed data) can lead to significant errors in the pressure and wind data. If the vehicle velocity changed by $>4 \text{ m s}^{-1}$ in a 6-s interval, wind data from that interval were excluded from the analysis.

In addition to the above quality control checks, significant biases were removed using vehicle intercomparisons. The intercomparisons involved assembling observations over a period of 30–60 min in relatively quiescent weather conditions, while the vehicles were moving as a caravan. Biases were removed if the intercomparison revealed a bias magnitude $>0.2 \text{ K}$ for “fast” temperature, $>0.2 \text{ K}$ for “slow” temperature, $>0.2 \text{ mb}$ for pressure, $>10^\circ$ for wind direction, and $>1 \text{ m s}^{-1}$ for wind

Measurement	Sensor type	Sensor range	Estimated total inaccuracy	Resolution	Response time
Pressure	Silicon capacitive	600-1100 mb	$< \pm 0.6$ mb	0.01 mb	< 1 s
Temperature (Fast)	Resistance	-30-+50°C	$< \pm 0.3^\circ$ C	0.01°C	0.6 s
Temperature (Slow)	Resistance	-30-+50°C	$< \pm 0.5^\circ$ C	0.01°C	~15 s
Relative humidity	Capacitance	0-100%	$< 5\%$	0.03%	15 s
Wind speed	Propeller vane	0-60 m s ⁻¹	$< 2-4\%$	0.03 m s ⁻¹	< 1 s
Wind direction	Propeller vane	0-355°	$< \pm 3-6^\circ$	0.05°	< 1 s
Vehicle heading (stationary)	Flux-gate compass	sin(-1-+1), cos(-1-+1)	$< \pm 2^\circ$	$< 1^\circ$	500 ms
Vehicle heading (moving)	GPS	0-360°	$< \pm 2^\circ$	$< 1^\circ$	< 1 s
Vehicle speed	GPS	unlimited	< 1 m s ⁻¹	< 1 m s ⁻¹	< 1 s
Vehicle location	GPS	0-±90° N/S, 0-±180° E/W	< 100 m	10 m	< 1 s

Table 4.3: Characteristics of the mobile mesonet [from Straka et al. (1996)].

speed. If biases were very large (5 times the above magnitudes), it was assumed that instrument performance was unacceptable and the data were excluded from the analysis entirely.

4.1.2 Time-to-space conversion

Quality-controlled observations used in the analyses usually were averaged over 12-s intervals (occasionally 6-s averaging was employed, if vehicle speeds relative to the storm were large). The data were plotted relative to the radar echoes using time-to-space conversion. In other words, if one could assume that the feature being analyzed did not change its character significantly over the time interval during which measurements were made [the “Taylor hypothesis;” Taylor (1938)], then if the velocity $\mathbf{v} = (u, v)$ of the feature was known, then the distance the feature traveled in time Δt was $u\Delta t$ in the x direction and $v\Delta t$ in the y direction. Therefore, a measurement made at time $\pm\Delta t$ was valid at the following position in space:

$$x' = x \pm u\Delta t \quad (4.1)$$

$$y' = y \pm v\Delta t, \quad (4.2)$$

where x and y are the coordinates of the location from which measurements were made at a reference time, t_{ref} .

For most analyses, the maximum allowed $|\Delta t|$ ($|\Delta t_{max}|$) was 2–3 min; i.e., a steady-state assumption was made for approximately the time it takes the WSR-88D to complete a volume scan. At analysis times in which features were evolving rapidly, such that the steady-state assumption could not be made reliably for ± 2 –3 min, smaller values of $|\Delta t_{max}|$ (sometimes < 1 min) were used.

All analyses presented in chapter 5 were obtained within 5 min of tornadogenesis or the time of strongest rotation on WSR-88D at the lowest (0.5°) elevation angle (defined as the time of “tornadogenesis failure”), whenever possible. For some cases this was not possible, owing to logistical problems common to data collection in the field; in such cases, the analysis time for which observation density was greatest is shown instead.

4.1.3 Density of mobile mesonet observations

The area sampled within RFDs and hook echoes varied from case to case, owing to logistical limitations inherent in storm intercept field research (e.g., road networks often do not allow observations to be collected in important regions of the thunderstorm). I have attempted to quantify the quality of the RFD sampling in each case by dividing the mesocyclone region (defined as having a radius of 4 km) into four quadrants, I–IV, with the line separating quadrants I and IV from quadrants II and III being parallel to the “neck” of the hook echo (Forbes 1978) and passing through the circulation center (Fig. 4.2). Within each quadrant, the fraction of the area that was within 1 km of a mobile mesonet observation was estimated to the nearest 10%. The fractions for each case are presented in Table 4.4.

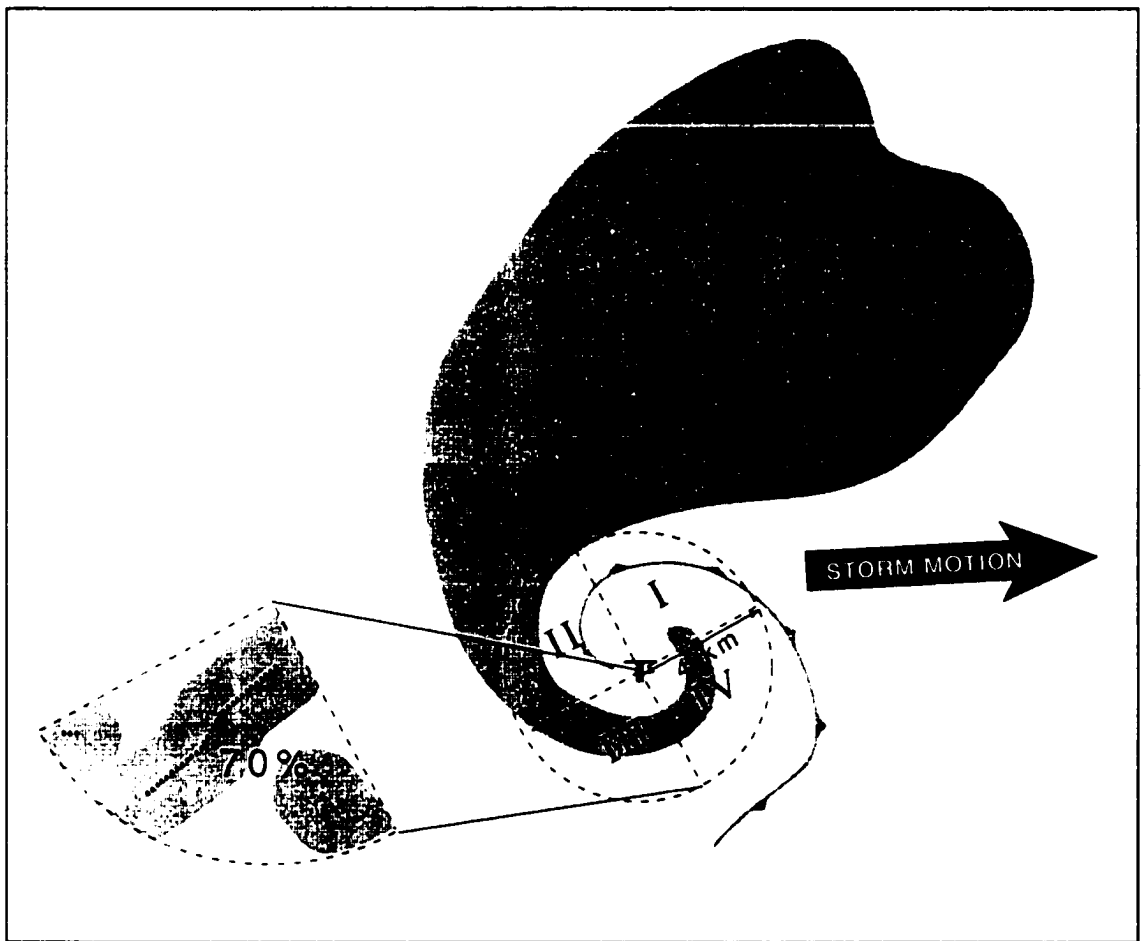


Figure 4.2: Schematic illustrating the arbitrarily defined quadrants I, II, III, and IV. In this depiction, 70% of the area of quadrant III is within 1 km of a mobile mesonet observation (denoted by black dots). Similarly, the densities of mobile mesonet observations for each analysis are summarized in Table 4.4.

Case	Date	Location	Quadrant I	Quadrant II	Quadrant III	Quadrant IV
1	5/29/94	Loving, TX	0	20	10	20
2	4/29/95	Sherman, TX	90	70	70	80
3	5/12/95	Hays, KS	50	0	30	10
4	5/22/95	Shamrock, TX	60	40	80	60
5	6/8/95	Elmwood, OK	10	50	70	70
6	5/19/98	Sidney, NE	90	50	50	70
7	5/20/98	Yuma, CO	50	40	60	0
8	5/24/98	Medicine Lodge, KS	50	20	50	70
9	6/8/98	Oklahoma City, OK	10	0	60	70
10	6/9/98	Seymour, TX	100	40	50	100
11	5/26/99	Carlsbad, NM	90	40	80	100
12	5/26/99	Mentone, TX	90	30	80	80
13	5/6/94	Kaw Lake, OK	100	50	70	80
14	5/25/94	Northfield, TX	0	0	50	0
15	4/17/95	Temple, OK	90	30	60	90
16	5/16/95	Jetmore, KS	0	0	30	50
17	5/16/95	Hanston, KS	100	50	50	0
18	6/2/95	Friona, TX	100	90	10	40
19	6/2/95	Dimmitt, TX	40	90	40	60
20	6/8/95	Wheeler, TX	100	80	40	30
21	6/8/95	Alhson, TX	50	70	50	80
22	5/25/97	South Haven, KS	0	0	20	70
23	6/7/98	Farwell, TX	90	10	70	100
24	5/3/99	Apache, OK	100	20	30	60
25	5/3/99	Minco, OK	100	70	20	100
26	5/20/99	Jericho, TX	10	30	40	70
27	5/25/99	Roswell, NM	0	50	80	0
28	5/31/99	Sitka, KS	40	70	50	0
29	6/1/99	Coleman, OK	90	30	20	40
30	6/2/99	Nazareth, TX	90	60	70	80

Table 4.4: Sampling densities by quadrant (Fig. 4.2) for each of the 30 hook echo cases *at the analysis times* appearing in chapter 5 (chosen to be as near as possible to the time of tornadogenesis or tornadogenesis failure). Numerals represent the percent of the area within each quadrant that was within 1 km of a mobile mesonet observation.

4.2 Radar data

For the cases analyzed from VORTEX (1994–1995), radar data were available from the P3 research aircraft operated by the National Oceanic and Atmospheric Administration (NOAA). The aircraft was equipped with two radars: a lower fuselage (LF) non-coherent radar and a Doppler tail (TA) radar. For detailed descriptions of these radars, the reader is referred to Jorgensen et al. (1983) and Ray et al. (1985).

During VORTEX, the antenna rotation rate of the lower fuselage radar was 2 rpm (Daugherty et al. 1996); lower fuselage radar data were often desirable for analysis with the mobile mesonet data because of the high temporal resolution of these radar data. Continuous altitude plan position indicators (CAPPIS) could be constructed from the tail radar data (reflectivity, velocity, and spectrum width), but only at roughly 7 min intervals.

The NOAA-P3 position (obtained from GPS) was saved only at the *beginning* of each scan. If the aircraft was moving at, e.g. 120 m s^{-1} , the aircraft would have traveled 3600 m in the time it takes to complete one scan, and significant errors in the locations of the reflectivity data would have been present in the data. To place mobile mesonet observations in the correct positions with respect to LF reflectivity data, WSR-88D images were overlaid atop the LF reflectivity and mobile mesonet data, and the LF reflectivity data were shifted so that the reflectivity cores sampled by the two radars were in phase.² Another effect owing to the updating of the NOAA-P3 position once per scan is that the shapes of echoes would be distorted. However, for the region of the storm of interest (e.g., the hook echo), echoes typically only subtended $10\text{--}20^\circ$ of azimuth (range $\sim 15\text{--}30$ km typically). In the time it takes the LF radar to scan $10\text{--}20^\circ$ (<2 s), the aircraft position only changes by 100–200 m (less than the 250 m gate spacing); thus, echo distortion in the regions of the hook echoes owing to position errors would not have been severe.

At some of the analysis times for 1995 cases, radar data from the Doppler On Wheels (DOW) radar were superposed. A full description of this 3-cm mobile radar appears in Wurman et al. (1997).

²Reflectivity core positions were compared because they appeared similar in the data collected by both radars; however, the hook echo regions can appear significantly different when viewed by WSR-88D versus the LF radar at close range.

Cases analyzed from 1997-1999 generally incorporated WSR-88D archive level II data. For two cases (7 June 1998 and 9 June 1998), level III data were used. Level II data are the base digital data (mean radial velocity, reflectivity, and spectrum width) produced by the signal processor at the full spatial and temporal resolution of the radar. Level III data only includes some of the graphic products archived by a radar site on a given day (typically includes base reflectivity and velocity at the lowest two elevation angles).

4.3 Thermodynamic variables analyzed

Analyses of virtual and equivalent potential temperature, RFD parcel origins (by examining sounding data and using entropy as a tracer), potential buoyancy in the RFD as measured by convective available potential energy (CAPE) and convective inhibition (CIN), and pressure were performed, using the data gathered by the mobile mesonet. For the analyses of virtual and equivalent potential temperature and pressure, the fluctuations of these variables were computed by subtracting a base ("reference") state value that depended on the large-scale atmospheric conditions (e.g., $p' = p - \bar{p}$, where p is pressure, p' is the pressure fluctuation, and \bar{p} is the base state pressure). The method by which the base state was determined is described in section 4.4. The potential errors of all variables (including derived variables) are analyzed in appendix A.

4.3.1 Virtual potential temperature

The virtual potential temperature, θ_v , is defined here as

$$\theta_v = \theta(1 + 0.61q_v - q_l), \quad (4.3)$$

where θ is the potential temperature, q_v is the water vapor mixing ratio, and q_l is the liquid water mixing ratio. Ice and cloud water concentrations have been neglected here, and the base state is assumed to contain no hydrometeors. Virtual potential temperature fluctuations are directly proportional to density fluctuations, which

appear in the buoyancy force (also see appendix B); however, historically, virtual potential temperature has been favored over the use of density in buoyancy analyses.

Liquid water mixing ratio was parameterized using radar reflectivity sampled at the lowest elevation angle obtainable, following Rutledge and Hobbs (1984).

$$q_l(\text{g kg}^{-1}) = 10^{\left(\frac{Z-42.2}{16.8}\right)}, \quad (4.4)$$

where Z is radar reflectivity in dBZ. The reliability of this parameterization is adversely affected by the presence of ice (especially hail); however, an under- or overestimate of Z by 15 dBZ when reflectivity lies in the 30–45 dBZ range has approximately the same effect on θ_v as a 0.3 K potential temperature fluctuation. The ice mixing ratio has been neglected in the buoyancy computations, although some ice probably is accounted for in the parameterization of q_l in terms of the radar reflectivity factor.

Radar reflectivity factors (dBZ) were objectively analyzed using a one-pass Barnes (1964) scheme, with a weight function, w_{ik} ,

$$w_{ik} = \exp\left(-\frac{x_{ik}^2}{\kappa_x} - \frac{y_{ik}^2}{\kappa_y}\right), \quad (4.5)$$

where $\kappa = \kappa_x = \kappa_y$ is the “smoothing parameter” and x_{ik} , and y_{ik} are the distances of the k th datum from the i th grid point in the x and y directions, respectively. For the NOAA-P3 data, a value of 0.04 km² was chosen for κ , which yielded a response of 0.5 at the minimum resolvable wavelength in the (horizontal) direction of worst data resolution (approximately 1 km, assuming four grid points are needed to resolve a wavelength). For the WSR-88D data, κ was chosen such that the response function was similar; however, the exact value varied from case to case because of widely varying ranges from the radars and thus, widely varying minimum resolvable scales.

The objectively analyzed radar reflectivity data were linearly interpolated to the mobile mesonet observation locations, where q_l and θ_v subsequently were computed.

4.3.2 Equivalent potential temperature

The equivalent potential temperature, θ_e , was analyzed in each case by first computing the pressure of the lifting condensation level (LCL) (using the θ and q_v of a surface parcel and iteratively solving for the pressure at which $q_v = q_{vs}$, the saturation mixing ratio), and then iteratively computing the temperature, T , on the moist adiabat from the LCL up to 200 mb, where

$$\frac{dT}{dp} = \frac{1}{\rho c_p} \frac{1 + L_v q_{vs} / R_d T}{1 + L_v^2 q_{vs} / c_p R_v T^2}, \quad (4.6)$$

where L_v is the latent heat of vaporization (a weak function of T), R_d is the gas constant for dry air, R_v is the gas constant for water vapor, ρ is air density, and c_p is the specific heat of dry air at constant pressure (e.g., Bohren and Albrecht 1998, p. 291).³

Often wet-bulb potential temperature (θ_w) is used in severe thunderstorm studies, because of its similar conservation property for dry and moist adiabatic processes. Bohren and Albrecht (1998, p. 298) showed that

$$\theta_e \approx \theta_w + \frac{L_v}{c_p} q_{vs}, \quad (4.7)$$

therefore,

$$\theta'_e \approx \theta'_w + \frac{\varepsilon L_v}{\rho c_p} e'_s, \quad (4.8)$$

where ε ($=0.622$) is the ratio of the gas constants of dry air and water vapor, and $e'_s = e'_s(T')$. For $T' \sim 2-3$ K, $e'_s \sim 3-6$ mb and $\theta'_e - \theta'_w \sim 5-10$ K.

³It may be worth stating that θ_e is defined for reversible adiabatic processes and is conserved for these processes. Therefore, the moist adiabatic lapse rate also should include the heat capacity of liquid water, since θ_e depends on q_l . However, since entropy is a function of T , p , and q_l , it cannot be represented on a single two-dimensional thermodynamic diagram; for this reason, it is convenient to define a pseudoadiabatic process as one in which the heat capacity of liquid water or ice is neglected (Emanuel 1994). The moist adiabatic lapse rate appearing on skew T -log p diagrams does not include the heat capacity of liquid water or ice, nor were these effects included in (4.6). Therefore, the θ_e computed here is really the "pseudo-equivalent potential temperature," $\theta_{e,p}$ (Bolton 1980), which assumes that liquid water falls out of the parcel, thus its heat-carrying capacity is neglected. Although $\theta_{e,p}$ is not exactly conserved for moist adiabatic processes, for all practical purposes, it can be considered to be conserved (Emanuel 1994).

4.3.3 Parcel origin

If entropy (θ_e) is approximately conserved for adiabatic processes, then it is possible to estimate the height from which surface parcels in the RFD have descended, if the vertical profile of θ_e is available from a nearby sounding. The height of parcel origins (z_o) assuming θ_e conservation (no entrainment) was analyzed for each case. However, z_o values should be viewed with caution, because lateral entrainment clearly must occur in order to satisfy mass continuity if vertical accelerations exist. Furthermore, if parcels reach the surface with the same θ_e as the inflow (and updraft), perhaps via forced descent, then the height from which they have descended cannot be determined, because the updraft has, to a good approximation (at least away from its lateral boundaries), no vertical θ_e gradient. It perhaps is most appropriate to denote z_o as simply the height on an inflow sounding where θ_e values are equal to those observed at the surface within the downdraft, rather than as a measure of parcel origin.

4.3.4 CAPE and CIN

CAPE and CIN were computed for parcels within the RFD by inserting the measured surface virtual temperature (T_v), dewpoint temperature (T_d), and p into the inflow sounding nearest to the observed storm in space and time. I am uncertain of the appropriateness of using RFD air parcels in “proximity soundings” to assess CAPE and CIN. It can be argued that CAPE and CIN, *by definition*, refer to the integrated buoyancy that is computed *relative to the base state*; i.e., surface parcels in the RFD should be inserted into inflow soundings rather than soundings obtained within the RFD when computing CAPE and CIN, assuming that the inflow sounding is representative of the base state (and an RFD sounding does not sample the base state atmosphere).⁴

While θ'_e is a measure of the actual buoyancy, CAPE is a measure of *potential* buoyancy (positive buoyancy that may be realized if the parcel can be lifted to its

⁴Of course, the atmosphere really does not “care” about “base states”—base states are arbitrarily defined by meteorologists to facilitate understanding of how pressure gradients arise that can yield motions such as those observed in thunderstorm updrafts. In this work, the usage of the term “base state” is consistent with long-standing convention.

level of free convection). I am not sure whether buoyancy itself or potential buoyancy is most relevant (or whether either is relevant) in tornadogenesis; for this reason, I have analyzed both θ'_v and CAPE. CIN was analyzed to assess whether the amount of work done by an updraft to lift a parcel to its level of free convection is possibly an important condition leading to tornadogenesis success or failure.

CAPE and CIN values do not depend on the specification (or misspecification) of a base state using an arbitrary method, such as that described in the next section, which was used to compute θ'_v . Instead, a single inflow sounding determines the profile of $\bar{\theta}(z)$. While the issue of deciding which arbitrary method to use to estimate the base state is avoided, the representativeness of the inflow sounding used in the CAPE and CIN calculations sometimes may be questionable. (Perhaps it would have been desirable to use a number of inflow soundings to construct a "composite" sounding, although this approach would have been just as arbitrary as any other.) It is believed that results obtained using the different approaches (θ'_v versus CAPE/CIN), if similar, would be more robust than if an analysis of only θ'_v or CAPE/CIN was performed.

Both CAPE and CIN were computed as follows (undiluted ascent from the surface was assumed):

$$CAPE = -R_d \int_{p_{LFC}}^{500} (\theta_p - \bar{\theta}) d \ln p \quad (4.9)$$

$$CIN = -R_d \int_{p_{sfc}}^{p_{LFC}} (\bar{\theta} - \theta_p) d \ln p. \quad (4.10)$$

where p_{LFC} is the pressure of the level of free convection, p_{sfc} is the surface pressure, θ_p is the potential temperature of the lifted parcel, $\bar{\theta}$ is the potential temperature of the environment, and CAPE was only computed below 500 mb, because many of the special soundings launched on operations days were terminated below the equilibrium level. For the soundings containing data to the height of the equilibrium level, on average, approximately 20% of the total CAPE was present below 500 mb.

4.3.5 Pressure

Pressure was reduced to the average height of the vehicle observations using the integrated hydrostatic equation of the form,

$$p = p_{obs} \exp \left[\frac{(z_{obs} - \bar{z})g}{R_d \bar{T}_v} \right], \quad (4.11)$$

where \bar{z} is the average elevation of the mobile mesonet observations within the analysis domain, p is the pressure reduced to \bar{z} , p_{obs} is the pressure observed by the mobile mesonet vehicle, z_{obs} is the elevation at which the mobile mesonet pressure p_{obs} was recorded, and \bar{T}_v is approximated as the average virtual temperature (liquid water effects neglected) recorded by the mobile mesonet within the analysis domain.

Elevation data were obtained from U.S. Geological Survey Level 2 Digital Elevation Model (DEM) data. Each 7.5-minute unit of DEM coverage has a horizontal resolution of 30 m, a vertical precision of 1 ft (0.31 m), and accuracy equal to or better than one-half of a contour interval of the 7.5-minute topographic quadrangle map [corresponds to 2.5–5.0 ft (0.78–1.6 m) accuracy]. Mobile mesonet elevations were obtained from a nearest-neighbor analysis of the DEM data. An analysis of the errors of reduced pressure values, owing to DEM errors, GPS position errors, and instrument errors, is presented in appendix A.

4.4 Specification of the base state

Computations of fluctuations of meteorological variables (e.g., θ'_v , p') depend on how the base state (e.g., $\bar{\theta}_v$, \bar{p}) is defined. It is difficult to define exactly what constitutes the “environment” of a storm, therefore it also is difficult to define the base state of the atmosphere in the environment of a storm (Brooks et al. 1994b; Markowski et al. 1998c).

While there is more than one way to estimate the base state (and while all techniques are arbitrary and imperfect), the base state of a meteorological quantity, $\bar{\xi}$, was estimated by a weighted mean of N convectively uncontaminated surface airways and Oklahoma Mesonet (Brock et al. 1995) observations within a 400 km radius of the updraft, where

$$\bar{\xi} = \frac{\sum_{i=1}^N w_i \xi_i}{\sum_{i=1}^N w_i}, \quad (4.12)$$

where w_i is the Barnes weight function.

$$w_i = \exp\left(-\frac{r_i^2}{\kappa_o}\right), \quad (4.13)$$

where r is the distance of the i th uncontaminated observation from the updraft and κ_o is chosen in a manner following Koch et al. (1983) where

$$\kappa_o = \bar{\delta} \left(\frac{2\Delta n}{\pi}\right)^2, \quad (4.14)$$

where Δn is the average spacing between standard observations [O(100) km]. [The weighted means of convectively uncontaminated observations using $\kappa_1 = 0.5\kappa_o$ and $\kappa_2 = 1.5\kappa_o$ also were computed to examine the sensitivity of the base state to the choice of κ (see appendix A).] For cases in which observation density varied considerably across the “influence region” (e.g., a case in which a storm was on the Oklahoma border, whereby half of the averaging region contained Oklahoma Mesonet observations at a density of several times the density of surface airways observations), “super-observations” were made by combining observations in the observationally dense regions, so that undue weight would not be given to the clustered observations.

Most often reference or base state quantities are taken to represent spatial or temporal averages (or both) and are assumed to be constant with respect to space or time derivatives (or both) (e.g., Stull 1988). However, in the method above, the base state computed at a storm is not necessarily constant in time nor space [although over the course of an hour, the $\bar{\theta}_v$, $\bar{\theta}_e$, and \bar{p} “experienced” by a single storm are constant for most practical purposes (changes of ~ 0.1 K and ~ 0.1 mb are typical over the distance a storm may move in ~ 1 h)]. Originally I proposed to define the base state using a simple arithmetic mean of observations within an arbitrary radius (in that case, the base state would be a spatial constant). However, I discovered that

this specification of the base state was overly sensitive to the choice of the radius of influence because of considerable environmental inhomogeneity on some days, and the inability of the surface network to adequately resolve the inhomogeneity (e.g., using a 400 km radius versus a 200 km radius to estimate the base state yielded $\bar{\theta}_v$ differences of 3-5 K on some occasions). The technique used for this work, on the other hand, yielded only small differences (generally <0.5 K) among reference values as the value of the smoothing parameter κ was varied.

While not rigorously justifiable, precedents do exist for defining the base state in the manner used herein. Fujita (1955) and Charba and Sasaki (1971) used a technique in which the base state was obtained at each observation location by interpolating from smooth contours obtained from the regular synoptic stations. Although it is unconventional to specify a reference state that is not constant in space or time (because linearization of the primitive equations loses its advantages), the choice is as arbitrary as the decision to make the reference state a constant with respect to space or time.

Typically station pressures are not routinely reported by surface observing stations. However, altimeter settings usually are reported. Because the altimeter setting is computed using a pre-specified lapse rate (the "standard atmosphere"), unlike computations of sea level pressure made at surface observing sites (in which the assumptions made about lapse rate are different each day and at each location), station pressures can be retrieved from altimeter setting values if the height of the observing station above mean sea level is known. Integration of the hydrostatic equation yields

$$p_{stn} = p_{alt} \exp \left[\frac{g}{R_d \Gamma} \ln \left(\frac{\bar{T}_{SL} - \Gamma z_{stn}}{\bar{T}_{SL}} \right) \right], \quad (4.15)$$

where p_{stn} is station pressure at the observing site, p_{alt} is the altimeter setting, $\Gamma = 6.5 \text{ K km}^{-1}$ is the lapse rate of the standard atmosphere, z_{stn} is the height above sea level of the observing site, and $\bar{T}_{SL} = 288 \text{ K}$ is the mean temperature at sea level in the standard atmosphere. Once the station pressure was determined, it was reduced to the mean height of the mobile mesonet observations using the technique described earlier in this section, and subsequent averaging of several surface pressure values employing the same methods ultimately allowed for the estimation of \bar{p} , the mean pressure at the mean height of the mobile mesonet observations.

4.5 Limitations

Limitations are unavoidable in observational research, and those that should be considered in this work are summarized below:

1. Road networks do not allow continuous sampling of moving updrafts for periods longer than about 5 min before repositioning of the armada requires that they temporarily forfeit data collection in critical regions of the storm; therefore, the time evolution of features is difficult to document. In all but a lucky few cases, all that can be obtained are snapshots of the hook echo and RFD region at various times from case to case (in some cases, the RFD is sampled near tornadogenesis; at other times, during the mature phase of a tornado; and at other times, during tornado demise). One case by itself probably offers little, but the ensemble of snapshots from different times relative to tornadogenesis from a variety of cases hopefully can lead to new understanding.
2. Time-to-space conversion was performed over ~ 5 min intervals—storms are not steady for 5 min periods, at least not near the time of tornadogenesis (if they were, then tornadogenesis would not occur). In order to maximize the coverage of data (gathered by a finite number of vehicles), ~ 5 min was reluctantly chosen as the time period over which steadiness was assumed. Other past studies have been forced to assume even longer periods of steadiness [e.g., 8–16 min in Johnson et al. (1987)]. Furthermore, dual-Doppler radar analyses also are not immune from the necessity to assume steadiness for “short” periods of time (5–10 min; e.g., Brandes 1977a,b, 1984a,b; Ray 1976; Ray et al. 1981; Wakimoto et al. 1998a,b). There is some confidence that the choice of $|\Delta t_{max}|$ of 2–3 min in this work was not too severe; the thermodynamic fields to be presented in chapter 5 are largely free of noise—if the choice of $|\Delta t_{max}|$ was made inappropriately large, one might expect that a time-to-space conversion analysis would yield noisy fields.
3. Thermodynamic fields and their gradients cannot be ascertained above the surface by direct means. At best, only the sign of the gradients can be inferred above the surface, based on assumptions of the lapse rates beneath and at a distance from the storm.

4. It is tempting to only investigate storms at or just prior to the time of tornadogenesis. Caution should be exercised when drawing conclusions based on such analyses—time histories of air parcels (following their trajectories) are important, including any baroclinity encountered possibly as much as 30 minutes prior to tornadogenesis. It is not possible to compute trajectories at the surface using direct observations over 30-minute intervals owing to observation density.

Chapter 5

Surface observations in hook echoes and RFDs

In this chapter, only a small, representative subset of the total assembly of surface analyses is included where appropriate. The complete collection of over 200 (color) RFD surface analyses, 30 plots of larger-scale surface observations, and over 30 proximity soundings is available electronically from the author. This approach was taken in order to keep the length of the dissertation manageable.

5.1 RFDs associated with non-tornadic supercells

The RFDs associated with non-tornadic supercells generally contained large θ_v deficits at the surface. Figs. 5.1 and 5.2 show analyses of θ_v in two representative non-tornadic supercell cases (29 April 1995 and 19 May 1998). Values of θ'_v within 2 km of the surface circulation centers ranged from approximately -4 K to -9 K.

The non-tornadic RFDs also were associated with large θ_e deficits (typically >10 K), with midlevel θ_e values commonly being detected at the surface (e.g., Figs. 5.3 and 5.4). Numerous past studies also have reported a similar finding, but it cannot be determined whether the low- θ_e surface parcels detected by the mobile mesonet have midlevel *origins*, or if the parcels comprise updraft air that has descended and been diluted by midlevel environmental air during the downward excursion. Surface θ_e values sampled within non-tornadic RFDs, on average, were similar to the θ_e values measured at heights (AGL) of 1.5–2.4 km on proximity soundings (e.g., Fig. 5.5).

CASE 2
0028:32 UTC 30 APRIL 1995

(t-0 min)

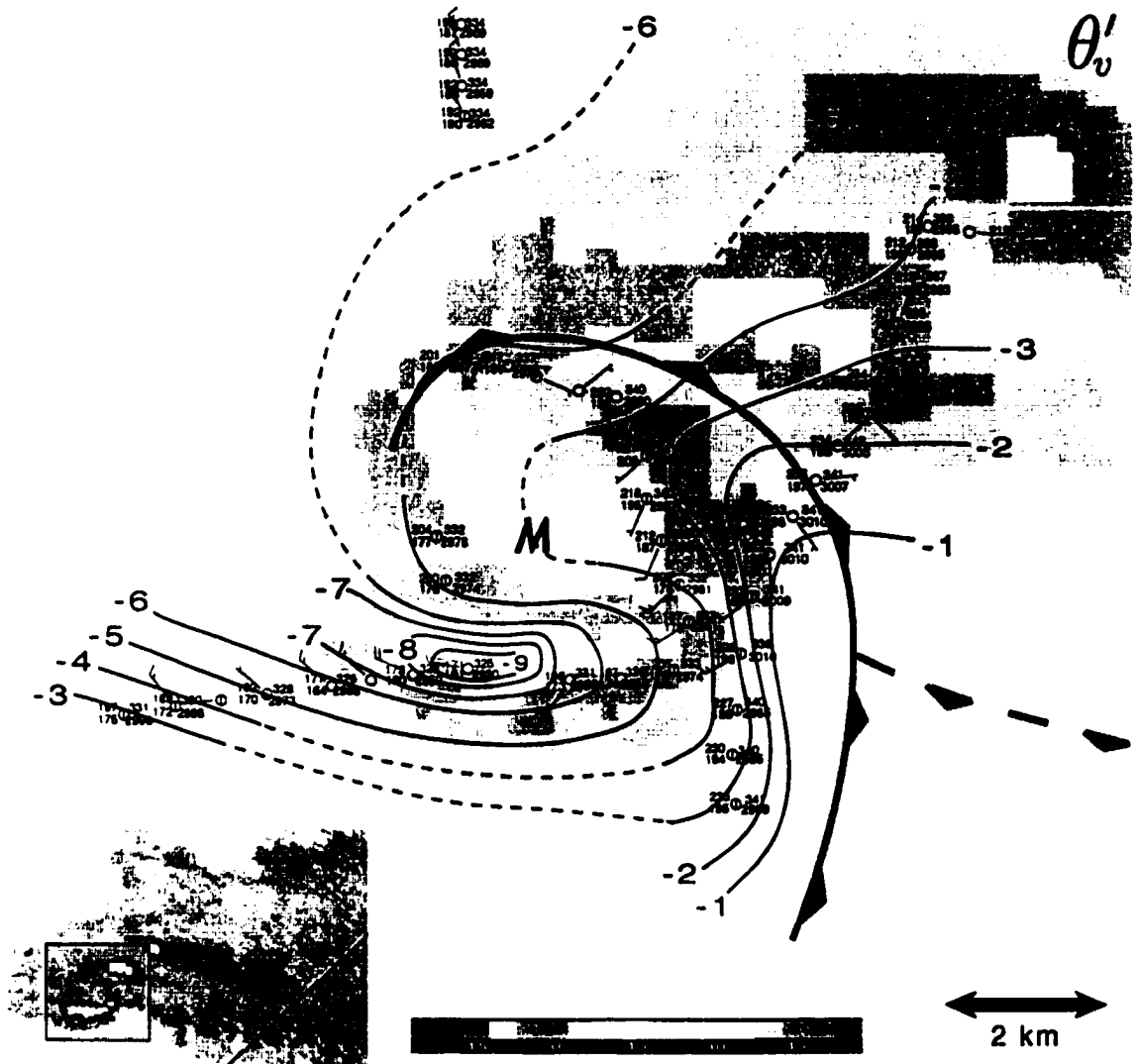


Figure 5.1: Subjective analysis of virtual potential temperature fluctuation, θ'_v (K), at 0028:32 UTC 30 April 1995. Dashed contours are used in regions where the analysis is less certain owing to low observation density. The "t-5 min" indicates that the analysis reference time is 5 min before tornadogenesis failure (the time of strongest low-level rotation on WSR-88D). Mobile mesonet station models include (reading counterclockwise, beginning with the three-digit numeral at the top left) temperature, T , in $^{\circ}\text{C}$ to the nearest 0.1°C with the decimal omitted, dew point temperature, T_d , in $^{\circ}\text{C}$ to the nearest 0.1°C with the decimal omitted, virtual potential temperature, θ_v , in K to the nearest 0.1 K with the decimal omitted, and equivalent potential temperature, θ_e , in K to the nearest 1 K. Wind barbs depict storm-relative winds and are in knots (1 full barb = 10 kt; 1 flag = 50 kt). Mobile mesonet observations have been averaged over 12-s intervals, and $|\Delta t_{max}| = 3$ min was used in the time-to-space conversion. Observations obtained more than 1 min before or after the analysis reference time are "flagged" with a vertical bar through the center of the station model. Storm-scale fronts are depicted using conventional frontal symbology (dashed boundaries are drawn where uncertainty exists). The letter "M" indicates the position of mesocyclone center at the lowest radar elevation angle. Radar reflectivity data were obtained from the NOAA-P3 LF radar.

CASE 6
0205:12 UTC 20 MAY 1998 (t-0 min)

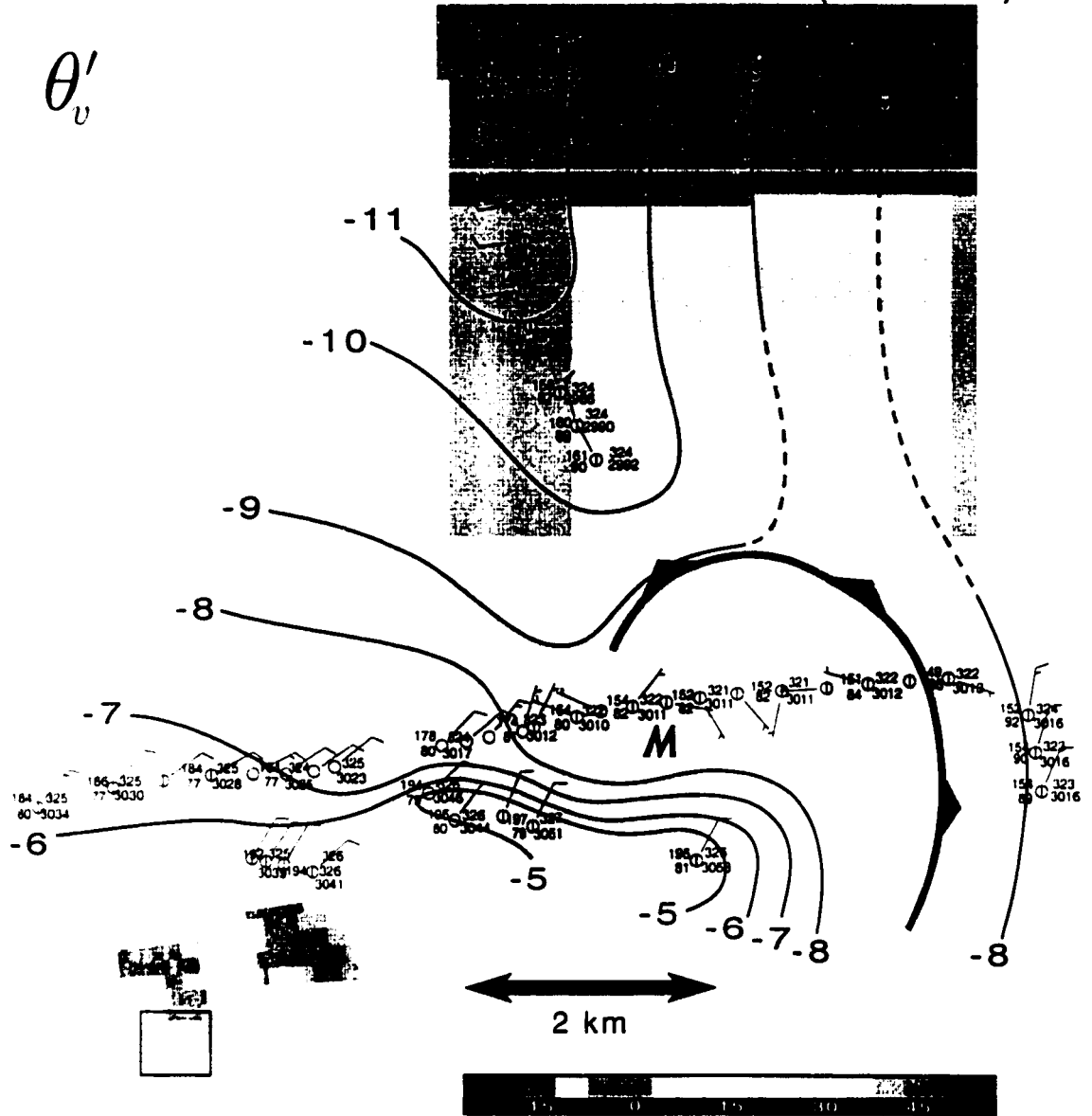


Figure 5.2: As in Fig. 5.1. for 0205:12 UTC 20 May 1998. Radar reflectivity data are from the KCYS WSR-88D radar.

CASE 2
0028:32 UTC 30 APRIL 1995

(t-0 min)

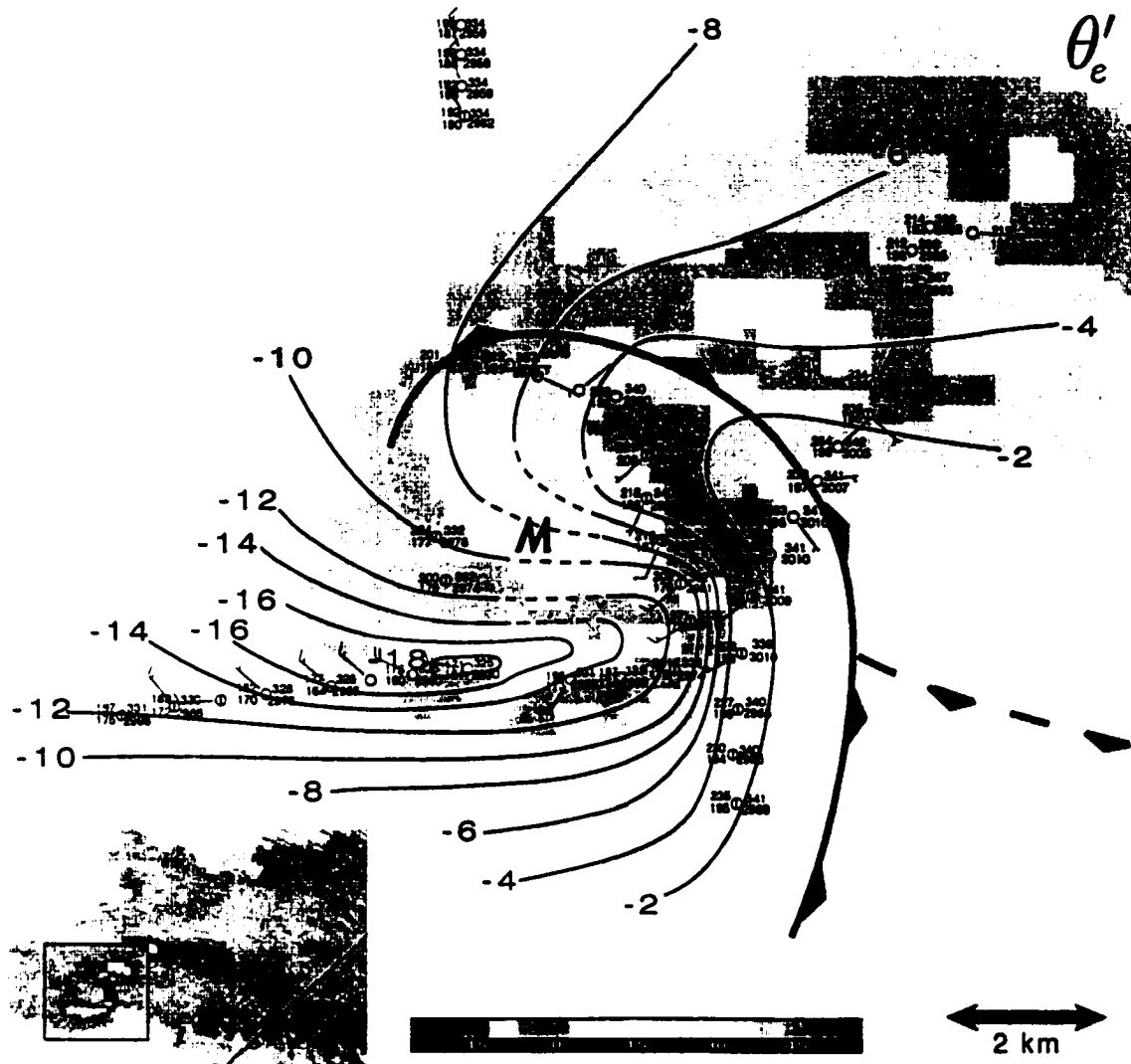


Figure 5.3: As in Fig. 5.1, but θ'_e is analyzed.

CASE 6
0205:12 UTC 20 MAY 1998 (t-0 min)

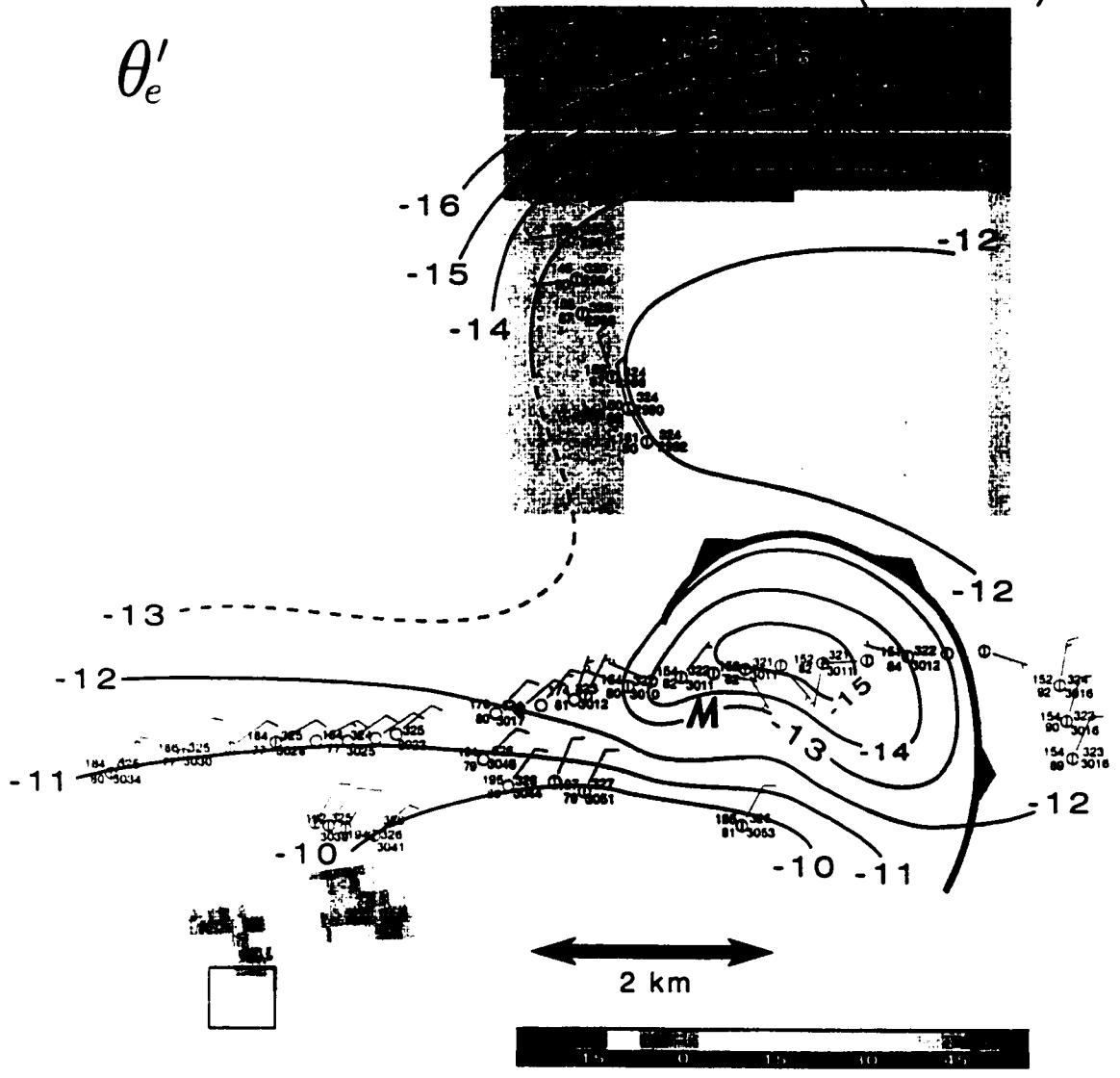


Figure 5.4: As in Fig. 5.2, but θ'_e is analyzed.

CASE 2

0028:32 UTC 30 APRIL 1995

(t-0 min)

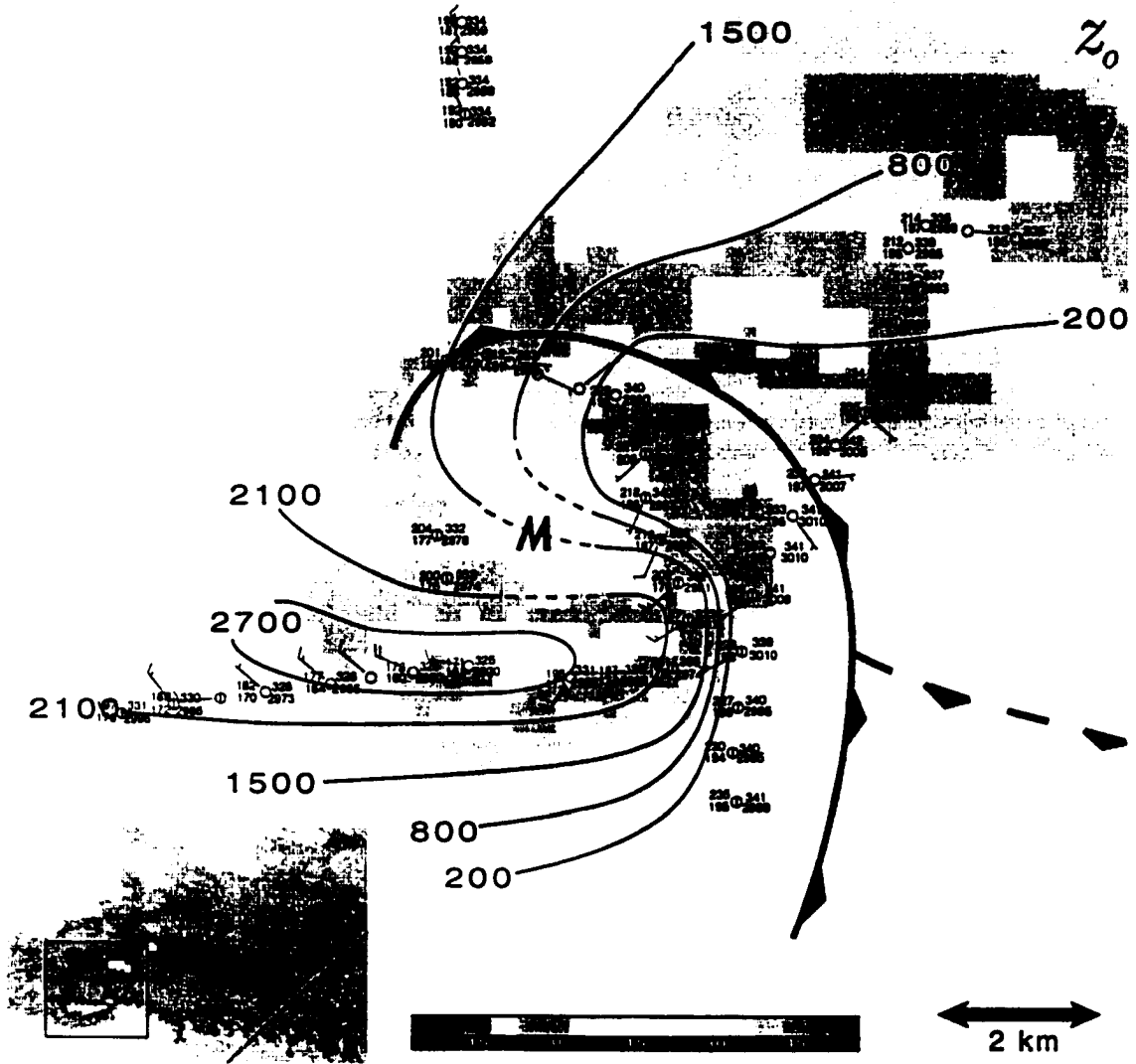


Figure 5.5: As in Fig. 5.1, but z_0 (m AGL) is analyzed.

Many RFDs associated with the non-tornadic supercells contained surface-based CAPE despite significant surface θ_v and θ_e deficits; however, in most cases, CIN was large within 4 km of the circulations (200–300 J kg⁻¹ in 4/12 cases, >500 J kg⁻¹ in 5/12 cases). In 3/12 cases, at least some surface parcels within 4 km of the circulation in the RFD did not contain any CAPE, and in 1/12 cases, no surface parcels within 2 km of the mesocyclone contained CAPE. In Figs. 5.6 and 5.7 analyses of surface-based CAPE (below 500 mb) and CIN are presented for the 29 April 1995 case. It is important to reiterate that CAPE and CIN values were obtained by inserting RFD surface measurements into *warm inflow* soundings, whose representativeness often is questionable.

Finally, it is worth noting that in a couple of non-tornadic supercell cases, smaller surface θ_v deficits of 3–5 K were observed in the RFDs, along with more substantial surface-based CAPE (e.g., Figs. 5.8 and 5.9).

5.2 RFDs associated with tornadic supercells

The RFDs associated with “weakly tornadic” supercells (e.g., those that produced F0–F1 tornadoes that persisted 5 min or less) often had surface thermodynamic characteristics that were similar to the RFDs associated with non-tornadic supercells. The surface θ_v and θ_e deficits in these RFDs generally were approximately 4–7 K and 10–12 K, respectively, within a few km of the vorticity centers (e.g., Figs. 5.10 and 5.11). These surface parcels were associated with generally >100 J kg⁻¹ CAPE (below 500 mb) and <150 J kg⁻¹ CIN.

In the RFDs associated with much more prolific tornado-producing supercells (e.g., those that produced tornadoes of \geq F2 intensity or tornadoes that persisted >5 min), surface θ_v and θ_e deficits were relatively small (typically <2 K and <4 K, respectively, within 2 km of the tornadoes)(e.g., Figs. 5.12, 5.13, 5.14, 5.15, 5.16, 5.17, and 5.18). In a few cases (e.g., Cases 18, 19, 20, 24, 25—note that all of these contained a strong tornado), the temperatures and θ_v values observed in the RFD were *warmer* than the inflow values. In such cases, the warm downdrafts *were not simply midlevel air that had descended dry adiabatically after all hydrometeors had evaporated or sublimated from the parcels* (i.e., the “heatburst mechanism”).

CASE 2
0028:32 UTC 30 APRIL 1995

(t-0 min)

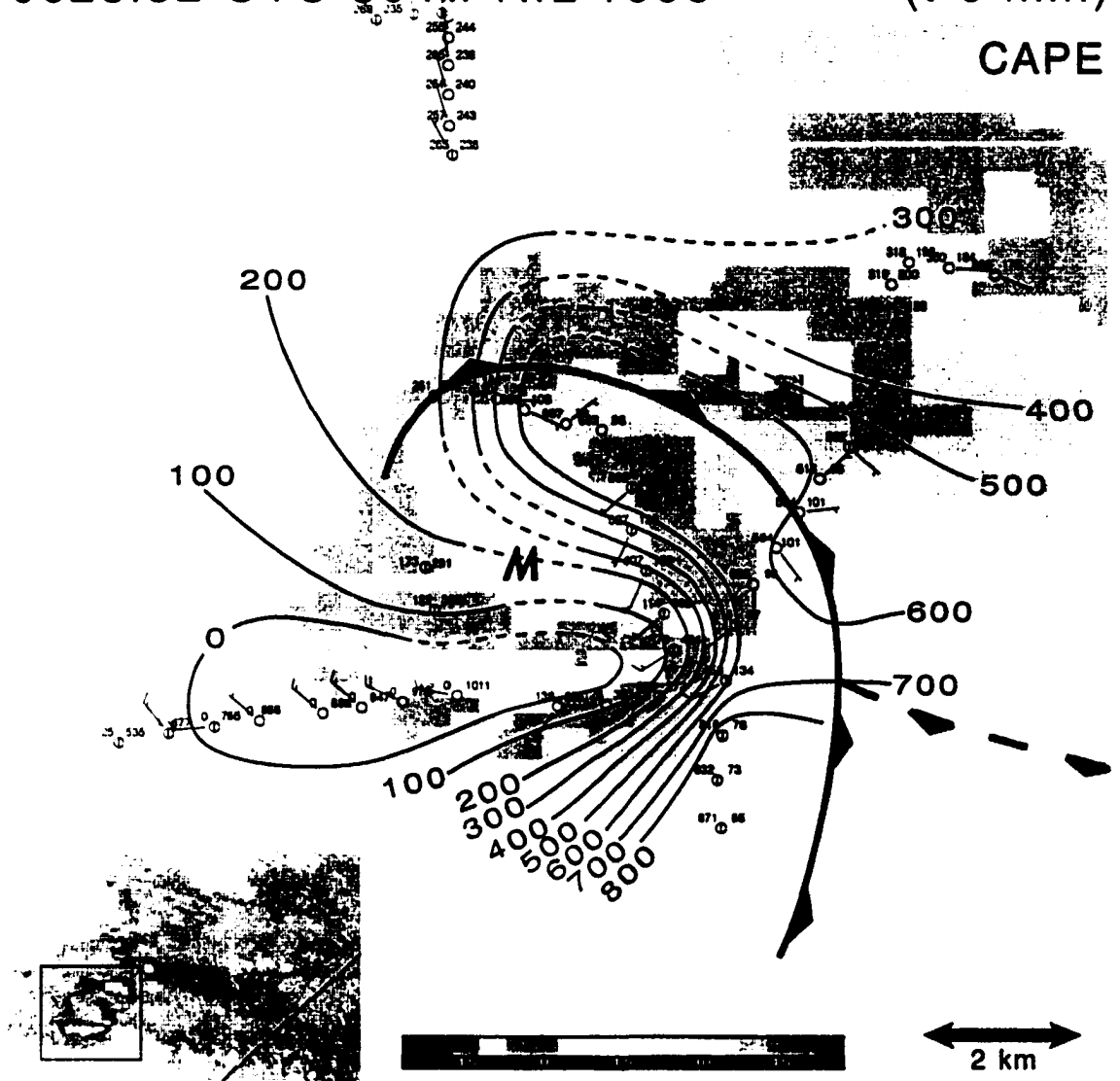


Figure 5.6: As in Fig. 5.1. but CAPE (J kg^{-1}) below 500 mb is analyzed assuming undiluted ascent from the surface and including virtual temperature effects. The station models display CAPE (left) and CIN (right).

CASE 2
0028:32 UTC 30 APRIL 1995

(t-0 min)

CIN

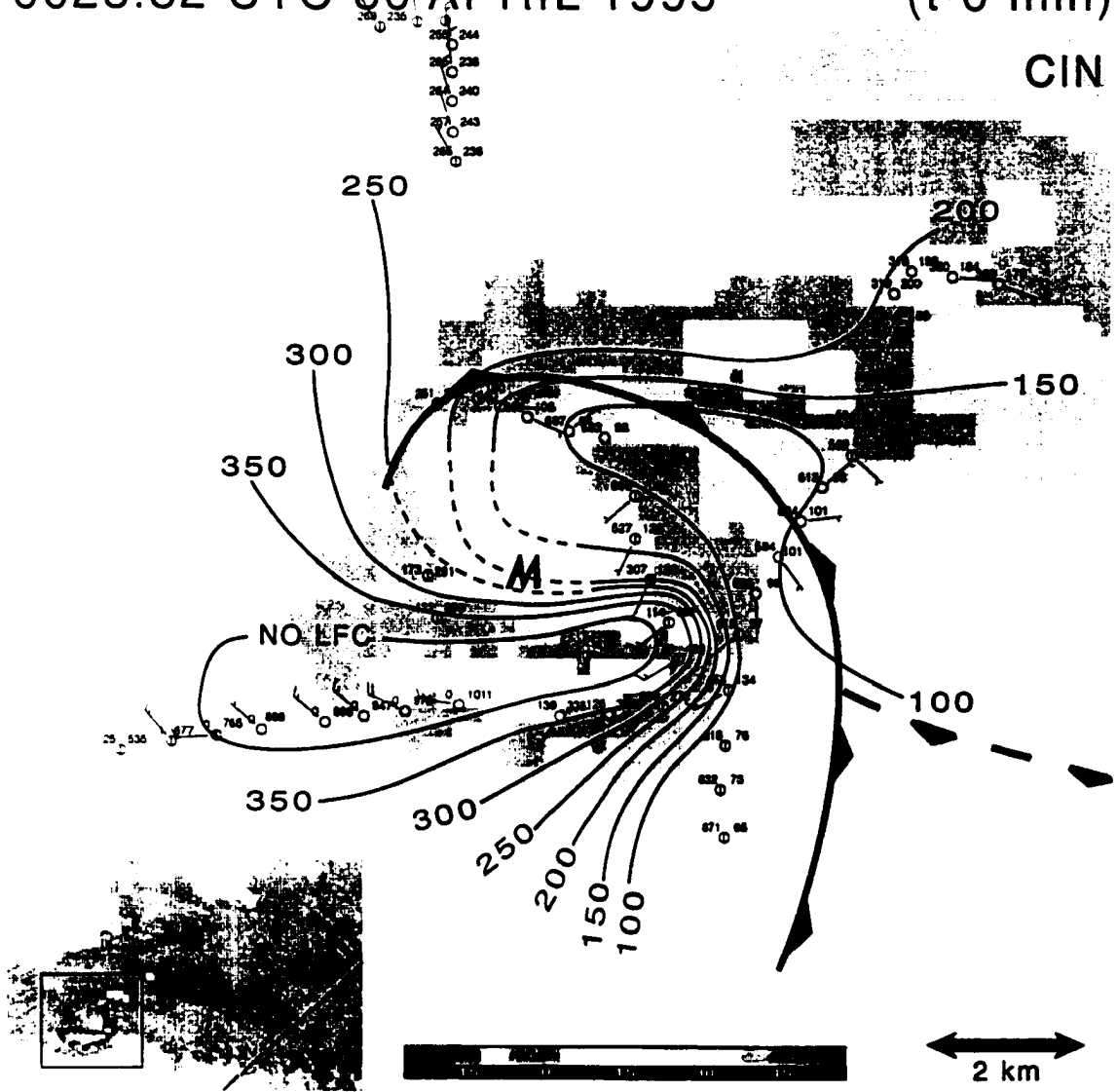


Figure 5.7: As in Fig. 5.6, but CIN is analyzed.

CASE 5
2014:43 UTC 8 JUNE 1995

(t-0 min)

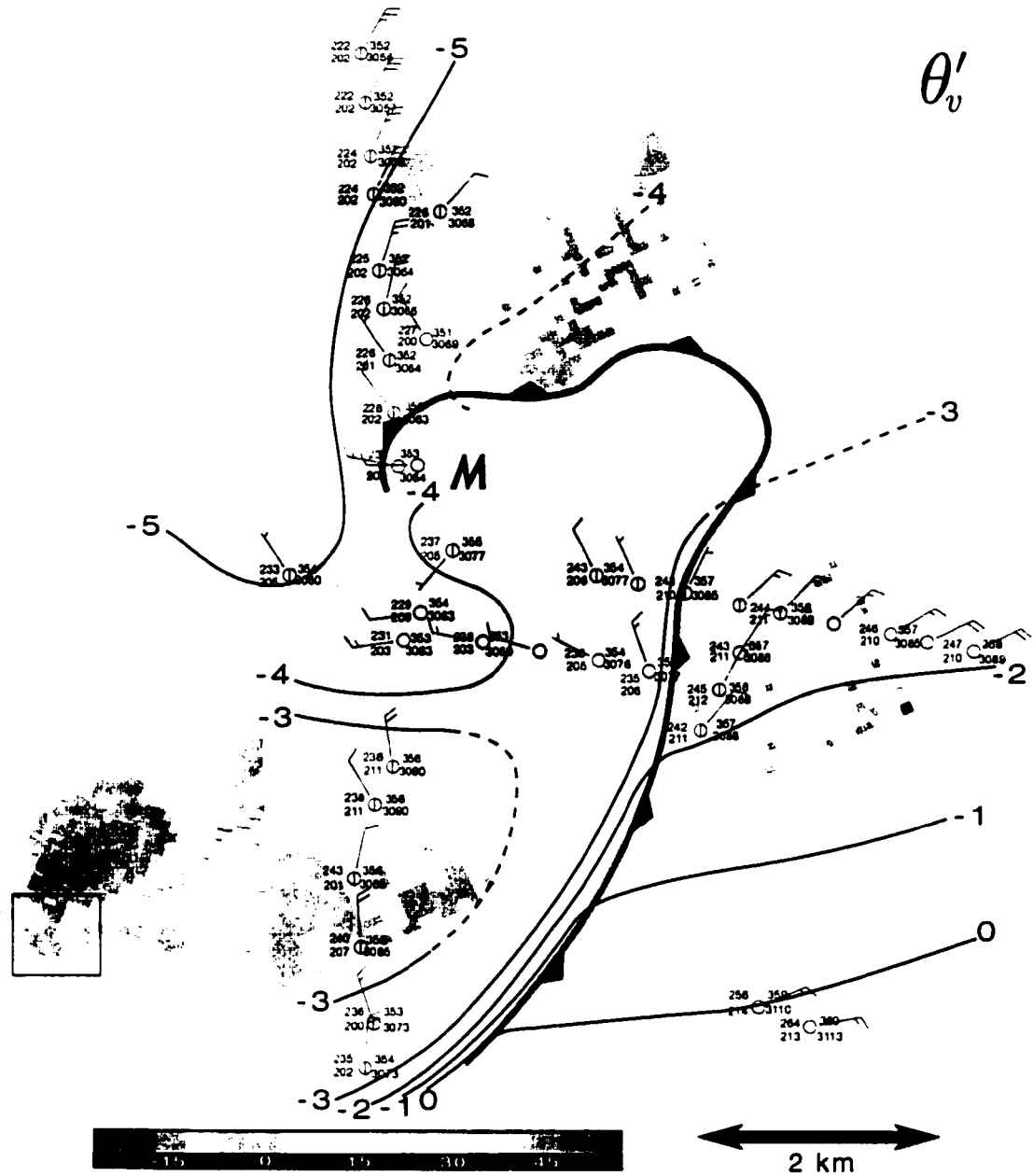


Figure 5.8: As in Fig. 5.1. for 2014:43 UTC 8 June 1995. Radar reflectivity data are from the DOW radar.

CASE 5
2014:43 UTC 8 JUNE 1995 (t-0 min)

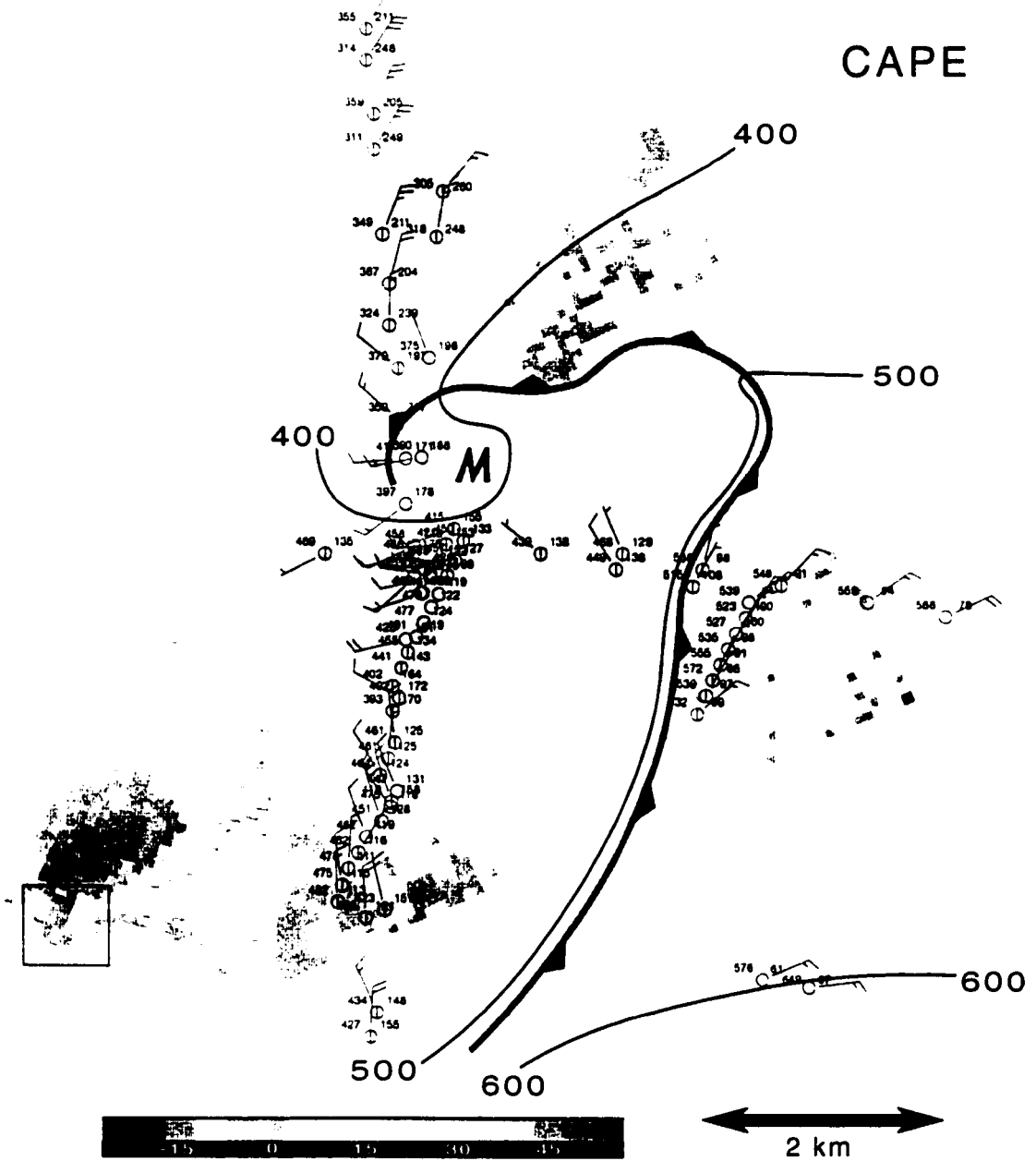


Figure 5.9: As in Fig. 5.8, but CAPE is analyzed.

CASE 13
2349:30 UTC 6 MAY 1994

(t-22 min)

θ'_v

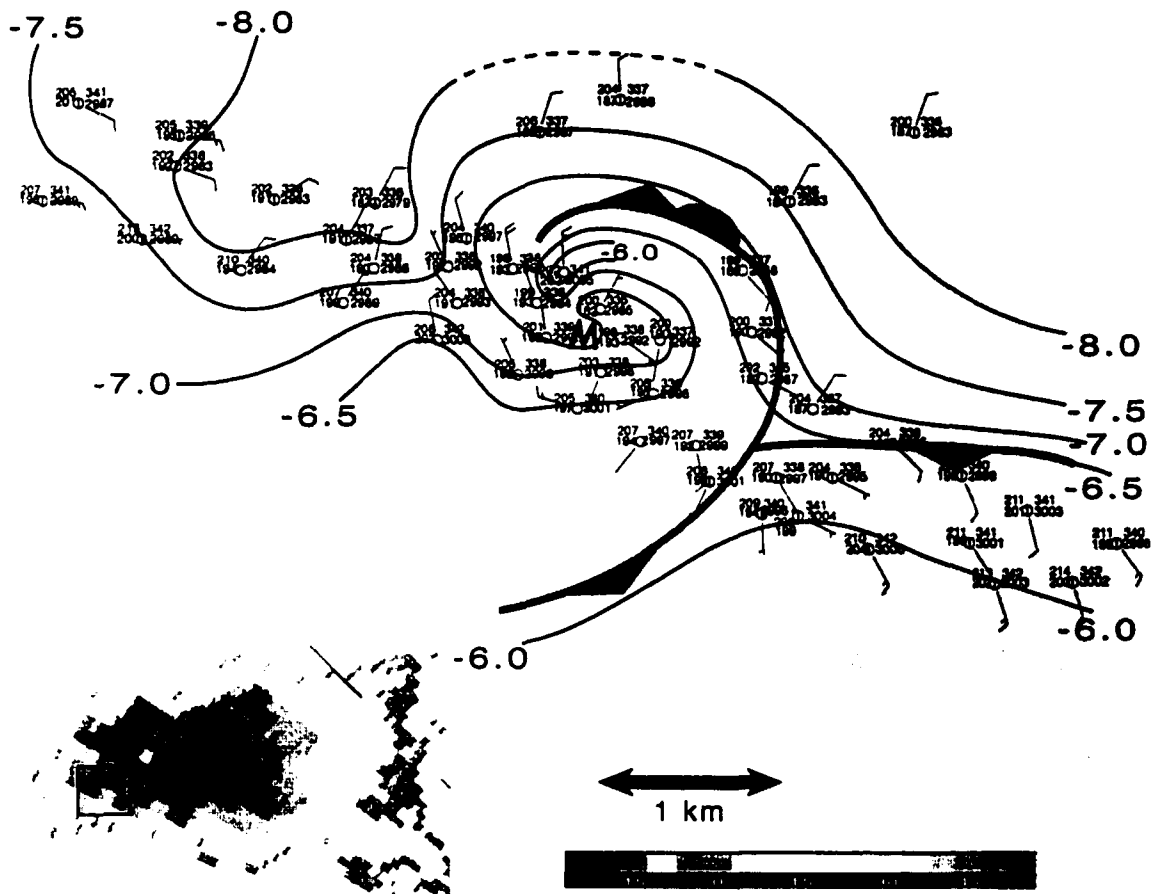


Figure 5.10: As in Fig. 5.1. for 2349:30 UTC 6 May 1994. Radar reflectivity data are from the KINX WSR-88D radar. The "t-22 min" indicates that the analysis time is 22 min prior to tornadogenesis.

CASE 30

0028:13 UTC 3 JUNE 1999

(t-12 min)

θ'_v

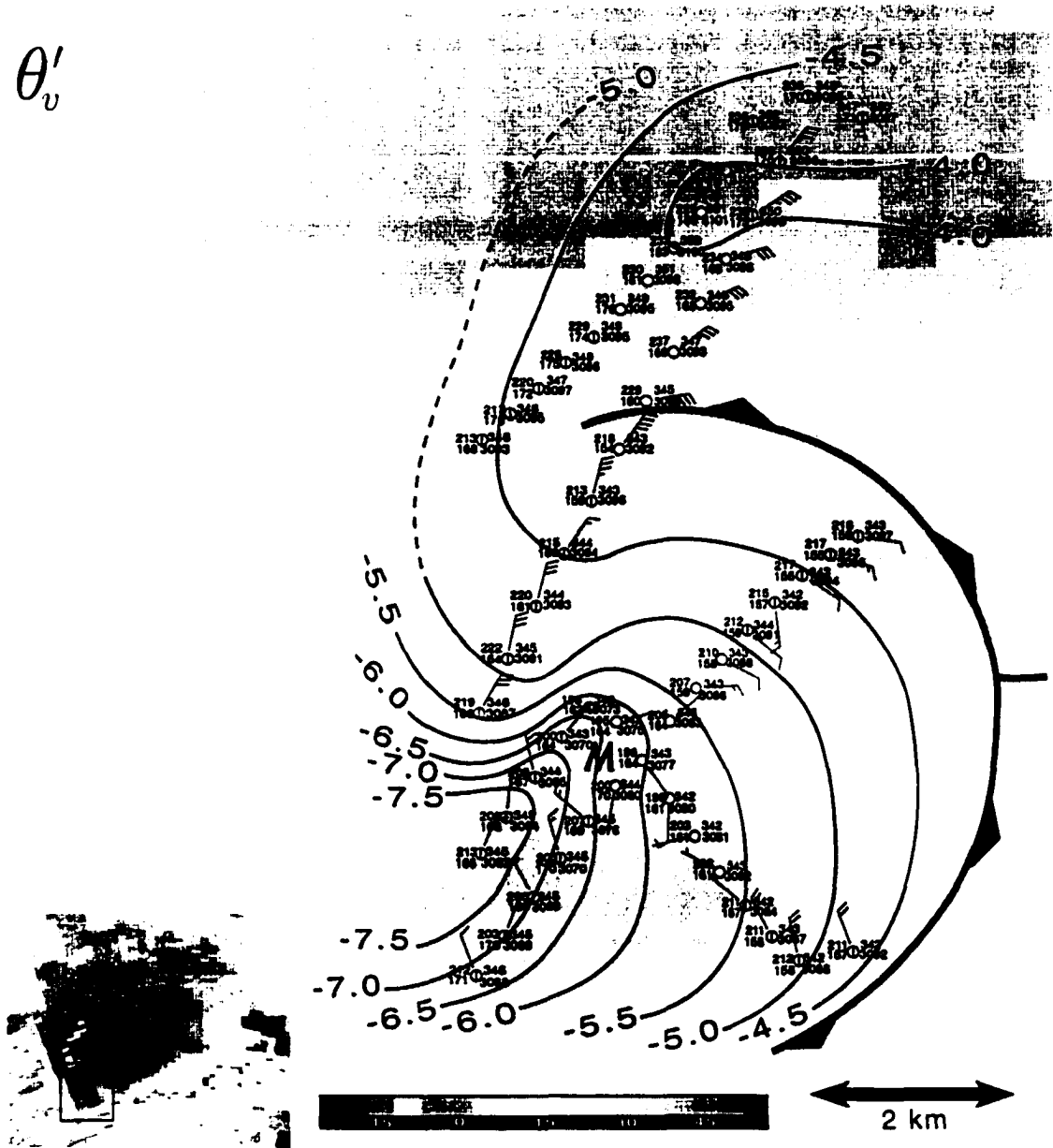


Figure 5.11: As in Fig. 5.10. for 0028:13 UTC 3 June 1999. Radar reflectivity data are from the KLBB WSR-88D radar.

Instead, these warm downdrafts had small (often <3 K) θ_e deficits, implying that the parcels did *not* have midlevel *environmental* origins. The implications of this finding will be discussed more fully in chapter 8.

The θ_e values measured at the surface within RFDs associated with tornadic supercells generally were similar to values observed at lower altitudes (often <1 km AGL) on nearby soundings, compared to the non-tornadic cases (and as mentioned above, sometimes RFD θ_e values were similar to inflow θ_e values)(e.g., Fig. 5.19). Furthermore, all of the RFDs associated with tornadic storms contained surface-based CAPE, with some RFDs containing extreme values of CAPE [e.g., >700 J kg^{-1} below 500 mb on 8 June 1995 and 3 May 1999 (Figs. 5.20 and 5.21)]. Values of CAPE within the RFDs of tornadic supercells increased as tornado intensity and longevity increased, and CIN values within the RFDs were often <50 J kg^{-1} , especially in the portions of the RFD northeast through southeast of the tornadoes (e.g., Figs. 5.20 and 5.21).

Although small θ_v and θ_e deficits were detected in most of the RFDs associated with strong tornadoes, in one well-sampled case, a relatively large θ_v and θ_e deficit (up to 7 K and 18 K, respectively) was observed within a hook echo associated with a strong (F4), long-lived (>20 min) tornado (e.g., Fig. 5.22). However, despite the large surface θ_v and θ_e deficits, the relatively cool parcels within the hook echo still were associated with significant surface-based CAPE (Fig. 5.23). It may be noteworthy that large-scale CAPE values for this case were exceptionally large (>4000 J kg^{-1}): thus, surface parcels with θ_v values as much as 7 K smaller than those on the large scale still were potentially buoyant.

5.3 Miscellaneous new observations

It may be noteworthy that in some of the most prolific tornadic storms intercepted (Cases 20, 24, and 25), surface baroclinity was weak (maximum $|\nabla_h \theta'_v| < 1$ K km^{-1}), absent, or oriented such that horizontal vorticity generation would be antistream-wise. These observations argue, at the least, that surface baroclinity is not a necessary condition for tornadogenesis. Moreover, the fact that these storms were able to produce so many long-lived, strong tornadoes may imply that the lack of baroclinity

CASE 18
2345:12 UTC 2 JUNE 1995 (t+2 min)

θ'

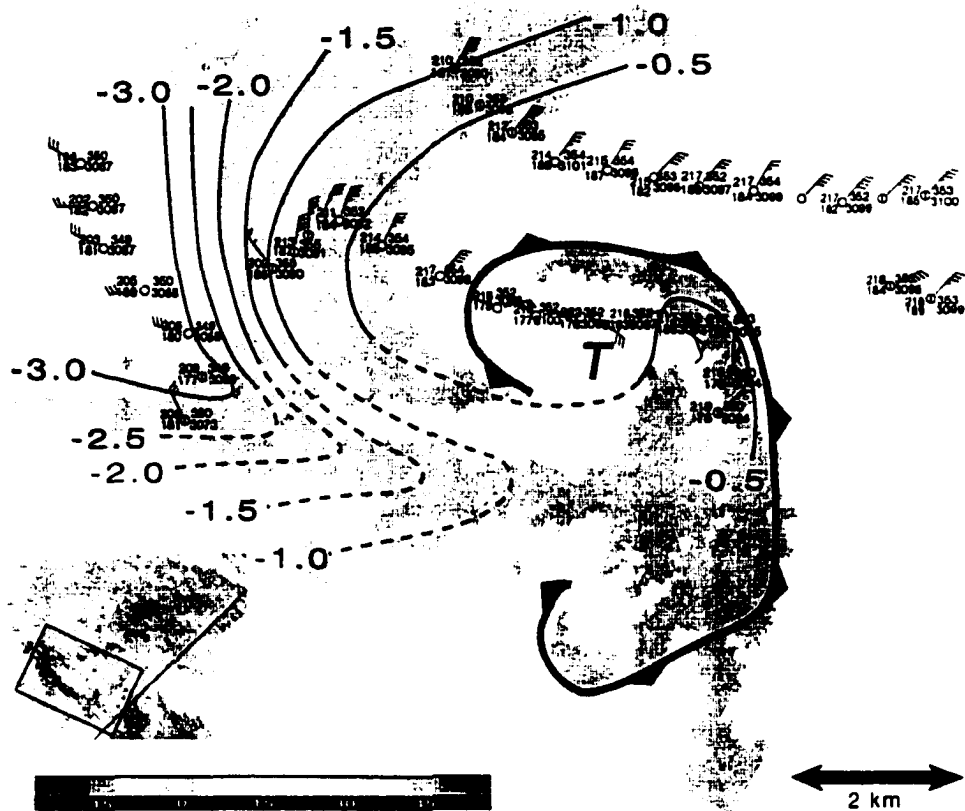


Figure 5.13: As in Fig. 5.10, for 2345:12 UTC 2 June 1995. Radar reflectivity data are from the DOW radar.

CASE 18

2345:12 UTC 2 JUNE 1995

(t+2 min)

θ'_e

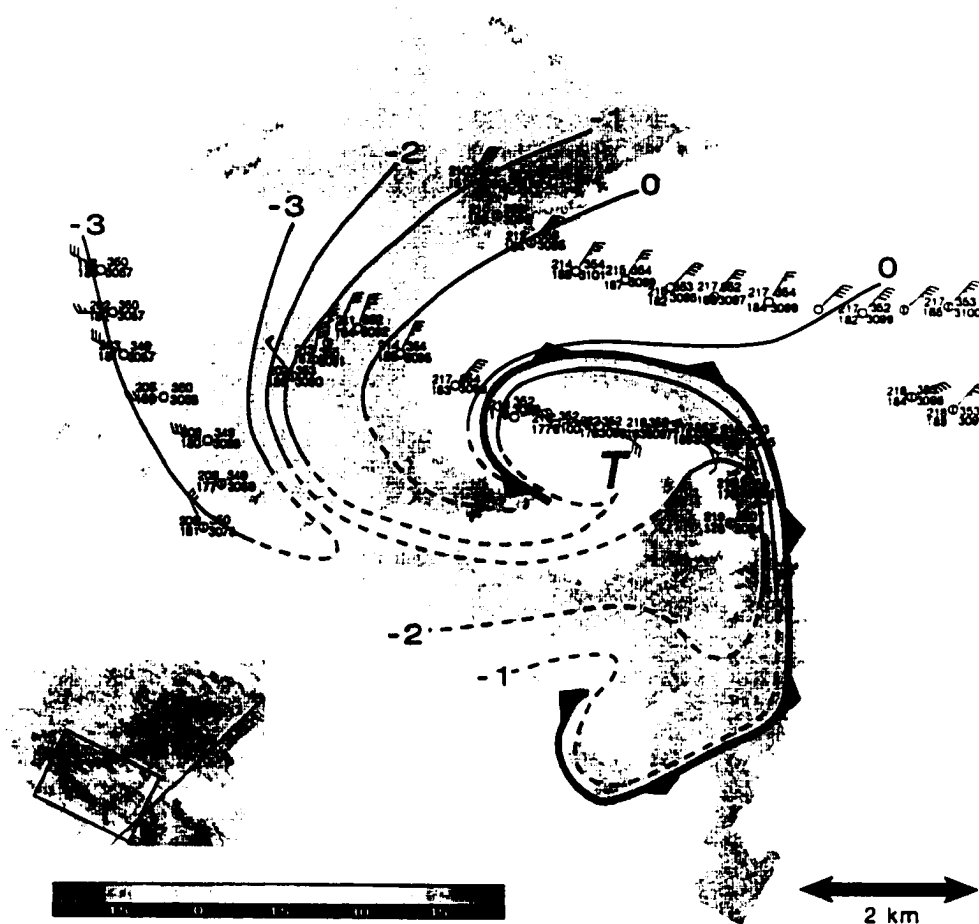


Figure 5.14: As in Fig. 5.13. but θ'_e is analyzed.

CASE 19
0106:00 UTC 3 JUNE 1995 (t+9 min)

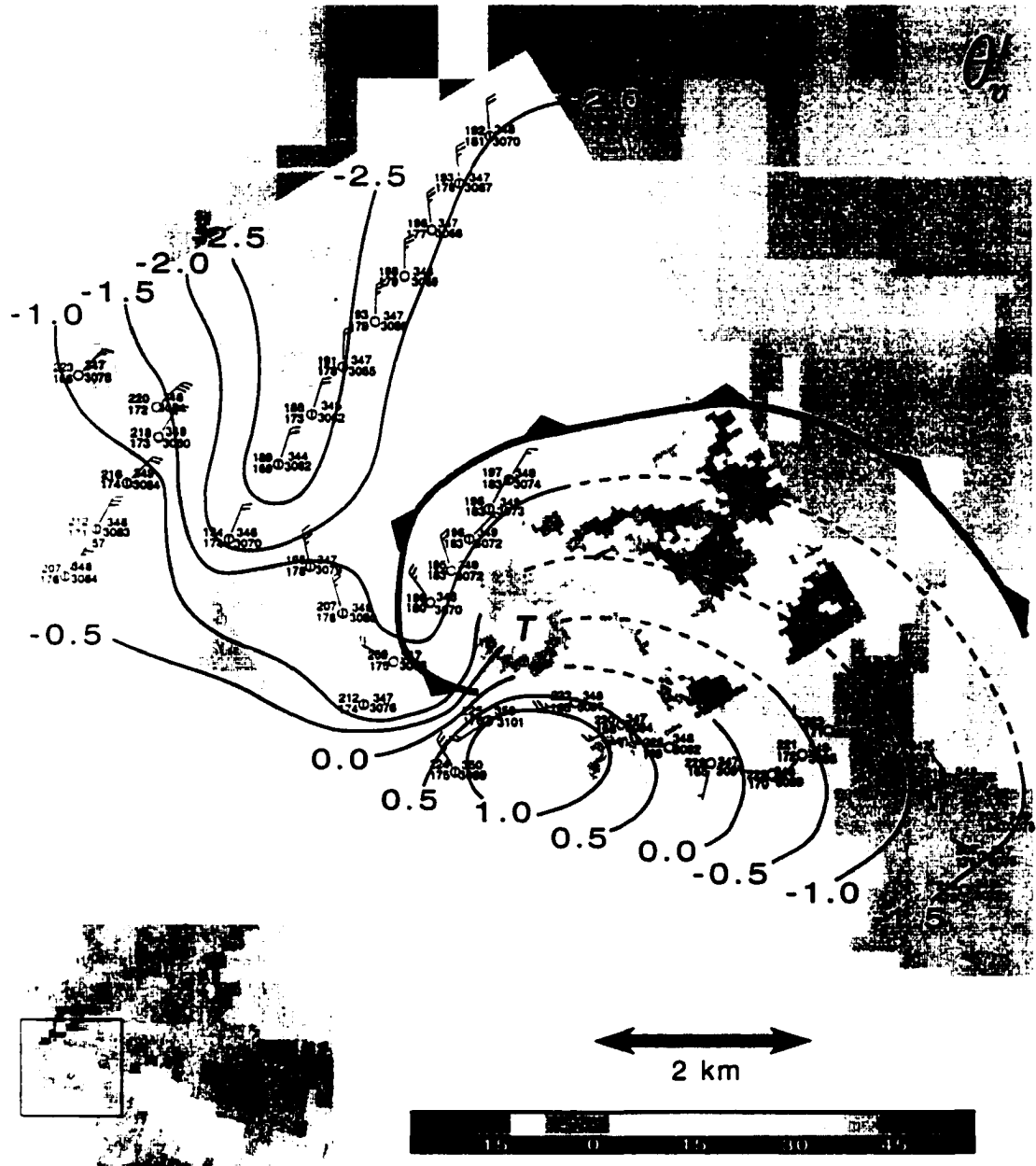


Figure 5.15: As in Fig. 5.10, for 0106:00 UTC 3 June 1995. Radar reflectivity data are from the NOAA-P3 LF and DOW (inset) radars.

CASE 20

0022:00 UTC 9 JUNE 1995

(t+47 min)

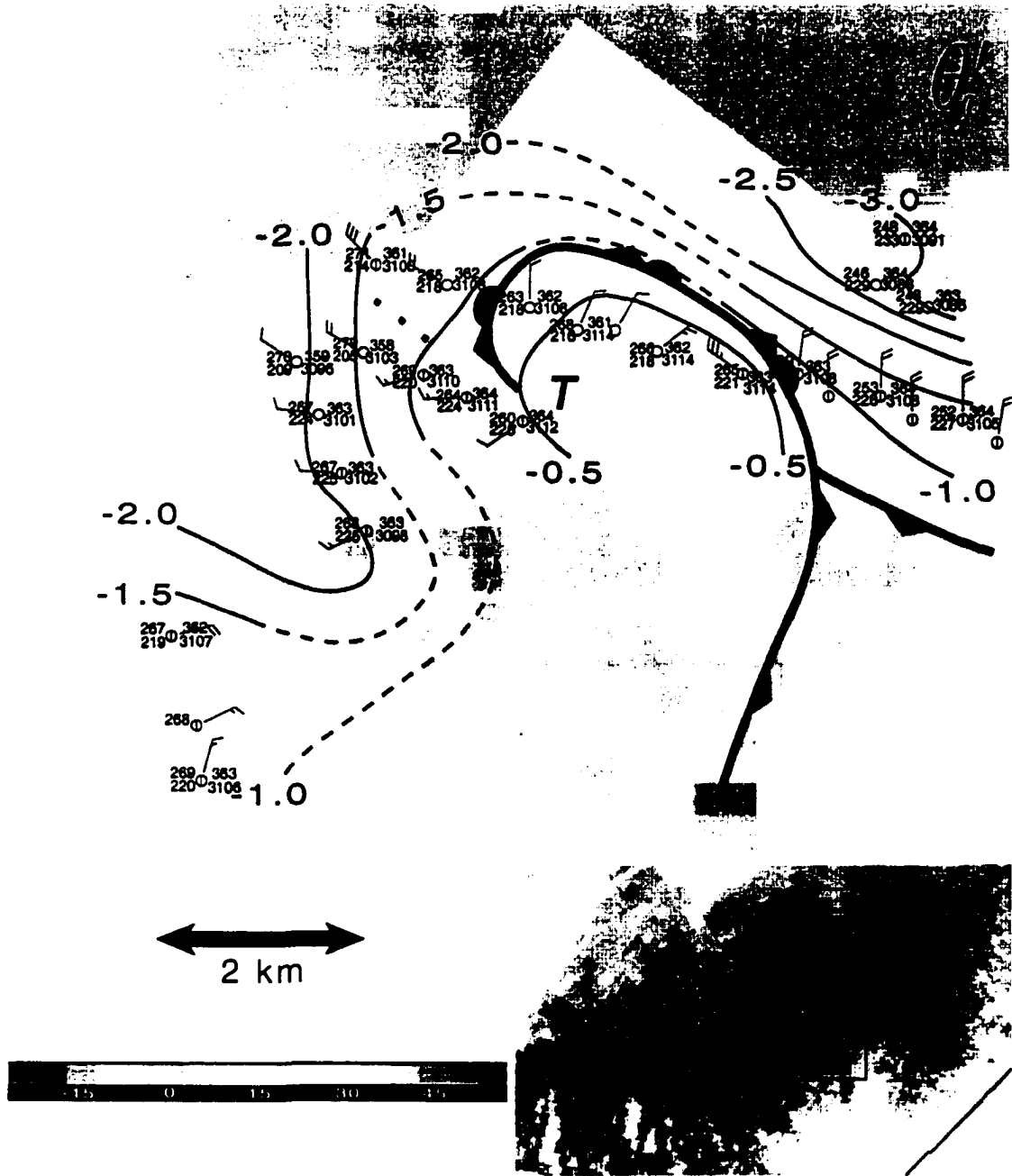


Figure 5.16: As in Fig. 5.10, for 0022:00 UTC 9 June 1995. Radar reflectivity data were obtained from the NOAA-P3 LF and DOW (inset) radars, and $|\Delta t_{max}| = 2.5$ min was used.

CASE 25
0052:04 UTC 4 MAY 1999

(t+5 min)

θ'_v

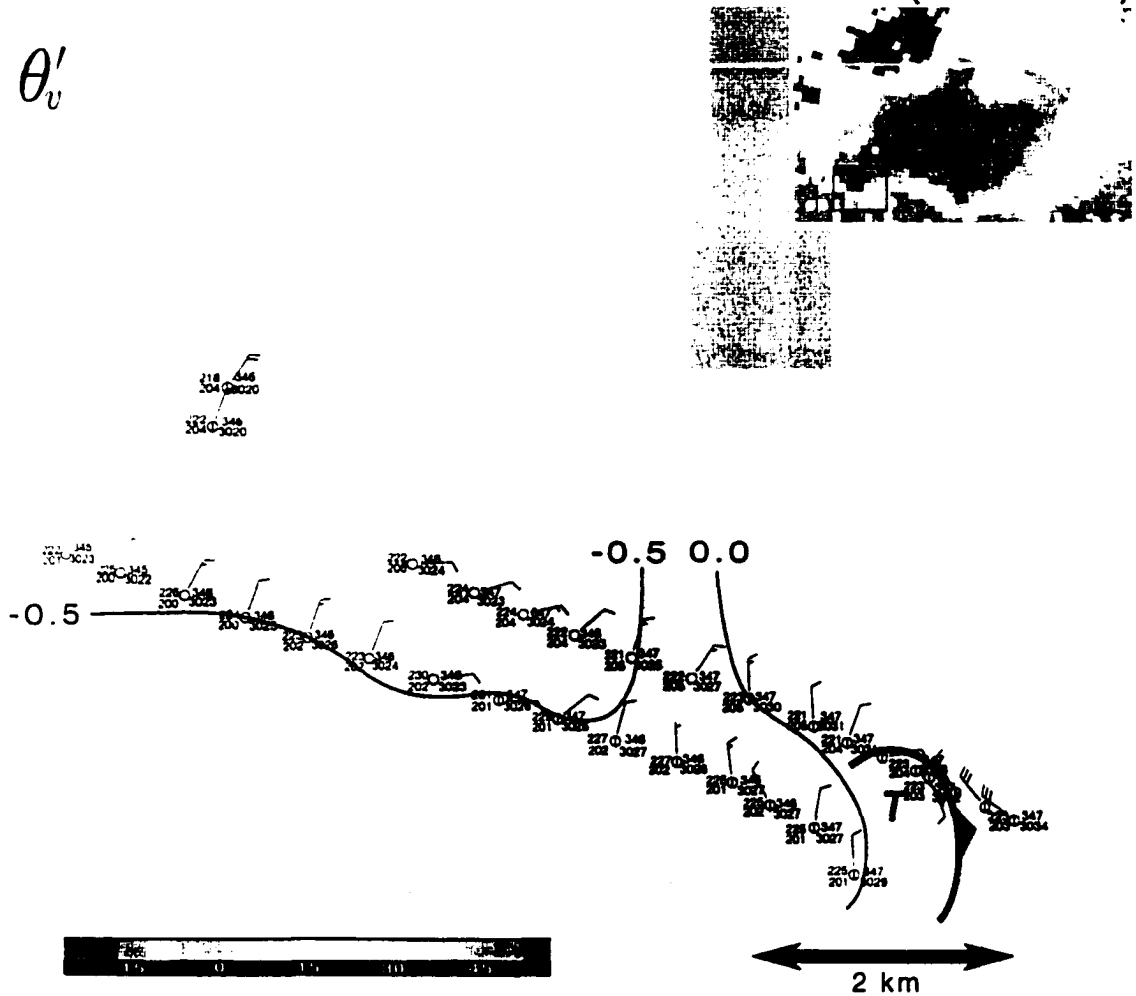


Figure 5.17: As in Fig. 5.10, for 0052:04 UTC 4 May 1999. Radar reflectivity data were obtained from the KTLX WSR-88D radar.

CASE 25
0052:04 UTC 4 MAY 1999

(t+5 min)

θ'_e

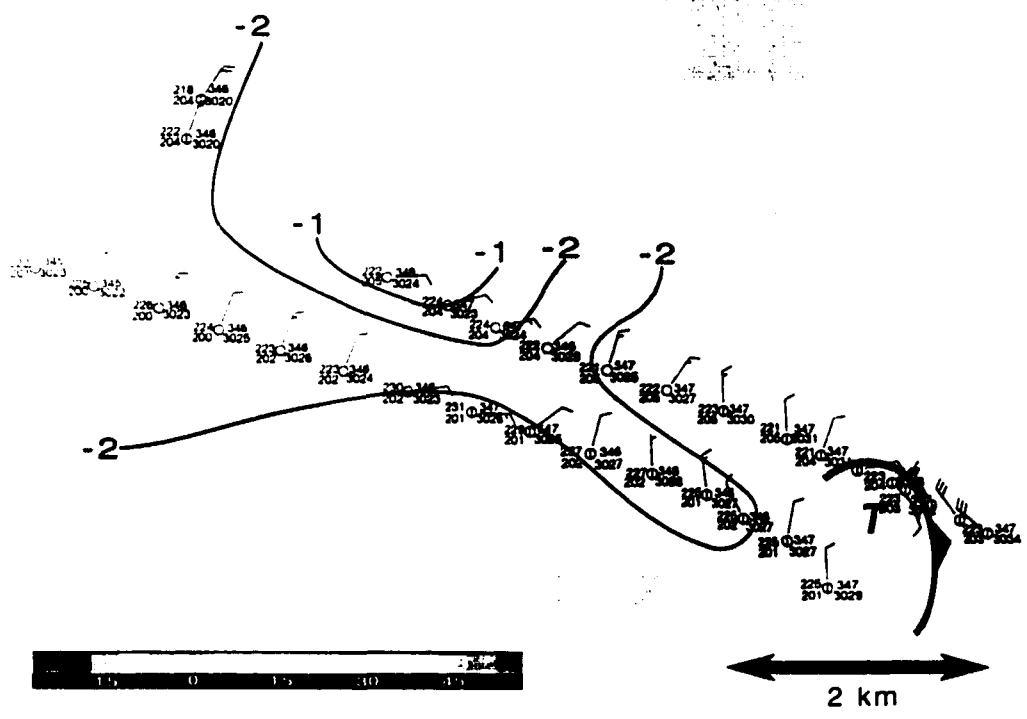


Figure 5.18: As in Fig. 5.17, but θ'_e is analyzed.

CASE 18
2345:12 UTC 2 JUNE 1995 (t+2 min)

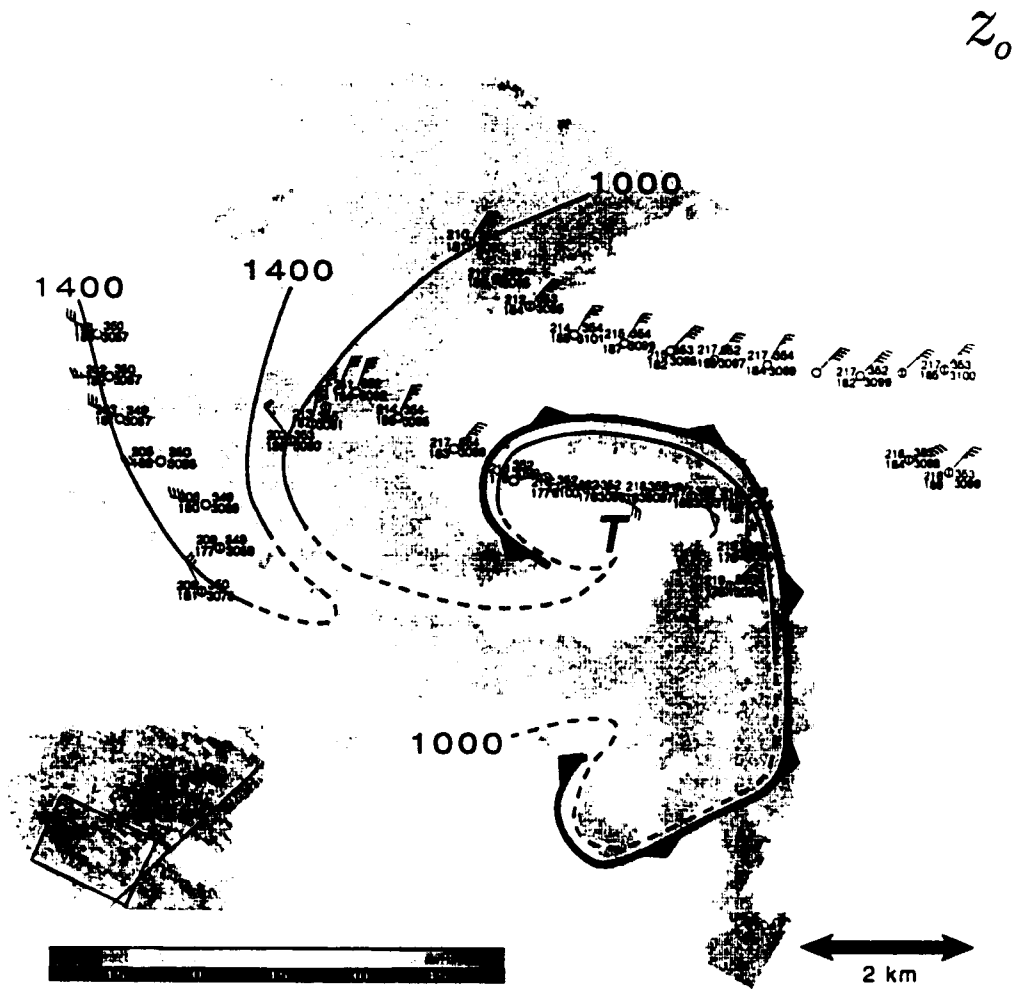


Figure 5.19: As in Fig. 5.13, but z_0 is analyzed.

CASE 25
0052:04 UTC 4 MAY 1999

(t+5 min)

CAPE

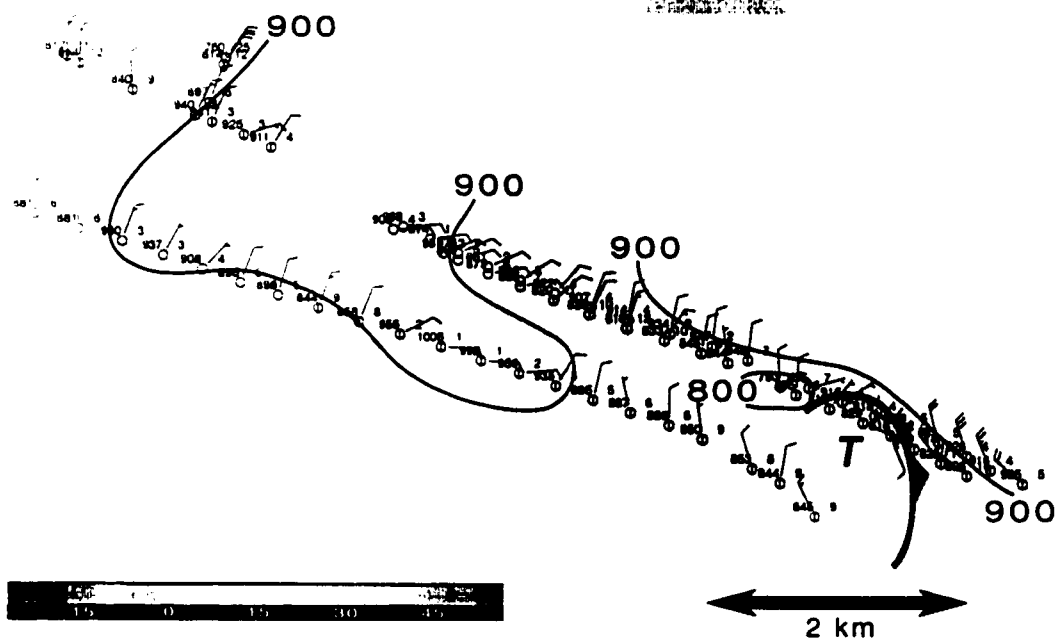


Figure 5.21: As in Fig. 5.17, but CAPE is analyzed.

CASE 21
0101:00 UTC 9 JUNE 1995 (t+16 min)

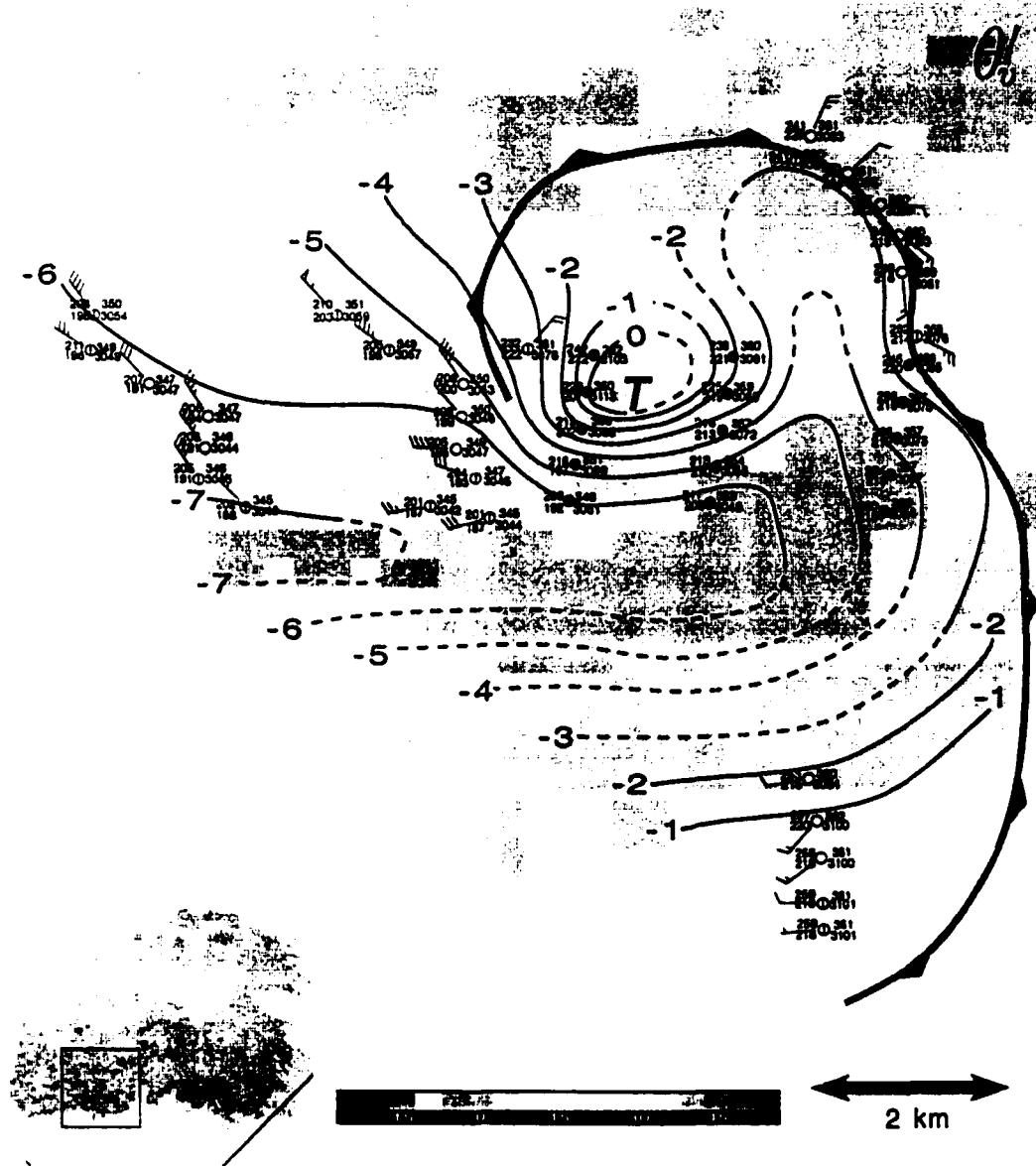


Figure 5.22: As in Fig. 5.10, for 0101:00 UTC 9 June 1995. Radar reflectivity data are from the NOAA-P3 LF radar, and $\Delta t_{max} = 2.5$ min was used. Data obtained from turtles (Winn et al. 1999) also have been incorporated into the analysis (turtle observations are denoted as black-filled station models). T readings from the turtles were not used in the first 2 min following deployment in order to allow the T to adjust to the environment after being transported inside an air-conditioned truck (the thermistor has a large time constant). Moisture was not measured by the turtles, but mixing ratios were interpolated to the turtle locations from the mobile mesonet locations in order to obtain estimated θ_e (sensitive to mixing ratio errors) and θ_v (not as sensitive to mixing ratio errors) values at the turtle locations. All T , T_d , θ_v , and θ_e measurements and estimates in the vicinity of the turtles should be viewed cautiously.

was symptomatic of a lack of cold air near the mesocyclone. Relatively cold, stable surface air parcels were found to be more widespread in non-tornadic RFDs, as documented in section 5.1.

In none of the cases was evidence found of a *separate* “occlusion downdraft” in the mobile mesonet data. While I agree that the dominant downdraft forcing may be different at various times in the evolution of the RFD, the surface data do not appear to indicate that the “occlusion downdraft” proposed by Klemp and Rotunno (1983) is anything more than a surging, intensification of the RFD (e.g., Fig. 5.1). Furthermore, no evidence was obtained of a tornado occurring prior to or in the absence of the occlusion of the mesocyclone that was originally described by Burgess et al. (1977) and Lemon and Doswell (1979).

Relatively high pressure was observed along the RFD gust fronts *and* within the RFDs of both tornadic and non-tornadic supercells—both are locations where convergence and divergence are a maximum, respectively, and therefore fluid extension¹ [proportional to $(\partial u/\partial x)^2 + (\partial v/\partial y)^2$] “contributes” to pressure excess there (Rotunno and Klemp 1982)(e.g., Figs. 5.24, 5.25, 5.26, and 5.27). Furthermore, the high pressure regions typically spiraled around the cyclonic vorticity maxima, forming nearly closed annuli of pressure excess, similar to what Fujita (1958b) had inferred (cf. Fig. 1.7).

It is worth mentioning that in all but one non-tornadic case, a mesocyclone was detected at the surface, in addition to an occluded gust front structure. In fact, the analyses presented in this chapter reveal that the surface gust front and streamline structures of the non-tornadic and tornadic cases often were indistinguishable (except for the obvious presence of the tornado in the latter cases). The only apparent significant difference appears to be the low-level stability. Furthermore, in a couple of cases, tornadogenesis occurred many minutes (as many as 10–20 min) after the occlusion of the low-level mesocyclone (e.g., Figs. 5.10 and 5.11).

Three-dimensional cloud simulation studies using a Kessler microphysics parameterization (Kessler 1969) have found the “undercutting” of the mesocyclone by outflow to be detrimental to storm sustenance (and presumably tornadogenesis) (Wilhelmson and Klemp 1978; Weisman and Klemp 1982; Brooks et al. 1993, 1994a,b;

¹“Fluid extension” is not invariant to rotation of coordinate axes.

CASE 6
0205:12 UTC 20 MAY 1998 (t-0 min)

p'

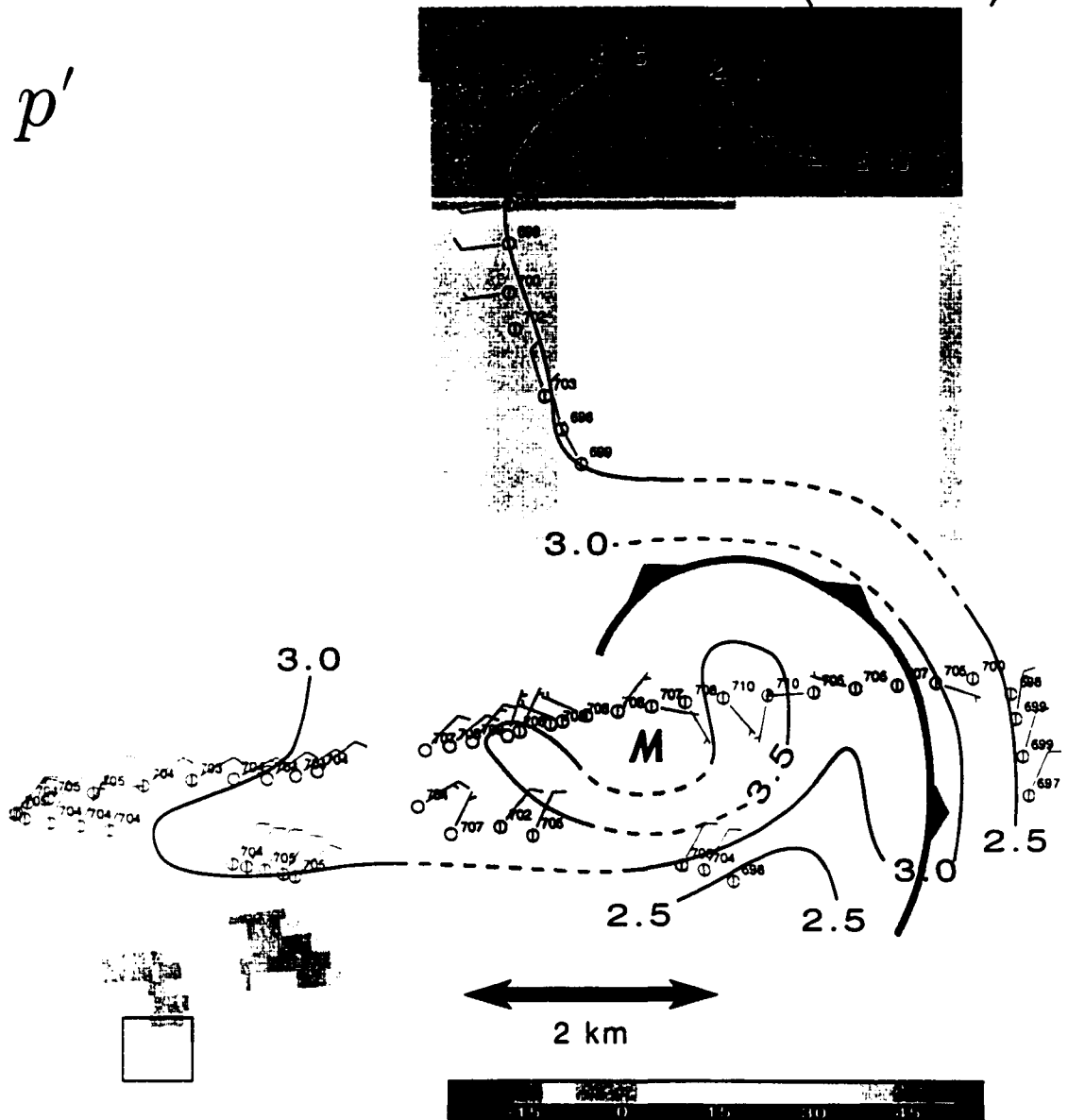


Figure 5.24: As in Fig. 5.2. but pressure fluctuation, p' (mb), is analyzed. Pressures reduced to the mean elevation of the mobile mesonet observations to the nearest 0.1 mb (decimal and leading "8" omitted) appear in the station models.

CASE 18

2345:12 UTC 2 JUNE 1995

(t+2 min)

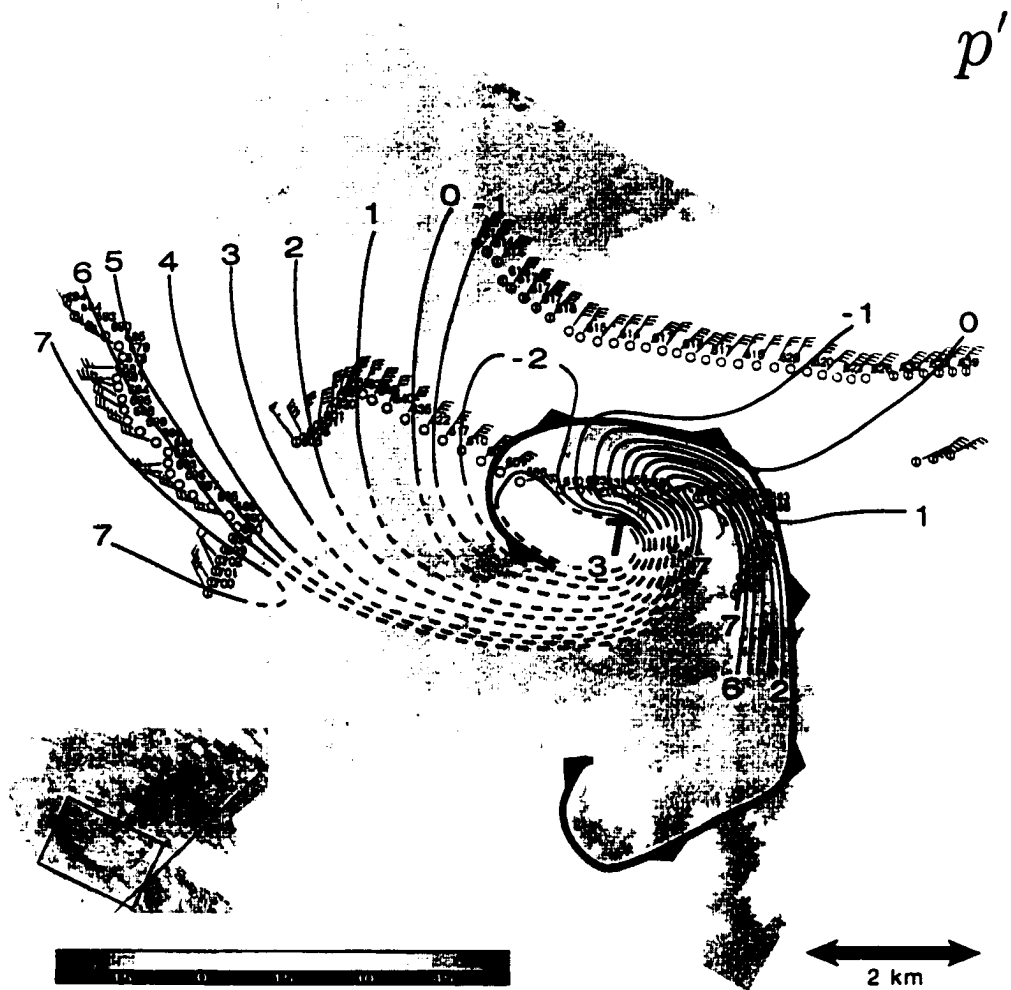


Figure 5.25: As in Fig. 5.13. but p' is analyzed.

CASE 21
0101:00 UTC 9 JUNE 1995 (t+16 min)

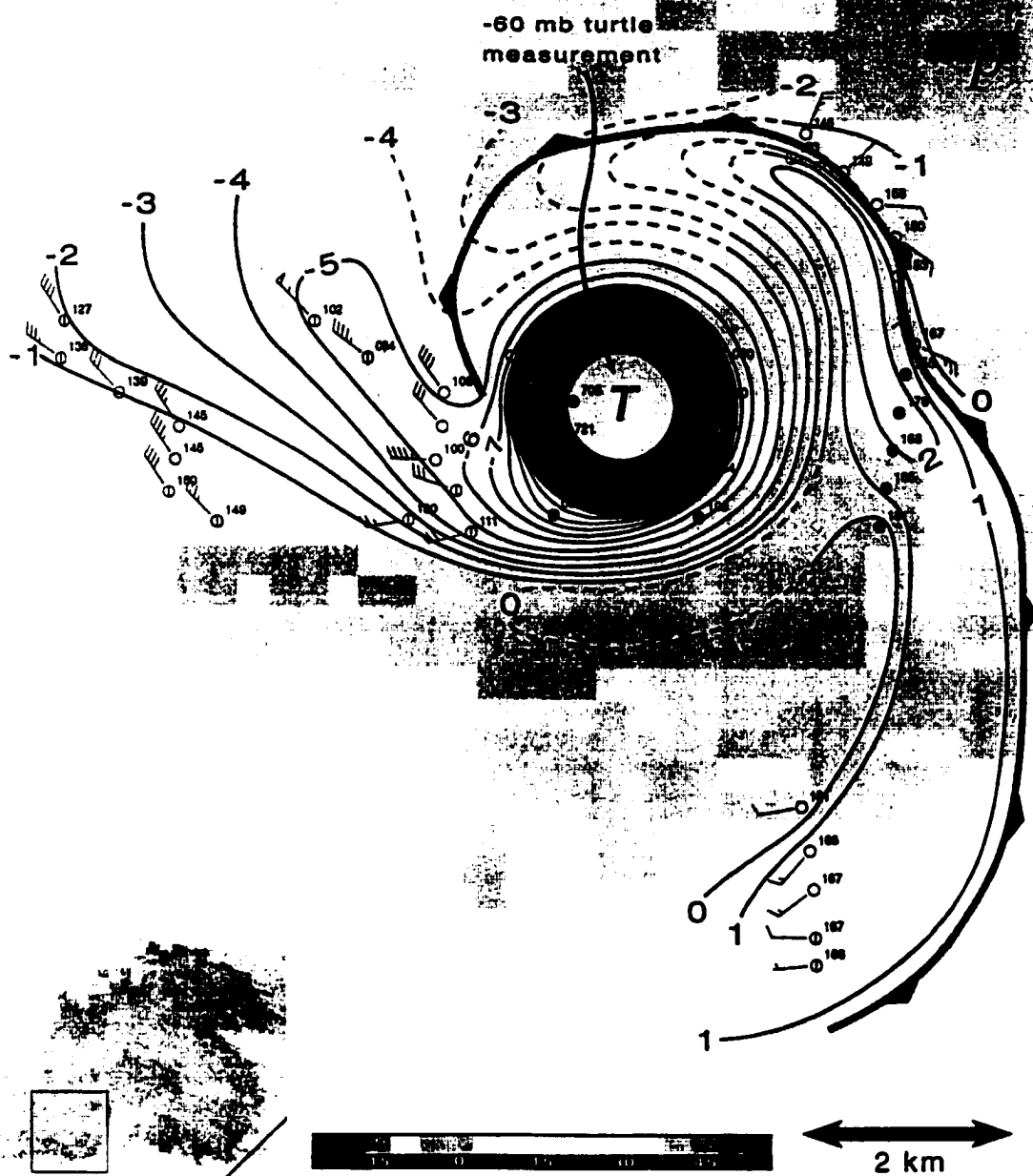


Figure 5.26: As in Fig. 5.22, but p' is analyzed.

CASE 30

0028:13 UTC 3 JUNE 1999

(t-12 min)

p'

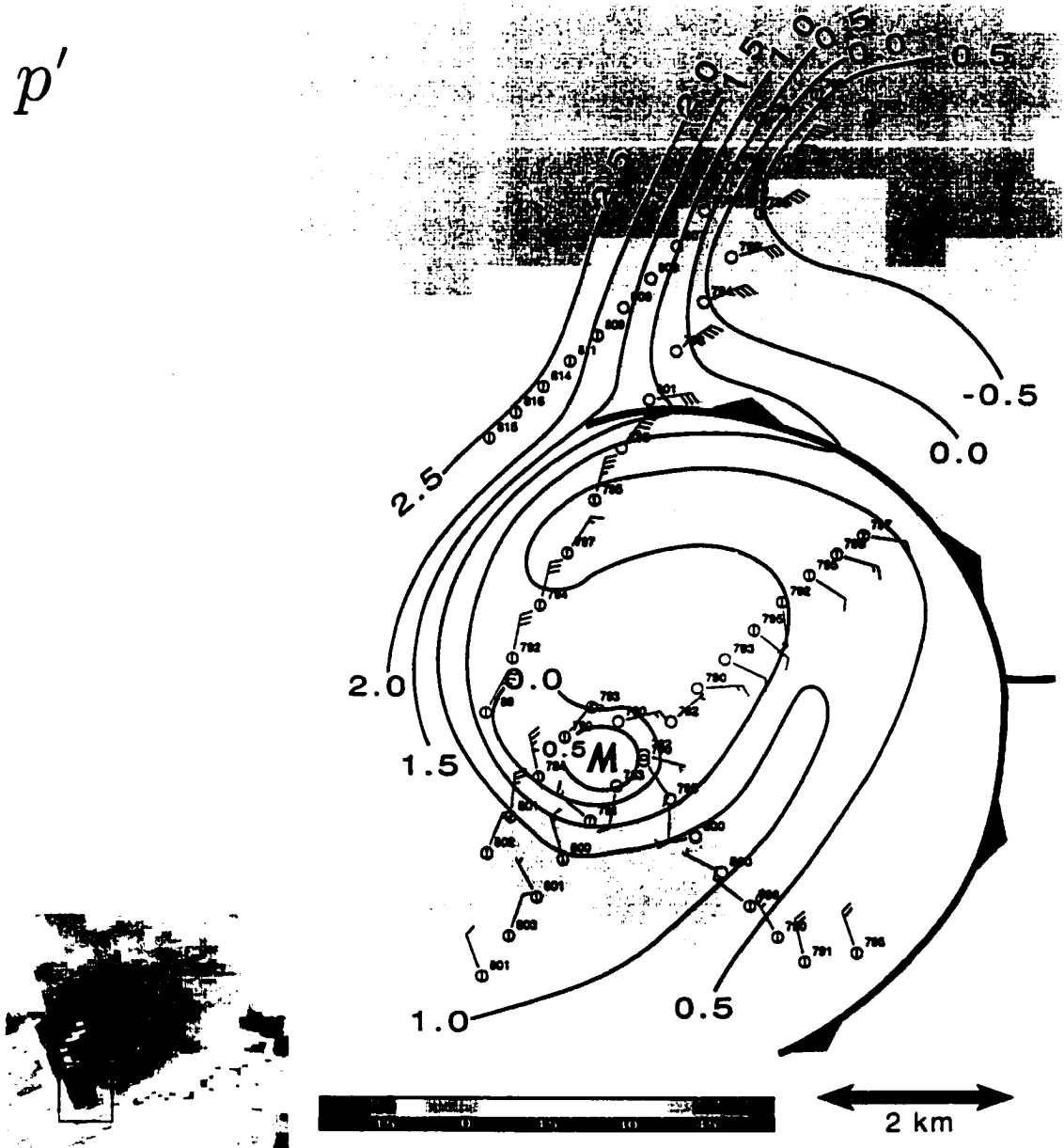


Figure 5.27: As in Fig. 5.11, but p' is analyzed.

Gilmore and Wicker 1998). However, in only one case did a mesocyclone appear to be undercut by outflow (and consequently, no surface mesocyclone was detected). This tornadogenesis failure mechanism may not be as common as suggested by previous simulation studies. However, it is possible that many storms that were undercut by RFD outflow were not sampled—updrafts that visually appeared to be undercut often were abandoned during field operations in favor of storms that did not appear visually to be undercut. A new hypothesis will be posed in chapter 8 that attempts to explain why tornadogenesis failure may occur if the RFD air mass is too cold and stable (and yet the mesocyclone may not be undercut by outflow).

Finally, several previous studies have analyzed a couplet of vertical vorticity straddling the hook echo and RFD (reviewed in chapter 1), although the feature has understandably escaped recognition in many of the past studies. The mobile mesonet detected a similar couplet of vertical vorticity at the surface within both tornadic and non-tornadic RFDs, when sampling allowed (e.g., Figs. 5.2, 5.15, and 5.16). No differences between the appearance of the couplet in the tornadic and non-tornadic cases was observed.

5.4 Summary

RFD characteristics for each case and mean RFD characteristics are summarized in Tables 5.1 and 5.2, respectively. A 4 km radius from the circulation center was used for the minimum θ'_v , θ'_e , and CAPE, and for the maximum z_o and CIN values that appear in the tables; however, a 2 km radius was used for the maximum θ'_v , θ'_e , and CAPE, and for the minimum z_o and CIN values that appear in the tables. The arbitrary choice of using a smaller radius for the aforementioned variables was made because I felt that warm regions, often in the wake of the updraft in regions where streamlines clearly diverge from the circulation and do not enter it, should not be considered in the results. In Figs. 5.28–5.34, the results are summarized graphically by way of scatter plots.

In Table 5.2 and in Figs. 5.28–5.34, the differences in the means of the groups were compared to determine if they were statistically significant. The common test

for significance is the t -test; however, a different approach was used instead, following Mielke et al. (1981). The same approach was used by Blanchard and Lopez (1985) and Rasmussen and Blanchard (1998), and is well-summarized by Blanchard and Lopez (1985): “The (t -test) ... assumes that the data sample follows the normal distribution. Since most atmospheric parameters are not normally distributed, but rather are highly skewed, this standard parametric test is inappropriate. A nonparametric test called Multi-Response Permutation Procedures (MRPP) is well suited to (atmospheric) data because it makes no assumption about the distribution of the population (Mielke et al. 1976, 1981). MRPP examines and compares the different data groups to determine whether they are from the same or different populations and gives the result in the form of a P -value of statistical significance.” MRPP can be used to indicate the similarity of any number of populations (2 in this case: tornadic and non-tornadic), and can be performed on one or several variables. The P -value is the probability that two sets of observations come from the same population (or $1 - P$ is the probability that two populations are different).

Case	Analysis time	min θ'_v within 4 km	max θ'_v within 2 km	min θ'_e within 4 km	max θ'_e within 2 km	min z_0 within 2 km	max z_0 within 4 km
1	2248 00 (-4)	-6.4±0.4 (II)	-4.1±0.4 (III)	-21.1±2.9 (II)	-3.1±2.9 (III)	0.1±0.2 (III)	1.5±0.2 (II)
2	0028 32 (+0)	-9.3±0.6 (III)	-3.6±0.6 (I)	-18.1±2.7 (III)	-3.1±2.7 (I)	0.2±0.2 (I)	2.8±0.3 (III)
3	2311 39 (+0)	-6.3±0.5 (III)	-3.8±0.7 (IV)	-9.6±2.6 (III)	-9.4±2.6 (I)	1.9±0.5 (IV)	2.0±0.5 (III)
4	0013 20 (+0)	-5.2±0.7 (III)	-1.2±0.7 (IV)	-11.7±2.7 (III)	-3.7±2.7 (IV)	2.0±0.3 (IV)	2.5±0.2 (III)
5	2014 43 (-0)	-5.6±0.5 (II)	-3.5±0.8 (I)	-12.1±2.6 (II)	-8.0±2.6 (IV)	1.0±0.8 (IV)	1.4±0.8 (II)
6	0205 12 (-0)	-11.1±0.5 (II)	-4.2±0.5 (IV)	-13.5±2.5 (II)	-9.5±2.5 (IV)	2.6±0.1 (IV)	5.4±0.6 (II)
7	0133 43 (-12)	-9.7±0.9 (II)	-5.7±0.9 (I)	-6.7±2.5 (III)	-2.7±2.5 (I)	0.3±0.1 (I)	0.4±0.1 (III)
8	0116 00 (-10)	-6.2±0.7 (III)	4.0±0.7 (IV)	-21.7±2.6 (II)	-14.7±2.6 (IV)	1.2±0.1 (IV)	1.7±0.1 (II)
9	0211 06 (-0)	0.2±0.7 (II)	3.0±0.8 (IV)	16.0±2.5 (II)	-8.1±2.6 (IV)	2.4±0.2 (IV)	3.1±0.2 (II)
10	0147 00 (-8)	-1.8±0.7 (I)	0.7±0.6 (IV)	12.9±2.8 (I)	6.9±2.8 (IV)	1.7±0.2 (IV)	1.9±0.2 (I)
11	2157 08 (-0)	-8.9±0.4 (III)	4.9±0.4 (III)	4.0±2.5 (IV)	+5.0±2.5 (IV)	unknown	1.2±1.2 (IV)
12	0101 00 (-5)	4.3±0.8 (II)	2.7±0.8 (IV)	3.1±2.8 (II)	-2.3±2.8 (IV)	unknown	unknown
13	2349 30 (-14)	-8.4±0.5 (II)	5.8±0.5 (II)	-16.4±2.5 (I)	-9.4±2.5 (III)	1.3±0.3 (III)	1.9±0.3 (I)
14	2221 06 (-7)	-10.8±0.5 (III)	-7.1±0.4 (III)	-8.9±2.6 (III)	-2.1±2.5 (III)	0.8±0.3 (III)	2.1±0.3 (III)
15	2255 55 (+0)	5.5±0.5 (II)	+0.1±0.5 (IV)	18.4±2.5 (II)	-1.4±2.5 (IV)	0.2±0.2 (IV)	1.6±0.2 (II)
16	0048 32 (-11)	4.3±0.5 (IV)	2.7±0.5 (II)	-16.1±2.6 (III)	-10.1±2.6 (IV)	1.0±0.1 (IV)	1.3±0.1 (III)
17	0138 00 (-0)	2.4±0.5 (II)	-0.6±0.5 (II)	-11.8±2.6 (III)	-0.8±2.6 (I)	0.4±0.2 (I)	1.5±0.1 (III)
18	2345 12 (-2)	-2.7±1.0 (III)	-0.1±0.7 (II)	-3.7±2.7 (III)	-1.2±2.7 (II)	1.0±0.1 (II)	1.4±0.1 (III)
19	0106 00 (-9)	3.0±0.8 (II)	+1.0±0.8 (III)	-8.0±2.6 (II)	-2.0±2.6 (III)	0.3±0.1 (III)	1.2±0.2 (II)
20	0022 00 (-47)	2.4±0.6 (III)	0.3±0.5 (I)	7.1±3.2 (II)	-1.1±2.7 (III)	unknown	1.4±0.1 (II)
21	0101 00 (-16)	7.2±0.5 (III)	-0.3±1.0 (II) [†]	-19.2±2.7 (III)	-2.2±2.9 (II) [†]	unknown	1.8±0.1 (III)
22	0146 22 (-1)	2.1±0.4 (III)	1.3±0.4 (IV)	-6.8±2.5 (III)	-4.8±2.5 (IV)	0.2±0.1 (IV)	0.4±0.1 (III)
23	0042 00 (-0)	2.9±0.7 (III)	1.0±0.7 (IV)	-2.0±2.6 (III)	0.0±2.6 (IV)	0.2±0.9 (IV)	0.8±0.9 (III)
24	2219 08 (-11)	-1.3±0.5 (I)	-0.1±0.5 (IV)	-3.2±2.5 (IV)	-1.2±2.5 (IV)	unknown	unknown
25	0052 04 (-5)	-0.5±0.5 (II)	+0.1±0.5 (I)	-2.0±2.5 (II)	-1.0±2.5 (I)	unknown	unknown
26	2311 18 (-12)	-5.7±0.7 (IV)	3.5±0.7 (I)	-5.0±2.5 (IV)	-3.0±2.5 (III)	unknown	unknown
27	2125 00 (-0)	6.6±0.7 (II)	2.0±1.7 (III)	-4.1±3.2 (II)	0.0±3.2 (III)	unknown	unknown
28	0036 44 (-8)	10.4±0.5 (II)	-5.0±0.5 (I)	-18.6±2.6 (III)	-5.6±2.6 (II)	0.1±0.1 (II)	1.1±0.1 (III)
29	0007 27 (-1)	4.5±0.5 (II)	-0.8±0.5 (III)	-10.1±3.0 (II)	-5.1±3.0 (III)	unknown	unknown
30	0028 13 (-12)	7.9±0.4 (III)	4.6±0.4 (I)	-12.2±2.7 (I)	-8.2±2.7 (II)	0.4±0.1 (II)	0.8±0.2 (I)

Table 5.1: Summary of RFD observations. Analysis times are in UTC, with the minutes before (<0) or after (>0) tornadogenesis or tornadogenesis failure provided in parentheses. Values of θ'_v and θ'_e are in K, values of z_0 are in km, values of CAPE and CIN are in J kg^{-1} , values of the maximum horizontal θ'_v gradient ($\nabla_h \theta'_v$) are in K km^{-1} , and values of p' are in mb. The uncertainty (see appendix A) appears beside each θ'_v , θ'_e , z_0 , CAPE, CIN, and p' value, along with the quadrant(s) where the measurement was obtained (e.g., I, II, III, or IV, as defined in chapter 4). The words “within 4 km” and “within 2 km” refer to the region within a 4 km and 2 km radius *within the RFD*, respectively, of the tornado or mesocyclone center. CAPE has only been integrated up to 500 mb, as discussed in chapter 4. Values of the maximum $\nabla_h \theta'_v$ only are considered if the baroclinic generation has a streamwise component (i.e., only if the sense of the horizontal baroclinic vorticity generated is such that tilting yields cyclonic vertical vorticity). E.g., if the only baroclinicity detected for a case is oriented such that horizontal vorticity generation has an antistreamwise component, then the value entered in the table for the maximum $\nabla_h \theta'_v$ is zero. In some cases, z_0 could not be determined because θ_e values measured at the surface were all larger than those observed on the proximity sounding. (Continued on next page.)

[†]This value was obtained from a turtle measurement—the uncertainty (estimated) includes the effect of interpolating water vapor mixing ratios as well as estimates of the uncertainty owing to the larger time constant of the thermistor.

Case	min CAPE within 4 km	max CAPE within 2 km	min CIN within 4 km	max CIN within 2 km	max $\nabla_k \theta'_0$ within RFD	max p' within RFD
1	202±72 (II)	530±203 (III)	20±29 (III)	405±168 (II)	2.8 (II)	1.4±0.8 (III)
2	0±0 (III)	669±145 (I)	102±25 (I)	1011±187 (III)	6.1 (III)	0.9±0.8 (III)
3	57±49 (IV)	116±54 (III)	454±53 (III)	533±64 (IV)	unknown	0.7±1.2 (III)
4	93±42 (III)	366±98 (IV)	31±18 (IV)	445±85 (II)	3.9 (III)	0.1±0.8 (III)
5	355±67 (II)	477±92 (III)	119±36 (III)	205±66 (II)	0.7 (II)	1.0±0.7 (III)
6	0±0 (I,II)	23±24 (III)	437±71 (III)	901±137 (I)	1.5 (II)	3.6±0.7 (I)
7	111±89 (II)	177±56 (I)	199±49 (II)	271±61 (II)	1.0 (II)	4.4±0.8 (III)
8	75±55 (II)	196±63 (IV)	439±66 (IV)	609±79 (II)	1.1 (III)	6.9±0.8 (III)
9	0±0 (I-IV)	0±0 (I-IV)	983±137 (IV)	1041±175 (III)	3.0 (I)	3.1±0.8 (III)
10	127±49 (I)	337±52 (IV)	246±71 (IV)	559±82 (I)	3.1 (III)	1.4±0.8 (II)
11	98±35 (III)	433±126 (I)	52±28 (I)	252±94 (III)	0.9 (II)	2.2±0.6 (III)
12	96±34 (III)	379±165 (IV)	8±10 (IV)	289±97 (III)	0.5 (III)	2.4±0.6 (III)
13	93±17 (I)	238±108 (III)	208±96 (III)	391±112 (I)	2.8 (II)	0.3±0.8 (II)
14	100±46 (III)	299±71 (III)	363±77 (III)	610±142 (III)	unknown	0.6±0.8 (II)
15	0±0 (II,III)	302±86 (IV)	50±47 (IV)	842±145 (III)	3.9 (II)	1.3±0.8 (III)
16	112±50 (III)	433±71 (IV)	284±53 (IV)	646±79 (III)	unknown	2.1±0.7 (IV)
17	268±62 (III)	620±84 (I)	171±48 (I)	438±64 (III)	1.3 (II)	1.4±0.7 (II)
18	345±93 (IV)	511±89 (II)	6±12 (II)	57±26 (IV)	1.5 (III)	7.0±0.8 (IV)
19	147±48 (II)	383±81 (III)	31±30 (III)	270±65 (II)	1.1 (II)	1.4±0.7 (IV)
20	571±78 (II)	707±101 (III)	19±24 (III)	59±40 (II)	0.8 (II)	-0.5±0.8 (I)
21	159±62 (III)	673±125 (II) [†]	26±32 (II) [†]	481±45 (III)	6.0 (III)	2.9±0.9 (IV)
22	199±83 (IV)	273±100 (IV)	209±43 (IV)	242±56 (IV)	unknown	-0.6±0.7 (IV)
23	159±80 (III)	345±103 (IV)	15±9 (IV)	77±38 (III)	1.9 (III)	2.8±0.7 (III)
24	821±131 (IV)	968±106 (III)	2±14 (III,IV)	11±12 (IV)	0.0	0.4±0.8 (III,IV)
25	793±126 (II)	947±116 (II)	2±12 (II)	17±13 (II)	0.6 (II)	0.6±0.8 (III)
26	334±63 (I)	519±87 (III)	18±21 (III)	79±37 (IV)	1.3 (III)	1.3±0.8 (II)
27	364±69 (III)	577±76 (III)	190±25 (III)	265±74 (II)	0.3 (II)	2.2±0.6 (III)
28	0±0 (III)	250±63 (II)	561±86 (II)	1314±180 (III)	4.2 (II)	1.1±0.7 (III)
29	566±83 (II)	996±208 (III)	3±18 (III)	119±57 (II)	5.7 (II)	0.0±0.8 (II)
30	38±49 (IV)	233±88 (III)	390±101 (III)	570±184 (IV)	2.5 (II)	2.6±0.7 (II)

Table 5.1 (continued).

	Non-tornadic	Tornadic	<i>P</i> -value
Minimum θ'_v within 4 km	-7.5 (2.6)	-3.2 (1.9)	0.001
Maximum θ'_v within 2 km	-3.8 (1.4)	-0.7 (1.2)	0.001
Minimum θ'_e within 4 km	-12.2 (5.7)	-7.0 (5.9)	0.089
Maximum θ'_e within 2 km	-4.9 (4.4)	-1.7 (1.6)	0.011
Minimum z_0 within 2 km	1.5 (1.0)	0.5 (0.4)	0.057
Maximum z_0 within 4 km	2.4 (1.3)	1.3 (0.4)	0.060
Minimum CAPE within 4 km	103 (110)	411 (293)	0.006
Maximum CAPE within 2 km	355 (266)	651 (283)	0.059
Minimum CIN within 2 km	245 (308)	33 (58)	0.032
Maximum CIN within 4 km	564 (313)	205 (291)	0.017
Maximum $\nabla_H \theta'_v$ within RFD	2.5 (1.8)	2.0 (1.9)	0.677
Maximum p' within RFD	1.7 (1.1)	1.9 (2.2)	0.857

Table 5.2: Mean thermodynamic variables (standard deviations in parentheses) in RFDs at the time of tornadogenesis or tornadogenesis failure. The words “within 4 km” and “within 2 km” refer to the region within a 4 km and 2 km radius *within the RFD*, respectively, of the tornado or mesocyclone center. *Only analyses within 5 min of tornadogenesis or tornadogenesis failure, and analyses in which observations were available in at least 3 of 4 quadrants (as defined in section 4.1.3), are included in the calculation of the means.* The *P*-values are the probabilities that the mean variables in the non-tornadic and tornadic cases are the same, and all *P*-values were computed using the Multi-Response Permutation Procedure technique described in Mielke et al. (1981). *P*-values that are smaller than 0.001 appear as 0.001. CAPE has been integrated to only 500 mb. Units of θ'_v and θ'_e are K, units of z_0 are km, units of CAPE and CIN are J kg^{-1} , units of $\nabla_H \theta'_v$ are K km^{-1} , and units of p' are mb.

The RFDs associated with tornadic supercells were approximately 3–4 K (3–5 K) warmer than the RFDs associated with non-tornadic supercells, in terms of θ'_v (θ'_e), on average (Table 5.2; also see Figs. 5.28 and 5.29). Moreover, parcels reaching the surface in non-tornadic RFDs had θ_e values similar to the θ_e values observed on soundings at elevations approximately 1 km AGL higher than in tornadic RFDs (Table 5.2, Fig. 5.30).

Surface-based CAPE (below 500 mb) was approximately 300 J kg^{-1} larger in the RFDs associated with tornadic supercells than in those associated with non-tornadic

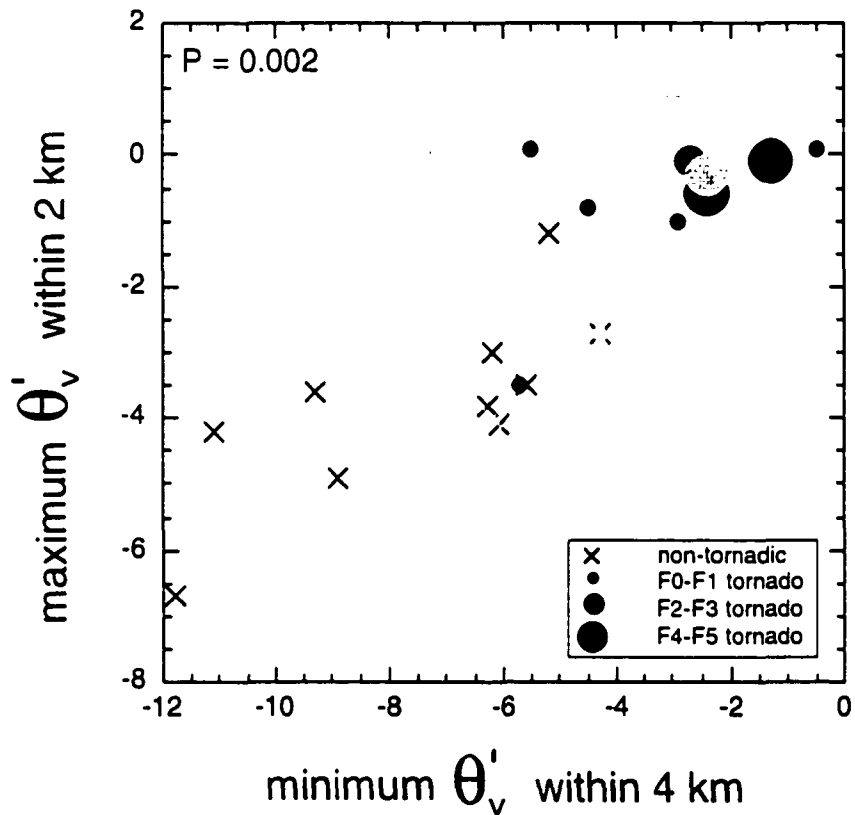


Figure 5.28: Scatter plot of maximum θ'_v versus minimum θ'_v values within the RFD. Black (gray) symbols refer to cases in which analyses were (not) obtained within 5 min of tornadogenesis or tornadogenesis failure, and observations were (not) obtained in at least 3 of 4 quadrants (see section 4.1.3). Units are K. The P -value displayed is the probability that the RFDs associated with non-tornadic and tornadic supercells contain the same θ'_v characteristics. The P -value was computed (using the Mielke et al. technique for bivariate data) by only including the analyses obtained within 5 min of tornadogenesis or tornadogenesis failure that contained surface observations in at least 3 of 4 quadrants.

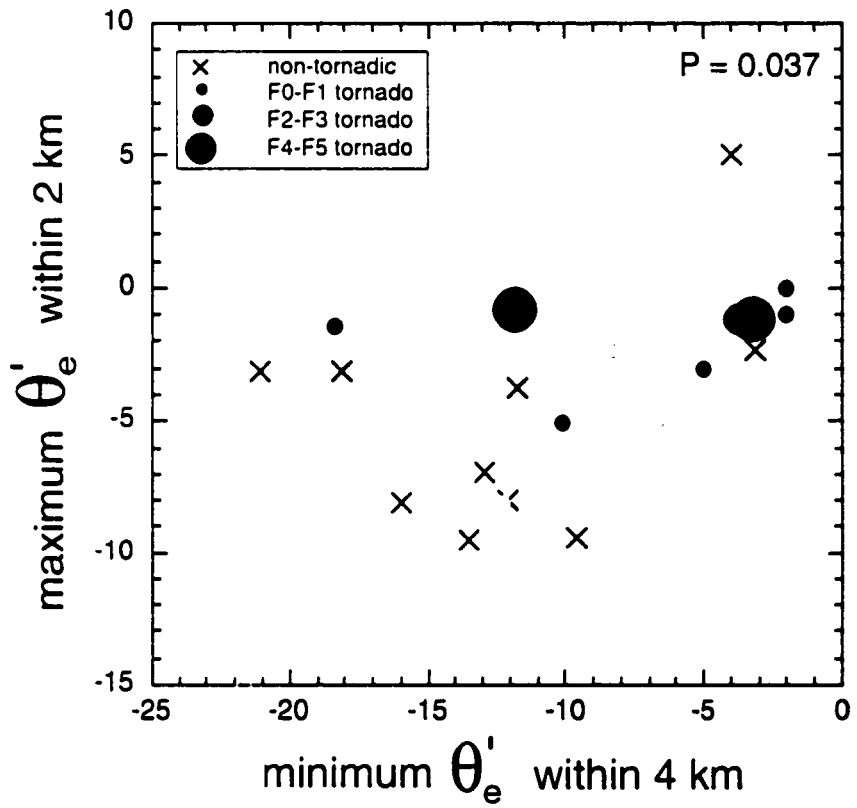


Figure 5.29: As in Fig. 5.28. but maximum θ'_e versus minimum θ'_e values are shown.

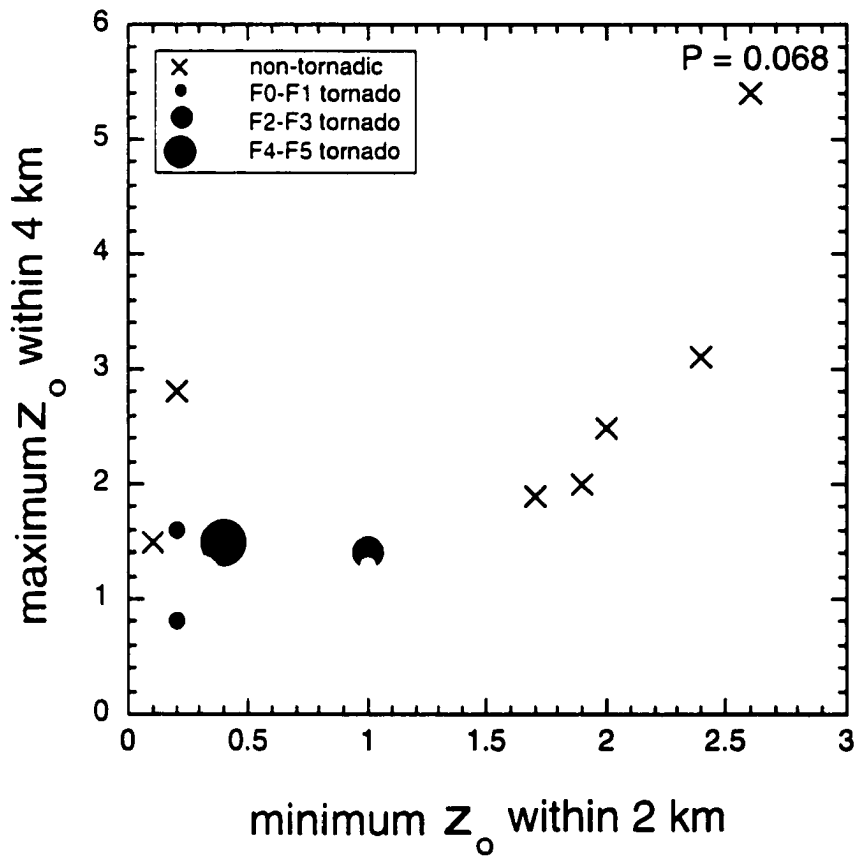


Figure 5.30: As in Fig. 5.28, but maximum z_0 versus minimum z_0 values are shown. Units are km.

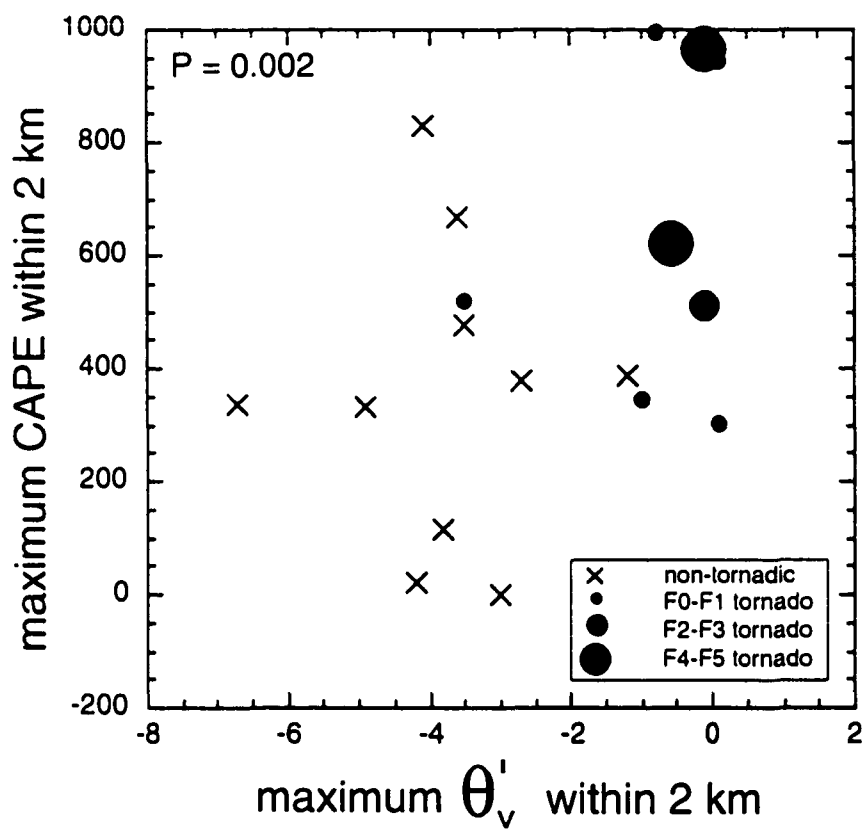


Figure 5.31: As in Fig. 5.28, but maximum θ'_v versus maximum CAPE values (J kg^{-1}) are shown.

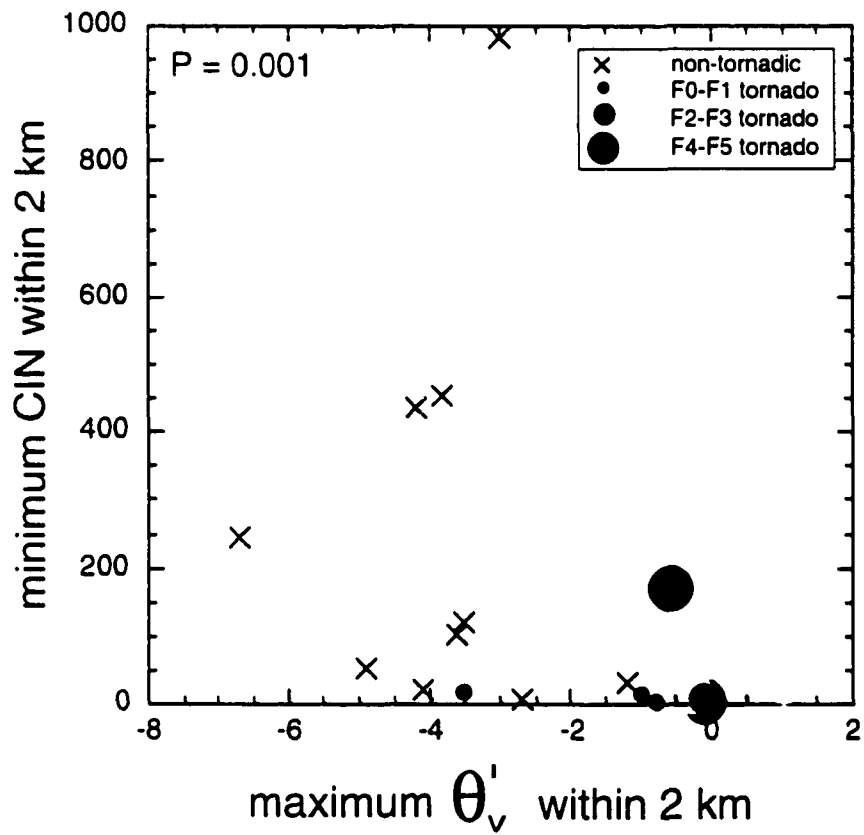


Figure 5.32: As in Fig. 5.28, but maximum θ'_v versus minimum CIN values (J kg^{-1}) are shown.

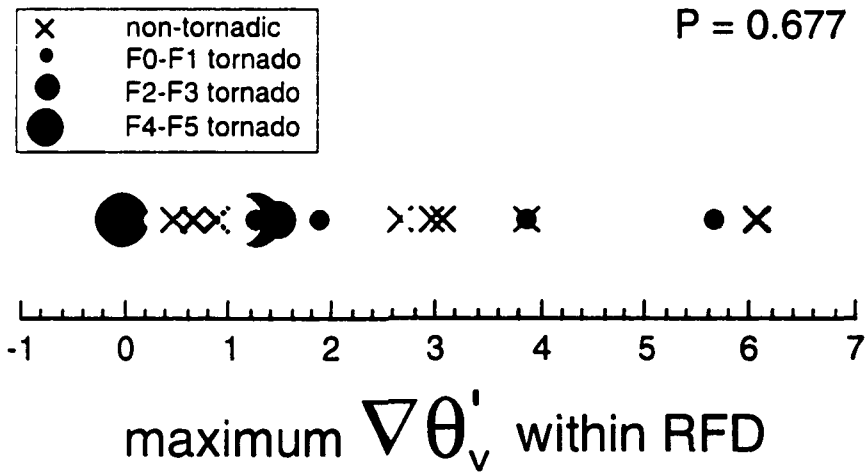


Figure 5.33: As in Fig. 5.28, but maximum $\nabla_h \theta'_v$ values measured within RFDs at the surface are shown. Units are K km^{-1} .

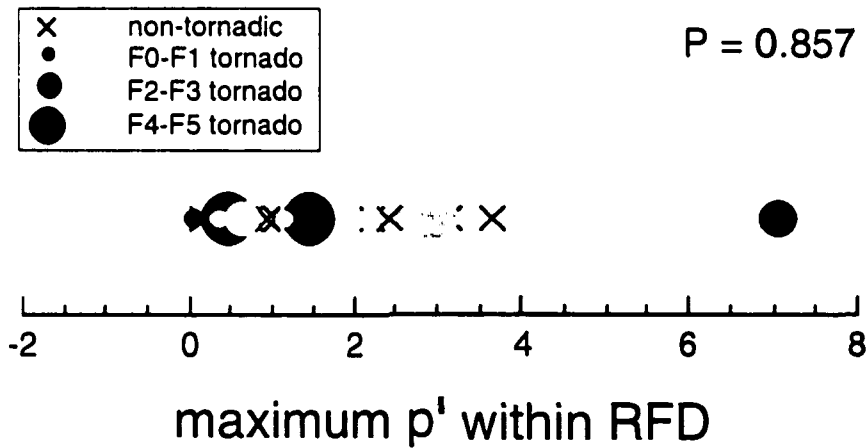


Figure 5.34: As in Fig. 5.28, but maximum p' values detected within the RFDs at the surface are shown.

supercells, on average (Table 5.2; Fig. 5.31). CIN was approximately $150\text{--}200 \text{ J kg}^{-1}$ larger in the RFDs of non-tornadic supercells compared to tornadic supercells, on average (Table 5.2; Fig. 5.32).

No significant differences were detected between the surface baroclinity ($\nabla_h \theta'_v$) within the hook echoes of non-tornadic and tornadic supercells (Table 5.2; Fig. 5.33). Furthermore, the pressure fields within RFDs associated with non-tornadic supercells were not significantly different from those associated with tornadic supercells (Table 5.2; Fig. 5.34). Perhaps the magnitude of p' is related largely to the strength of the downdrafts (i.e., perhaps the p' largely owes to dynamic effects), which does not appear to be related to tornadogenesis based on the lack of observations of obvious differences between the RFD surface divergence in the non-tornadic and tornadic cases. (Using a Bernoulli equation, it is easy to show that stronger downdrafts must contain larger p' in order to deflect streamlines at the surface toward the horizontal.)

While the above comparisons represent the average differences, mean θ'_v , θ'_c , CAPE, and CIN values were computed *by quadrant* (refer to Fig. 4.2) for non-tornadic, “weakly tornadic” (defined arbitrarily as producing F0–F1 tornadoes for ≤ 5 min), and “significantly tornadic” (those producing long-lived F0–F1 tornadoes or \geq F2 tornadoes) supercells (Fig. 5.35). The largest surface thermodynamic differences between RFDs associated with tornadic and non-tornadic supercells were detected east of the circulation centers (quadrants I and IV). In terms of θ'_v and θ'_c , RFDs associated with weakly tornadic supercells were more similar to those associated with non-tornadic supercells than those associated with significantly tornadic supercells. On the other hand, in terms of CAPE and CIN, in quadrants II and III, RFDs associated with weakly tornadic and significantly tornadic supercells were similarly different from non-tornadic RFDs.

Finally, the most significant observational findings also are highlighted by way of a composite illustration that generalizes the main characteristics of RFDs associated with non-tornadic and tornadic supercells (Fig. 5.36).

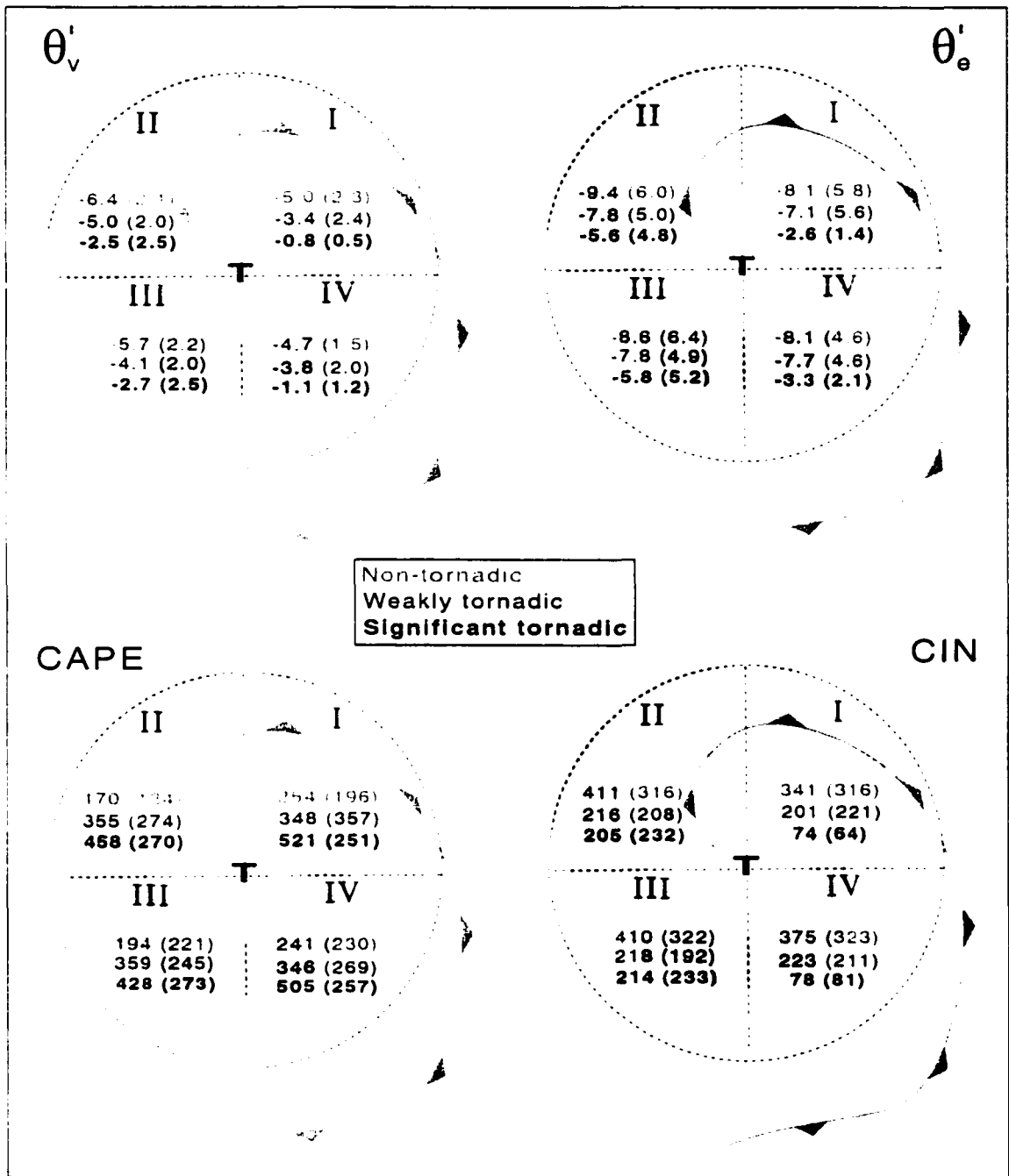
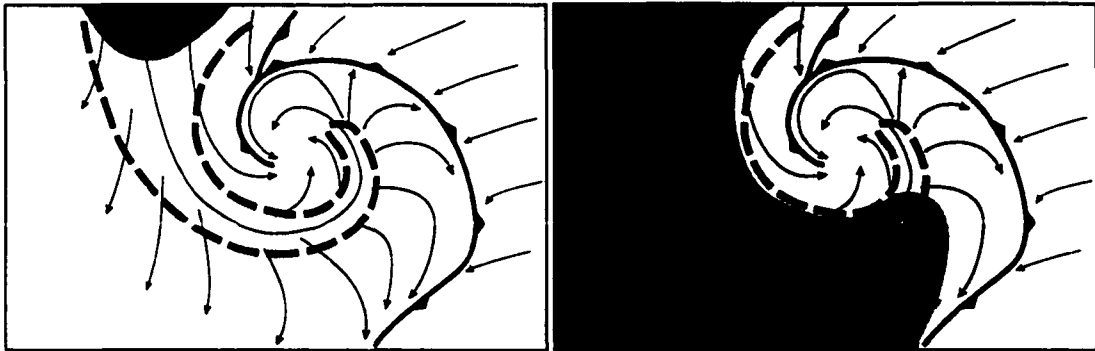


Figure 5.35: Mean θ'_v , θ'_e , CAPE, and CIN values by quadrant (refer to Fig. 4.2) are shown for non-tornadic (gray text), "weakly tornadic" (producing F0-F1 tornadoes for ≤ 5 min; black text), and "significantly tornadic" (producing long-lived F0-F1 tornadoes or $\geq F2$ tornadoes; bold black text) supercells. Standard deviations are included in parentheses.

**RFDs ASSOCIATED WITH
SIGNIFICANT TORNADIC SUPERCELLS**



**RFDs ASSOCIATED WITH WEAKLY TORNADIC
OR NON-TORNADIC SUPERCELLS**

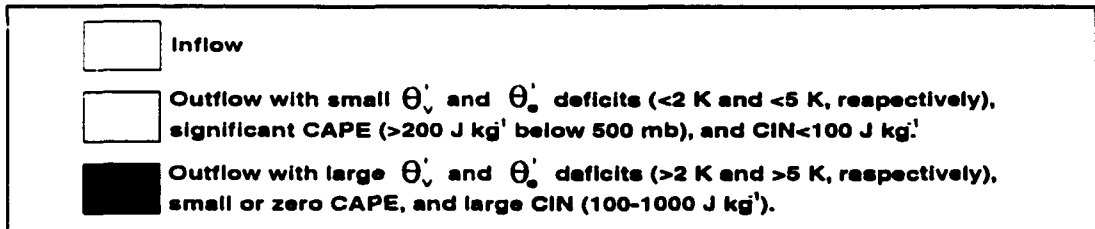


Figure 5.36: Composite diagram illustrating the general characteristics of RFDs associated with supercells that produce "significant" (e.g., F2 or stronger, or F0-F1 persisting >5 min) tornadoes versus RFDs associated with non-tornadic supercells or those that produce weak, brief tornadoes. The thick, dashed contour is the outline of the hook echo, and thin, solid arrows represent idealized streamlines. In the bottom two depictions, the illustration on the left was representative of 11/12 tornadogenesis failures, while the illustration on the right depicts an evolution that was observed in only one non-tornadic case.

5.5 Reconciliation of findings with past observations

A review of past surface observations obtained within RFDs was presented in chapters 1 and 2. Observations were made on several occasions from the 1950s through the 1970s of low θ_e and θ_w air at the surface within RFDs (e.g., van Tassell 1955; Beebe 1959; Ward 1961; Browning and Ludlam 1962; Browning and Donaldson 1963; Charba and Sasaki 1971; Lemon 1976a; Nelson 1977; Brandes 1977a; Barnes 1978a,b). A major finding of this dissertation research, as iterated throughout this chapter, is that low θ_e or θ_w RFD air is associated with tornadogenesis *failure*. In this section I attempt to reconcile this finding with past observations of *low* θ_e/θ_w RFD air.

Many of the observations of T and θ_e deficits in the literature were observed in non-tornadic, rather than tornadic supercells. Among these include Browning and Ludlam's (1962) study of the Wokingham, England supercell, Lemon's (1976a) analysis of a supercell on 25 June 1969, Brandes' (1977a) analysis of a supercell on 6 June 1974, and Nelson's (1977) analysis of a supercell on 25 May 1974.

The eyewitness reports of "cold" downdrafts documented by van Tassell (1955) and Beebe (1959) near the Scottsbluff, Nebraska tornado may be the most difficult observations to reconcile. The observations were reportedly within 1 km of the tornado, to its south. However, we cannot know precisely how cold (in terms of T and θ_e/θ_w) the downdrafts were because no meteorological instrumentation was present. Ward's (1961) observations of "cold" air also were made without a thermometer, and the observations were a "couple miles" southwest of the tornado.

Other observations of low θ_e air in RFDs associated with tornadic storms were documented on 3 April 1964 by Charba and Sasaki (1971), in the Geary, Oklahoma supercell analyzed by Browning and Donaldson (1963), and in two tornadic supercells on 29 April 1970 that Barnes (1978a,b) studied. In all of these examples, however, the surface data were of much lower horizontal resolution than those data available in this dissertation. For example, in Charba and Sasaki's study, surface observing stations (in a mesonet) were spaced 20–30 km apart, and in Barnes' studies, the observing stations were spaced 8–9 km apart. The regions of relatively small θ_e and θ_e deficits documented in the tornadic RFDs in this dissertation were characterized by a horizontal length scale of only a few km; a network of stations spaced 10 km

apart would not sample the possibly critical near-tornado RFD air mass unless by luck. Therefore it is argued that the resolution of the observing systems available in past studies simply did not allow for the detection of relatively warm RFDs in tornadic supercells on a consistent basis.

It may be worth adding that Klemp et al. (1981) found low θ_e air in their simulation of the 20 May 1977 Del City tornadic supercell. While their simulation appeared to have many similarities with the observed Del City storm, no direct measurements of low θ_e air in the RFD within a few km of the tornado were made. Brandes (1981) did hypothesize, however, from his analysis of the Del City storm, that the RFD was thermodynamically driven; this conclusion was based on the apparent erosion of midlevel echo, and not on direct observations of low θ_e air at the surface.

Chapter 6

Anticipation of surface RFD characteristics from sounding data

The findings presented in the previous chapter, while significant, do not directly benefit operational meteorologists responsible for issuing tornado warnings, because direct surface measurements within RFDs are not available in real-time. Therefore, if the findings are to have any operational value, a means must be found by which “unobservable-scale” RFD characteristics can be inferred from “observable-scale” environmental sounding data that are collected routinely.

Soundings were obtained for each of the 30 cases and are available electronically from the author. The most representative sounding was sought; however, the definition of storm “environment” is ambiguous. Darkow (1969), Darkow and McCann (1977) and Kerr and Darkow (1996) used the following criteria for choosing tornado “proximity” soundings: (1) the tornado must have been between 15 min prior to and 105 min after the sonde launch; (2) the tornado must have been within 50 statute miles of the launch site; (3) the sonde must have been launched in the air mass that produced the tornadic storm. Even with these relatively strict criteria, the findings of Brooks et al. (1994b) and Markowski et al. (1998c) argue that one still cannot be certain that the sonde sampled the actual storm environment due to enormous environmental variability. In the present study, of the 30 “best proximity” soundings obtained for the tornadic and non-tornadic cases (these were chosen to be as close in space and time as possible to tornadogenesis or tornadogenesis failure, and those

with wind data were selected over those with missing wind data), only 12 met the criteria put forth by Darkow and his collaborators.¹

For each case, numerous hodograph characteristics were computed. These included storm-relative (s-r) winds at 2, 3, 4, 6, and 9 km AGL, storm-relative helicity (SRH) in the lowest 1, 2, and 3 km AGL, vertical shear in the 0–6, 2–4, 3–6, and 4–9 km AGL layers, and mean storm-relative wind speeds (Table 6.1). Furthermore, the lifting condensation level, level of free convection, and CAPE were computed for each sounding. From the surface data, dewpoint depressions (T_{dd}) also were reported in Table 6.1 (the values appearing in the table represented an average of the minimum and maximum T_{dd} values observed within a sector of arc width 90°, centered on the storm motion vector).

Few, if any, significant differences stood out between soundings obtained near tornadic supercells and those near non-tornadic supercells (Fig. 6.1). P -values (obtained using the MRPP technique described in section 5.4) computed to test the hypothesis that the tornadic and non-tornadic supercells came from identical environments generally were greater than 0.75 (i.e., the probability that the environments were different generally was less than 25%) for univariate tests of SRH, 0–6 km shear, 3–6 km shear, 6 km s-r winds, and 4–6 km mean s-r winds (the small sample size, especially since only soundings meeting Darkow’s criteria were considered, made it difficult to establish statistically significant differences; only one sounding satisfying Darkow’s criteria in a non-tornadic environment attained a height of 9 km, therefore no significance tests could be done on the 9 km s-r winds or 4–9 km shear). However, there was some suggestion that storm-relative winds in the 3–4 km layer were (statistically) significantly *weaker* in the tornadic cases than in the non-tornadic cases (Fig. 6.1; P -value=0.02 for 3 and 4 km s-r wind).

¹The criteria used by Darkow (1969) et al. were modified to allow “tornadogenesis failure” to replace “tornado” in the non-tornadic cases.

Case	Darkow criteria met [†]	LCL	LFC	CAPE	$T_{dd,fc}$	storm motion	0-1 km SRH	0-2 km SRH	0-3 km SRH	$ \Delta\mathbf{v} _{0-6}$
1	Y	1.0	2.8	>1500	6.7	353 / 11	213	270	348	23.5
2	N	1.2	1.6	2400	6.4	350 / 10	61	123	134	16.3
3	Y	1.0	2.3	>1900	3.1	275 / 14	457	638	822	37.5
4	N	1.3	3.5	>2000	10.2	285 / 5	85	363	760	26.5
5	Y	1.1	1.1	4100	5.4	230 / 10	22	111	195	26.7
6	N	1.7	3.1	1300	13.9	265 / 8	70	130	139	23.5
7	N	1.5	3.4	2700	10.8	370 / 8	50	121	117	22.3
8	N	1.2	2.6	>2000	6.9	328 / 13	98	232	252	21.6
9	N	1.1	2.6	>2000	3.2	266 / 17	269	277	275	27.4
10	N	1.3	1.3	1900	15.1	265 / 12	112	96	202	11.8
11	N	1.0	3.2	600	12.0	265 / 14	38	12	70	26.9
12	N	1.0	3.2	600	13.5	300 / 13	31	80	116	26.9
13	Y	1.2	1.5	>1800	4.6	290 / 12	61	73	123	9.0
14	Y	1.3	2.1	>1500	10.6	255 / 10	81	72	110	23.8
15	Y	0.8	3.1	1100	2.8	253 / 13	449	558	517	37.9
16	Y	1.3	2.4	>2500	4.7	251 / 10	53	90	116	30.3
17	Y [†]	0.9	0.9	>2500	4.4	260 / 9	M	M	M	M
18	Y	0.7	1.3	>2000	5.6	225 / 13	324	459	440	M
19	Y	1.1	2.6	>1500	6.0	220 / 7	M	M	M	M
20	N	0.9	2.5	>3000	5.9	221 / 10	M	M	M	21.1
21	Y	0.9	2.5	>3000	5.4	225 / 11	M	M	M	21.1
22	N	1.3	2.2	1400	3.3	270 / 11	67	55	80	27.7
23	N	0.7	2.3	800	1.4	270 / 12	360	356	412	27.2
24	Y	0.4	2.4	>2500	2.6	225 / 14	236	291	300	21.4
25	N	0.4	2.4	>2500	2.5	220 / 11	219	288	306	21.4
26	N	1.3	3.9	900	8.3	330 / 10	153	354	329	22.6
27	N	2.4	2.6	M	12.0	255 / 6	-13	-10	28	19.7
28	N	1.8	2.9	1900	7.6	280 / 13	150	181	229	31.1
29	N	1.4	2.9	2700	5.9	300 / 7	17	27	8	20.7
30	N	1.8	2.9	>500	9.5	240 / 15	235	298	326	M

Table 6.1: Environmental characteristics as measured by the “best” proximity soundings available for each of the 30 cases. The Darkow (1969) criteria are described in the text. Heights of the lifting condensation level (LCL) and level of free convection (LFC) are given in km AGL. CAPE is given to the nearest 100 J kg⁻¹ and values preceded by a “>” indicate that the sounding data were not available up to the equilibrium level, thus the total CAPE could not be computed. LCL and LFC heights and CAPE were computed by lifting a parcel with the mean thermodynamic properties of the lowest 100 mb. The surface dew point depression, $T_{dd,fc}$, was computed by averaging the maximum and minimum values measured within 45° of the storm motion vector and within 150 km of the updraft, by observing sites that report routinely. The storm motion represents the mean updraft motion (in degrees from true north and in m s⁻¹) in the 30-min period prior to tornadogenesis (tornadic cases) or strongest low-level rotation (non-tornadic cases). Storm-relative helicity (SRH) has units of m² s⁻². The 0–6 km, 2–4 km, 3–6 km, and 4–9 km shear vector magnitudes (m s⁻¹) are denoted by $|\Delta\mathbf{v}|_{0-6}$, $|\Delta\mathbf{v}|_{2-4}$, $|\Delta\mathbf{v}|_{3-6}$, and $|\Delta\mathbf{v}|_{4-9}$, respectively. The 2, 3, 4, 6, and 9 km storm-relative winds (m s⁻¹) are denoted as $|\mathbf{v} - \mathbf{c}|_2$, $|\mathbf{v} - \mathbf{c}|_3$, $|\mathbf{v} - \mathbf{c}|_4$, $|\mathbf{v} - \mathbf{c}|_6$, and $|\mathbf{v} - \mathbf{c}|_9$, respectively. The mean 2–4, 4–6, and 6–9 km storm-relative winds are denoted as $|\overline{\mathbf{v} - \mathbf{c}}|_{2-4}$, $|\overline{\mathbf{v} - \mathbf{c}}|_{3-6}$, and $|\overline{\mathbf{v} - \mathbf{c}}|_{6-9}$, respectively. Missing values are denoted with “M.” (Continued on next page.)

[†]This was launched in the RFD outflow, but the hodograph above 1 km is presumed to satisfy the proximity criteria.

Case	Δv_{2-4}	Δv_{3-6}	Δv_{4-9}	$v - c _2$	$v - c _3$	$v - c _4$	$v - c _6$	$v - c _9$	$ v - c _{2-4}$	$ v - c _{3-6}$	$ v - c _{6-9}$
1	11.8	13.7	M	10.3	19.2	18.2	17.3	M	17.0	17.8	M
2	10.2	4.9	15.1	6.1	12.2	16.2	16.7	22.8	12.3	15.5	21.7
3	14.6	14.2	M	20.5	17.9	18.4	22.4	M	18.4	20.1	M
4	20.4	4.5	M	20.0	17.3	19.3	19.6	M	19.0	20.2	M
5	9.8	9.7	38.2	10.5	13.1	14.3	21.0	26.9	13.9	16.4	19.1
6	6.5	12.9	21.2	12.0	5.2	7.0	9.1	19.9	6.9	7.4	14.4
7	4.6	8.8	10.0	3.7	1.1	5.2	9.2	12.5	2.4	7.7	10.4
8	9.1	12.0	12.2	18.5	16.0	14.7	18.5	22.3	16.1	16.1	20.1
9	11.9	14.2	29.4	6.0	3.4	12.0	14.2	29.4	5.1	12.4	18.8
10	6.8	4.3	25.2	11.8	13.1	9.8	8.7	25.2	13.0	6.6	15.7
11	13.1	16.9	17.4	9.3	10.5	11.7	12.6	18.1	10.0	10.3	14.3
12	13.4	16.9	17.4	8.4	14.1	18.4	20.7	25.8	12.9	18.0	22.3
13	13.5	16.6	M	9.5	10.1	10.0	6.5	M	9.5	8.0	M
14	5.2	4.2	15.5	13.1	14.7	9.7	17.1	25.0	12.4	12.7	18.1
15	11.0	15.9	25.3	7.2	12.7	17.8	25.0	40.0	13.4	21.9	34.1
16	7.3	15.5	35.1	3.8	9.1	10.7	24.2	40.2	8.3	15.5	28.2
17	1.5	4.6	28.0	10.7	12.4	10.7	15.2	38.7	12.5	15.1	28.6
18	12.3	M	M	11.0	5.4	4.2	M	M	6.9	M	M
19	4.5	M	M	7.6	11.1	12.1	M	M	10.1	M	M
20	M	M	M	M	M	M	10.8	M	M	M	M
21	M	M	M	M	M	M	10.3	M	M	M	M
22	11.0	12.7	13.6	2.7	5.8	9.0	15.4	19.8	5.8	11.3	18.4
23	8.2	10.9	19.4	11.6	14.7	13.6	18.0	26.8	13.5	14.8	21.5
24	3.7	6.0	7.4	8.2	5.2	6.0	8.4	8.7	5.9	6.0	8.0
25	3.7	6.0	7.4	10.7	8.0	9.0	11.5	11.4	8.8	9.1	11.1
26	3.8	11.0	9.0	13.1	20.4	16.5	18.6	15.8	18.8	18.7	16.6
27	6.2	6.2	M	7.3	8.1	4.9	14.3	M	6.0	13.4	M
28	7.6	17.4	11.6	12.5	12.9	14.3	19.3	18.6	12.9	14.6	17.0
29	13.2	6.6	3.7	3.5	15.9	16.6	15.6	13.4	14.2	16.0	14.2
30	M	M	M	M	M	M	M	M	M	M	M

Table 6.1 (continued).

Many studies have sought relationships between hodograph characteristics and the behavior of supercells, but none have yet compared the s-r winds in the 3–4 km layer in tornadic and non-tornadic supercells. Darkow (1969), Maddox (1976), and Darkow and McCann (1977) looked at the s-r winds over a large depth in tornadic storms, but the wind profiles of non-tornadic storms were not explored. Kerr and Darkow (1996) found a relative minimum in the 3–4 km s-r flow in tornadic storm environments, but no comparisons were made with non-tornadic storms either. Brooks et al. (1994a) studied the role of s-r winds above approximately 5 km in numerical simulations, but the importance of s-r winds below 5 km was not probed. Brooks

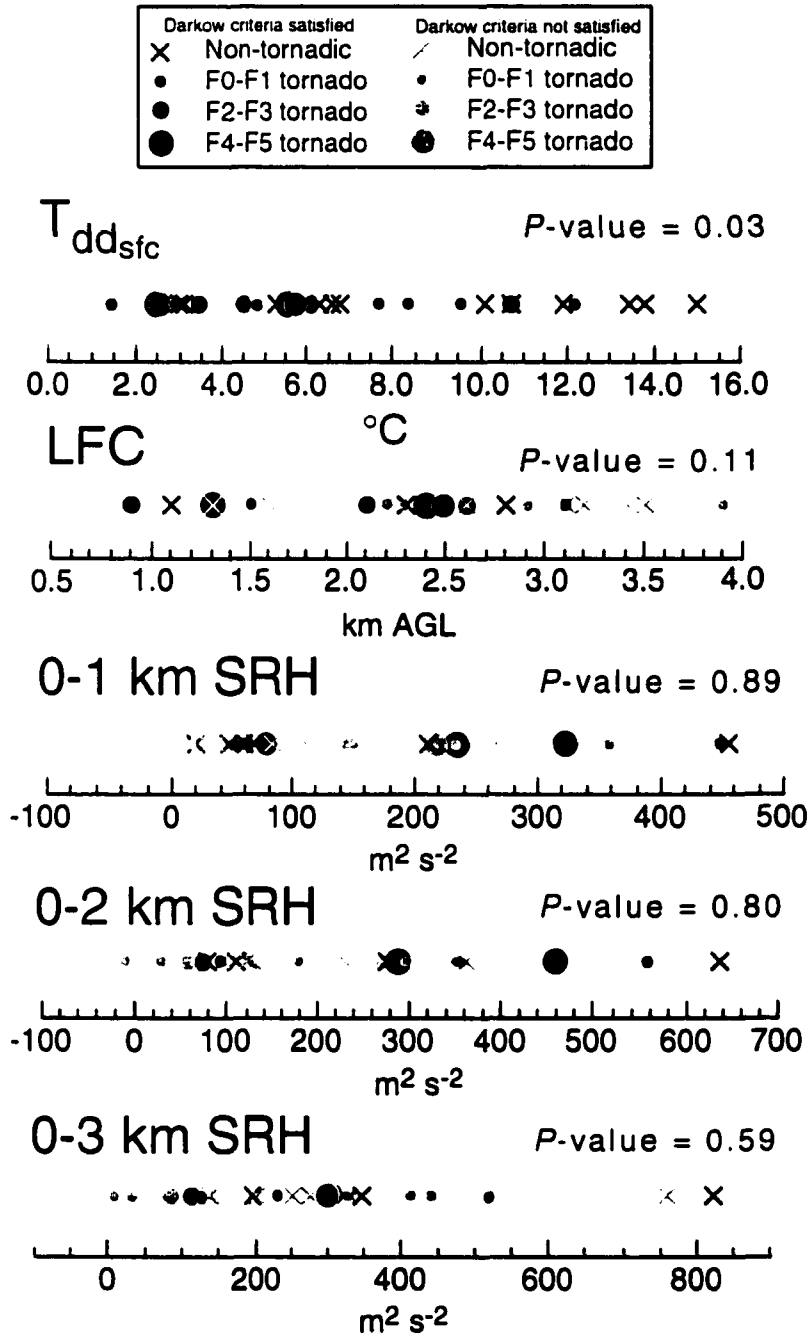


Figure 6.1: Scatter plots of environmental conditions for the 30 RFD data sets using the best available "proximity soundings." Surface dewpoint depressions ($T_{dd_{sfc}}$) were not obtained from soundings, but rather from surface inflow observations (the largest and smallest T_{dd} values within an inflow sector 90° wide with radius 100 km, centered on the storm motion vector, were averaged). Soundings that satisfy Darkow's proximity sounding criteria are shown using bold symbology. (Continued on next 2 pages.)

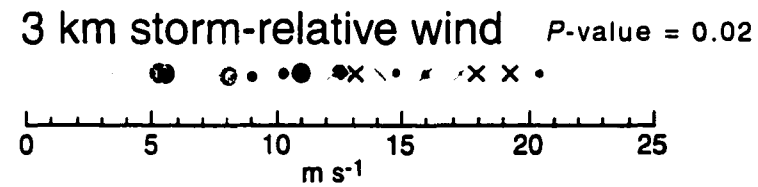
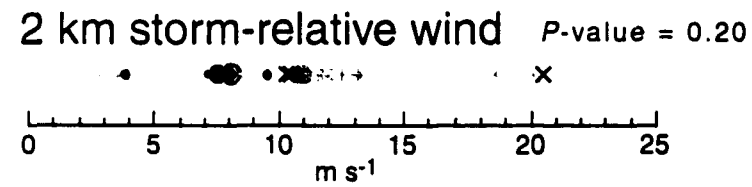
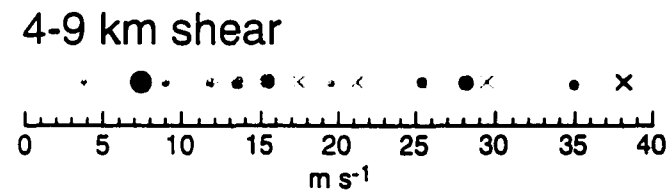
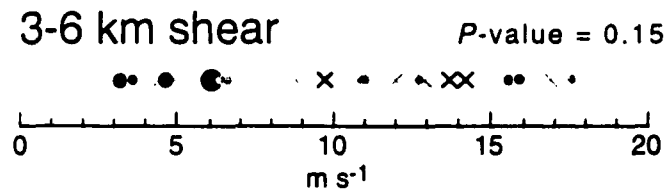
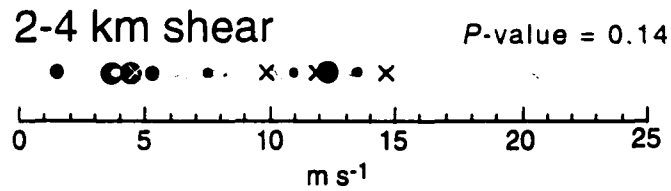
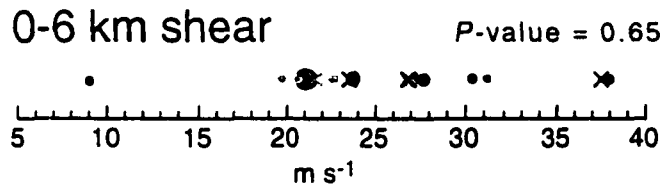
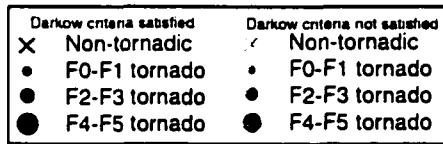
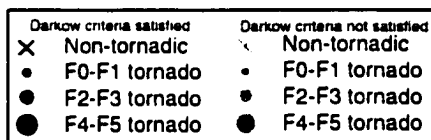
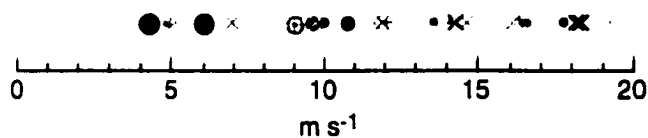


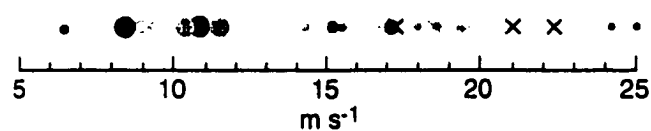
Figure 6.1 (continued).



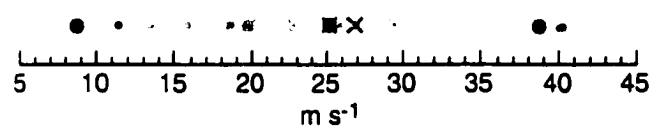
4 km storm-relative wind P -value = 0.02



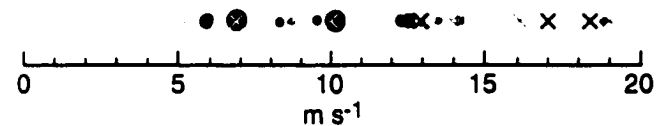
6 km storm-relative wind P -value = 0.19



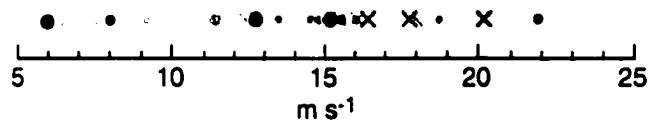
9 km storm-relative wind



2-4 km mean storm-relative wind P -value = 0.07



4-6 km mean storm-relative wind P -value = 0.13



6-9 km mean storm-relative wind

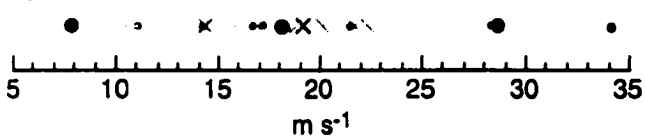


Figure 6.1 (continued).

et al. (1994b) looked at the relationship between tornadic and non-tornadic mesocyclones and the ratio of SRH to the minimum s-r wind speed in the 2–7 km layer, but the level of the minimum s-r flow varied from case to case. Their results suggested that a tornadic mesocyclones occur in a regime in which s-r flow is neither too weak nor too strong. Davies and Johns (1993) investigated magnitudes of shear and helicity in supercell environments, but s-r winds were not included in their study. Thompson (1998) did compare tornadic and non-tornadic s-r wind environments; however, only the s-r winds at 500 and 250 mb were explored (tornadic supercells were associated with larger s-r speeds at those pressure levels than non-tornadic supercells). Rasmussen and Straka (1998) and Rasmussen and Blanchard (1998) most recently have compared s-r winds at high levels (9 km) in environments associated with supercells occurring in various portions of the supercell spectrum [e.g., low-precipitation, classic, and high-precipitation supercells (Doswell and Burgess 1993)] as well as in environments favoring non-tornadic supercells and non-supercell thunderstorms. These studies did not examine any possible relationships between supercell behavior and lower level s-r winds.

In numerical simulations, Gilmore and Wicker (1998) found that low-level θ_e deficits increased as the altitude of middle to upper level dry air decreased and as the vertical shear increased. Weisman and Klemp (1982) also found that low-level outflow increased as shear decreased; their explanation was that the updraft entrains less and is therefore stronger in weak-shear environments—thus, the stronger updraft can suspend larger precipitation amounts that, after leaving the updraft, create greater evaporative cooling and precipitation loading, and ultimately a stronger downdraft and cold pool. Gilmore and Wicker found that the downdrafts in their study entrained more high θ_e air in the boundary layer as the shear increased, thereby reducing the outflow strength. Although vertical wind shear cannot be present in storm environments without the additional presence of s-r (at least at some level), Gilmore and Wicker did not explicitly study the effects of various s-r wind environments. Curiously, Shaefer and Livingston (1988) showed that tornado environments with drier midlevels contain stronger shear than tornado environments with moister midlevels. However, Schaefer and Livingston did not examine s-r flow either.

The finding herein of slightly weaker s-r winds in the 3–4 km layer should be viewed with the utmost caution, since there is no way of knowing the extent of the

environmental variability on each day. The representativeness of no sounding within the sample of 30 can be guaranteed. Furthermore, the difference of only 6.7 m s^{-1} (6.8 m s^{-1}) between the average 3 km s-r winds (4 km s-r winds) in the tornadic and non-tornadic cases may be small (and therefore not *meteorologically* significant). Relatively minor changes in the motion of an updraft could cause the s-r winds to be altered by several m s^{-1} , and small fluctuations in the environmental hodograph could alter 3–4 km s-r flow and shear by several m s^{-1} as well. Thompson and Edwards (2000) also recently found in a larger climatology that the strength of the midlevel storm-relative flow in tornadic and non-tornadic supercell environments differed by only a few m s^{-1} on average. Based on this evidence, along with the sounding evidence presented herein, combined with the uncertainties in diagnosing storm motion (e.g., motion depends on whether the mesocyclone, bounded weak echo region, or echo centroid is tracked), it probably is unlikely that hodograph traits (at least those popular today) can reliably anticipate RFD thermodynamic properties and tornado threat. A more extensive climatological study may be warranted in the future, but such an endeavor is well beyond the scope of this dissertation.

A statistically significant difference between surface T_{dd} ($T_{dd,fc}$) values in the tornadic and non-tornadic supercell environments also was found (P -value=0.03), with $T_{dd,fc}$ values being smaller in tornadic supercell environments in general (Fig. 6.1; the mean $T_{dd,fc}$ in tornadic environments was 5.7 K, and the mean $T_{dd,fc}$ in non-tornadic environments was 8.9 K). Rasmussen and Blanchard (1998) made a similar observation in their much larger sounding climatology. The effects of the ambient relative humidity profile on surface RFD characteristics will be investigated using idealized numerical simulations in chapter 7.

Finally, RFD thermodynamic characteristics such as θ'_v , θ'_e , CAPE, and CIN were shown in section 5.4 to be able to discriminate between tornadic and non-tornadic supercells. If the parameters $T_{dd,fc}$ and 3–4 km s-r flow also can discriminate between tornadic and non-tornadic supercell environments, then θ'_v , θ'_e , etc., must be relatively highly correlated with $T_{dd,fc}$ and the 3–4 km s-r flow. Although this may be an obvious result, a figure showing θ'_v at the surface within RFDs versus the inflow surface dewpoint depressions is included as an example (Fig. 6.2). [The example in Fig. 6.2 shows that θ'_v and $T_{dd,fc}$ arguably are better related to each other than either variable is with tornadogenesis or tornadogenesis failure (cf. Figs. 5.28 and 6.1).

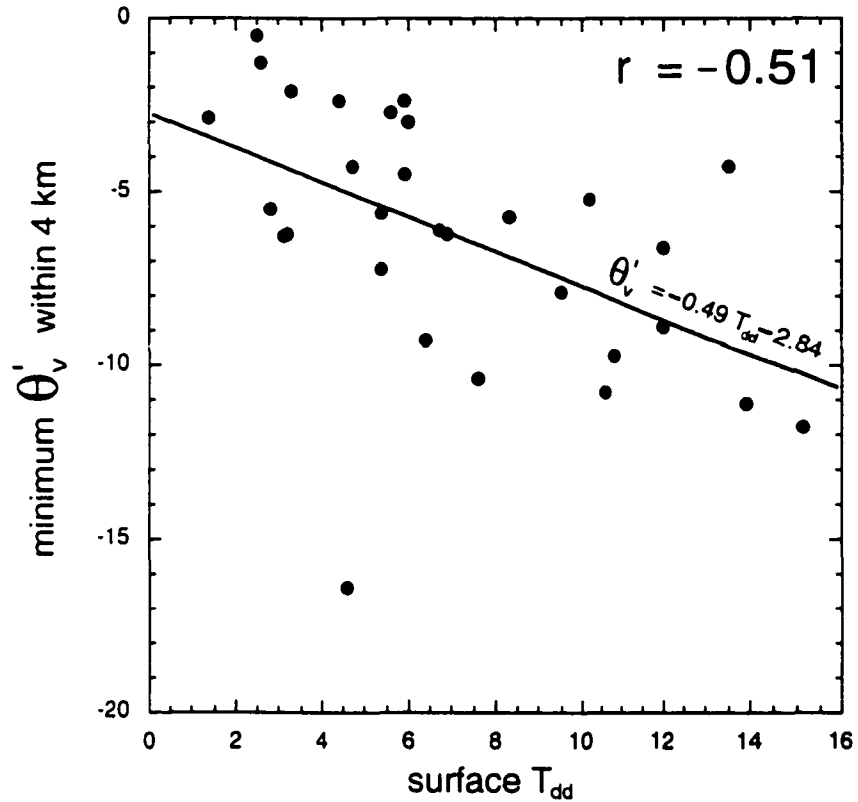


Figure 6.2: Scatter plot of minimum θ'_v values versus surface T_{dd} values for the 30 cases. The linear correlation appears at the top right and a best-fit line has been added. The correlation increases in magnitude to -0.65 when the outlier at the lower left is excluded.

This may not be surprising, for it simply indicates that there are more factors involved in tornadogenesis (e.g., surface roughness and turbulence) than just the θ'_v characteristics of the RFD and the $T_{da,jc}$ measured in the inflow: however, while *all* observations of tornadic and non-tornadic supercell behavior cannot be accounted for by simply the surface thermodynamics of the RFD, the surface thermodynamic characteristics of the RFD do appear to be important in tornadogenesis, as revealed by Figs. 5.28-5.32.]

Chapter 7

Idealized numerical simulations

7.1 Rationale and experiment design

In chapter 5 it was shown that the air parcels within the RFDs of tornadic supercells tend to be significantly more buoyant and potentially buoyant than those associated with non-tornadic supercells. However, at the end of the previous chapter, it was revealed that the only statistically significant differences between the environments of the tornadic and non-tornadic mesocyclones, in the 30 cases studied, were in the 3–4 km storm-relative flow and the low-level relative humidity. This finding is the motivation for an idealized numerical study investigating the effects of the ambient relative humidity profile on the low-level thermodynamic characteristics of a downdraft, and the ensuing vortex intensification at the surface. A study of the effects of various storm-relative wind profiles is not performed herein, in order to maintain simplicity and because it is believed closure of the RFD forcing and thermodynamic issues is beyond the scope of what presently can be done; it is believed that more observational data are needed in order to determine whether or not the most sophisticated cloud models have reasonable representations of the cloud water and precipitation type and spatial distribution, as well as realistic mixing and entrainment in supercell-storm flows.

The idealized simulations performed herein are axisymmetric and designed with some similarities to the simulations conducted by Das (1983) and Walko (1988).

Walko simulated a rotating, moist but rain-free updraft in its entirety, whereby the conditionally unstable base state was specified using a sounding obtained on a day on which supercell thunderstorms were observed. The updraft rotation was imposed at the beginning of the integration, and the base of the initial vortex extended to the ground. Therefore, stretching of vorticity alone was able to rapidly spawn intense surface rotation. Das' (1983) simulations were designed to investigate vortex spin-up within the subcloud layer beneath an updraft. A body force was prescribed at the top of the domain, which was situated entirely within the implied (2 km deep) subcloud layer. The initial wind field was in solid body rotation that decreased exponentially to zero at the lower boundary. Precipitation was inserted at the top boundary, and the ensuing precipitation-driven downdraft was shown to be capable of transporting sufficient angular momentum to the surface for the genesis of a tornado-like vortex.

In the axisymmetric experiments conducted for this dissertation, a rotating, moist updraft is simulated in its entirety, as in the study by Walko (1988). However, no rotation is initially present in the lowest 250 m (rotation is a maximum at 2.5 km and decreases sinusoidally to zero at 250 m AGL); thus, tornadogenesis cannot proceed without the presence of a downdraft. Rain water is not permitted to form within the cloudy updraft (by way of a microphysical parameterization); instead, rain water is introduced at midlevels on the periphery of the updraft once an approximately steady state is achieved. This methodology was used to obtain greater control over the experiment (the rain water field could be made to be identical in each simulation at the time of downdraft-genesis; it also will be shown that the angular momentum distributions within the updrafts just prior to downdraft initiation were identical from run to run). The negative buoyancy owing to the rain water initiates a downdraft which advects angular momentum downward, as in the Das experiments. The final concentration of vorticity at the surface depends upon the low-level stability [as shown by Leslie and Smith (1978)¹], which ultimately is

¹Leslie and Smith (1978) showed that the low-level static stability can have a significant effect on vortex intensification at the surface; in their simple, dry experiments, the stability profile was specified *a priori*. A swirling wind velocity was imposed on inflow entering the domain through the lateral boundary. In the experiments herein, the low-level stability evolves in time as evaporation and entrainment within the downdraft alter the low-level thermodynamic characteristics. No swirling wind component is imposed at the inflow boundary. Instead, the downdraft is responsible for the low-level vortex generation.

governed by the ambient environmental conditions. Fig. 7.1 illustrates the design of the experiments, along with the model boundary conditions, which will be discussed in the next section.

Although hook echoes (which long have been associated with RFDs) do not completely encircle the parent updrafts in observed supercells, radar observations reveal that hook echoes are downward extensions of the rear side of an elevated reflectivity region (e.g., Forbes 1981). Thus, the method of introducing a “cascade” of rain water in order to generate a downdraft in these numerical experiments does have some observational justification. In the simulations herein, the introduction of rain water is analagous to hook echo formation. The experiments are designed to address the question: under what conditions can a hook echo reach the ground such that relatively large buoyancy is observed at the surface?

7.2 Methods

7.2.1 Model and domain description

The model uses an axisymmetric domain that is 12 km deep and extends outward from the center axis to a radius of 8 km. The prognostic equations for the wind velocity components (u, v, w) are written in cylindrical coordinates (r, ϕ, z) as follows:

$$\frac{\partial u}{\partial t} = -u \frac{\partial u}{\partial r} - w \frac{\partial u}{\partial z} + \frac{v^2}{r} - c_p \bar{\theta}_v \frac{\partial \pi'}{\partial r} + \frac{1}{r} \frac{\partial (r \sigma_{rr})}{\partial r} - \frac{\sigma_{\phi\phi}}{r} + \frac{\partial \sigma_{rz}}{\partial z} \quad (7.1)$$

$$\frac{\partial v}{\partial t} = -u \frac{\partial v}{\partial r} - w \frac{\partial v}{\partial z} - \frac{uv}{r} + \frac{1}{r^2} \frac{\partial (r^2 \sigma_{r\phi})}{\partial r} + \frac{\partial \sigma_{\phi z}}{\partial z} \quad (7.2)$$

$$\begin{aligned} \frac{\partial w}{\partial t} = & -u \frac{\partial w}{\partial r} - w \frac{\partial w}{\partial z} - c_p \bar{\theta}_v \frac{\partial \pi'}{\partial z} + \frac{\theta'_v}{\bar{\theta}_v} g + \frac{1}{r} \frac{\partial (r \sigma_{rz})}{\partial r} + \frac{\partial \sigma_{zz}}{\partial z} \\ & + F_U + F_D \end{aligned} \quad (7.3)$$

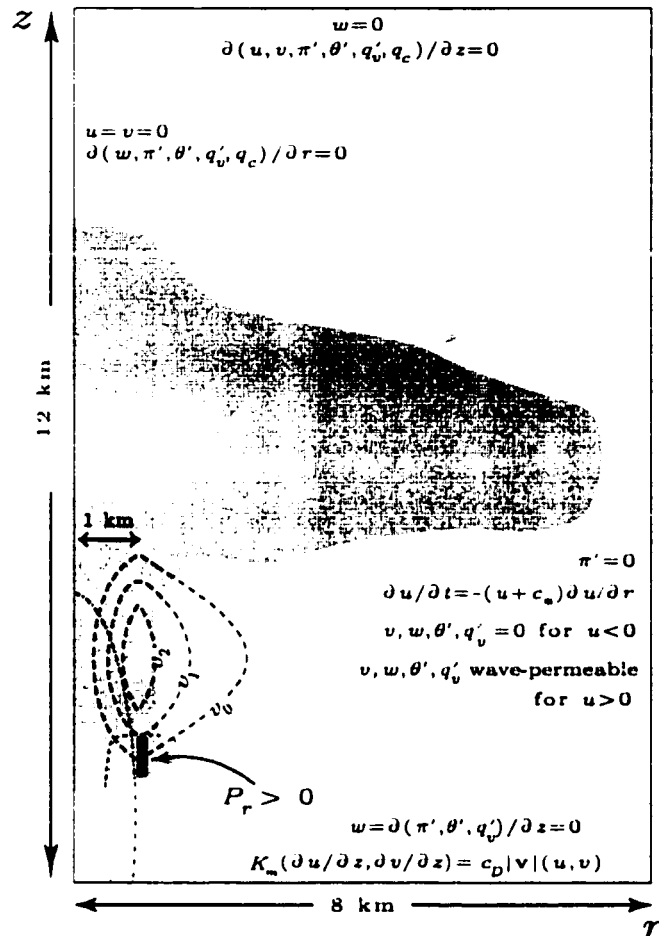


Figure 7.1: Idealized axisymmetric simulations design. A moist, rotating updraft (rotation is imposed) free of rain water is generated along the axis (light gray shading denotes the cloud water field: bold, dashed contours are tangential wind isotachs). In order to sustain the updraft, a weak positive updraft forcing, F_{DU} , is applied (see section 7.2.2) within the region enclosed by the larger of the two dash-dot contours. Once a steady state is achieved, rain water is introduced at midlevels on the periphery of the updraft within the dark gray region (rain water is imposed by way of a production term, P_r ; the details appear in section 7.2.3). As precipitation is imposed, a downward forcing, F_{DD} , also is applied within the region bounded by the thin dashed line (also see section 7.2.3), and the width of the updraft forcing is reduced to one half of its original width. The resulting precipitation- and dynamically-driven downdraft transports angular momentum toward the ground. The boundary conditions are indicated at their respective locations. All variables are defined as in section 7.2.1. As defined by Klemp and Wilhelmson (1978b), c_s is an assumed intrinsic phase speed of the dominant gravity wave modes moving out through the lateral boundary.

where c_p is the specific heat at constant pressure, g is the constant gravitational acceleration. θ_v is the virtual potential temperature, and $\pi = T/\theta = (p/p_o)^{R_d/c_p}$, where T is the temperature, θ is the potential temperature, R_d is the specific gas constant for dry air, and p_o is the base state pressure at the ground, and $\theta_v = \theta(1 + 0.61q_v - q_c - q_r)$, where q_v , q_c , and q_r are the water vapor, cloud water, and rain water mixing ratios, respectively (the base state contains no cloud or rain water). The additional terms F_U and F_D in the vertical momentum equation are additional forcing terms for updraft and downdraft, respectively. These forcings will be justified and described in the subsequent subsections.

The total π and θ_v are expanded about an unperturbed base state $\bar{\pi}$ and $\bar{\theta}_v$ according to

$$\pi(r, z, t) = \bar{\pi}(z) + \pi'(r, z, t) \quad (7.4)$$

$$\theta_v(r, z, t) = \bar{\theta}_v(z) + \theta'_v(r, z, t), \quad (7.5)$$

where the base state is hydrostatic,

$$\frac{\partial \bar{\pi}}{\partial z} = -\frac{g}{c_p \bar{\theta}_v}. \quad (7.6)$$

The (eddy) deviatoric stress dyadic components are

$$\sigma_{rr} = K_m \left[2 \frac{\partial u}{\partial r} - \frac{2}{3} \text{div} \right],$$

$$\sigma_{\phi\phi} = K_m \left[2 \frac{u}{r} - \frac{2}{3} \text{div} \right],$$

$$\sigma_{zz} = K_m \left[2 \frac{\partial w}{\partial z} - \frac{2}{3} \text{div} \right],$$

$$\sigma_{r\phi} = K_m \left[r \frac{\partial}{\partial r} \left(\frac{v}{r} \right) \right],$$

$$\begin{aligned}\sigma_{\phi z} &= K_m \left[\frac{\partial v}{\partial z} \right], \\ \sigma_{rz} &= K_m \left[\frac{\partial w}{\partial r} + \frac{\partial u}{\partial z} \right].\end{aligned}\quad (7.7)$$

where

$$\text{div} = \frac{1}{r} \frac{\partial(ur)}{\partial r} + \frac{\partial w}{\partial z} \quad (7.8)$$

is the axisymmetric divergence and K_m is the eddy viscosity for momentum.

The pressure equation is obtained from taking the material derivative ($d/dt = \partial/\partial t + u\partial/\partial r + w\partial/\partial z$) of $\pi = (p/p_o)^{R_d/c_p}$ and using the compressible continuity equation,

$$\frac{d\rho}{dt} + \rho \left[\frac{1}{r} \frac{\partial(ur)}{\partial r} + \frac{\partial w}{\partial z} \right] = 0, \quad (7.9)$$

where ρ is the air density, to eliminate $d\rho/dt$:

$$\begin{aligned}\frac{\partial \pi'}{\partial t} &= -\frac{\bar{c}_s^2}{c_p \bar{\rho} \bar{\theta}_v^2} \left[\frac{1}{r} \frac{\partial}{\partial r} (\bar{\rho} \bar{\theta}_v ur) + \frac{\partial}{\partial z} (\bar{\rho} \bar{\theta}_v w) \right] \\ &\quad - u \frac{\partial \pi'}{\partial r} - w \frac{\partial \pi'}{\partial z} - \frac{R_d}{c_v} \frac{\pi'}{r} \frac{\partial(ur)}{\partial r} - \frac{R_d}{c_v} \pi' \frac{\partial w}{\partial z} + \frac{c^2}{c_p \bar{\theta}_v^2} \frac{d\theta_v}{dt},\end{aligned}\quad (7.10)$$

where $c_s = \sqrt{c_p R_d \pi \theta_v / c_v}$ is the speed of sound. Following Klemp and Wilhelmson (1978b), all but the first term on the right hand side are neglected.

The prognostic equation for θ is

$$\frac{\partial \theta}{\partial t} = -u \frac{\partial \theta}{\partial r} - w \frac{\partial \theta}{\partial z} + \frac{1}{r} \frac{\partial}{\partial r} \left(K_h r \frac{\partial \theta}{\partial r} \right) + \frac{\partial}{\partial z} \left(K_h \frac{\partial \theta}{\partial z} \right) + H, \quad (7.11)$$

where K_h is the eddy mixing coefficient for heat and H is the rate of latent heating by condensation of water vapor, q_v .

The prognostic equation for q_v is

$$\frac{\partial q_v}{\partial t} = -u \frac{\partial q_v}{\partial r} - w \frac{\partial q_v}{\partial z} + \frac{1}{r} \frac{\partial}{\partial r} \left(K_h r \frac{\partial q_v}{\partial r} \right) + \frac{\partial}{\partial z} \left(K_h \frac{\partial q_v}{\partial z} \right) - S_c + S_e, \quad (7.12)$$

where S_c is the sink of water vapor owing to condensation,

$$S_c = \frac{c_p T H}{L_v \theta}. \quad (7.13)$$

where L_v is the latent heat of vaporization, and S_e is the source of water vapor owing to evaporation. The latent heating owing to freezing is not included. The evaporation rate is determined using the same formulation used by Klemp and Wilhelmson (1978b), where

$$S_e = \frac{1}{\bar{\rho}} \frac{(1 - q_v/q_{vs}) C (\bar{\rho} q_r)^{0.525}}{5.4 \times 10^5 + 2.55 \times 10^6 / (\bar{\rho} q_{vs})}, \quad (7.14)$$

where q_{vs} is the saturation mixing ratio, $\bar{p} = \bar{p}(z)$ is the base state pressure in millibars, $\bar{\rho}$ is in g cm^{-3} , and C is the ventilation factor parameterized as

$$C = 1.6 + 124.9 (\bar{\rho} q_r)^{0.2046}. \quad (7.15)$$

The prognostic equations for cloud water and rain water (Marshall-Palmer drop-size distribution assumed) are, respectively,

$$\begin{aligned} \frac{\partial q_c}{\partial t} = & -u \frac{\partial q_c}{\partial r} - w \frac{\partial q_c}{\partial z} \\ & + \frac{1}{r} \frac{\partial}{\partial r} \left(K_h r \frac{\partial q_c}{\partial r} \right) + \frac{\partial}{\partial z} \left(K_h \frac{\partial q_c}{\partial z} \right) + S_c \end{aligned} \quad (7.16)$$

$$\begin{aligned} \frac{\partial q_r}{\partial t} = & -u \frac{\partial q_r}{\partial r} - \frac{1}{r} \frac{\partial (u_p q_r r)}{\partial r} - w \frac{\partial q_r}{\partial z} + \frac{1}{\bar{\rho}} \frac{\partial (\bar{\rho} w_t q_r)}{\partial z} \\ & + \frac{1}{r} \frac{\partial}{\partial r} \left(K_h r \frac{\partial q_r}{\partial r} \right) + \frac{\partial}{\partial z} \left(K_h \frac{\partial q_r}{\partial z} \right) + P_r - S_e, \end{aligned} \quad (7.17)$$

where u_p and w_t represent the horizontal and vertical separation of precipitation from the flow of air. Autoconversion and collection rates are missing from (7.16) and (7.17) because no rain is allowed to be produced by the model. Instead, rain water production, $P_r = P_r(r, z, t)$, is imposed at a specified time and location in order to control the initiation of a downdraft. The form of P_r will be described later. Centrifuging of rain water occurs when $u_p > 0$, and following Das (1983), u_p is parameterized as

$$u_p = \frac{v^2}{r} \frac{w_t}{g}, \quad (7.18)$$

where, following Soong and Ogura (1973) and Klemp and Wilhelmson (1978b), the terminal fall speed is parameterized according to

$$w_t = 3634(\bar{\rho}q_r)^{0.1346} \left(\frac{\bar{\rho}}{\rho_o} \right)^{-\frac{1}{2}}, \quad (7.19)$$

where $\bar{\rho} = \bar{\rho}(z)$ is the base state density, ρ_o is the base state density at the ground and w_t , $\bar{\rho}$, and q_r have units of cm s^{-1} , g cm^{-3} , and g g^{-1} , respectively.

The eddy viscosity coefficient for momentum was prescribed as a function of the deformation field (Smagorinsky 1963). In the axisymmetric model it is

$$K_m = (c\Delta)^2 \left\{ \left(\frac{\partial w}{\partial r} + \frac{\partial u}{\partial z} \right)^2 + 2 \left[\left(\frac{\partial u}{\partial r} \right)^2 + \left(\frac{\partial w}{\partial z} \right)^2 + \left(\frac{u}{r} \right)^2 \right] + \left(\frac{\partial v}{\partial r} - \frac{v}{r} \right)^2 + \left(\frac{\partial v}{\partial z} \right)^2 \right\}^{\frac{1}{2}}, \quad (7.20)$$

where $\Delta = (\Delta r \Delta z)^{1/2}$ and c is a nondimensional constant chosen to be 0.2 following Deardorff (1972). Also following Deardorff, $K_h = 3K_m$ is specified.

The momentum equations are solved on a uniform C grid (Arakawa and Lamb 1981) using a Klemp-Wilhelmson time splitting scheme utilizing 3rd-order Runge-Kutta time differencing for the large time step [a description of a similar 2nd-order Runge-Kutta time differencing scheme appears in Wicker and Skamarock (1998)]. The horizontal and vertical grid resolution is $\Delta r = \Delta z = 32$ m. A large (small)

timestep of 0.4 (0.4/12.0) s is used. Fifth (third) order spatial differences are used for the horizontal (vertical) advection computations. All other spatial finite differences are second order. No explicit horizontal or vertical numerical filtering is used.

The upper boundary is rigid and a wave-radiation open boundary condition is employed on the large timestep at the lateral boundary (Klemp and Wilhelmson 1978b). At the lower boundary, $w = 0$, but the horizontal flow satisfies the semi-slip condition

$$\left(\frac{\partial u}{\partial z}, \frac{\partial v}{\partial z} \right) = -\frac{1}{K_m} (\overline{u'u'}, \overline{v'u'}), \quad (7.21)$$

where the surface fluxes are given by

$$\overline{u'u'} = c_D \sqrt{u^2 + v^2} u \quad (7.22)$$

$$\overline{v'u'} = c_D \sqrt{u^2 + v^2} v, \quad (7.23)$$

where the drag coefficient is $c_D = 0.003$. A schematic depicting the remaining conditions appears in Fig. 7.1.

Some of the experiments conducted by Howells et al. (1988) were reproduced in order to validate the model. A few examples are presented in appendix C.

7.2.2 Initial conditions

Four different environments initialized the base states: a high-CAPE/high-LCL environment (HCHL), a high-CAPE/low-LCL environment (HCLL), a low-CAPE/high-LCL environment (LCHL), and a low-CAPE/low-LCL environment (LCLL). The high-CAPE (low-CAPE) environments contained approximately 1500 (500) J kg⁻¹ CAPE. The high-LCL (low-LCL) environments had LCLs at 1600 (800) m.

The soundings (Fig. 7.2) were constructed using profiles similar to those used by Weisman and Klemp (1982), where

$$\bar{\theta}(z) = \begin{cases} \theta_o + (\theta_{tr} - \theta_o) \left(\frac{z}{z_{tr}} \right)^m, & z \leq z_{tr} \\ \theta_{tr} \exp \left[\frac{g}{c_p T_{tr}} (z - z_{tr}) \right], & z > z_{tr} \end{cases} \quad (7.24)$$

Sounding	θ_o	q_{vo}	θ_{tr}	T_{tr}	m	CAPE	CIN	LCL	LFC
HCHL	303.0	12.4	337.9	238.0	1.9	1505	27	1600	1800
HCLL	301.0	16.4	345.2	244.0	1.5	1502	18	800	1000
LCHL	303.0	12.4	355.6	253.0	2.1	544	27	1800	1800
LCLL	301.0	16.4	358.7	254.0	1.6	538	18	800	1000

Table 7.1: Model sounding parameters. Units of θ_o , θ_{tr} , and T_{tr} are K. Units of q_{vo} are g kg^{-1} . Units of CAPE and CIN are J kg^{-1} . Units of LCL and LFC are m.

$$\hat{h}(z) = \begin{cases} \min \left[1 - (1 - h_{min}) \left(\frac{z}{z_{tr}} \right)^m, \frac{q_{vo}}{q_{vs}(\theta)} \right], & z \leq z_{tr} \\ h_{min}. & z > z_{tr}. \end{cases} \quad (7.25)$$

where \hat{h} is the environmental relative humidity, θ_o is the potential temperature at the surface, θ_{tr} and T_{tr} are the potential temperature and absolute temperature at the tropopause, z_{tr} is the height of the tropopause, h_{min} is the minimum upper-level relative humidity, q_{vo} is the mixing ratio at the surface, and m is a “shape parameter.” The initial \hat{q}_v profile is assigned by applying the Clausius-Clapeyron equation to the $\hat{\theta}$ and \hat{h} profiles. On all soundings, $z_{tr} = 9500$ m and $h_{min} = 0.25$. The remaining parameters appear in Table 7.1.

The updrafts are initiated on the model axis by a thermal bubble with a horizontal radius of 7.5 km and a vertical radius of 1.5 km, centered 1.5 km above the surface. The maximum amplitude of the initial θ perturbation is 2 K for each sounding. Regardless of the initial bubble amplitude and dimensions, considerable difficulty was encountered in sustaining an updraft beyond 10 min (dozens of different soundings also were tested to no avail). The difficulty possibly arises from unrealistically strong vertical motions in an axisymmetric model (Ogura 1963; Soong and Ogura 1973), which would lead to unrealistically strong compensating subsidence and dynamic entrainment. Walko (1988) reported a similar problem; he circumvented the problem

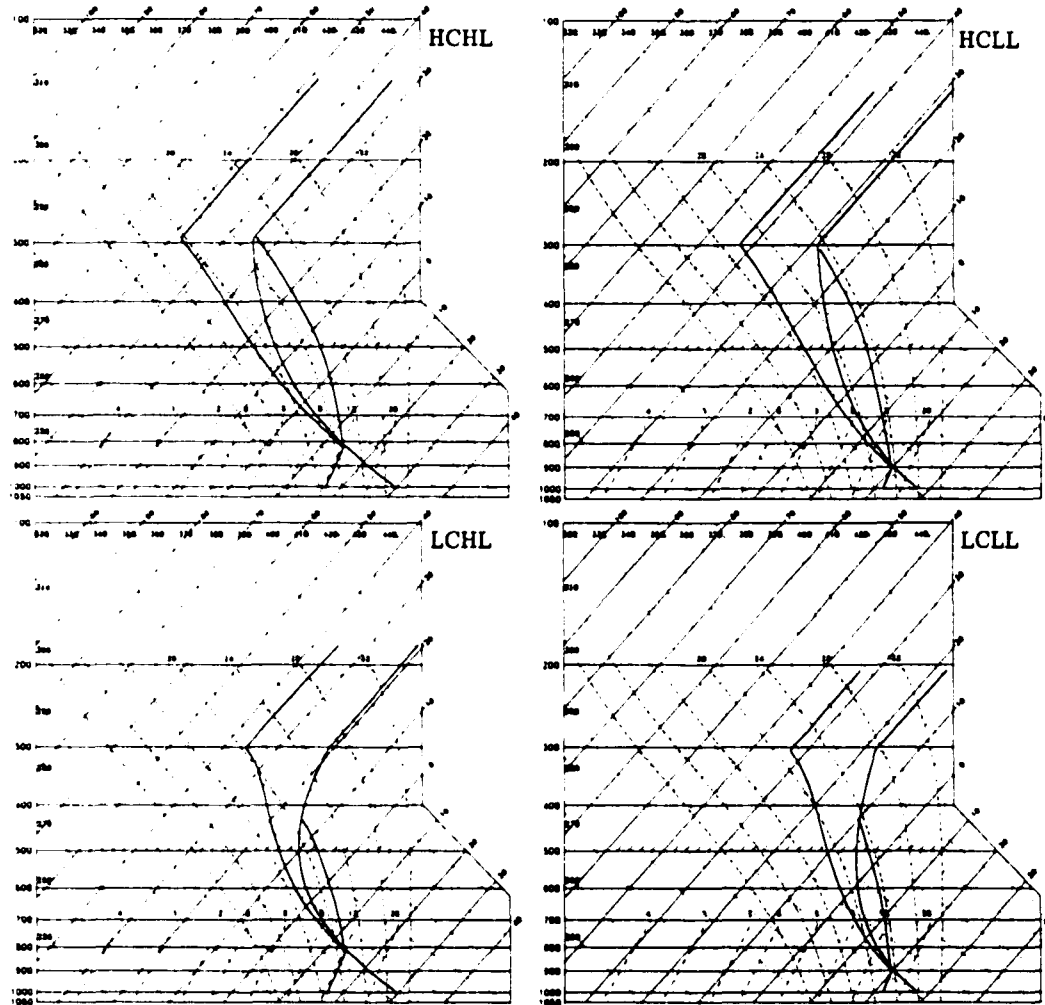


Figure 7.2: Skew T -log p diagrams showing the analytic soundings used to initialize the model base state in the eight experiments. The high-CAPE (low-CAPE) soundings contain approximately 1500 (500) J kg^{-1} CAPE; the high-LCL (low-LCL) soundings have an LCL at 1600 (800) m.

using an initialization with “unrealistically deep” (3.5 km) moisture.² Clark (1973) also presents plots of cloud water fields that reveal skinny, nearly inactive cloudy updrafts less than 30 min into the simulations. Smith and Leslie (1978) simulated a moist, cloudy updraft for at least 20 min; however, the sounding was not typical of severe storm environments (CAPE was $<150 \text{ J kg}^{-1}$). Soong (1974) was able to simulate a long-lived (>60 min) moist updraft within his axisymmetric model; however, the cloud was <3 km tall, had a radius of <600 m, and maximum vertical motions were $<6 \text{ m s}^{-1}$. Thus, CAPE presumably was miniscule and not typical of a severe storm environment.

In addition to the updraft maintenance difficulties arising from the model dimensionality, it may be difficult to sustain an updraft in environments entirely absent of vertical wind shear. Dynamic vertical pressure gradients owing to interaction of the updraft with the mean shear (Rotunno and Klemp 1982) cannot arise. Owing to the symmetry of an axisymmetric model, mean vertical wind shear cannot exist; therefore, the only dynamic pressure force that can promote the lifting of air parcels to their LFCs is that which is associated with the vertical gradient of vertical vorticity (which arises when a tangential wind field is imposed)³.

Because of the difficulty in sustaining an updraft, it was necessary to include an additional updraft forcing term in (7.4), F_U . It can be argued that F_U is essentially a parameterization of the dynamic pressure forcing associated with vertical velocity gradients interacting with the mean shear [a “linear” forcing that is proportional to $\nabla w \cdot \partial \mathbf{v} / \partial z$; see Rotunno (1981) or Rotunno and Klemp (1982)]. The addition of F_U to (7.4) perhaps is justified by the fact that the simulations are designed to simulate a supercell updraft: by imposing a tangential wind profile (to be described below), we already are parameterizing the process of tilting and stretching of horizontal vorticity that leads to mesocyclogenesis. In such environments, the horizontal vorticity is associated with a mean vertical wind shear; therefore, linear dynamic pressure forces also are inevitably present. Because such effects cannot be explicitly produced in

²Furthermore, condensation had to be turned off outside of the main updraft in order to prevent the formation of “spurious” convection owing to the deep moisture.

³A hydrostatic perturbation pressure gradient associated with the presence of a warm, buoyant air column also can force low-level ascent.

an axisymmetric model, we argue that some attempt should be made to artificially include them in order to add to the realism of the supercell updraft simulations.

The additional updraft forcing has the form

$$F_U(r, z, t) = \begin{cases} F_{U_0} \left[\frac{\cos(\pi\alpha)+1}{2} \right], & \alpha \leq 1 \\ 0, & \text{otherwise,} \end{cases} \quad (7.26)$$

where F_{U_0} is the amplitude of the updraft forcing and

$$\alpha = \left[\left(\frac{r}{r_{U_r}} \right)^2 + \left(\frac{z - z_{U_{max}}}{z_{U_r}} \right)^2 \right]^{\frac{1}{2}}, \quad (7.27)$$

where r_{U_r} and z_{U_r} are the horizontal and vertical radii of the updraft forcing, and $z_{U_{max}}$ is the height of the maximum updraft forcing. For all of the experiments, $F_{U_0} = 0.02 \text{ m s}^{-2}$ is used. The parameterized dynamic forcing is sufficient for maintenance of the updrafts, yet it is not so strong that it dominates the vertical motion forcing. In each experiment, $r_{U_r} = 1000 \text{ m}$ (until rain water is inserted at 900 s, after which $r_{U_r} = 500 \text{ m}$), $z_{U_r} = 3500$, and $z_{U_{max}} = 1000 \text{ m}$. The shape and magnitude of the forcing field is similar to the linear dynamic pressure forcing field shown by Rotunno and Klemp (1982) in a cross-section through one of their simulated supercells. (It is recognized that the dynamic pressure gradient forcing for a supercell updraft often is strongest on the updraft *flanks*, which leads to deviant updraft propagation. In the axisymmetric model, it is deemed most appropriate that the forcing be centered on the axis.)

Beginning at $t = 300 \text{ s}$ (in the wake of the initial thermal pulse), a vortex is “spun-up” over a 10-min period, by which time the updrafts acquire an approximately steady state. By $t = 900 \text{ s}$ (15 min), the tangential wind profile in each updraft is that of an elevated Rankine vortex, with rotation that decays to zero at a height of 250 m:

$$v = \frac{1}{2} \zeta_0 R_v(r) Z_v(z), \quad (7.28)$$

where

$$R_v(r) = \begin{cases} r, & r \leq r_c \\ r/r_c^2, & r > r_c \end{cases} \quad (7.29)$$

$$Z_v(z) = \begin{cases} \cos\left(\frac{\pi}{2} \frac{|z - z_{v_{max}}|}{z_{v_r}}\right), & z_{v_{max}} - z_{v_r} \leq z \leq z_{v_{max}} + z_{v_r} \\ 0, & \text{otherwise} \end{cases} \quad (7.30)$$

where $u=w=0$ initially. ζ_0 is the maximum vertical vorticity (0.03 s^{-1}), r_c is the vortex core radius (1000 m), $z_{v_{max}}$ is the height of maximum rotation (2500 m), and z_{v_r} is the vertical radius of the vortex (2250 m). No rotation is present below 250 m; thus, surface rotation cannot develop without the formation of a downdraft. The chosen value of ζ_0 yields a maximum circulation of approximately $10^5 \text{ m}^2 \text{ s}^{-1}$ (located at $z = 2500 \text{ m}$ for $r \geq r_c$).

The steady state updrafts have maximum vertical velocities of $54\text{-}59 \text{ m s}^{-1}$ in the high-CAPE environments and $25\text{-}30 \text{ m s}^{-1}$ in the low-CAPE environments (Fig. 7.3). Regardless of the CAPE, the size and amplitude of the initial thermal bubble, and the shape and amplitude of F_U , the high-LCL soundings yield updrafts having radii of $1.5\text{-}1.8 \text{ km}$, and the low-LCL soundings yield updrafts having radii of $1.1\text{-}1.2 \text{ km}$. The low-LCL soundings contain shallower moist layers than the high-LCL soundings. The deeper moist layers in the high-LCL environments appear to be capable of supporting wider updrafts than the low-LCL environments. While the updraft depths, shapes, and maximum vertical velocities differ in each case, the prescribed steady state tangential wind profiles are identical at 900 s. At this time, a downdraft is initiated by imposing rain water and a forcing F_D in (7.4). Also note that the vertical velocity fields in the lowest 1500 m are nearly identical in all of the updrafts at 900 s (Fig. 7.3).

7.2.3 Downdraft generation

At $t = 900 \text{ s}$ (15 min), an annular downdraft is generated at a radius of 1000 m. It was found that realistic amounts of precipitation loading alone could not initiate a downdraft rapidly enough and sufficiently strong so that the rain curtain

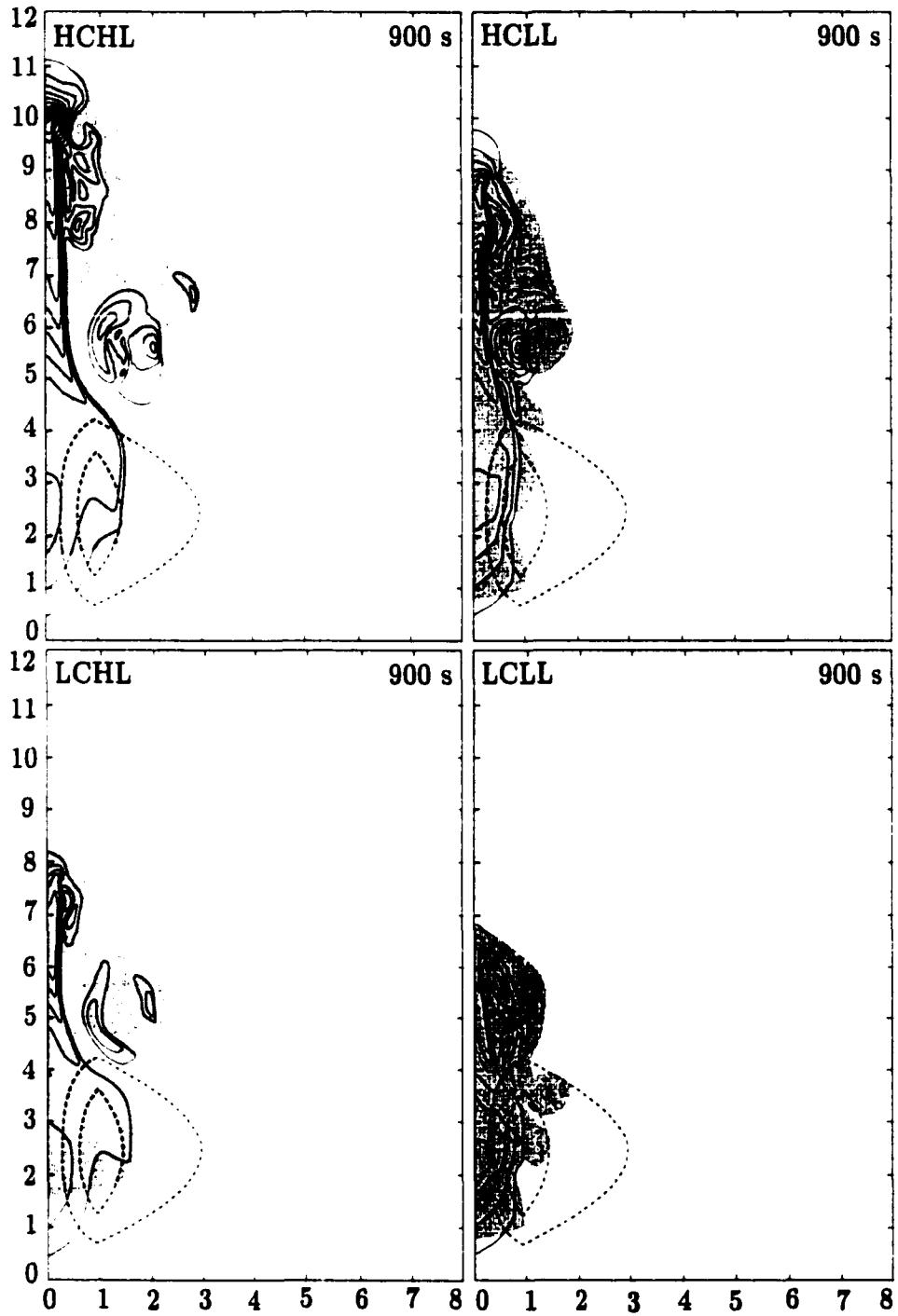


Figure 7.3: Steady-state updrafts in the control simulations. Regions where cloud water mixing ratio exceeds 0.1 g kg^{-1} is shaded gray. Vertical velocity contours (solid) are drawn at 5 m s^{-1} intervals starting at 5 m s^{-1} . Tangential wind velocity contours (dashed) also are drawn at 5 m s^{-1} intervals starting at 5 m s^{-1} .

could fall to the ground without being advected toward the updraft axis by the radial inflow (and subsequently leading to updraft demise). Therefore, an additional forcing for the downdraft, F_D , was added to (7.4). In a real supercell, the rain curtain comprising the hook echo falls down the rear side of the updraft, where inflow (that could advect the precipitation toward the updraft axis) is typically weaker than on the forward side of the updraft, where inflow typically is strongest (i.e., the inflow of real supercells is *not* symmetric with respect to the updraft). In the axisymmetric model, radial inflow is symmetric about the axis and probably unrealistically strong in the region where the rain curtain descends. Without an additional downdraft forcing, the rain curtain (imposed on the updraft periphery) never reaches the ground, but instead is carried by the inflow toward the axis (where large vertical velocities exist) where the rain water then ascends through the updraft, eventually leading to demise of the updraft. This obviously is not a realistic behavior for the precipitation streamers that comprise the hook echo. Therefore, an additional dynamic forcing was imposed to allow the rain curtain to descend to the surface some distance away from the axis.

As with F_U , F_D arguably can be included as a parameterized (downward) dynamic pressure forcing owing to interactions of mean shear with an updraft, which an axisymmetric model cannot produce. Yet the presence of downward-directed dynamic pressure gradient forces on the periphery of supercell updrafts is well-known (e.g., Bonesteel and Lin 1978; Rotunno and Klemp 1985), particularly near the time of tornadogenesis. While the exact forcing mechanisms for the RFD remain unknown and are beyond the scope of the present work, observational and numerical modeling efforts suggest that both precipitation loading (within the hook echo) and downward-directed dynamic pressure gradients are present in the RFD. For these reasons, the downdraft initiated at $t = 900$ s is driven by both water loading and a parameterized forcing term in (7.4).

The contribution by F_D to the downward acceleration is approximately 2.5 times larger than the contribution by the imposed rain water. The q_r concentration within the downdraft is approximately $4\text{--}10 \text{ g kg}^{-1}$ and the specified amplitude of F_D is 0.25 m s^{-2} [while this acceleration is relatively large, it is not unrealistic when compared to the retrieved vertical pressure gradients in observed storms (e.g., Wakimoto et

al. 1998a)⁴]. Rain water is inserted into the updraft by way of the production term, P_r , in (7.17), where

$$P_r(r, z, t) = \begin{cases} P_{r0} R_P(r) Z_P(z), & t \geq 900 \text{ s} \\ 0, & \text{otherwise} \end{cases} \quad (7.31)$$

where

$$R_P(r) = \begin{cases} 1 - \left(\frac{r - r_{Pc}}{r_{Pr}} \right)^4, & r_{Pc} - r_{Pr} \leq r \leq r_{Pc} + r_{Pr} \\ 0, & \text{otherwise} \end{cases} \quad (7.32)$$

$$Z_P(z) = \begin{cases} \cos\left(\frac{\pi}{2} \frac{z - z_{Pc}}{z_{Pr}}\right), & z_{Pc} - z_{Pr} \leq z \leq z_{Pc} + z_{Pr} \\ 0, & \text{otherwise} \end{cases} \quad (7.33)$$

where r_{Pr} and z_{Pr} are the horizontal and vertical radii of the rain water production zone (chosen to be 100 m and 250 m, respectively), and r_{Pc} and z_{Pc} are the coordinates representing where the rain water production zone is centered (chosen to be at $r = 1000$ m and $z = 1850$ m). In other words, P_r generates an annular curtain of rain water beginning at $t = 900$ s, and the rain curtain is 200 m wide, has a radius of 1000 m, and extends to 2100 m above the ground. The value of P_{r0} is chosen to be $5 \times 10^{-3} \text{ g g}^{-1} \text{ s}^{-1}$, which leads to maximum q_r values within the rain curtain of approximately $8 \text{ } 10 \text{ g kg}^{-1}$.

The downdraft forcing F_D in (7.4) is

$$F_D(r, z, t) = \begin{cases} -F_{D0} R_D(r) Z_D(z), & t \geq 900 \text{ s} \\ 0, & \text{otherwise} \end{cases} \quad (7.34)$$

where F_{D0} is the amplitude of the downdraft forcing and

$$R_D(r) = \begin{cases} 1 - \left(\frac{r - r_{Pc}}{r_{Dr}} \right)^2, & r_{Pc} - r_{Dr} \leq r \leq r_{Pc} + r_{Dr} \\ 0, & \text{otherwise} \end{cases} \quad (7.35)$$

⁴Furthermore, Wakimoto et al. (1998a) found that the dynamic forcing for the occlusion downdraft was considerably larger than the forcing owing to precipitation loading; thus, it is believed that the amplitude of the imposed downdraft forcing also is justifiable.

$$Z_D(z) = \begin{cases} \cos \left[\frac{\pi}{2} \frac{z - 0.5(z_{P_c} + z_{P_r})}{0.5(z_{P_c} + z_{P_r})} \right], & z \leq z_{P_c} + z_{P_r} \\ 0, & \text{otherwise,} \end{cases} \quad (7.36)$$

where r_{Dr} is the horizontal radius of the downdraft forcing, and $r_{Dr} = 500$ m is used. In other words, F_D contributes to a downward acceleration from the surface to the top of the zone in which rain water is artificially produced, and in a region 1000 m wide centered along the rain water production zone (Fig. 7.3). The forcing is a maximum at $z = (z_{P_c} + z_{P_r})/2$ m and $r = r_{P_c}$ m. The sensitivity of the downdraft location with respect to the cloud boundary will be explored at the conclusion of the next section.

The precipitation- and dynamically-driven downdraft advects angular momentum toward the surface. During the forced descent, evaporation and entrainment occur. The effects of the initial CAPE and LCL height on the near-ground thermodynamic characteristics of the downdraft, and ultimately, on the near-ground intensification of vorticity, are discussed in the next section.

7.3 Results

Within only a few minutes after its initiation, the precipitation- and dynamically-driven downdraft, bearing high-angular momentum air parcels from aloft, reaches the surface. Upon reaching the ground, the high-angular momentum air parcels experience convergence beneath the updraft, and swirling velocities increase. The time of tornadogenesis arbitrarily is defined as the time when the vertical vorticity at the lowest grid level (16 m) exceeds 0.75 s^{-1} . The time of tornado dissipation arbitrarily is defined as the time when the vertical vorticity falls below 0.75 s^{-1} for at least 30 s.

7.3.1 Experiments HCHL and HCLL

In Experiment HCHL, by $t = 964$ s, negative vertical velocities extended to cloud base on the periphery of the updraft, and the rain curtain extended about halfway to the ground (Fig. 7.4). By $t = 1028$ s, the downdraft exceeded 10 m s^{-1} and angular momentum-rich air nearly had reached the surface. Tornadogenesis occurred at $t = 1076$ s. By $t = 1092$ s there was some indication that the vortex was beginning to weaken (Fig. 7.8), and by this time, θ'_v deficits exceeding 3 K were within 500 m of the vortex at the surface. At $t = 1116$ s, the tornado dissipated, and a large region of substantial θ'_v deficit was located at the surface. CIN values at the surface also were larger at the time of dissipation than at the time of tornadogenesis (Table 7.3). Over the next few minutes, a circulation persisted at the surface, but the circulation was fairly broad and relatively weak (Fig. 7.4). Upward vertical velocities below cloud base also weakened during this time.

The evolution of Experiment HCLL was similar to Experiment HCHL through $t = 1080$ s, although the maximum downdraft in Experiment HCHL was approximately 5 m s^{-1} stronger, owing to larger negative buoyancy in the downdraft in Experiment HCHL (Fig. 7.5). Tornadogenesis occurred at $t = 1080$ s. At this time, upward vertical velocities were approximately 5 m s^{-1} larger than in Experiment HCHL, probably because the low-level static stability was smaller than in Experiment HCHL (the largest θ'_v deficits at the ground within a 1 km radius of the vortex were approximately 2 K). A nearly steady tornado, stronger than in Experiment HCHL, persisted for over 3 min , and demise (at $t = 1292$ s) was not associated with the development of large θ'_v deficits at the surface, as was the case in Experiment HCHL. Instead, by the time of demise, the midlevel updraft had nearly dissipated, with the weakening apparently being related to the intense low-level vorticity (the updraft persisted considerably longer without an imposed downdraft and ensuing tornadogenesis). Only small θ'_v deficits ($<3 \text{ K}$) were present at the ground at the time of dissipation.

Midlevel, environmental low- θ'_v air was entrained by the downdraft in Experiment HCLL owing to the proximity of the downdraft to the lateral boundary of the cloud (because the updraft was narrower and the downdraft was initiated in the same location in each case with respect to the angular momentum distribution).

This low- θ_e air was not ingested by the updraft until late in the simulation, and θ_e fluctuations at the ground in both high-CAPE experiments were small (θ_e is not perfectly conserved during the evaporation process). Moreover, significant CAPE values were present in the downdrafts at the ground in both simulations (Table 7.3). This result agrees with the measurements of surface-based CAPE within the RFDs associated with observed tornadic supercells (chapter 5).

7.3.2 Experiments LCHL and LCLL

Descent of the rain curtain and high-angular momentum air between $t = 900$ s and $t = 1020$ s proceeded in the low-CAPE simulations in a manner similar to the high-CAPE runs. The qualitative differences between Experiments LCHL and LCLL were similar to the differences between Experiments HCHL and HCLL (Figs. 7.6 and 7.7; Tables 7.2 and 7.3). In Experiment LCLL, the maximum downdraft was approximately 5 m s^{-1} weaker than in Experiment LCHL. The downdraft in Experiment LCHL was associated with θ'_e values approximately 2 K colder on average, compared to Experiment LCLL. Just prior to tornadogenesis (at $t = 1072$ s in Experiment LCHL and $t = 1080$ s in Experiment LCLL), the updraft in Experiment LCLL was approximately 5 m s^{-1} stronger than in Experiment LCHL. The maximum intensity of the vortex in Experiment LCLL was not significantly different from that in Experiment HCLL, but the strength of the vortex in Experiment LCHL was weaker than in Experiment HCHL. Similar to the high-CAPE cases, tornado longevity was greater in the low-LCL environment (LCLL).

Tornado demise occurred at $t = 1104$ s in Experiment LCHL, and at $t = 1180$ s in Experiment LCLL. In both low-CAPE experiments, the surface parcels supplying the vortices contained larger amounts of CIN at the time of tornado demise compared to the time of tornadogenesis, although CIN values in Experiment LCLL were not particularly large ($22\text{-}38 \text{ J kg}^{-1}$) near the circulation. It is not known why the vortex in Experiment LCLL did not maintain its intensity longer. Surface parcels in both experiments were associated with significant CAPE. In Experiment LCLL, as in Experiment HCLL, midlevel, environmental low- θ_e air was entrained by the downdraft, although low θ_e values never reached the ground.

EXPERIMENT HCHL

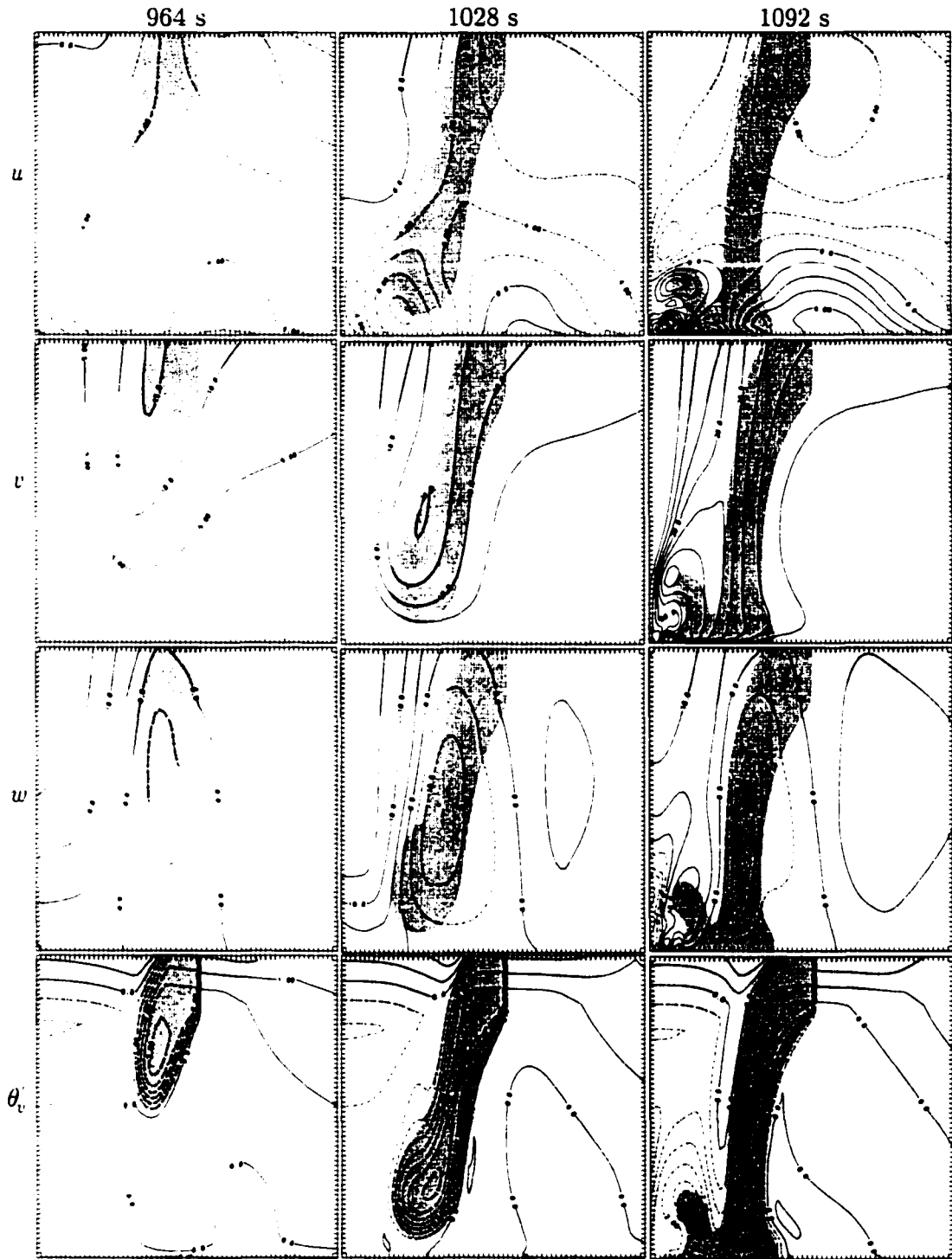
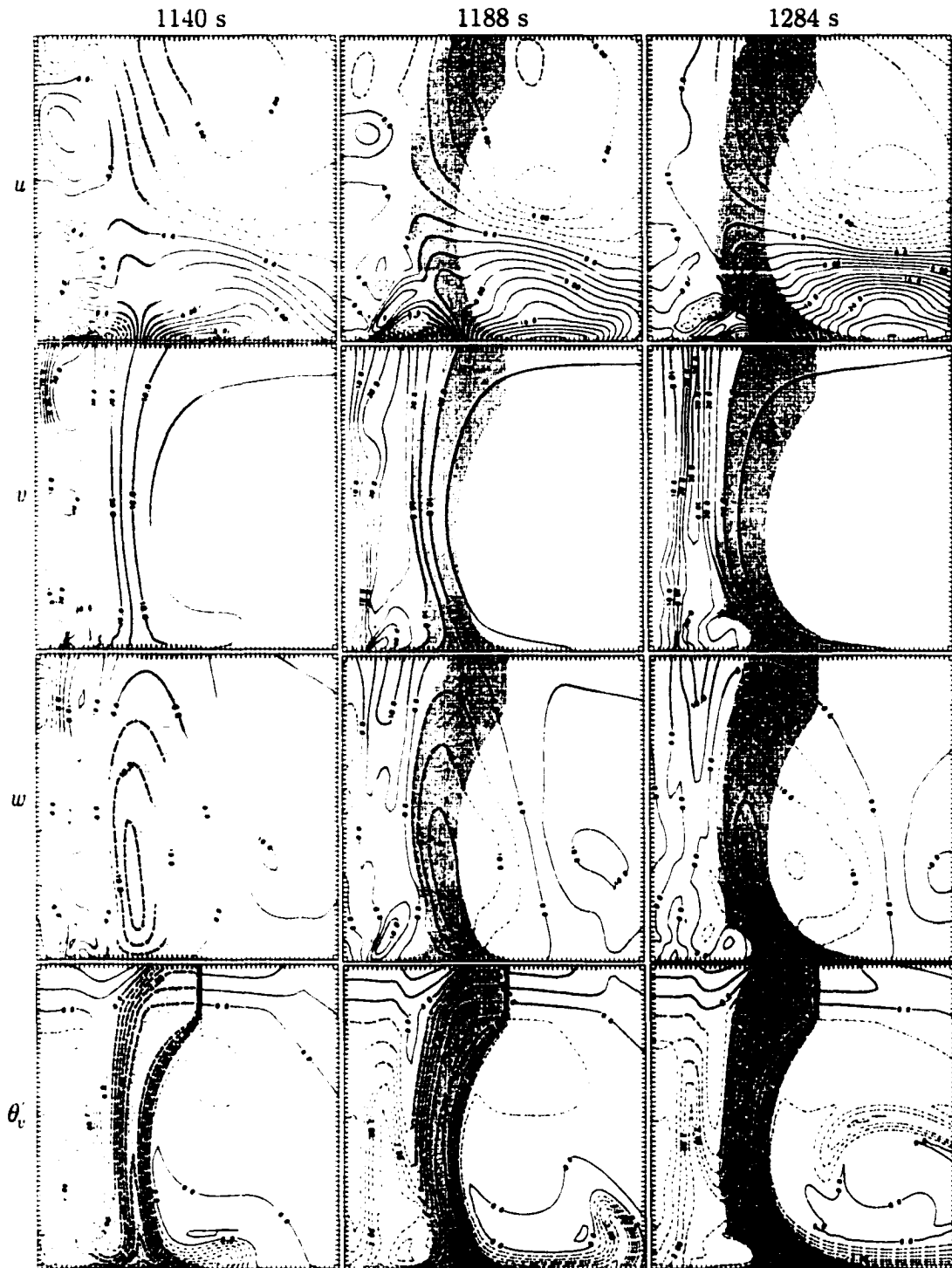


Figure 7.4: Meridional cross sections of radial, tangential, and vertical velocity, and virtual potential temperature fluctuation for Experiment HCHL at various times (refer to Table 7.2 for the times of the tornado as defined in section 7.3). (Continued on next page.)

EXPERIMENT HCHL



The light gray region indicates where $q_c > 0.1 \text{ g kg}^{-1}$, and the dark gray region indicates where $q_c > 2 \text{ g kg}^{-1}$. The abscissa range is $0 \leq r \leq 2 \text{ km}$ and the ordinate range is $0 \leq z \leq 2 \text{ km}$. Radial velocity is contoured at 2 m s^{-1} intervals, tangential and vertical velocity are contoured at 5 m s^{-1} intervals, and virtual potential temperature is contoured at 0.5 K intervals. Negative contours are dashed.

EXPERIMENT HCLL

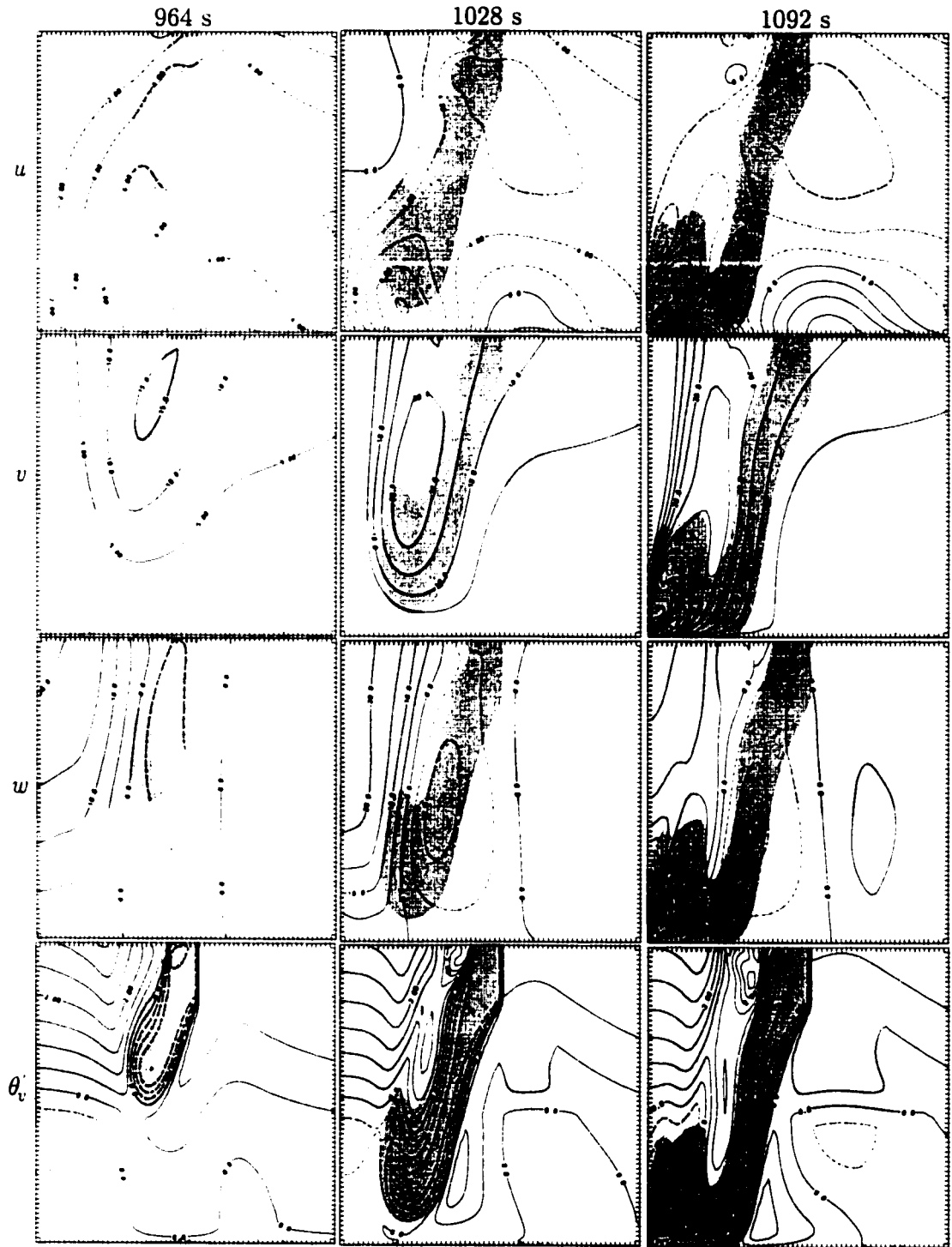


Figure 7.5: As in Fig. 7.4. but for Experiment HCLL. (Continued on next page.)

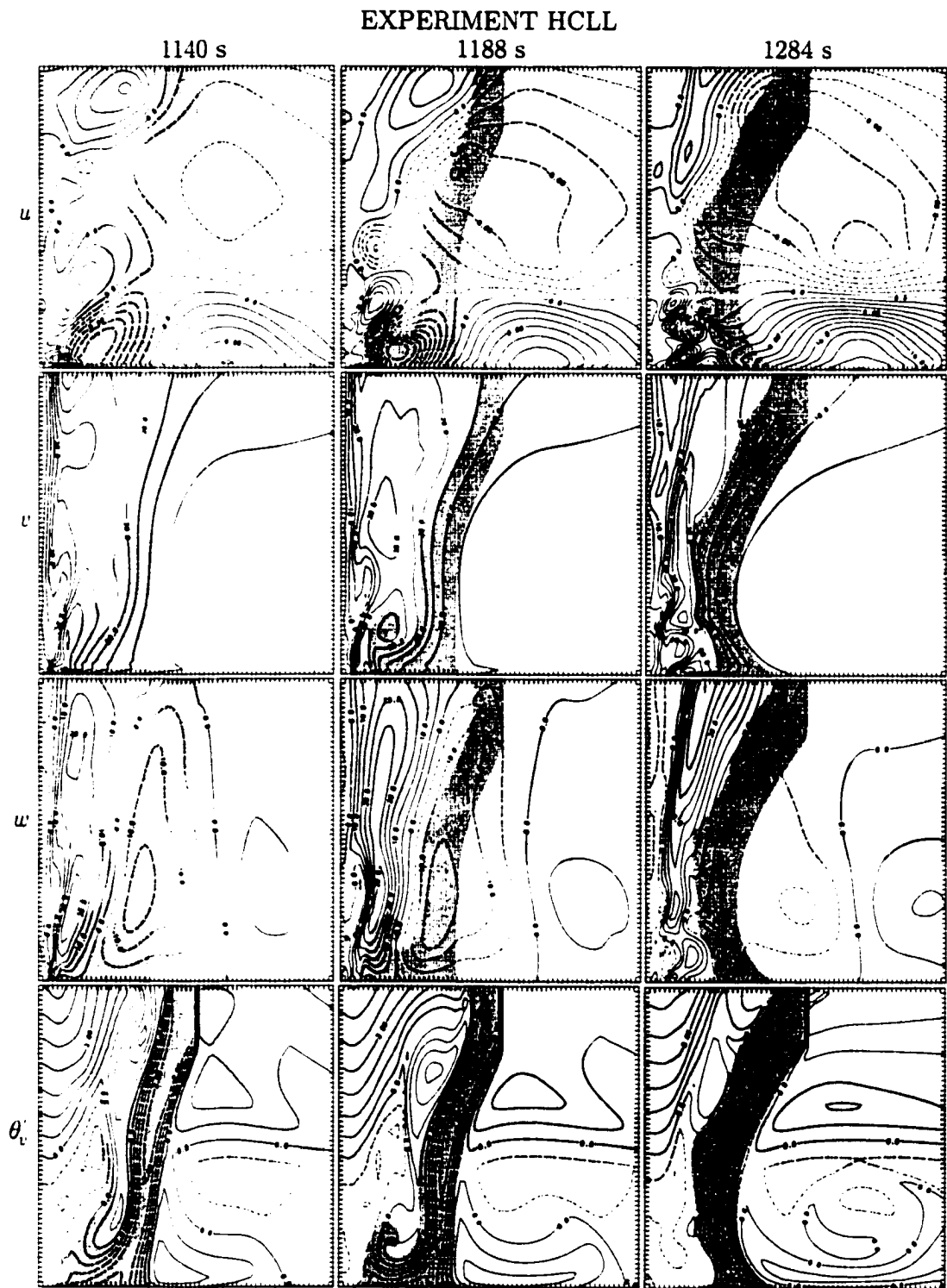


Figure 7.5 (continued).

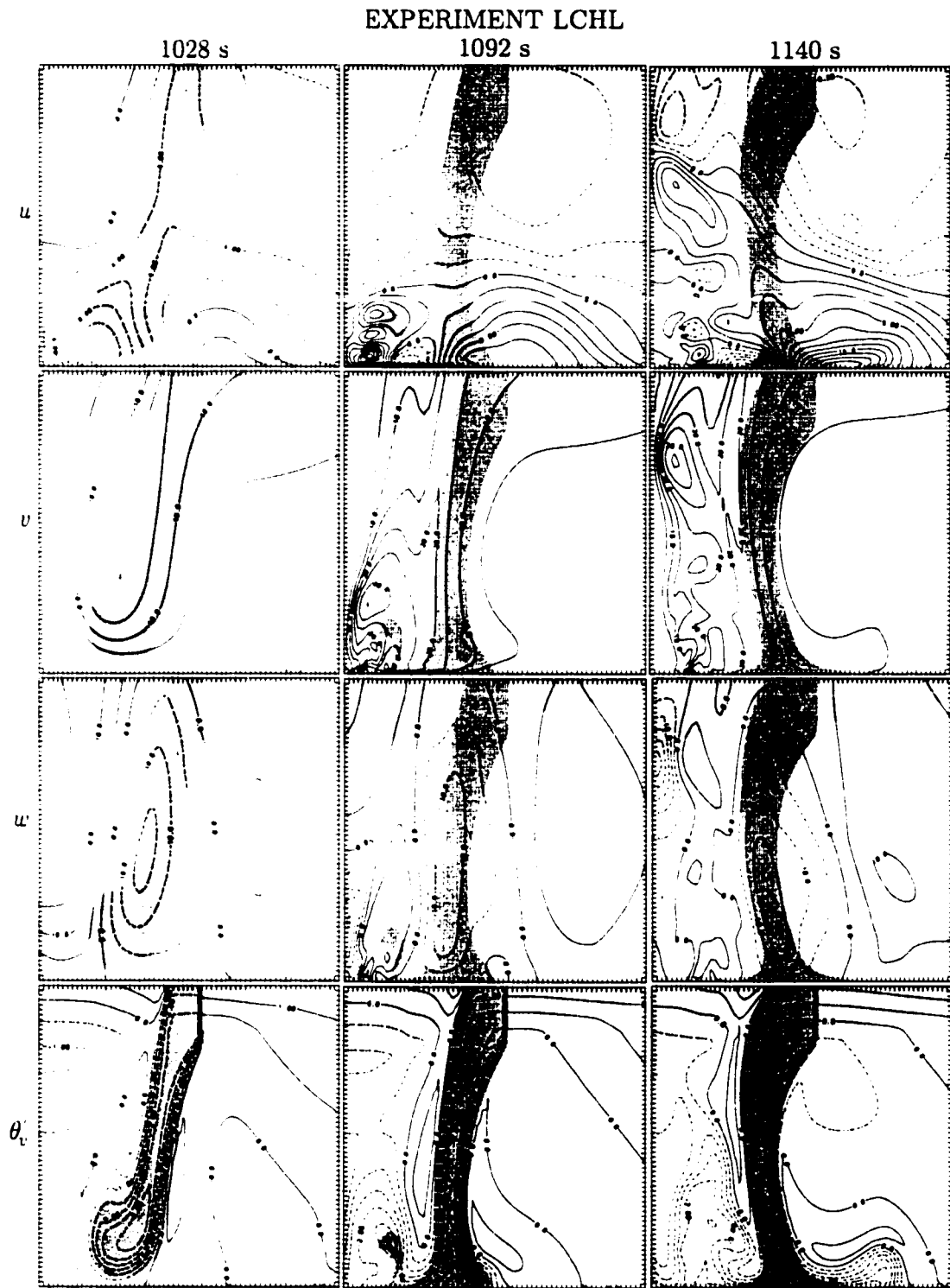


Figure 7.6: As in Fig. 7.4, but for Experiment LCHL.

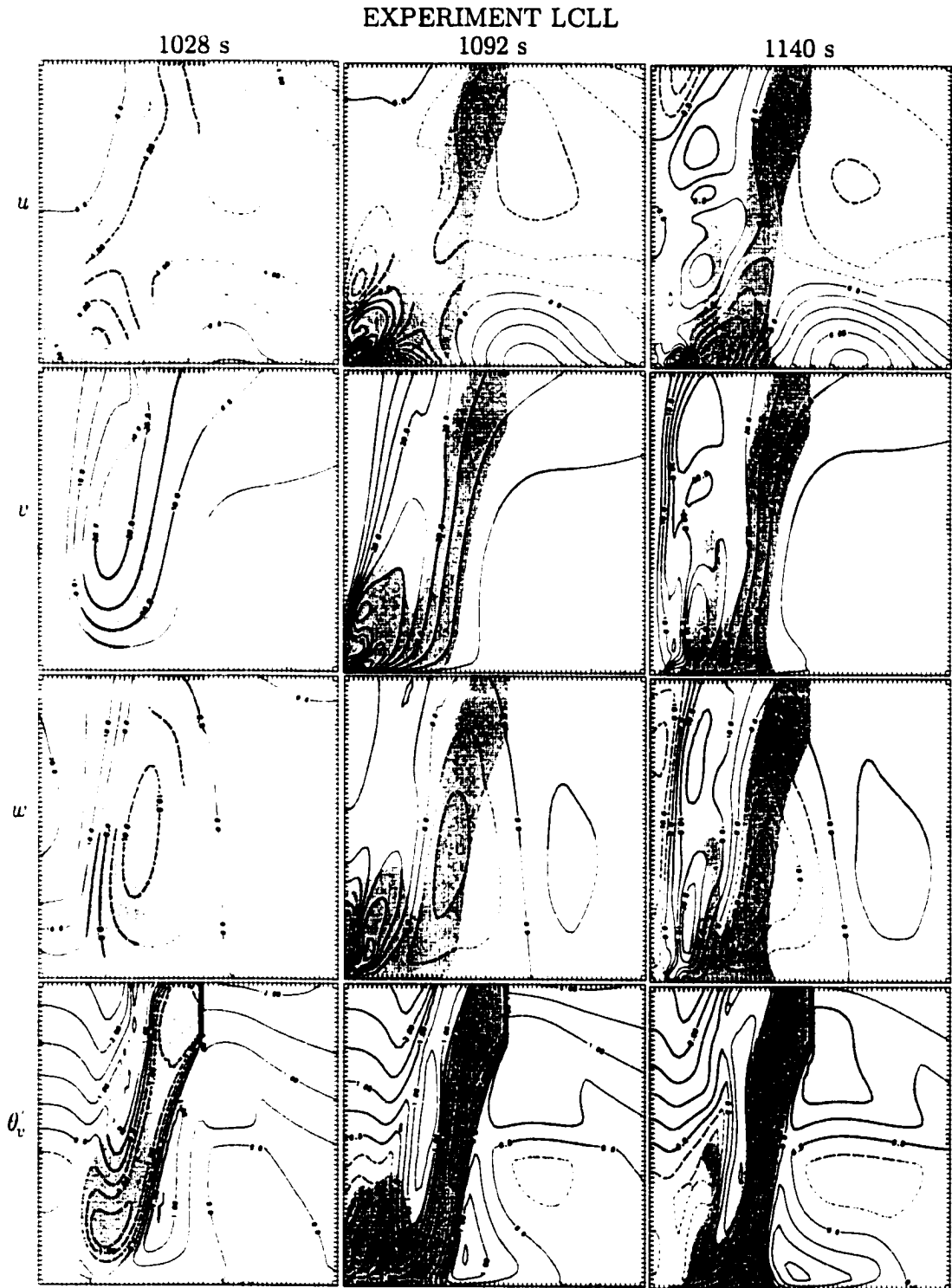


Figure 7.7: As in Fig. 7.4, but for Experiment LCLL.

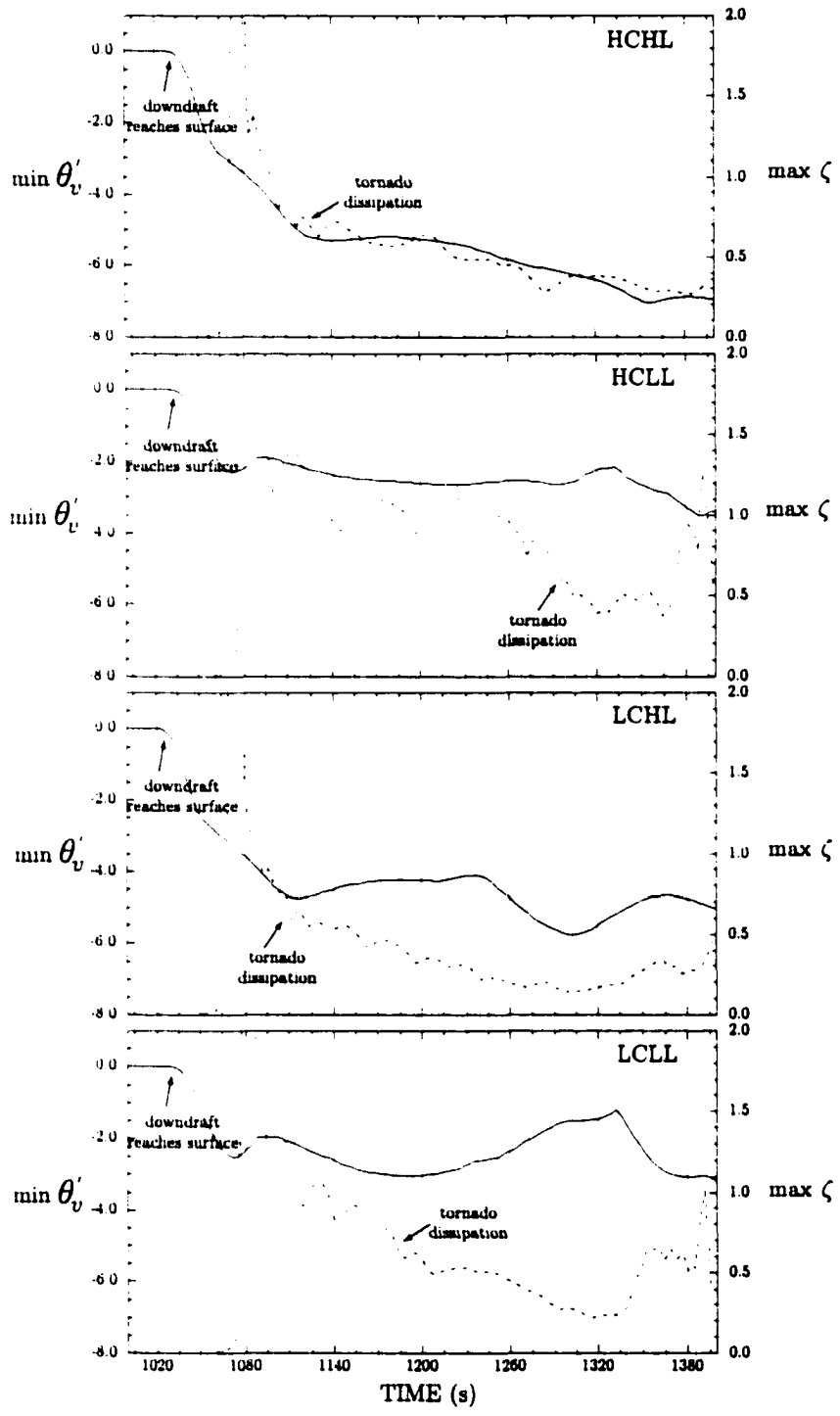


Figure 7.8: Time series of minimum θ'_v (solid, K) and maximum ζ (dashed, s^{-1}) at the lowest model grid level (16 m) within the region $r \leq 1000$ m.

Experiment	Tornado times (s)	Tornado duration (s)	u_{min}	v_{max}	ζ_{max}	Γ_{max}	w_{max}	p'_{min}
HCHL	1076-1116	40	-45.1	73.2	3.89	2.8×10^4	35.6	-37.6
HCLL	1080-1292	212	-48.8	86.0	5.28	2.6×10^4	42.8	-52.8
LCHL	1072-1104	32	-43.8	61.9	4.05	2.5×10^4	29.3	-34.5
LCLL	1080-1180	100	-48.4	85.3	4.69	2.6×10^4	42.9	-43.5

Table 7.2: Summary of idealized simulation results. The tornado lifetime is as defined in section 7.3. The largest radial inflow speed (m s^{-1}) is u_{min} , the largest tangential wind speed (m s^{-1}) is v_{max} , the largest vertical vorticity (s^{-1}) is ζ_{max} , the largest surface circulation ($\text{m}^2 \text{s}^{-1}$) at the time of v_{max} is Γ_{max} , the largest vertical velocity (m s^{-1}) is w_{max} , and the largest pressure deficit (mb) is p'_{min} . Values of u_{min} , v_{max} , ζ_{max} , and Γ_{max} are at the lowest model level (16 m). Values of w_{max} and p'_{min} are below 2 km (and are associated with the vortices).

Experiment	At tornadogenesis					At tornado demise				
	θ'_v	θ'_e	CAPE	CAPE ₅₀₀	CIN	θ'_v	θ'_e	CAPE	CAPE ₅₀₀	CIN
HCHL	3.2-0.0	0.0-0.2	1480-1570	661-691	26-87	-5.0--1.6	0.0-0.8	1498-1652	667-719	95-139
HCLL	-2.1-0.2	0.1-0.5	1491-1603	767-810	11-19	-2.6--0.3	-3.3-0.4	1063-1577	599-800	24-34
LCHL	3.3-0.0	0.0-0.3	528-580	435-469	27-95	-4.6--1.7	0.0-0.9	534-624	439-497	101-133
LCLL	-2.3-0.2	0.1-0.5	531-586	473-512	12-22	-3.0--0.5	0.1-0.9	528-611	471-529	22-38

Table 7.3: Surface thermodynamic data at the times of tornadogenesis and demise. The CAPE below 500 mb (CAPE₅₀₀) also is included to facilitate comparison with the CAPE values computed in chapter 5. The ranges of θ'_v (K), θ'_e (K), CAPE (J kg^{-1}), CAPE₅₀₀ (J kg^{-1}), and CIN (J kg^{-1}) values span the minimum and maximum values at the lowest grid level (16 m) within the region $r \leq 1000$ m. CAPE and CIN values were computed as in chapter 5, whereby surface thermodynamic data were inserted into the base state sounding.

7.4 Discussion

The results of the previous section (Tables 7.2 and 7.3) underscore the role that environmental low-level relative humidity may play in influencing the low-level thermodynamic characteristics of RFDs, as well as the role of those characteristics on the ensuing intensification of vorticity at the ground. The numerical simulation findings—that vortices are more intense and persistent as the buoyancy ($\propto \theta'_v$) of the downdraft increases, and as the CIN of the downdraft decreases—augments the observational findings summarized in chapter 5. Furthermore, the simulations also agree with the observation that high boundary layer relative humidity values (i.e., low LCL height and small surface dewpoint depression) are associated with relatively warmer RFDs and more significant tornadogenesis than environments of relatively low boundary layer relative humidity.

It may be worth noting that the surface θ'_v differences between the experiments might not be what one would consider to be “large.” The θ'_v values at the surface differed by only 1–2 K at the time of tornadogenesis among the four experiments (Table 7.3). Yet this seemingly small difference was associated with tornadoes of considerably varying longevities and intensities (Table 7.2). Furthermore, the surface θ'_v deficits in the high-LCL runs, especially at the time of tornadogenesis, were not as large as commonly observed by the mobile mesonet (deficits of 4–8 K often were recorded in “cold” RFDs), probably owing, at least in part, to the moist midlevel environment in the model and to the experiment design. It is speculated, based on the trends of the simulations herein, that the presence of larger (perhaps more realistic) θ'_v deficits in the model downdrafts in the high-LCL cases would have led to even weaker vortices, or perhaps no tornadogenesis at all.

In all four experiments, CIN values were roughly similar. Moreover, the low-LCL cases also had lower LFCs. Lowering of the LCL typically cannot occur without also lowering of the LFC unless CIN is increased substantially (if CIN becomes too large, then a surface-based storm cannot develop at all). Thus, it is possible that the argument for a low LFC being propitious for tornadogenesis may not differ fundamentally from the argument for a low LCL favoring tornadogenesis.

To most simply explore why tornadogenesis was more intense and longer-lived in the low-LCL cases, it may be beneficial to consider the Boussinesq, inviscid vorticity equation.

$$\frac{\partial \boldsymbol{\omega}}{\partial t} = -\mathbf{v} \cdot \nabla \boldsymbol{\omega} + \boldsymbol{\omega} \cdot \nabla \mathbf{v} + \nabla \times B \hat{\mathbf{e}}_z, \quad (7.37)$$

where $\boldsymbol{\omega} = (\xi \hat{\mathbf{e}}_r + \eta \hat{\mathbf{e}}_\phi + \zeta \hat{\mathbf{e}}_z)$, $\mathbf{v} = (u \hat{\mathbf{e}}_r + v \hat{\mathbf{e}}_\phi + w \hat{\mathbf{e}}_z)$, and $\nabla = (\frac{\partial}{\partial r} \hat{\mathbf{e}}_r + \frac{1}{r} \frac{\partial}{\partial \phi} \hat{\mathbf{e}}_\phi + \frac{\partial}{\partial z} \hat{\mathbf{e}}_z)$, and assuming $\frac{\partial}{\partial \phi} = 0$ by symmetry. The vorticity components are

$$\xi = -\frac{\partial v}{\partial z} \quad (7.38)$$

$$\eta = \frac{\partial u}{\partial z} - \frac{\partial w}{\partial r} \quad (7.39)$$

$$\zeta = \frac{\partial v}{\partial r} + \frac{v}{r}. \quad (7.40)$$

and from (7.37), we obtain

$$\frac{\partial \xi}{\partial t} = -u \frac{\partial \xi}{\partial r} - w \frac{\partial \xi}{\partial z} + \xi \frac{\partial u}{\partial r} + \zeta \frac{\partial u}{\partial z} \quad (7.41)$$

$$\frac{\partial \eta}{\partial t} = -u \frac{\partial \eta}{\partial r} - w \frac{\partial \eta}{\partial z} + \xi \frac{\partial v}{\partial r} + \zeta \frac{\partial v}{\partial z} - \frac{\partial B}{\partial r} - \frac{u \eta}{r} + \frac{v \xi}{r} \quad (7.42)$$

$$\frac{\partial \zeta}{\partial t} = -u \frac{\partial \zeta}{\partial r} - w \frac{\partial \zeta}{\partial z} + \xi \frac{\partial w}{\partial r} + \zeta \frac{\partial w}{\partial z}. \quad (7.43)$$

In (7.41), the terms on the right hand side are horizontal advection, vertical advection, stretching, and tilting of vertical vorticity into the radial direction, respectively. In (7.42), the terms on the right hand side are horizontal advection, vertical advection, reorientation of horizontal vorticity from the radial direction into the azimuthal direction, tilting of vertical vorticity into the azimuthal direction, baroclinic generation, and two curvature terms, respectively. In (7.43), the terms on the right hand

side are horizontal advection, vertical advection, tilting of azimuthal vorticity into the vertical, and stretching, respectively.

Notice that in the axisymmetric model that baroclinic generation of vorticity only affects the azimuthal vorticity, η . Furthermore, azimuthal vorticity cannot be tilted to produce vertical vorticity: thus, baroclinic vorticity generation cannot contribute to vertical vorticity (this result is not necessarily true in three dimensions). Calculation of the forcing terms in (7.43) indicates that the most significant differences between the high-LCL and low-LCL cases owed to stretching differences (Figs. 7.9 and 7.10). As the static stability increases (owing to larger θ'_v deficits within the RFD), vertical motions are inhibited; thus, radial convergence is weaker and the local tangential wind velocity is lessened for a given angular momentum. Leslie and Smith (1978) reached a similar conclusion in their dry vortex simulations. In all four experiments herein, the angular momentum reaching the surface was similar (or even slightly larger in Experiment HCHL compared to the other runs), yet larger local swirling velocities were produced in the low-LCL cases, which were associated with warmer downdrafts and a greater amount of stretching than the high-LCL cases (Fig. 7.11, Table 7.2).

These simple simulations were used to (1) obtain some physical interpretation of the observations and (2) suggest possible fruitful routes for further exploration. In the future, it may be beneficial also to perform trajectory analyses and a pressure decomposition (e.g., Weisman and Klemp 1984); however, such analyses have not been conducted herein.

7.5 Extension to three dimensions

An axisymmetric model was used owing to its simplicity and the high spatial resolution achievable with a manageable number of grid points. But real supercells are not axisymmetric. In real supercells, the RFD typically forms on the upshear flank of the updraft. Thus, downward transport of angular momentum occurs only on the upshear flank. Furthermore, baroclinically-generated horizontal vorticity within the hook echo, if present, may be converted to vertical vorticity by tilting. As the RFD descends in a spiraling manner (photographs of clear slots reveal that RFDs

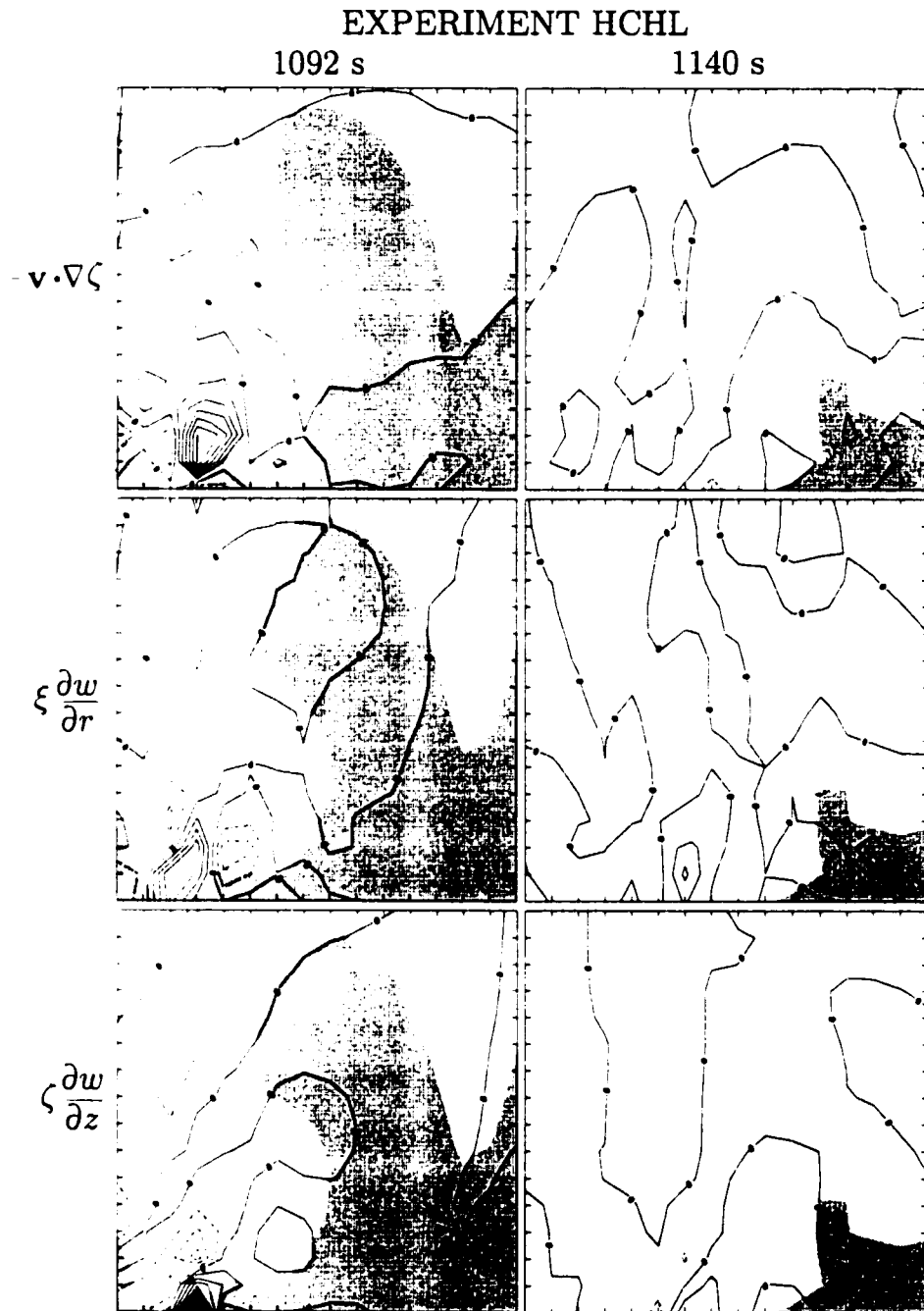


Figure 7.9: As in Fig. 7.4. but the advection, tilting, and stretching terms in (7.43) are plotted. The abscissa range is $0 \leq r \leq 500$ m and the ordinate range is $0 \leq z \leq 500$ m. The contour interval is $2.5 \times 10^{-2} \text{ s}^{-2}$ in each plot, and negative contours are dashed.

EXPERIMENT HCLL

1092 s

1140 s

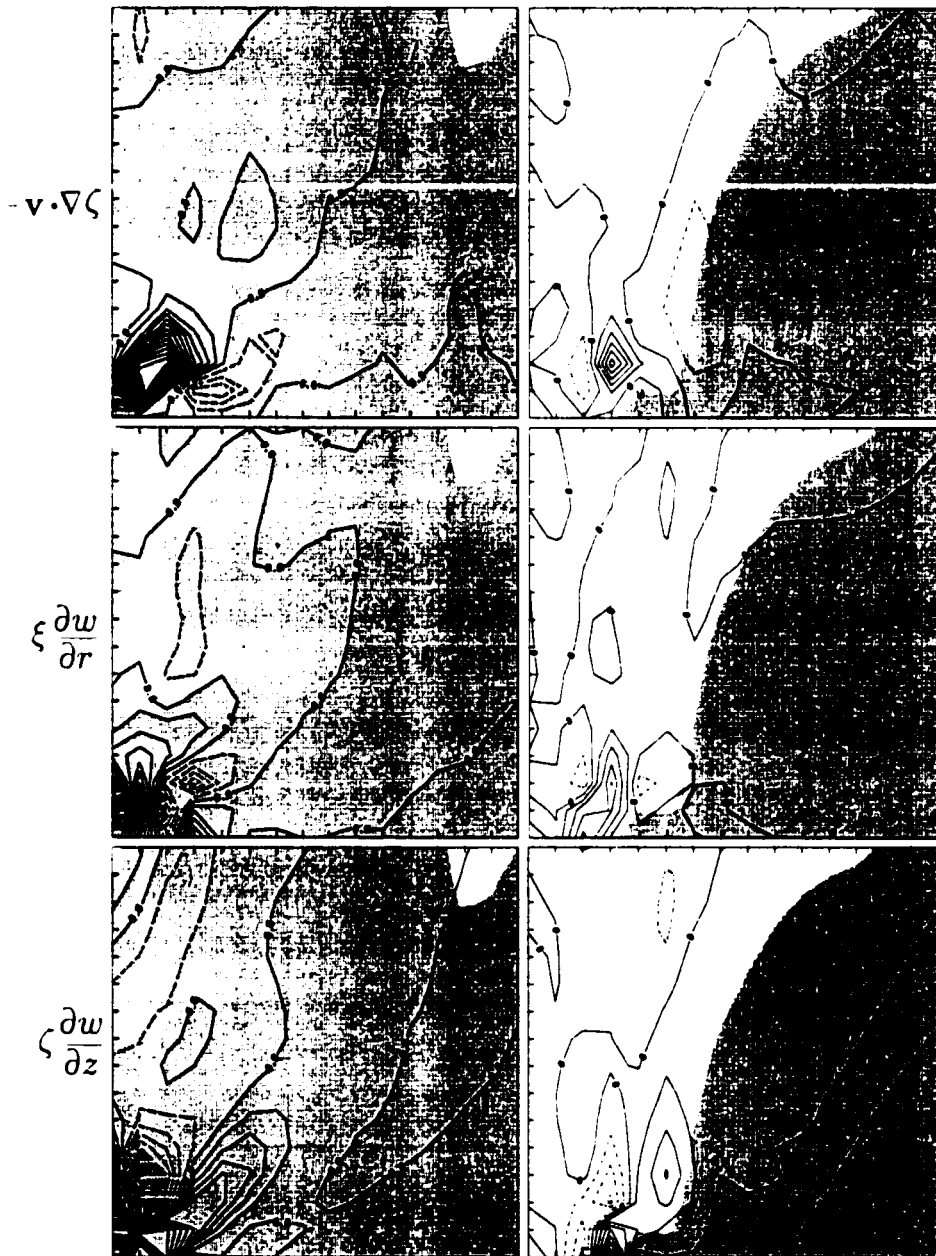


Figure 7.10: As in Fig. 7.9, but for Experiment HCLL.

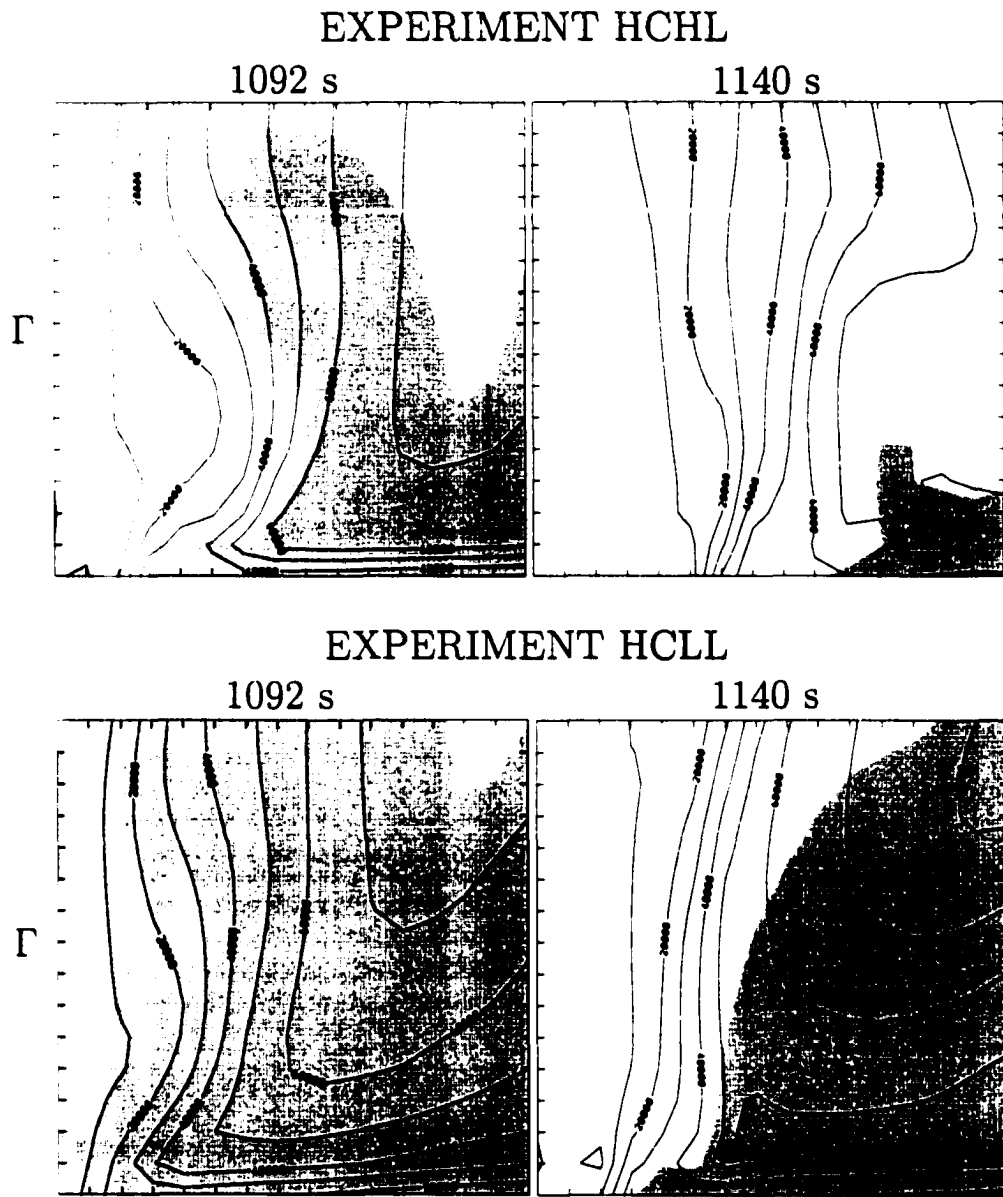


Figure 7.11: Circulation contoured at $10^4 \text{ m}^2 \text{ s}^{-1}$ intervals. The abscissa range is $0 \leq r \leq 500 \text{ m}$ and the ordinate range is $0 \leq z \leq 500 \text{ m}$.

wrap cyclonically around the parent updraft, to the extent that the cloud erosion is associated with descending air), it may eventually nearly encircle the updraft. By this stage, it is possible that the axisymmetric model of the updraft-downdraft system may not be terribly unrealistic.

In three-dimensional supercell environments, significant mean storm-relative flow typically is present; in an axisymmetric model, mean storm-relative flow is precluded by the model symmetry. Therefore, the role of entrainment of midlevel environmental air probably is not adequately represented by an axisymmetric model. In real supercells, the entrainment of potentially cold midlevel air may assume larger importance than in the idealized simulations performed within this chapter. On the other hand, the surface thermodynamic properties (e.g., θ'_v , θ'_e , CAPE, CIN) in the simulations in which the strongest, longest-lived vortices developed were similar to the surface thermodynamic characteristics *observed* in the RFDs associated with prolific tornado-producing supercells. Thus, perhaps entrainment of midlevel environmental air is *not* significant in the RFDs associated with the most severe tornadic supercells.

In non-tornadic supercells, θ'_v deficits >5 K commonly were observed at the surface in close proximity to low-level mesocyclones. Such deficits could not be generated in the idealized simulations. It is not known whether tornadoes would have formed in the simulations if such θ'_v values would have been generated, nor is it known why θ'_v values as small as observed in non-tornadic supercell RFDs (chapter 5) could not be produced in the model. Furthermore, low θ'_e values did not reach the surface in any of the experiments. In the high-CAPE runs, this probably was because the downdraft was positioned away from the lateral cloud boundary, therefore environmental air was not entrained. In the low-CAPE runs, low θ'_e air was entrained from the environment, but it did not reach the surface during the time that the simulations were carried out. In contrast, observations reported in chapter 5 and by numerous past studies have documented the presence of downdraft parcels at the surface in which at least some depletion of θ'_e had occurred during the descent. Perhaps the lack of mean storm-relative flow in the axisymmetric model limited the entrainment of potentially cold into the downdraft. Or perhaps the answer lies in the soundings used, which were considerably moister at midlevels than the soundings typically observed on the Great Plains on days in which the chapter 5 observations were collected.

In chapter 8, the idealized results of this chapter are extrapolated to supplement a three-dimensional conceptual model of tornadogenesis.

7.6 Sensitivity studies

Additional simulations were conducted to explore the sensitivity of the results to the location and width of the downdraft. Increasing the width of the rain curtain (r_{Pr}) did not significantly affect the maximum vortex intensities, but vortex longevity was shortened, owing to the development of a larger cold pool that adversely affected the vortex after less time had elapsed. Increasing the radius of the rain annulus (r_{Pc}) and associated downdraft also did not significantly affect vortex intensity or longevity, although tornadogenesis did not proceed as quickly as in the former cases because more time was needed for the high-angular momentum air to spread beneath the updraft axis. Because of the closer proximity of the downdraft to the lateral cloud boundary in this test, a greater amount of environmental air was entrained by the downdraft; however, this low θ_e air never reached the surface during the lifetime of the updraft. As alluded to at the conclusion of section 7.5, this aspect of the simulations appears to lack realism when compared to observations of at least some low θ_e air reaching the surface in both tornadic and non-tornadic supercell RFDs.

Experiments also were conducted in which the depth of the downdraft (z_{Pr} and z_{Pc}) was increased. In these runs, more intense and longer-lived vortices were produced because the air parcels reaching the surface contained larger angular momentum than the former cases (the angular momentum of the steady-state rotating updrafts increased with height below 2500 m).

Only a relatively small part of the parameter space was explored by these idealized simulations. In the future it will be beneficial to investigate how the results depend on the strength and profile of the elevated vortex and on the updraft characteristics (which may be governed by the imposed vortex and on the CAPE and CAPE distribution). Repetition of the experiments using soundings that are drier in the middle troposphere (like those commonly observed in supercell environments) also should be attempted. Moreover, the microphysics were treated very simply in the simulations (Marshall-Palmer distribution implied). Additional experiments

should be conducted to explore the effects of various drop-size distributions and rain water concentrations.

Other known sensitivities undoubtedly exist, such as the sensitivity to the turbulence parameterization and spatial resolution (e.g., Straka and Rasmussen 1998). A full exploration of these effects is beyond the scope of this dissertation, and may be studied more thoroughly later on. Therefore, the results presented in this section probably should be viewed in a qualitative sense.

Chapter 8

Implications for tornado genesis and maintenance

8.1 RFD forcing mechanisms

Although the presence of RFDs in both non-tornadic and tornadic supercells is well-documented, the forcing for the RFD is not yet agreed upon. Some have argued that the RFD is thermodynamically driven by evaporative cooling as dry, environmental air impinges on the updraft aloft (e.g., Browning and Ludlam 1962; Browning and Donaldson 1963; Nelson 1977; Barnes 1978a,b; Klemp et al. 1981), while others have questioned whether dynamic vertical pressure gradients play a role in the initiation of the RFD (e.g., Bonesteel and Lin 1978; Lemon and Doswell 1979). The identification of a smaller-scale “occlusion downdraft” in simulations conducted by Klemp and Rotunno (1983), which was apparently dynamically driven by low-level pressure deficits, raised further questions. Throughout this dissertation, the RFD has been referred to as the *contiguous downdraft region that surrounds the low-level mesocyclone or tornado*. Visual observations of RFDs suggest that the downdraft is a single entity (e.g., only one “clear slot” is visible). Therefore, discrimination between what Klemp and Rotunno (1983) called an “occlusion downdraft” and the major downdraft first identified by Browning and Ludlam (1962) on the rear flank of a supercell (later called an “RFD”) has not been attempted, although it is probable that different forcings dominate the vertical momentum equation at different times and different locations during the evolution of the downdraft.

Chapter 5 presented surface observations of small θ_e deficits within RFDs associated with many tornadic supercells. These observations imply that the entrainment of midlevel, potentially cold (low θ_e) air, and subsequent evaporation of updraft hydrometeors, is *not* a viable mechanism for driving such RFDs. The only means by which a downdraft may reach the surface with θ_e values within a few K of the inflow values (after a significant downward excursion) in environments characterized by low midlevel θ_e values is if air parcels *within the updraft* (which contains θ_e values similar to the low-level inflow) are forced to descend owing to precipitation drag or downward-directed non-hydrostatic pressure gradients. Below cloud base, evaporation of precipitation within the RFD (hook echo) may occur, and this process essentially conserves θ_e but reduces θ_w . Surface θ_e deficits within RFDs associated with tornadic supercells also were generally small (<3 K), implying that large amounts of evaporative cooling generally did not occur in the subcloud layer within the hook echoes associated with tornadic supercells.

Within the RFDs associated with non-tornadic supercells, the finding of generally large (>8 K) surface θ_e deficits suggests that entrainment of midlevel environmental air (characterized by low θ_e typically) plays a significant role in driving non-tornadic RFDs, in contrast to RFDs associated with significantly tornadic supercells. It cannot be known whether mainly *updraft air* initially undergoes forced descent (owing to precipitation drag or dynamic pressure gradients in a manner similar to that which was hypothesized to occur in tornadic supercells) during which mixing dilutes the θ_e of the descending parcels, or whether the descent in non-tornadic RFDs is initiated by the impingement of midlevel *environmental* air, which subsequently becomes negatively buoyant owing to the evaporation and melting of condensate.

8.2 Effects of low-level stability

Three-dimensional numerical simulations of supercells have not been able to produce warm RFDs, probably owing to inadequate representations of microphysical processes and possibly owing to insufficient spatial resolution. Many simulations are performed without the inclusion of ice. The inclusion of ice typically allows for hydrometeors to be distributed over larger areas; thus, cold pools near the updraft

tend to be weaker. On the other hand, the idealized simulation results of the previous chapter indicate that relatively warm downdrafts may be more favorable for tornadogenesis than downdrafts that arrive at the surface relatively cold.

The observational and idealized simulation results presented herein suggest—as implied by Ludlam’s (1963) prediction (chapter 3) and also implied by the findings of Leslie and Smith (1978) that even a shallow stable layer could prevent an intense vortex from extending to the ground—that the thermodynamic properties of the downdraft air parcels, which have been shown to be the ones that enter the tornado (Brandes 1978; Klemp and Rotunno 1983; Davies-Jones and Brooks 1993; Wicker and Wilhelmson 1995), play a role in the final concentration of vorticity (or lack thereof) at the surface. As the static stability increases, radial convergence is weakened as the vertical motion becomes inhibited. Thus, a given angular momentum is associated with smaller local tangential wind speeds and a wider vortex core.

The precipitation concentration and distribution within the hook echo must, to a considerable degree, control the amount of evaporation and resulting thermodynamic characteristics of the RFD. Perhaps not inconsequentially, Wakimoto and Cai (2000) observed that the “. . . only difference between the Garden City storm and Hays storm (during VORTEX) was the more extensive precipitation echoes behind the rear-flank gust front for the Hays storm.” It is speculated that RFD surface thermodynamic characteristics someday may be inferred using information about the drop size distribution within hook echoes available from dual-polarization radars [e.g., relatively numerous, small drops may imply colder hooks and RFDs because of increased evaporation potential (Hookings 1964; Kamburova and Ludlam 1966)].

8.3 A new hypothesis

Visual and dual-Doppler radar observations of RFDs (e.g., Moller et al. 1974; Rasmussen et al. 1982; Dowell and Bluestein 1997), theoretical considerations (e.g., Davies-Jones 1982a; Davies-Jones and Brooks 1993), and numerical simulations (e.g., Wicker and Wilhelmson 1995) have led to the general agreement that reorientation of vortex lines by the RFD is a fundamental step in tornadogenesis. A conceptual

model in which downward tilting of vortex lines by the RFD is assumed to play a primary role in tornadogenesis (e.g., Davies-Jones and Brooks 1993; Rasmussen and Straka 1997) is presented in Fig. 8.1. The conceptual model illustrates the role of the thermodynamic characteristics of the RFD in tornadogenesis failure as well as tornadogenesis “success.”

In panels 1–3 of Fig. 8.1, a helical updraft (with vortex lines spiraling upward and to the right as viewed by an observer on the ground) is quickly transformed into an updraft-downdraft couplet as the RFD intensifies. Based on the observations and idealized simulation results, it is hypothesized that if the RFD air is characterized by large θ_c and θ_e deficits (and consequently large CIN and little or no CAPE at the surface), then the incipient tornado, which is located in the vertical velocity gradient but in a region where vertical velocity is upward (e.g., Lemon and Doswell 1979), fails to intensify. Tornadogenesis failure results from insufficient stretching owing to the presence of large CIN. If the RFD reaches the ground with only a small θ_c and θ_e deficit (and consequently small CIN and substantial CAPE), then explosive stretching can occur and tornadogenesis “succeeds.” The preceding model probably is overly simplistic [more complex real storm behaviors are documented by Wakimoto et al. (1998a,b) and Rasmussen and Straka (2001)], but it is believed that the most important processes are represented (some sort of downward displacement and tilting of vortex lines followed by stretching of vertical vorticity).

A question remaining to be addressed is what governs the amount of CAPE and CIN at the surface within the RFD. The CAPE at the ground within an RFD may be written as

$$CAPE_{RFD} = CAPE_{ENV} - \Psi, \quad (8.1)$$

where $CAPE_{RFD}$ is the CAPE of the surface parcels within the RFD, $CAPE_{ENV}$ is the CAPE measured in the large-scale storm environment (a function of the θ_e of the inflow environment), and Ψ represents a sink of $CAPE_{RFD}$ arising from dilution of θ_e by entrainment along a trajectory. Note that while evaporation reduces the θ_e of a parcel, θ_e is nearly conserved for an evaporation process; thus, $CAPE_{RFD}$ is

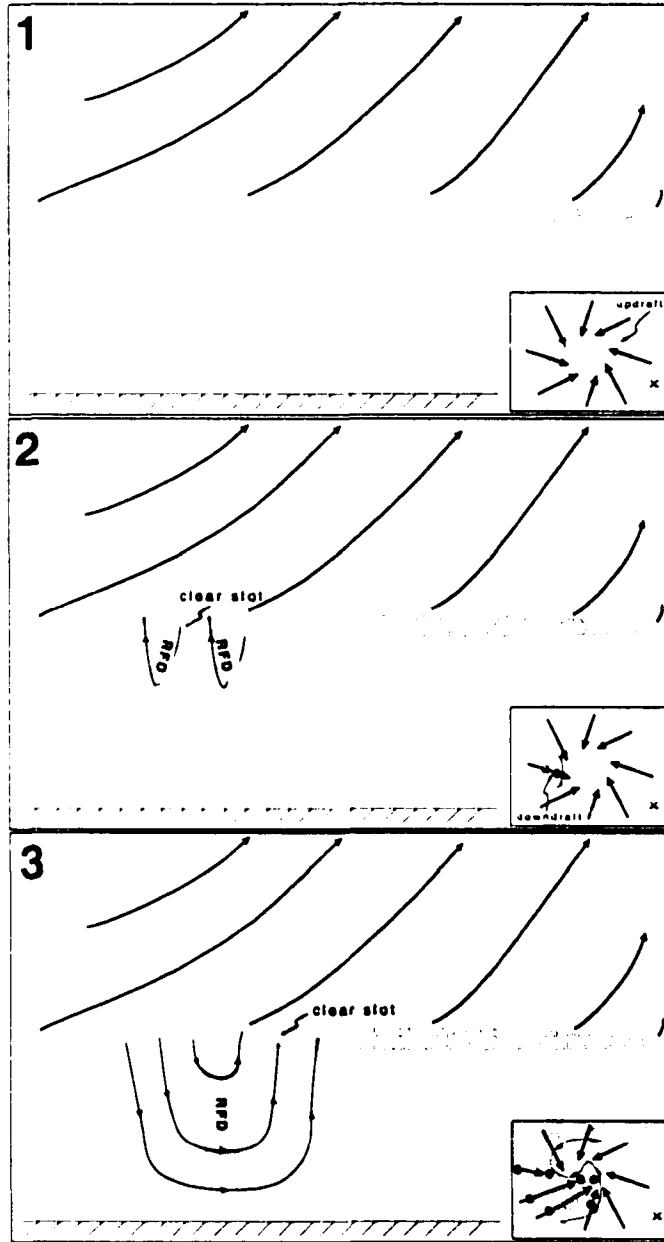


Figure 8.1: Conceptual model of tornadogenesis in which reorientation of vortex lines by the RFD assumes primary importance (e.g., Davies-Jones and Brooks 1993; Rasmussen and Straka 1997), with modification to illustrate the hypothesized role of RFD thermodynamic characteristics in both tornadogenesis success and failure. A few vortex lines have been drawn in black (arrows indicate direction of local vorticity vector). A plan view is included at the bottom right of each panel. The vorticity vectors in the horizontal planes of the plan views are those located at approximately 1 km AGL. The “+” and “-” signs on the plan views indicate where tilting has produced positive and negative vertical vorticity, respectively. The “x” on the plan view indicates the vantage point from which the supercell is viewed. (Continued on next page.)

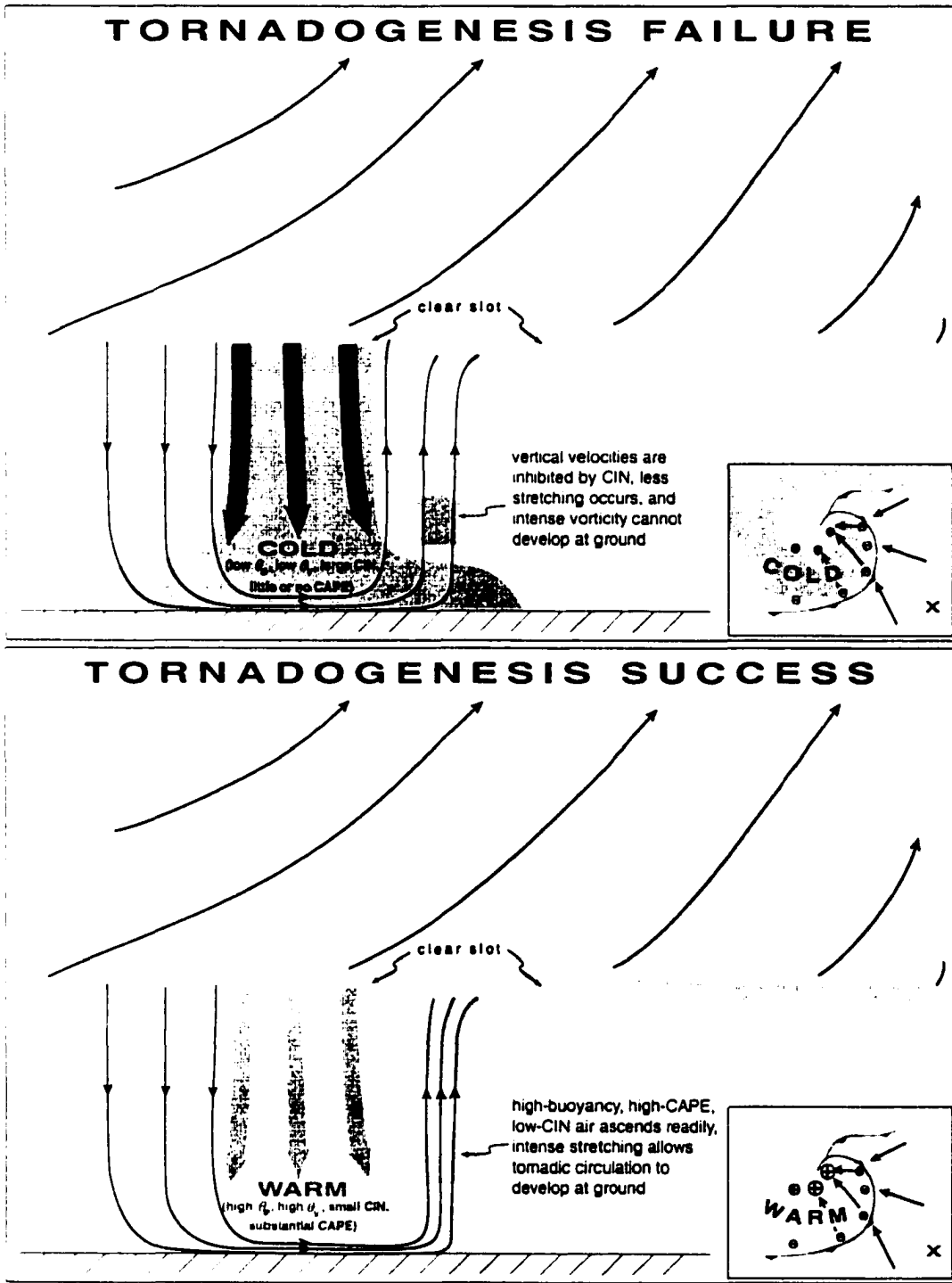


Figure 8.1 (continued).

not altered significantly by evaporation.¹ [This approach tacitly assumes that RFDs comprise at least some updraft air (with $CAPE > 0$) that is forced to descend as in the idealized numerical simulations. Observations of at least some surface-based CAPE in most of the RFDs analyzed (29/30) support this assumption. While the presence of surface-based CAPE in the RFD assures us that at least a portion of the mixture of air parcels that comprises the RFD has updraft origins, the absence of surface-based CAPE in the RFD does not preclude the presence of air parcels with updraft origins in the RFD.]

Similarly, the CIN at the ground within an RFD may be written as

$$CIN_{RFD} = CIN_{ENV} - \Lambda + \Upsilon, \quad (8.2)$$

where CIN_{RFD} is the CIN of the surface parcels within the RFD, CIN_{ENV} is the CIN measured in the large-scale storm environment (mainly a function of the θ_v of the inflow environment, and Λ and Υ represent sink and source terms, respectively. CIN, unlike CAPE, is affected by θ_v changes below the LFC even when θ_e is nearly conserved. Therefore, it seems plausible that a dry adiabatic descent and warming of RFD parcels could serve as an RFD_{CIN} sink (Λ). Furthermore, CIN_{RFD} sources (Υ) arise from processes that reduce the θ_v and θ_e of downdraft parcels: thus, *both* entrainment (lowers θ_e and possibly θ_v) and subcloud-layer evaporation (lowers θ_e) contribute to Υ . (Note that $CAPE_{RFD}$ largely is unaffected by subcloud-layer evaporation, yet CIN_{RFD} is increased by subcloud-layer evaporation.)

Let us also assume that there exists a critical (denoted by a subscript c) $CAPE_{RFD}$ and CIN_{RFD} , whereby if

$$CAPE_{RFD} > CAPE_{RFD_c}$$

and

$$CIN_{RFD} < CIN_{RFD_c},$$

¹Evaporation slightly increases θ_e (entropy), which may give rise to small CAPE increases. However, this effect has been neglected: therefore, no $CAPE_{RFD}$ source term appears in (8.1).

then tornadogenesis can occur. Therefore, tornadogenesis becomes more likely as $CAPE_{ENV}$ increases, CIN_{ENV} increases, Ψ decreases, Λ increases, and Υ decreases. If such thresholds such as $CAPE_{RFD_c}$ and CIN_{RFD_c} exist, then the thresholds likely would depend on individual storm characteristics, such as the dynamic vertical pressure gradient and interaction with the terrain, making such thresholds difficult to quantify.

Figs. 8.2 and 8.3 are an attempt to illustrate as concisely as possible how θ_e and θ_v , respectively, are modified within descending RFD parcels, and how these modifications ultimately affect values of $CAPE_{RFD}$ and CIN_{RFD} . Table 8.1 summarizes the effects of Ψ , Λ , and Υ .

In Fig. 8.2, if *environmental* air is forced to descend to the ground from point "A" (owing to the generation of negative buoyancy within the parcel), it may mix with updraft air en route, but the parcel reaches the surface with a large θ_e deficit. If an *updraft* parcel is forced to descend from point "B" (owing to a downward-directed non-hydrostatic pressure gradient or precipitation loading) and the descending parcel entrains a considerable amount of environmental air (low θ_e), then Ψ is large and the parcel reaches the ground with a large θ_e deficit. The value of $CAPE_{RFD}$ is small, and tornadogenesis is unlikely. On the other hand, if an updraft parcel is forced to descend from point "B" and the descending parcel does not entrain a significant amount of environmental air en route, then Ψ is small and the parcel arrives at the ground with only a small θ_e deficit. The value of $CAPE_{RFD}$ is large and tornadogenesis can occur.

In Fig. 8.3, if *environmental* air is forced to descend to the ground from point "A" (owing to the generation of negative buoyancy within the parcel), its density excess may amplify en route owing to continued evaporation and melting of condensate, and the parcel reaches the surface with a large θ_v deficit. If an *updraft* parcel is forced to descend from point "B" (owing to a downward-directed non-hydrostatic pressure gradient or precipitation loading), the parcel does not acquire a significant θ_v deficit unless it entrains subsaturated environmental air (allowing evaporation and melting of condensate to occur) or until it emerges from the saturated environment at cloud base (beneath which evaporation and melting of hydrometeors cause cooling within the parcel). If the subcloud relative humidity is large, Υ is >0 but relatively small, and CIN_{RFD} also is relatively small. If the subcloud relative humidity is

Variable	Description	Arises from
Ψ	CAPE_{RFD} sink	θ_e reduction owing to entrainment of low θ_e midlevel environmental air
Λ	CIN_{RFD} sink	net θ_e increase owing to pseudoadiabatic ascent followed by dry adiabatic descent of RFD parcels that have exhausted their condensate via evaporation/melting
Υ	CIN_{RFD} source	θ_e reduction owing to entrainment of subsaturated midlevel environmental air and subsequent evaporation/melting of condensate and/or evaporation/melting of condensate below cloud base (increases as boundary layer relative humidity decreases)

Table 8.1: Description of Ψ , Λ , and Υ .

small and/or the parcel has acquired a substantial θ_v deficit from entrainment of potentially cold midlevel air, then Υ is large and CIN_{RFD} also is large. If a parcel forced to descend from position “B” exhausts its condensate during the descent (owing to the irreversible nature of earlier ascent), then the parcel may reach the surface with a θ_e excess. Λ is >0 , and CIN_{RFD} is reduced. For small values of CIN_{RFD} , tornadogenesis is likely.

Because it has been shown observationally and numerically that tornadogenesis is more favored as CAPE_{RFD} (CIN_{RFD}) increases (decreases), the above framework implies that within large-scale environments containing large CAPE_{ENV} and small CIN_{ENV} values, a “sufficient” amount of CAPE_{RFD} ($>\text{CAPE}_{RFD_c}$) and a “surmountable” amount of CIN_{RFD} ($<\text{CIN}_{RFD_c}$) may be achieved despite substantial CAPE_{RFD} sinks and CIN_{RFD} sources. The words “sufficient” and “surmountable” deliberately are chosen to be ambiguous since the values of CAPE_{RFD_c} and CIN_{RFD_c} , if they indeed exist, are not known. For example, if large-scale CAPE is exceptionally large (e.g., $\text{CAPE}_{ENV} > 4000 \text{ J kg}^{-1}$), then CAPE_{RFD} still may be substantial despite relatively large surface θ_e deficits in the RFD. This may have been the case on 8 June 1995 in the RFD of the tornadic supercell near the Allison, Texas—surface parcels associated with θ_e deficits $>15 \text{ K}$ still were associated with positive CAPE_{RFD} . Moreover, in large-scale environments containing small CAPE_{ENV} or large CIN_{ENV} , only relatively small amounts of entrainment or evaporation could

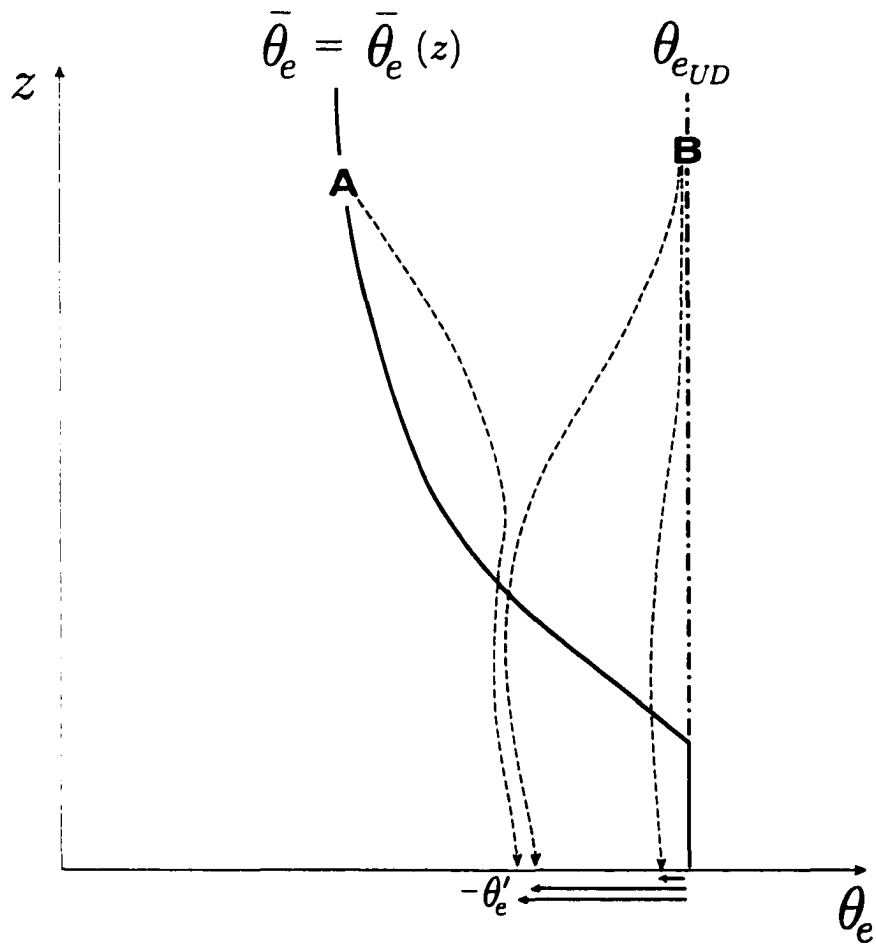


Figure 8.2: Schematic illustrating what controls surface θ_e values in the RFD. The base state (environmental) θ_e profile ($\bar{\theta}_e$) is drawn as a solid black line (nearly constant at low levels and typically decreases with height to midlevels). The θ_e within the updraft (θ_{eUD}) is nearly constant (and equal to the low-level θ_e value); this profile is indicated with a line of alternating dashes and dots. Dashed lines with arrows indicate possible parcel paths during descent (see text for discussion). The positions marked "A" and "B" are possible parcel origins (also see text for discussion).

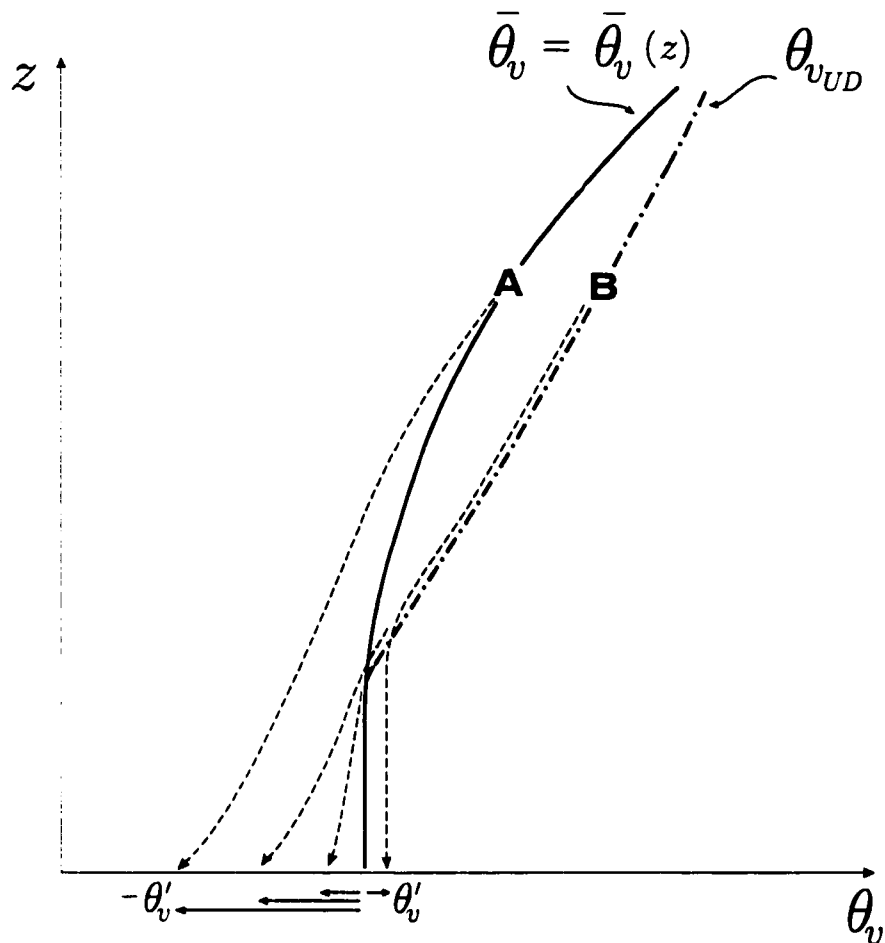


Figure 8.3: Schematic illustrating what controls surface θ_v values in the RFD. The base state (environmental) θ_v profile ($\bar{\theta}_v$) is drawn as a solid black line (nearly constant at low levels and increases with height above the boundary layer). The θ_v within the updraft (θ_{vUD}) exceeds $\bar{\theta}_v$ above the level of free convection: this profile is indicated with a line of alternating dashes and dots. Dashed lines with arrows indicate possible parcel paths during descent (see text for discussion). The positions marked "A" and "B" are possible parcel origins (also see text for discussion).

lead to $CAPE_{RFD}$ sink and CIN_{RFD} source terms (Ψ and Υ) large enough to result in zero $CAPE_{RFD}$ or very large CIN_{RFD} values.

In other words, if $CAPE_{ENV}$ (CIN_{ENV}) is large (small), Ψ (Υ) can become significant while preserving a “sufficient” (“surmountable”) amount of $CAPE_{RFD}$ (CIN_{RFD}) (it is hypothesized that when $\Psi \geq CAPE_{ENV}$, tornadogenesis cannot occur). On the other hand, when $CAPE_{ENV}$ (CIN_{ENV}) is small (large), then the amount of θ_e dilution (due to entrainment) and θ_v reduction (due to evaporation) within descending RFD parcels is more critical than when $CAPE_{ENV}$ (CIN_{ENV}) is large (small), because only a small reduction of θ_e and θ_v (associated with a decrease of $CAPE_{RFD}$ and an increase of CIN_{RFD}) within RFD parcels during their descent would render them unable to readily feed the incipient tornado, owing to values of $CAPE_{RFD} < CAPE_{RFD_c}$ or $CIN_{RFD} > CIN_{RFD_c}$. Is this the reason why forecasters tend to favor days on which environmental CAPE is large, and not because of the more direct relationship between CAPE and maximum updraft vertical velocity?

In tornadic supercell cases in which strong to violent tornadoes were spawned (e.g., 2 June 1995 at Friona, Texas; 8 June 1995 at Kellerville, Texas; 3 May 1999), $CAPE_{RFD}$ and CIN_{RFD} values often were observed to be nearly equal to the $CAPE_{ENV}$ and CIN_{ENV} values; thus, the terms Ψ and $\Upsilon - \Lambda$ were approximately zero. At the other extreme, in non-tornadic supercell cases, in which RFD_{CAPE} (RFD_{CIN}) values were relatively small (large), the terms Ψ and $\Upsilon - \Lambda$ generally ranged from 100–500 J kg⁻¹ and 150–800 J kg⁻¹, respectively.

8.4 Additional implications for operational meteorology

A plethora of studies have documented an association between tornadogenesis in supercells and preexisting mesoscale boundaries (e.g., Purdom 1976; Maddox et al. 1980; Weaver and Nelson 1982; Weaver and Purdom 1995; Markowski et al. 1998b; Atkins et al. 1999; Rasmussen et al. 2000). It is fair to ask how the results of this dissertation fit into the context of such earlier studies.

Markowski et al. (1998), Atkins et al. (1999), and Rasmussen et al. (2000) argued that the horizontal vorticity generated by preexisting boundaries was an important source of localized vorticity augmentation. Without such augmentation, supercells were more likely to be non-tornadic. In small-scale corridors where horizontal vorticity was enhanced by a preexisting boundary, tilting could produce significant vertical vorticity at a lower altitude than in regions where horizontal vorticity was not enhanced. In the simulations of the previous chapter, if the initial tangential wind field at low-levels had been increased, the imposed downdraft would have naturally transported larger amounts of angular momentum to the surface, resulting in the genesis of a more intense vortex.

But another possible favorable role of boundaries in tornadogenesis also may be inferred from the results of this dissertation. Low-level convergence commonly is associated with boundaries; thus, we might anticipate that boundary layer moisture would be locally deeper and have larger concentrations along boundaries. With the presence of enhanced moisture, it would be expected that cloud bases would lower. And the findings herein indicate that relatively warm and moist RFDs would be more likely to reach the surface in such environments, even if the environments are relatively small in horizontal scale. Thus, the importance of preexisting boundaries in tornadogenesis may be twofold: (1) to augment low-level horizontal vorticity and provide a stronger mesocyclone at low levels; and (2) to provide a region where boundary layer moisture depth and concentration are locally enhanced, and updraft bases are locally lowered (which may then favor RFDs that are suitable for tornadogenesis).

Lastly, it may be worth commenting on a recommendation for “storm spotters,” whose real-time, ground truthing, visual observations often are the only difference between the issuance of a tornado warning or no warning. Storm spotters often are positioned southeast of the updraft, which typically provides the best view (least obstructed by precipitation) of the updraft base. From this vantage, it is possible to observe cool, westerly outflow winds that could give the impression that the updraft has been undercut by stable air. While this certainly may be the case in many instances, it may be difficult to be confident of the thermodynamic “quality” of the air supplying the updraft nearer to the low-level mesocyclone center. In other words, on many occasions, cool, westerly outflow could be experienced 2-5 km east

or southeast of a rotating updraft base, yet a region of relatively warm, moist, and potentially unstable air could be present directly beneath the updraft base, followed shortly by significant tornadogenesis (Fig. 5.36). The 2 June 1995, 8 June 1995, 25 May 1997, 31 May 1999, and 2 June 1999 cases are just a few examples of storms that may have appeared to have been undercut by stable air from an observer situated a few km to the east or southeast; yet all were associated with tornadogenesis, with a few of the tornadoes being long-lived and violent. It is recommended that visual monitoring of the updraft base (for signs of increasing rotation) be maintained, even if apparently cool, westerly outflow air is detected east of the updraft. Furthermore, it may be possible for spotters to someday infer the buoyancy characteristics of RFD air based on the visual appearance of cloud fragments at the interface between the clear slot and updraft.²

²This idea was put forth by Mr. Al Moller at the Twentieth Conference on Severe Local Storms sponsored by the American Meteorological Society.

Chapter 9

Summary and conclusions

The objectives of this dissertation were twofold: (1) document the surface thermodynamic fields in the proximity of tornadic and non-tornadic low-level mesocyclones; (2) determine if differences exist at the surface in the hook echoes and RFDs of tornadic and non-tornadic supercells. Given the prior emphasis on the RFD in the tornadogenesis process and the apparent consensus that RFD air parcels enter the tornado, the study naturally was interested in the buoyancy and buoyancy gradients within hook echoes and RFDs – is there something thermodynamically special about RFDs associated with tornadoes compared to other thunderstorm downdrafts and RFDs associated with non-tornadic supercells?

Evidence was presented in support of the following conclusions:

1. RFDs associated with non-tornadic supercells are driven largely by evaporation and entrainment of potentially cold midlevel air.
2. Evaporative cooling and entrainment of midlevel potentially cold air play a smaller role in the forcing of RFDs associated with tornadic supercells compared to non-tornadic supercells.
3. Tornadogenesis is more likely as the surface buoyancy, potential buoyancy (CAPE), and equivalent potential temperature in the RFD increase, and as the CIN associated with RFD parcels at the surface decreases.
4. Tornado longevity and intensity increase as CAPE increases and CIN decreases in the surface RFD parcels.

5. The presence of a surface mesocyclone is not a sufficient condition for tornadogenesis.
6. Baroclinity at the surface within the hook echo is not a necessary condition for tornadogenesis.

The final five conclusions are more tentative:

7. Downward-directed non-hydrostatic pressure gradients and/or precipitation drag play a substantial role in the formation of RFDs associated with supercells that produce significant tornadoes.
8. The presence of surface-based convective available potential energy (CAPE) in the RFD is a necessary condition for tornadogenesis.
9. Most non-tornadic supercells contain mesocyclones at the surface.
10. The present upper-air network and even special sounding networks used during field experiments cannot resolve meteorologically significant differences in environmental hodographs, at least in terms of popular derived storm-relative flow or vertical shear parameters, that are associated with RFDs that reach the surface either relatively warm or cold. If systematic hodograph differences do exist between tornadic and non-tornadic supercell environments, these differences probably cannot be detected reliably in most cases.
11. The ambient relative humidity profile, at least at low levels, plays a role in determining how cold an RFD will be upon reaching the surface; environments characterized by high boundary layer relative humidity (and low cloud base) are more conducive to RFDs associated with relatively high buoyancy than environments characterized by low boundary layer relative humidity (and high cloud base).

It should be emphasized that while relatively warm, moist, and potentially buoyant RFD air parcels appear to be necessary for the genesis of significant tornadoes, this condition is not sufficient for tornadogenesis. Additional factors are almost

certainly important (e.g., surface roughness, the effects of which cannot be studied observationally at the present time and can only be crudely parameterized in numerical simulations).

It is worth reiterating some of the limitations of this research. The time evolution of features is difficult to document. In most instances, all that can be obtained are snapshots of the hook echo and RFD region at various times from case to case (in some cases, the RFD is sampled near tornadogenesis; at other times, during the mature phase of a tornado; and at other times, during tornado demise). One case by itself probably offers little, but the ensemble of snapshots from different times relative to tornadogenesis from a variety of cases hopefully has led to new understanding. Furthermore, steady-state assumptions (as long as a few minutes) must unavoidably be made during the data analysis. Another limitation is that thermodynamic fields and their gradients cannot be ascertained above the surface by direct means. Moreover, we should be cautious when drawing conclusions based on analyses made near the time of tornadogenesis or failure—the time histories of air parcels are important, possibly as long as 30 min prior to tornadogenesis. It is not possible to compute trajectories at the surface using direct observations over 30 min intervals owing to observation density.

In the future we may have a means of obtaining direct observations from above the ground (e.g., rockets, unmanned aircraft). Furthermore, the existence of differences between the RFDs of tornadic and non-tornadic supercells, in terms of their surface buoyancy characteristics, suggest that microphysical aspects of tornadic and non-tornadic supercells also are likely to be different; thus, observations of microphysics-related variables in supercells probably are well worth exploring. Perhaps we may determine whether there is a unique character to the concentration and species of hydrometeors within the hook echo that is associated with a unique type of RFD capable of supporting tornado formation. Possibly the most critical question remaining unanswered is this—how does the RFD form?

References

- Adlerman, E. J., K. K. Droegemeier, and R. P. Davies-Jones. 1999: A numerical simulation of cyclic mesocyclogenesis. *J. Atmos. Sci.* **56**, 2045–2069.
- Alberty, R. L., 1969: A proposed mechanism for cumulonimbus persistence in the presence of strong vertical shear. *Mon. Wea. Rev.*, **97**, 590–596.
- Arakawa, A., and V. Lamb, 1981: A potential enstrophy and energy conserving scheme for the shallow water equations. *Mon. Wea. Rev.*, **109**, 18–36.
- Atkins, N. T., M. L. Weisman, and L. J. Wicker. 1999: The influence of preexisting boundaries on supercell evolution. *Mon. Wea. Rev.*, **127**, 2910–2927.
- Barnes, S. L., 1964: A technique for maximizing details in numerical weather map analysis. *J. Appl. Meteor.*, **3**, 396–409.
- Barnes, S. L., 1968: On the source of thunderstorm rotation. National Severe Storms Laboratory, Tech. Memo. ERLTM-NSSL 38, 38 pp.
- Barnes, S. L., 1970: Some aspects of a severe, right-moving thunderstorm deduced from mesonet network rawinsonde observations. *J. Atmos. Sci.*, **27**, 634–648.
- Barnes, S. L., 1978a: Oklahoma thunderstorms on 29–30 April 1970. Part I: Morphology of a tornadic storm. *Mon. Wea. Rev.*, **106**, 673–684.
- Barnes, S. L., 1978b: Oklahoma thunderstorms on 29–30 April 1970. Part II: Radar-observed merger of twin hook echoes. *Mon. Wea. Rev.*, **106**, 685–696.
- Beebe, R. G., 1959: Notes on the Scottsbluff, Nebraska tornado, 27 June 1955. *Bull. Amer. Meteor. Soc.*, **40**, 109–116.
- Blanchard, D. O., and R. E. Lopez, 1985: Spatial patterns of convection in South Florida. *Mon. Wea. Rev.*, **113**, 1282–1299.
- Blanchard, D. O., and J. M. Straka, 1998: Some possible mechanisms for tornadogenesis failure in a supercell. Preprints, *Nineteenth Conf. on Severe Local Storms*, Minneapolis, Amer. Meteor. Soc., 116–119.

- Bluestein, H. B., 1983: Surface meteorological observations in severe thunderstorms. Part II: Field experiments with TOTO. *J. Clim. Appl. Meteorol.*, **22**, 919-930.
- Bluestein, H. B., and J. H. Golden, 1993: A review of tornado observations. *The Tornado: Its Structure, Dynamics, Prediction, and Hazards*, Geophys. Monogr., No. 79, Amer. Geophys. Union, 319-352.
- Bluestein, H. B., W. P. Unruh, D. C. Dowell, T. A. Hutchinson, T. M. Crawford, A. C. Wood, and H. Stein, 1997a: Doppler radar analysis of the Northfield, Texas, Tornado of 25 May 1994. *Mon. Wea. Rev.*, **125**, 212-230.
- Bluestein, H. B., S. G. Gaddy, D. C. Dowell, A. L. Pazmany, J. C. Galloway, R. E. McIntosh, and H. Stein, 1997b: Doppler radar observations of substorm-scale vortices in a supercell. *Mon. Wea. Rev.*, **125**, 1046-1059.
- Bohren, C. F., and B. A. Albrecht, 1998: *Atmospheric Thermodynamics*. Oxford University Press, 402 pp.
- Bolton, D., 1980: The computation of equivalent potential temperature. *Mon. Wea. Rev.*, **108**, 1046-1053.
- Bonesteele, R. G., and Y. J. Lin, 1978: A study of updraft-downdraft interaction based on perturbation pressure and single-Doppler radar data. *Mon. Wea. Rev.*, **105**, 113-120.
- Brandes, E. A., 1977a: Flow in a severe thunderstorm observed by dual-Doppler radar. *Mon. Wea. Rev.*, **105**, 113-120.
- Brandes, E. A., 1977b: Gust front evolution and tornado genesis as viewed by Doppler radar. *J. Appl. Meteor.*, **19**, 333-338.
- Brandes, E. A., 1978: Mesocyclone evolution and tornadogenesis: Some observations. *Mon. Wea. Rev.*, **106**, 995-1011.
- Brandes, E. A., 1981: Finestructure of the Del City-Edmond tornadic mesocirculation. *Mon. Wea. Rev.*, **109**, 635-647.
- Brandes, E. A., 1984a: Relationships between radar-derived thermodynamic variables and tornadogenesis. *Mon. Wea. Rev.*, **112**, 1033-1052.
- Brandes, E. A., 1984b: Vertical vorticity generation and mesocyclone sustenance in tornadic thunderstorms: The observational evidence. *Mon. Wea. Rev.*, **112**, 2253-2269.

- Brandes, E. A., 1993: Tornadic thunderstorm characteristics determined with Doppler radar. *The Tornado: Its Structure, Dynamics, Prediction, and Hazards*, Geophys. Monogr., No. 79, Amer. Geophys. Union, 143-159.
- Brandes, E. A., R. P. Davies-Jones, and B. C. Johnson, 1988: Streamwise vorticity effects on supercell morphology and persistence. *J. Atmos. Sci.*, **45**, 947-963.
- Brock, F. V., K. Crawford, R. Elliot, G. Cupernus, S. Stadler, H. Johnson, and M. Eilts, 1995: The Oklahoma Mesonet: A technical overview. *J. Atmos. Oceanic Technol.*, **12**, 5-19.
- Brooks, E. M., 1949: The tornado cyclone. *Weatherwise*, **2**, 32-33.
- Brooks, H. E., C. A. Doswell III, and R. P. Davies-Jones, 1993: Environmental helicity and the maintenance and evolution of low-level mesocyclones. *The Tornado: Its Structure, Dynamics, Prediction, and Hazards*, Geophys. Monogr., No. 79, Amer. Geophys. Union, 97-104.
- Brooks, H. E., C. A. Doswell, and R. B. Wilhelmson, 1994a: The role of midtropospheric winds in the evolution and maintenance of low-level mesocyclones. *Mon. Wea. Rev.*, **122**, 126-136.
- Brooks, H. E., C. A. Doswell, and J. Cooper, 1994b: On the environments of tornadic and nontornadic mesocyclones. *Wea. Forecasting*, **9**, 606-618.
- Brown, R. A., 1992: Initiation and evolution of updraft rotation within an incipient supercell thunderstorm. *J. Atmos. Sci.*, **49**, 1997-2014.
- Brown, R. A., D. W. Burgess, and K. C. Crawford, 1973: Twin tornado cyclones within a severe thunderstorm: Single-Doppler radar observations. *Weatherwise*, **26**, 63-71.
- Brown, R. A., L. R. Lemon, and D. W. Burgess, 1978: Tornado detection with pulsed Doppler radar. *Mon. Wea. Rev.*, **106**, 29-38.
- Brown, J. M., and K. R. Knupp, 1980: The Iowa cyclonic-anticyclonic tornado pair and its parent thunderstorm. *Mon. Wea. Rev.*, **108**, 1626-1646.
- Browning, K. A., 1964: Airflow and precipitation trajectories within severe local storms which travel to the right of the winds. *J. Atmos. Sci.*, **21**, 634-639.
- Browning, K. A., 1965a: Some inferences about the updraft within a severe local storm. *J. Atmos. Sci.*, **22**, 669-678.
- Browning, K. A., 1965b: The evolution of tornadic storms. *J. Atmos. Sci.*, **22**, 664-668.

- Browning, K. A., 1968: The organization of severe local storms. *Weather*, **23**, 429-434.
- Browning, K. A., and F. H. Ludlam, 1962: Airflow in convective storms. *Quart. J. Roy. Meteor. Soc.*, **88**, 117-135.
- Browning, K. A., and R. J. Donaldson, 1963: Airflow and structure of a tornadic storm. *J. Atmos. Sci.*, **20**, 533-545.
- Burgess, D. W., R. A. Brown, L. R. Lemon, and C. R. Safford, 1977: Evolution of a tornadic thunderstorm. Preprints, *Tenth Conf. on Severe Local Storms*, Omaha, Amer. Meteor. Soc., 84-89.
- Byers, H. R., and R. P. Braham, 1949: *The Thunderstorm*. U. S. Government Printing Office, Washington, D. C., 287 pp.
- Carbone, R. E., 1983: A severe frontal rainband. Part II: Tornado parent vortex circulation. *Mon. Wea. Rev.*, **111**, 2639-2654.
- Charba, J., and Y. Sasaki, 1971: Structure and movement of the severe thunderstorms of 3 April 1964 as revealed from radar and surface mesonet network data analysis. *J. Meteor. Soc. Japan*, **49**, 191-214.
- Chisholm, A. J., 1973: Alberta hailstorms. Part I: Radar case studies and airflow models. *Meteor. Monogr.*, **14**, Boston, Amer. Meteor. Soc., 1-36.
- Clark, T. L., 1973: Numerical modeling of the dynamics and microphysics of warm cumulus convection. *J. Atmos. Sci.*, **30**, 857-878.
- Clark, T. L., and R. List, 1971: Dynamics of a falling particle zone. *J. Atmos. Sci.*, **28**, 718-727.
- Darkow, G. L., 1969: An analysis of over sixty tornado proximity soundings. Preprints, *Sixth Conf. on Severe Local Storms*, Chicago, Amer. Meteor. Soc., 218-221.
- Darkow, G. L., and D. W. McCann, 1977: Relative environmental winds for 121 tornado bearing storms. Preprints, *Tenth Conf. on Severe Local Storms*, Omaha, Amer. Meteor. Soc., 413-417.
- Das, P., 1983: Vorticity concentration in the subcloud layers of a rotating cloud. National Science Foundation Final Report (ATM-8023825), 78 pp. [Available from NSF.]
- Daugherty, J. R., A. I. Watson, T. R. Shepherd, and C. L. Ziegler, 1996: The evolution of tornadic supercells during VORTEX-95 as observed by the NOAA P-3 lower-fuselage C-band radar. Preprints, *Eighteenth Conf. on Severe Local Storms*, San Francisco, Amer. Meteor. Soc., 128-132.

- Davies, J. M., and R. H. Johns, 1993: Some wind and instability parameters associated with strong and violent tornadoes. 1. Wind shear and helicity. *The Tornado: Its Structure, Dynamics, Prediction, and Hazards, Geophys. Monogr.*, No. 79. Amer. Geophys. Union, 573–582.
- Davies-Jones, R. P., 1982a: A new look at the vorticity equation with application to tornadogenesis. Preprints, *Twelfth Conf. on Severe Local Storms*, San Antonio. Amer. Meteor. Soc., 249–252.
- Davies-Jones, R. P., 1982b: Observational and theoretical aspects of tornadogenesis. *Intense Atmospheric Vortices*. L. Bengtsson and J. Lighthill, Editors. Springer-Verlag, 175–189.
- Davies-Jones, R. P., 1984: Streamwise vorticity: The origin of updraft rotation in supercell storms. *J. Atmos. Sci.*, **41**, 2991–3006.
- Davies-Jones, R. P., 1985: Dynamical interaction between an isolated convective cell and a veering environmental wind. *Preprints, Seventeenth Conf. on Severe Local Storms*, St. Louis. Amer. Meteor. Soc., 216–219.
- Davies-Jones, R. P., 1986: Tornado dynamics. *Thunderstorm Morphology and Dynamics*, 2nd ed., E. Kessler, Editor, University of Oklahoma Press, 197–236.
- Davies-Jones, R. P., 1996: Inclusion of boundary conditions on pressure in conceptual models of updraft-environment interaction. Preprints, *Eighteenth Conf. on Severe Local Storms*, San Francisco. Amer. Meteor. Soc., 713–717.
- Davies-Jones, R. P., 1998: Tornadoes and tornadic storms. Preprints, *Nineteenth Conf. on Severe Local Storms*, Minneapolis. Amer. Meteor. Soc., 185.
- Davies-Jones, R. P., 2000: A Lagrangian model for baroclinic genesis of mesoscale vortices. Part I: Theory. *J. Atmos. Sci.*, **57**, 715–736.
- Davies-Jones, R. P., and H.E. Brooks, 1993: Mesocyclogenesis from a theoretical perspective. *The Tornado: Its Structure, Dynamics, Prediction, and Hazards*. Geophys. Monogr., No. 79. Amer. Geophys. Union, 105–114.
- Davies-Jones, R. P., C. A. Doswell, and H. E. Brooks, 1994: Comments on “Initiation and evolution of updraft rotation within an incipient supercell thunderstorm.” *J. Atmos. Sci.*, **51**, 326–331.
- Deardorff, J. W., 1972: Numerical investigation of neutral and unstable planetary boundary layers. *J. Atmos. Sci.*, **29**, 91–115.
- Donaldson, R. J., 1970: Vortex signature recognition by a Doppler radar. *J. Appl. Meteor.*, **9**, 661–670.

- Doswell, C. A., 1985: *The operational meteorology of convective weather. Vol. 2: Storm scale analysis*. NOAA Tech. Memo. ERL ESG-15, 240 pp.
- Doswell, C. A., and D. W. Burgess, 1993: Tornadoes and tornadic storms: A review of conceptual models. *The Tornado: Its Structure, Dynamics, Prediction, and Hazards*. Geophys. Monogr., No. 79, Amer. Geophys. Union, 161-172.
- Dowell, D. C., and H. B. Bluestein, 1997: The Arcadia, Oklahoma, storm of 17 May 1981: Analysis of a supercell during tornadogenesis. *Mon. Wea. Rev.*, **125**, 2562-2582.
- Emanuel, K. A., 1994: *Atmospheric Convection*. Oxford University Press, 580 pp.
- Eskridge, R. E., and P. Das, 1976: Effect of a precipitation-driven downdraft on a rotating wind field: A possible trigger mechanism for tornadoes? *J. Atmos. Sci.*, **33**, 70-84.
- Fankhauser, J. C., 1971: Thunderstorm environment interactions determined from aircraft and radar observations. *Mon. Wea. Rev.*, **99**, 171-192.
- Fiedler, B. H., 1993: Numerical simulation of axisymmetric tornadogenesis in forced convection. *The Tornado: Its Structure, Dynamics, Prediction, and Hazards*. Geophys. Monogr., No. 79, Amer. Geophys. Union, 41-48.
- Forbes, G. S., 1975: Relationship between tornadoes and hook echoes on April 3, 1974. Preprints. *Ninth Conf. on Severe Local Storms*, Norman, Amer. Meteor. Soc., 280-285.
- Forbes, G. S., 1978: Three scales of motion associated with tornadoes. Nuclear Regulatory Commission report CR-0363, 359 pp. [NTIS No. PB288291].
- Forbes, G. S., 1981: On the reliability of hook echoes as tornado indicators. *Mon. Wea. Rev.*, **109**, 1457-1466.
- Freund, R. F., 1966: Radar echo signature of tornadoes. Preprints, *Twelfth Conf. on Radar Meteorology*, Norman, Amer. Meteor. Soc., 362-365.
- Fujita, T. T., 1955: Results of detailed synoptic studies of squall lines. *Tellus*, **4**, 405-436.
- Fujita, T. T., 1958a: Mesoanalysis of the Illinois tornadoes of 9 April 1953. *J. Meteor.*, **15**, 288-296.
- Fujita, T. T., 1958b: Tornado cyclone: Bearing system of tornadoes. *Proceedings of the Seventh Conf. on Radar Meteorology*, Miami Beach, Amer. Meteor. Soc., K31-K38.

- Fujita, T. T., 1965: Formation and steering mechanisms of tornado cyclones and associated hook echoes. *Mon. Wea. Rev.*, **93**, 67-78.
- Fujita, T. T., 1973: Proposed mechanism of tornado formation from rotating thunderstorms. Preprints, *Eighth Conf. on Severe Local Storms*, Denver, Amer. Meteor. Soc., 191-196.
- Fujita, T. T., 1974a: Overshooting thunderheads observed from ATS and Lear Jet. SMRP Research Paper 117A, University of Chicago, 29 pp.
- Fujita, T. T., 1974b: Overshooting tops of severe thunderstorms revealed by Lear Jet, satellite, and radar observations. SMRP Research Paper 117B, University of Chicago, 48 pp.
- Fujita, T. T., 1975a: Color map of super outbreak tornadoes of 3-4 April 1974. *Weatherwise*, **28**, 55.
- Fujita, T. T., 1975b: New evidence from the April 3-4, 1974 tornadoes. Preprints, *Ninth Conf. on Severe Local Storms*, Norman, Amer. Meteor. Soc., 248-255.
- Fujita, T. T., 1979: Objectives, operation, and results of Project NIMROD. Preprints, *Eleventh Conf. on Severe Local Storms*, Kansas City, Amer. Meteor. Soc., 259-266.
- Fujita, T. T., 1981: Tornadoes and downbursts in the context of generalized planetary scales. *J. Atmos. Sci.*, **38**, 1511-1534.
- Fujita, T. T., and H. Grandoso, 1968: Split of a thunderstorm into anticyclonic and cyclonic storms and their motion as determined by numerical model experiments. *J. Atmos. Sci.*, **25**, 416-439.
- Fujita, T. T., and R. M. Wakimoto, 1982: Anticyclonic tornadoes in 1980 and 1981. Preprints, *Twelfth Conf. on Severe Local Storms*, San Antonio, Amer. Meteor. Soc., 213-216.
- Fulks, J. R., 1962: *On the Mechanics of the Tornado*. National Severe Storms Project Report No. 4, U. S. Weather Bureau.
- Gaddy, S. G., and H. B. Bluestein, 1998: Airborne dual-Doppler analysis of a supercell hailstorm. Preprints, *Nineteenth Conf. on Severe Local Storms*, Minneapolis, Amer. Meteor. Soc., 60-63.
- Gal-Chen, T., 1978: A method for the initialization of the anelastic equations: Implications for matching models with observations. *Mon. Wea. Rev.*, **106**, 587-606.

- Garrett, R. A., and V. D. Rockney, 1962: Tornadoes in northeastern Kansas, May 19, 1960. *Mon. Wea. Rev.*, **90**, 231-240.
- Gilmore, M. S., and L. J. Wicker, 1998: The influence of midtropospheric dryness on supercell morphology and evolution. *Mon. Wea. Rev.*, **126**, 943-958.
- Golden, J. H., 1974: Scale interaction implications for the waterspout life cycle. Part II. *J. Appl. Meteor.*, **13**, 693-709.
- Golden, J. H., and B. J. Morgan, 1972: The NSSL/Notre Dame tornado intercept program, spring 1972. *Bull. Amer. Meteor. Soc.*, **53**, 1178-1179.
- Golden, J. H., and D. Purcell, 1978: Airflow characteristics around the Union City tornado. *Mon. Wea. Rev.*, **106**, 22-28.
- Haglund, G. T., 1969: A study of the severe local storm of 16 April 1967. ESSA Tech. Memo. ERLTM-NSSL 44, 54 pp. [NTIS No. PB188315].
- Hane, C. E., R. B. Wilhelmson, and T. Gal-Chen, 1981: Retrieval of thermodynamic variables within deep convective clouds: Experiments in three dimensions. *Mon. Wea. Rev.*, **109**, 564-576.
- Hane, C. E., and P. S. Ray, 1985: Pressure and buoyancy fields derived from Doppler radar data in a tornadic thunderstorm. *J. Atmos. Sci.*, **42**, 18-35.
- Heymsfield, G. M., 1978: Kinematic and dynamic aspects of the Harrah tornadic storm analyzed from dual-Doppler radar data. *Mon. Wea. Rev.*, **106**, 233-254.
- Hoecker, W. H., 1961: Wind speed and air flow patterns in the Dallas tornado of April 2, 1957. *Mon. Wea. Rev.*, **88**, 167-180.
- Hoecker, W. H., 1961: Three-dimensional pressure pattern of the Dallas tornado and some resultant implications. *Mon. Wea. Rev.*, **89**, 533-542.
- Hookings, G. A., 1964: Precipitation-maintained downdrafts. *J. Appl. Meteor.*, **4**, 190-195.
- Houze, R. A., 1993: *Cloud Dynamics*. Academic Press, 573 pp.
- Houze, R. A., W. Schmid, R. G. Fovell, and H.-H. Schiesser, 1993: Hailstorms in Switzerland: Left movers, right movers, and false hooks. *Mon. Wea. Rev.*, **124**, 3345-3370.
- Howells, P. A., R. Rotunno, and R. K. Smith, 1988: A comparative study of atmospheric and laboratory-analogue numerical tornado-vortex models. *Quart. J. Roy. Meteor. Soc.*, **114**, 801-822.

- Jensen, B., T. P. Marshall, M. A. Mabey, and E. N. Rasmussen, 1983: Storm scale structure of the Pampa storm. Preprints, *Thirteenth Conf. on Severe Local Storms*, Tulsa, Amer. Meteor. Soc., 85-88.
- Johnson, K. W., P. S. Ray, B. C. Johnson, and R. P. Davies-Jones, 1987: Observations related to the rotational dynamics of the 20 May 1977 tornadic storms. *Mon. Wea. Rev.*, **115**, 2463-2478.
- Jorgensen, D. P., P. H. Hildebrand, and C. L. Frush, 1983: Feasibility test of an airborne pulse-Doppler meteorological radar. *J. Clim. Appl. Meteor.*, **22**, 744-757.
- Kamburova, P. L., and F. H. Ludlam, 1966: Rainfall evaporation in thunderstorm downdrafts. *Quart. J. Roy. Meteor. Soc.*, **92**, 510-518.
- Kerr, B. W., and G. L. Darkow, 1996: Storm-relative winds and helicity in the tornadic thunderstorm environment. *Wea. Forecasting*, **11**, 489-505.
- Kessler, E., 1969: On the distribution and continuity of water substance in atmospheric circulations. *Meteor. Monogr.*, **10**, No. 32, 84 pp.
- Klemp, J. B., 1987: Dynamics of tornadic thunderstorms. *Ann. Rev. Fluid Mech.*, **19**, 369-402.
- Klemp, J. B., and R. B. Wilhelmson, 1978a: Simulations of right- and left-moving storms produced through storm splitting. *J. Atmos. Sci.*, **35**, 1097-1110.
- Klemp, J. B., and R. B. Wilhelmson, 1978b: The simulation of three-dimensional convective storm dynamics. *J. Atmos. Sci.*, **35**, 1070-1096.
- Klemp, J. B., R. B. Wilhelmson, and P. S. Ray, 1981: Observed and numerically simulated structure of a mature supercell thunderstorm. *J. Atmos. Sci.*, **38**, 1558-1580.
- Klemp, J. B., and R. Rotunno, 1983: A study of the tornadic region within a supercell thunderstorm. *J. Atmos. Sci.*, **40**, 359-377.
- Koch, S. E., M. DesJardins, and P. J. Kocin, 1983: An interactive Barnes objective map analysis scheme for use with satellite and conventional data. *J. Clim. Appl. Meteor.*, **22**, 1487-1503.
- Kundu, P. K., 1990: Fluid Mechanics. *Academic Press*, 638 pp.
- LaDue, J. G., 1993: Vortex formation from a helical inflow tornado vortex simulator. *The Tornado: Its Structure, Dynamics, Prediction, and Hazards*, Geophys. Monogr., No. 79, Amer. Geophys. Union, 105-114.

- Lemon, L. R., 1974: Interaction of two convective scales within a severe thunderstorm: A case study. NOAA Tech. Memo. ERL-NSSL, 71, 43 pp. [NTIS No. COM-74-11642/AS].
- Lemon, L. R., 1976a: The flanking line, a severe thunderstorm intensification source. *J. Atmos. Sci.*, **33**, 686-694.
- Lemon, L. R., 1976b: Wake vortex structure and aerodynamic origin in severe thunderstorms. *J. Atmos. Sci.*, **33**, 678-685.
- Lemon, L. R., 1977: Severe thunderstorm evolution: Its use in a new technique for radar warnings. Preprints, *Tenth Conf. on Severe Local Storms*, Omaha, Amer. Meteor. Soc., 77-83.
- Lemon, L. R., 1982: New severe thunderstorm radar identification techniques and warning criteria: A preliminary report. NOAA Tech. Memo. NWS NSSFC-1, 60 pp. [NTIS No. PB-273049].
- Lemon, L. R., D. W. Burgess, and R. A. Brown, 1975: Tornado production and storm sustenance. Preprints, *Ninth Conf. on Severe Local Storms*, Norman, Amer. Meteor. Soc., 100-104.
- Lemon, L. R., and D. W. Burgess, 1976: Tornadic storm airflow and morphology derived from single Doppler radar measurements. Chapter 8, *The Union City, Oklahoma Tornado of 24 May 1973*, R. A. Brown, Editor. NOAA Tech. Memo. ERL-80, Norman, National Severe Storms Laboratory, 85-106.
- Lemon, L. R., D. W. Burgess, and R. A. Brown, 1978: Tornadic thunderstorm airflow and morphology derived from single Doppler radar measurements. *Mon. Wea. Rev.*, **106**, 48-61.
- Lemon, L. R., and C. A. Doswell, 1979: Severe thunderstorm evolution and mesocyclone structure as related to tornadogenesis. *Mon. Wea. Rev.*, **107**, 1184-1197.
- Leslie, L. M., and R. K. Smith, 1978: The effect of vertical stability on tornadogenesis. *J. Atmos. Sci.*, **35**, 1281-1288.
- Lilly, D. K., 1982: The development and maintenance of rotation in convective storms. *Intense Atmospheric Vortices*, L. Bengtsson and J. Lighthill, Editors. Springer-Verlag, 149-160.
- Lilly, D. K., 1986a: The structure, energetics, and propagation of rotating convective storms. Part I: Energy exchange with the mean flow. *J. Atmos. Sci.*, **43**, 113-125.

- Lilly, D. K., 1986b: The structure, energetics, and propagation of rotating convective storms. Part II: Helicity and storm stabilization. *J. Atmos. Sci.*, **43**, 126-140.
- Ludlam, F. H., 1963: *Severe Local Storms: A review*. *Meteor. Monogr.*, No. 27, 1-30.
- Maddox, R. A., 1976: An evaluation of tornado proximity wind and stability data. *Mon. Wea. Rev.*, **104**, 133-142.
- Maddox, R. A., L. R. Hoxit, and C. F. Chappell, 1980: A study of tornadic thunderstorm interactions with thermal boundaries. *Mon. Wea. Rev.*, **108**, 322-336.
- Markowski, P. M., J. M. Straka, and E. N. Rasmussen, 1998a: A preliminary investigation of the importance of helicity 'location' in the hodograph. Preprints, *Nineteenth Conf. on Severe Local Storms*, Minneapolis, Amer. Meteor. Soc., 230-233.
- Markowski, P. M., E. N. Rasmussen, and J. M. Straka, 1998b: The occurrence of tornadoes in supercells interacting with boundaries during VORTEX-95. *Wea. Forecasting*, **13**, 852-859.
- Markowski, P. M., J. M. Straka, E. N. Rasmussen, and D. O. Blanchard, 1998c: Variability of storm-relative helicity during VORTEX. *Mon. Wea. Rev.*, **126**, 2942-2958.
- Markowski, P. M., E. N. Rasmussen, J. M. Straka, and D. C. Dowell, 1998d: Observations of low-level baroclinity generated by anvil shadows. *Mon. Wea. Rev.*, **126**, 2942-2958.
- Marshall, J. S., and W. M. Palmer, 1948: The distribution of raindrops with size. *J. Meteor.*, **5**, 165-166.
- Marshall, T. P., and E. N. Rasmussen, 1982: The mesocyclone evolution of the Warren, Oklahoma tornadoes. Preprints, *Twelfth Conf. on Severe Local Storms*, San Antonio, Amer. Meteor. Soc., 375-378.
- Marwitz, J. D., 1972a: The structure and motion of severe hailstorms. Part I: Supercell storms. *J. Appl. Meteor.*, **11**, 166-179.
- Marwitz, J. D., 1972b: The structure and motion of severe hailstorms. Part II: Multicell storms. *J. Appl. Meteor.*, **11**, 180-188.
- Marwitz, J. D., 1972c: The structure and motion of severe hailstorms. Part III: Severely sheared storms. *J. Appl. Meteor.*, **11**, 189-201.

- McCaul, E. W., and M. L. Weisman, 1996: Simulations of shallow supercell storms in landfalling hurricane environments. *Mon. Wea. Rev.*, **124**, 408–429.
- McCaul, E. W., and M. L. Weisman, 2001: The sensitivity of simulated supercell structure and intensity to variations in the shapes of environmental buoyancy and shear profiles. *Mon. Wea. Rev.*, **129**, in press.
- Mielke, P. W., K. J. Berry, and E. S. Johnson, 1976: Multi-response permutation procedures for a priori classifications. *Commun. Stat. Theor. Meth.*, **A5**, 1409–1424.
- Mielke, P. W., K. J. Berry, and G. W. Brier, 1981: Application of multi-response permutation procedures for examining seasonal changes in monthly mean sea-level pressure patterns. *Mon. Wea. Rev.*, **109**, 120–126.
- Moller, A., C. A. Doswell, J. McGinley, S. Tegtmeier, and R. Zipser, 1974: Field observations of the Union City tornado in Oklahoma. *Weatherwise*, **27**, 68–77.
- Nelson, S. P., 1977: Rear flank downdraft: A hailstorm intensification mechanism. Preprints, *Tenth Conf. on Severe Local Storms*, Omaha, Amer. Meteor. Soc., 521–525.
- Newton, C. W., and H. R. Newton, 1959: Dynamical interactions between large convective clouds and environmental vertical shear. *J. Meteor.*, **16**, 483–496.
- Ogura, Y., 1963: The evolution of a moist convective element in a shallow, conditionally unstable atmosphere: A numerical calculation. *J. Atmos. Sci.*, **20**, 407–424.
- Peterson, R. E., 1976: The Sunray tornado. *Bull. Amer. Meteor. Soc.*, **57**, 805–807.
- Purdum, J.F.W., 1976: Some uses of high resolution GOES imagery in the mesoscale forecasting of convection and its behavior. *Mon. Wea. Rev.*, **104**, 1474–1483.
- Rasmussen, E. N., R. E. Peterson, J. E. Minor, and B. D. Campbell, 1982: Evolutionary characteristics and photogrammetric determination of windspeeds within the Tulia outbreak tornadoes 28 May 1980. Preprints, *Twelfth Conf. on Severe Local Storms*, San Antonio, Amer. Meteor. Soc., 301–304.
- Rasmussen, E. N., J. M. Straka, R. P. Davies-Jones, C. A. Doswell, F. H. Carr, M. D. Eilts, and D. R. MacGorman, 1994: Verification of the Origins of Rotation in Tornadoes Experiment: VORTEX. *Bull. Amer. Meteor. Soc.*, **75**, 995–1006.
- Rasmussen, E. N., and J. M. Straka, 1996: Mobile mesonet observations of tornadoes during VORTEX-95. Preprints, *Eighteenth Conf. on Severe Local Storms*, San Francisco, Amer. Meteor. Soc., 1–5.

- Rasmussen, E. N., and J. M. Straka, 1997: Tornadogenesis: A review and a new conceptual model. Submitted to *Mon. Wea. Rev.* Manuscript available from P. Markowski.
- Rasmussen, E. N., and D. O. Blanchard, 1998: A baseline climatology of sounding-derived supercell and tornado forecast parameters. *Wea. Forecasting*, **13**, 1148–1164.
- Rasmussen, E. N., and J. M. Straka, 1998: Variations in supercell morphology. Part I: Observations of the role of upper level storm-relative flow. *Mon. Wea. Rev.*, **126**, 2106–2121.
- Rasmussen, E. N., S. J. Richardson, J. M. Straka, P. M. Markowski, and D. O. Blanchard, 2000: The association of significant tornadoes with a baroclinic boundary on 2 June 1995. *Mon. Wea. Rev.*, **128**, 174–191.
- Rasmussen, E. N., and J. M. Straka, 2001: The Dimmitt, Texas tornadic storm of 2 June 1995: Tornadogenesis. Submitted to *Mon. Wea. Rev.*
- Ray, P. S., 1976: Vorticity and divergence fields within tornadic storms from dual-Doppler observations. *J. Appl. Meteor.*, **15**, 879–890.
- Ray, P. S., R. J. Doviak, G. B. Walker, D. Sirmans, J. Carter, and B. Bumgarner, 1975: Dual-Doppler observation of a tornadic storm. *J. Appl. Meteor.*, **14**, 1521–1530.
- Ray, P. S., B. C. Johnson, K. W. Johnson, J. S. Bradberry, J. J. Stephens, K. K. Wagner, R. B. Wilhelmson, and J. B. Klemp, 1981: The morphology of several tornadic storms on 20 May 1977. *J. Atmos. Sci.*, **38**, 1643–1663.
- Ray, P. S., D. P. Jorgensen, and S.-L. Wang, 1985: Airborne Doppler radar observations of a convective storm. *J. Clim. Appl. Meteor.*, **24**, 687–698.
- Rotunno, R., 1981: On the evolution of thunderstorm rotation. *Mon. Wea. Rev.*, **109**, 577–586.
- Rotunno, R., 1986: Tornadoes and tornadogenesis. *Mesoscale Meteorology and Forecasting*, Ch. 15. P. S. Ray, Editor, 414–436.
- Rotunno, R., 1993: Supercell thunderstorm modeling and theory. *The Tornado: Its Structure, Dynamics, Prediction, and Hazards*, Geophys. Monogr., No. 79. Amer. Geophys. Union, 143–159.
- Rotunno, R., and J. B. Klemp, 1982: The influence of the shear-induced pressure gradient on thunderstorm motion. *Mon. Wea. Rev.*, **110**, 136–151.

- Rotunno, R., and J. B. Klemp, 1985: On the rotation and propagation of simulated supercell thunderstorms. *J. Atmos. Sci.*, **42**, 271-292.
- Rutledge, S. A., and P. V. Hobbs, 1984: The mesoscale and microscale structure and organization of clouds and precipitation in midlatitude cyclones. Part XII: A diagnostic modeling study of precipitation development in narrow cold-frontal rainbands. *J. Atmos. Sci.*, **41**, 2949-2972.
- Sadowski, A., 1958: Radar observations of the El Dorado, Kansas tornado, June 10, 1958. *Mon. Wea. Rev.*, **86**, 405-408.
- Sadowski, A., 1969: Size of tornado warning area when issued on basis of radar hook echo. ESSA Tech. Memo. WBTM Fcst. 10, 26 pp. [NTIS No. PB 184613].
- Schlesinger, R. E., 1975: A three-dimensional numerical model of an isolated deep convective cloud: Preliminary results. *J. Atmos. Sci.*, **32**, 934-964.
- Shaefer, J. T., and R. L. Livingston, 1988: The typical structure of tornado proximity soundings. *J. Geophys. Res.*, **93**, 6351-6364.
- Shapiro, A., and P. M. Markowski, 1999: Dynamics of elevated vortices. *J. Atmos. Sci.*, **56**, 1101-1122.
- Smagorinsky, J., 1963: General circulation experiments with the primitive equations. Part I: The basic experiment. *Mon. Wea. Rev.*, **91**, 99-164.
- Smith, R. K., and L. M. Leslie, 1979: A numerical study of tornadogenesis in a rotating thunderstorm. *Quart. J. Roy. Meteor. Soc.*, **105**, 107-127.
- Snow, J. T., C. R. Church, and B. J. Barnhart, 1980: An investigation of the surface pressure fields beneath simulated tornado cyclones. *J. Atmos. Sci.*, **37**, 1013-1026.
- Soong, S.-T., 1974: Numerical simulation of warm rain development in an axisymmetric cloud model. *J. Atmos. Sci.*, **31**, 1262-1285.
- Soong, S.-T., and Y. Ogura, 1973: A comparison between axisymmetric and slab-symmetric cumulus cloud models. *J. Atmos. Sci.*, **30**, 879-893.
- Stanford, J. L., 1977: Tornado: *Accounts of Tornadoes in Iowa*. Iowa State University Press, 120 pp.
- Stout, G. E., and F. A. Huff, 1953: Radar records Illinois tornadogenesis. *Bull. Amer. Meteor. Soc.*, **34**, 281-284.
- Straka, J. M., E. N. Rasmussen, and S. E. Fredrickson, 1996: A mobile mesonet for fine-scale meteorological observations. *J. Atmos. Oceanic Tech.*, **13**, 921-936.

- Straka, J. M., and E. N. Rasmussen, 1998: Thirty years of cloud modeling: Does the emperor wear clothes? Preprints, *Nineteenth Conf. on Severe Local Storms*, Minneapolis. Amer. Meteor. Soc., 342–347.
- Stull, R. B., 1988: *An Introduction to Boundary Layer Meteorology*. Kluwer Academic, 666 pp.
- Taylor, G. I., 1938: The spectrum of turbulence. *Proc. R. Soc.*, **A164**, 476–490.
- Taylor, J. R., 1982: *An Introduction to Error Analysis*. University Science Books, 327 pp.
- Tepper, M., and W. E. Eggert, 1956: Tornado proximity traces. *Bull. Amer. Meteor. Soc.*, **37**, 152–159.
- Thompson, R. L., 1998: Eta model storm-relative winds associated with tornadic and nontornadic supercells. *Wea. Forecasting*, **13**, 125–137.
- Thompson, R. L., and R. Edwards, 2000: RUC-2 supercell proximity soundings. Part I: An examination of storm-relative winds normalized to supercell depth. Preprints, *Twentieth Conf. on Severe Local Storms*, Orlando, Amer. Meteor. Soc., 431–434.
- Trapp, R. J., 1999: Observations of non-tornadic low-level mesocyclones and attendant tornadogenesis failure during VORTEX. *Mon. Wea. Rev.*, **127**, 1693–1705.
- Trapp, R. J., and B. H. Fiedler, 1995: Tornado-like vortexgenesis in a simplified numerical model. *J. Atmos. Sci.*, **52**, 3757–3778.
- Trapp, R. J., E. D. Mitchell, G. A. Tipton, D. W. Effertz, A. I. Watson, D. L. Andra, and M. A. Magsig, 1999: Descending and nondescending tornadic vortex signatures detected by WSR-88Ds. *Wea. Forecasting*, **14**, 625–639.
- U.S. Department of the Interior, 1992: *Standards for Digital Elevation Models*. U.S. Geological Survey National Mapping Division, 77 pp. [Available from U.S. Geological Survey.]
- van Leer, B., 1977: Towards the ultimate conservative difference scheme. Part IV: A new approach to numerical convection. *J. Comput. Phys.*, **23**, 276–299.
- van Tassel, E. L., 1955: The North Platte Valley tornado outbreak of June 27, 1955. *Mon. Wea. Rev.*, **83**, 255–264.
- Vasiloff, S. V., E. A. Brandes, R. P. Davies-Jones, and P. S. Ray, 1986: An investigation of the transition from multicell to supercell storms. *J. Clim. Appl. Meteor.*, **25**, 1022–1036.

- Wakimoto, R. M., and N. T. Atkins, 1996: Observations on the origins of rotation: The Newcastle tornado during VORTEX 94. *Mon. Wea. Rev.*, **124**, 384–407.
- Wakimoto, R. M., C. Liu, and H. Cai, 1998a: The Garden City, Kansas, storm during VORTEX 95. Part I: Overview of the storm life cycle and mesocyclogenesis. *Mon. Wea. Rev.*, **126**, 372–392.
- Wakimoto, R. M., and C. Liu, 1998b: The Garden City, Kansas, storm during VORTEX 95. Part II: The wall cloud and tornado. *Mon. Wea. Rev.*, **126**, 393–408.
- Wakimoto, R. M., and H. Cai, 2000: Analysis of a nontornadic storm during VORTEX 95. *Mon. Wea. Rev.*, **128**, 565–592.
- Walko, R. L., 1988: Plausibility of substantial dry adiabatic subsidence in a tornado core. *J. Atmos. Sci.*, **45**, 2251–2267.
- Walko, R. L., 1993: Tornado spin-up beneath a convective cell: Required basic structure of the near-field boundary layer winds. *The Tornado: Its Structure, Dynamics, Prediction, and Hazards*, Geophys. Monogr., No. 79, Amer. Geophys. Union, 89–95.
- Ward, N. B., 1961: Radar and surface observations of tornadoes of 4 May 1961. Proceedings, *Ninth Weather Radar Conf.*, Boston, Amer. Meteor. Soc., 175–180.
- Ward, N. B., 1964: The Newton, Kansas, tornado cyclone of May 24, 1962. Proceedings, *Eleventh Weather Radar Conf.*, Boston, Amer. Meteor. Soc., 410–415.
- Ward, N. B., 1972: The exploration of certain features of tornado dynamics using a laboratory model. *J. Atmos. Sci.*, **29**, 1194–1204.
- Weaver, J. F., and S. P. Nelson, 1982: Multiscale aspects of thunderstorm gust fronts and their effects on subsequent storm development. *Mon. Wea. Rev.*, **110**, 707–718.
- Weaver, J. F., and J. F. W. Purdom, 1995: An interesting mesoscale storm-environment interaction observed just prior to changes in severe storm behavior. *Wea. Forecasting*, **10**, 449–453.
- Weisman, M. L., 1993: The genesis of severe, long-lived bow echoes. *J. Atmos. Sci.*, **50**, 645–670.
- Weisman, M. L., and J. B. Klemp, 1982: The dependence of numerically simulated convective storms on vertical wind shear and buoyancy. *Mon. Wea. Rev.*, **110**, 504–520.

- Weisman, M. L., and J. B. Klemp, 1984: The structure and classification of numerically simulated convective storms in directionally varying wind shears. *Mon. Wea. Rev.*, **112**, 2479-2498.
- Weisman, M. L., M. S. Gilmore, and L. J. Wicker, 1998: The impact of convective storms on their local environment: What is a proximity sounding? Preprints, *Nineteenth Conf. on Severe Local Storms*, Minneapolis. Amer. Meteor. Soc., 238-241.
- Wicker, L. J., and R. B. Wilhelmson, 1995: Simulation and analysis of tornado development and decay within a three-dimensional supercell thunderstorm. *J. Atmos. Sci.*, **52**, 2675-2703.
- Wicker, L. J., and W. C. Skamarock, 1998: A time-splitting scheme for the elastic equations incorporating second-order Runge-Kutta time differencing. *Mon. Wea. Rev.*, **126**, 1992-1999.
- Wilhelmson, R. B., and J. B. Klemp, 1978: A numerical study of storm splitting that leads to long-lived storms. *J. Atmos. Sci.*, **35**, 1974-1986.
- Williams, D. T., 1963: The thunderstorm wake of May 4, 1961. National Severe Storms Project Report No. 18, 23 pp. [NTIS No. PB 168223].
- Winn, W. P., S. J. Hunyady, and G. D. Aulich, 1999: Pressure at the ground in a large tornado. *J. Geophys. Res.*, **104**, 22,067-22,082.
- Wurman, J., J. M. Straka, and E. N. Rasmussen, 1996: Fine-scale Doppler radar observations of tornadic storms. *Science*, **272**, 1774-1777.
- Wurman, J., J. M. Straka, E. N. Rasmussen, M. Randall, and A. Zahrai, 1997: Design and deployment of a portable, pencil-beam, pulsed, 3-cm Doppler radar. *J. Atmos. Oceanic Technol.*, **14**, 1502-1512.
- Young, K. C., 1993: *Microphysical Processes in Clouds*. Oxford University Press, 427 pp.

Appendix A

Error analysis

The errors of temperature (T), pressure (p), and relative humidity (h) measurements appeared in Table 4.3. In this appendix, the errors associated with the derived variables of reduced pressure, virtual and equivalent potential temperature fluctuations, dew point temperature, parcel origin height, convective available potential energy (CAPE), and convective inhibition (CIN) are estimated.

A.1 Reduced pressure errors

Level 2 Digital Elevation Model (DEM) accuracy, $\delta z'$, is within one-half contour interval on a 7.5-minute quadrangle map (U.S. Department of the Interior, 1992). This corresponds to 2.5 ft (0.78 m) on the "High Plains" of the United States (west of $\sim 101^\circ$ W longitude) and to 5 ft (1.6 m) on the "Low Plains" (east of $\sim 101^\circ$ W longitude). Comparisons at random locations with elevation values obtained directly from U.S. Geological Survey 7.5-minute topographic maps revealed slightly better accuracy.

Global Positioning System (GPS) uncertainty in the horizontal positions of mobile mesonet observations is approximately 100 m. Tests were performed at 100 random locations on the High Plains and at 100 random locations on the Low Plains to ascertain the elevation uncertainty owing to the uncertainty in position, $\delta z''$. On the High Plains, the RMS elevation error ($\delta z''$) was 1.1 m (obtained by using the

largest elevation differences at all points within 100 m of the 100 randomly chosen reference positions). On the Low Plains, the RMS elevation error was 3.8 m.

The total elevation uncertainty, δz , can be estimated as

$$\delta z = \sqrt{(\delta z')^2 + (\delta z'')^2}. \quad (\text{A.1})$$

On the High Plains,

$$\delta z \approx \sqrt{(0.78 \text{ m})^2 + (1.1 \text{ m})^2} \approx 1.3 \text{ m}, \quad (\text{A.2})$$

and on the Low Plains,

$$\delta z \approx \sqrt{(1.6 \text{ m})^2 + (3.8 \text{ m})^2} \approx 4.1 \text{ m}. \quad (\text{A.3})$$

Pressure was reduced to the average height of the vehicle observations using the integrated hydrostatic equation of the form,

$$p = p_{obs} \exp \left[\frac{(z - \bar{z})g}{R_d \bar{T}_v} \right]. \quad (\text{A.4})$$

where \bar{z} is the average elevation of the mobile mesonet observations within the analysis domain, p is the pressure reduced to \bar{z} , p_{obs} is the pressure observed by the mobile mesonet vehicle, z is the elevation at which the mobile mesonet pressure p_{obs} was recorded, R_d is the gas constant for dry air, and \bar{T}_v is approximated as the average virtual temperature (liquid water effects neglected) recorded by the mobile mesonet within the analysis domain.

The uncertainty of a reduced pressure measurement (δp) owing to elevation errors (δz) and instrument errors (δp_{obs}), assuming that the elevation and instrument errors are independent and random, is

$$\delta p = \sqrt{\left(\frac{\partial p}{\partial p_{obs}} \delta p_{obs} \right)^2 + \left(\frac{\partial p}{\partial z} \delta z \right)^2 + (\delta \psi)^2}, \quad (\text{A.5})$$

following Taylor (1982), where the uncertainty of \bar{z} ($\delta \bar{z}$) has been assumed to be zero, and the effect on reduced p values owing to errors in \bar{T}_v is not considered because it is small. The last term on the right side of (A.5) has been added in a

purely *ad hoc* manner to account for the subjective analysis uncertainty in regions where observations are sparse. This term is arbitrarily modeled as

$$\delta\psi = |\nabla p| \cdot 0.5 \text{ km}, \quad (\text{A.6})$$

where the factor 0.5 km is multiplied to the magnitude of the pressure gradient in the region of interest with the justification being that $\delta\psi$ is then equal to roughly one-half of a contour interval where the interval is chosen so that the average contour spacing is approximately 1 km. For example, if a weak pressure gradient exists [$|\nabla p| = 1 \text{ mb } (5 \text{ km})^{-1}$], then the uncertainty owing to the subjective contour analysis would be estimated to be 0.1 mb.

Because

$$\frac{\partial p}{\partial p_{obs}} = \exp \left[\frac{(z - \bar{z})g}{R_d \bar{T}_v} \right] = \frac{p}{p_{obs}} \approx 1 \quad (\text{A.7})$$

and

$$\frac{\partial p}{\partial z} = \frac{pg}{R_d \bar{T}_v}, \quad (\text{A.8})$$

(A.5) can be written as

$$\delta p = \sqrt{(\delta p_{obs})^2 + \left(\frac{pg}{R_d \bar{T}_v} \delta z \right)^2 + (\delta\psi)^2}. \quad (\text{A.9})$$

Assuming $p \approx 950 \text{ mb}$ and $\bar{T}_v \approx 300 \text{ K}$, substituting $\delta p_{obs} = 0.6 \text{ mb}$ (Table 4.3), and neglecting $\delta\psi$, the uncertainty of a pressure measurement owing to elevation errors (owing to both DEM and GPS position errors) and instrument errors is estimated to be approximately

$$\delta p \approx 0.62 \text{ mb on High Plains } (\delta z = 1.3 \text{ m}) \quad (\text{A.10})$$

$$\delta p \approx 0.75 \text{ mb on Low Plains } (\delta z = 4.1 \text{ m}). \quad (\text{A.11})$$

Furthermore, because $p' = p - \bar{p}$, it can be shown that

$$\delta p' = \sqrt{(\delta p)^2 + (\delta \bar{p})^2}, \quad (\text{A.12})$$

where $\delta p'$ and $\delta \bar{p}$ are the uncertainties of the fluctuation and base state pressure, respectively. In other words, additional uncertainty (and perhaps the largest amount) is introduced by misspecification of the base state pressure when pressure fluctuations are analyzed.

It is difficult to quantify the error associated with the estimation of the base state, since no theoretically justifiable means exists for defining the base state in a network of spatially and temporally discrete observations. The method for estimating the base state is described in section 4.4. If N observations are available within a 400 km radius to estimate the base state (where $\bar{p} = \sum_{i=1}^N w_i p_i / \sum_{i=1}^N w_i$), then the uncertainty of the base state, $\delta \bar{p}$, can be crudely represented by the sensitivity of \bar{p} to the choice of κ that appears in w_i . Thus, I arbitrarily define the base state pressure uncertainty to be

$$\delta \bar{p} = \max (|\bar{p}_{\kappa_1} - \bar{p}_{\kappa_o}|, |\bar{p}_{\kappa_2} - \bar{p}_{\kappa_o}|), \quad (\text{A.13})$$

where $\delta \bar{p}$ is taken to be the larger of the differences between the weighted average of observations using κ_1 ($= 0.5\kappa_o$) and κ_o and the weighted average of observations using κ_o and κ_2 ($= 1.5\kappa_o$).

A.2 Virtual potential temperature fluctuation errors

Errors in pressure, temperature, and relative humidity observations are accompanied by errors in computed values of virtual potential temperature fluctuations. The inaccuracies of these measurements are approximately 0.6 mb, 0.3–0.5 K (“fast” versus “slow” temperature), and <5%, respectively (Table 4.3). Furthermore, errors in the parameterization of q_l in terms of the radar reflectivity factor as well as misspecification of the base state also adversely affect computations of virtual potential temperature fluctuations. In this section, the error associated with buoyancy calculations also is included in the investigation.

The total buoyancy, B , neglecting ice, can be expressed as

$$B = g \frac{\theta'_v}{\bar{\theta}_v} = g \left(\frac{\theta'}{\bar{\theta}} + 0.61q'_v - q_l \right), \quad (\text{A.14})$$

where (θ'_v) θ' is the (virtual) potential temperature fluctuation, $(\bar{\theta}_v)$ $\bar{\theta}$ is the base state (virtual) potential temperature, q'_v is the water vapor mixing ratio fluctuation, and q_l is the liquid water mixing ratio. If the uncertainties of θ'_v and $\bar{\theta}_v$ are independent and random, then the uncertainty of the buoyancy calculation, δB , is

$$\delta B = \sqrt{\left(\frac{\partial B}{\partial \theta'_v} \delta \theta'_v \right)^2 + \left(\frac{\partial B}{\partial \bar{\theta}_v} \delta \bar{\theta}_v \right)^2 + (\delta \psi)^2}, \quad (\text{A.15})$$

following Taylor (1982), where $\delta \theta'_v$ and $\delta \bar{\theta}_v$ are the uncertainties of θ'_v and $\bar{\theta}_v$, and $\delta \psi$ has been added in an *ad hoc* manner similar to the previous section to account for the subjective analysis uncertainty [$\delta \psi$ may be modeled using a form similar to (A.6)]. The $\delta \psi$ term will be excluded in the analysis hereafter: it should be remembered that in regions where observations are sparse, such that subjective analysis of the meteorological fields is required, this term is estimated and included in the uncertainty analyses that appear in the main body of this document.

We can simplify (A.15) as

$$\delta B = \sqrt{\left(\frac{g}{\bar{\theta}_v} \delta \theta'_v \right)^2 + \left(-\frac{B}{\bar{\theta}_v} \delta \bar{\theta}_v \right)^2}. \quad (\text{A.16})$$

It is desirable to express $\delta \theta'_v$ in terms of δT , δp , and δh . By definition,

$$\begin{aligned} \theta'_v &= T_v \left(\frac{p_0}{p} \right)^\kappa - \bar{\theta}_v \\ &= T(1 + 0.61q_v) \left(\frac{p_0}{p} \right)^\kappa - \bar{\theta}_v. \end{aligned} \quad (\text{A.17})$$

where $\theta_v = \bar{\theta}_v + \theta'_v$, T_v is the virtual temperature, $p_0=1000$ mb, and $\kappa = R_d/c_p$, where c_p is the specific heat of dry air at constant pressure. The effect of liquid

water loading errors have been neglected here. The errors of the parameterization (or any microphysical parameterization) cannot be quantified easily.

From (A.17), we can express the uncertainty of θ'_v (assuming T , p , q_v , and $\bar{\theta}_v$ errors are independent and random) as

$$\delta\theta'_v = \sqrt{\left(\frac{\partial\theta'_v}{\partial T}\delta T\right)^2 + \left(\frac{\partial\theta'_v}{\partial p}\delta p\right)^2 + \left(\frac{\partial\theta'_v}{\partial q_v}\delta q_v\right)^2 + \left(\frac{\partial\theta'_v}{\partial\bar{\theta}_v}\delta\bar{\theta}_v\right)^2} \quad (\text{A.18})$$

$$= \sqrt{\left(\frac{\theta_v}{T}\delta T\right)^2 + \left(-\frac{\kappa\theta_v}{p}\delta p\right)^2 + (0.61\theta\delta q_v)^2 + (\delta\bar{\theta}_v)^2}. \quad (\text{A.19})$$

But

$$\begin{aligned} q_v &= hq_s \\ &\approx \frac{6.112h\varepsilon}{p} \exp\left(\frac{17.67T}{T+243.5}\right). \end{aligned} \quad (\text{A.20})$$

where q_s is the saturation mixing ratio and has been approximated using the formula presented in Bolton (1980). ε (=0.622) is the ratio of the gas constants of dry air and water vapor, and T is in °C. From (A.20) the following is obtained:

$$\begin{aligned} \delta q_v &= \sqrt{\left(\frac{\partial q_v}{\partial h}\delta h\right)^2 + \left(\frac{\partial q_v}{\partial p}\delta p\right)^2 + \left(\frac{\partial q_v}{\partial T}\delta T\right)^2} \quad (\text{A.21}) \\ &= \sqrt{\left[\frac{6.112\varepsilon}{p} \exp\left(\frac{17.67T}{T+243.5}\right) \delta h\right]^2 + \left[-\frac{6.112\varepsilon h}{p^2} \exp\left(\frac{17.67T}{T+243.5}\right) \delta p\right]^2} \\ &\quad + \left[\frac{17.67^2 \cdot 6.112\varepsilon h}{p(T+243.5)^2} \exp\left(\frac{17.67T}{T+243.5}\right) \left(1 - \frac{T}{T+243.5}\right) \delta T\right]^2. \end{aligned}$$

(A.22)

Using (A.19) and (A.22), the total buoyancy uncertainty, δB , can be evaluated. For typical conditions, if we assume $\theta=300$ K, $\theta_v=304$ K, $\bar{\theta}_v=303$ K, $p=950$ mb, $T=296$ K, $h=0.45$ (corresponds to $q_v \approx 0.015$), $\delta T = 0.3$ K or 0.5 K [“fast” temperature ($\delta T=0.3$ K) is used for calculations of variables that do not depend on moisture and “slow” temperature ($\delta T=0.5$ K) is used for calculations that depend on moisture], $\delta p=0.6$ mb [only instrument uncertainty affects δp because station p , not reduced p , is used to compute q (in the preceding section, this uncertainty was referred to as δp_{obs})], and $\delta h=0.03$, yields

$$\delta\theta'_v \approx \sqrt{(0.34 \text{ K})^2 + (\delta\bar{\theta}_v)^2}, \quad (\text{A.23})$$

and

$$\delta B \approx \sqrt{(0.011 \text{ m s}^{-2})^2 + (0.033 \text{ m s}^{-2} \text{ K}^{-1} \delta\bar{\theta}_v)^2}, \quad (\text{A.24})$$

where $\delta\theta'_v$ is modeled in a manner identical to $\delta\bar{p}$.

A.3 Errors associated with other derived quantities

If we use Bolton’s (1980) formula for vapor pressure, then the following expression for the dew point temperature ($^{\circ}\text{C}$) may be obtained:

$$T_d \approx \frac{243.5 \ln\left(\frac{pq_v}{6.112\varepsilon}\right)}{17.67 - \ln\left(\frac{pq_v}{6.112\varepsilon}\right)}, \quad (\text{A.25})$$

where p is in mb and q_v is in g g^{-1} . If p and q_v errors are independent and random, then the uncertainty associated with the calculation of the dew point temperature may be estimated as

$$\begin{aligned}
\delta T_d &\approx \sqrt{\left(\frac{\partial T_d}{\partial p} \delta p\right)^2 + \left(\frac{\partial T_d}{\partial q_v} \delta q_v\right)^2} \\
&\approx \sqrt{\left[\left(\frac{\delta p}{p}\right)^2 + \left(\frac{\delta q_v}{q_v}\right)^2\right] \left[\frac{T_d + 243.5}{17.67 - \ln\left(\frac{p q_v}{6.112 \varepsilon}\right)}\right]^2} \\
&\approx 0.75 \text{ K.}
\end{aligned} \tag{A.26}$$

when $p=950$ mb, $T_d=20^\circ\text{C}$, $q_v=0.015$, $\delta q_v=7 \times 10^{-4}$, and $\delta p=0.6$ mb (based on the result of the unreduced pressure error analysis) are used.

Equivalent potential temperature (θ_e) was computed by first computing the pressure of the lifting condensation level (using the θ and q_v of a surface parcel and iteratively solving for the pressure at which q_v attains the saturation mixing ratio) and then iteratively computing T on the moist adiabat from the lifting condensation level up to 200 mb.

Assessing the effects of T , p , and q_v error propagation into calculations of θ'_e analytically is difficult owing to the iterative techniques used. The uncertainty of θ'_e can be expressed as

$$\delta \theta'_e = \sqrt{(\delta \theta_e)^2 + (\delta \bar{\theta}_e)^2}, \tag{A.27}$$

where $\delta \theta_e$ was investigated numerically by perturbing T , p , and h by their respective errors given in Table 4.3. For $T=300$ K, $p=925$ mb, and $h=0.6$, $\delta \theta_e \approx 2.5$ K. The component of the uncertainty owing to uncertainty of the base state, $\delta \bar{\theta}_e$, was modeled in the same way that $\delta \bar{p}$ and $\delta \bar{\theta}_v$ were modeled.

The uncertainty of the height from which a surface parcel of air has descended (assuming that θ_e has been approximately conserved) depends on the potential instability, i.e., as $|\partial \theta_e / \partial z|$ increases, the origin of the air parcel that has reached the surface becomes more certain. The uncertainty of the height from which a surface parcel has descended, δz_o (where the "o" subscript denotes origin), can be written as

$$\delta z_o \approx \left| \frac{\partial \theta_e}{\partial z} \right|^{-1} \delta \theta_e, \quad (\text{A.28})$$

where $\partial \theta_e / \partial z$ is evaluated at z_o . Using $\delta \theta_e \approx 2.5$, δz_o ranges from ~ 500 m for large (5 K km^{-1}) magnitudes of $\partial \theta_e / \partial z$ to ~ 1 km for small (2 K km^{-1}) magnitudes of $\partial \theta_e / \partial z$.

Lastly, the propagation of T , T_d , and p errors into CAPE and CIN calculations also depends on the vagaries of the sounding. This error was evaluated numerically on a case-by-case basis by perturbing surface parcels by the δT , δT_d , and δp values obtained previously.

Appendix B

Buoyancy formulation

Virtual potential temperature fluctuations were analyzed in chapter 5 because the units (K) probably are more intuitive than the units that appear in analyses of density fluctuations (kg m^{-3}) or buoyancy itself (m s^{-2}). Furthermore, the analyses presented in many past retrieval studies (e.g., Brandes 1984a, Hane and Ray 1985) also considered perturbations of virtual potential temperature. In this appendix, it is shown that virtual potential temperature fluctuations are directly proportional to the density fluctuations that give rise to the familiar “buoyancy force.”

In the equation of motion written in terms of the deviations of pressure (p') and density (ρ') from a hydrostatically balanced reference state ($\partial\bar{p}/\partial z = -\bar{\rho}g$), whose properties vary only with height [i.e., $\bar{p} = \bar{p}(z)$, $\bar{\rho} = \bar{\rho}(z)$],

$$\frac{d\mathbf{v}}{dt} = -\frac{1}{\bar{\rho}}\nabla p' + B\mathbf{k} + \mathbf{F}, \quad (\text{B.1})$$

where $\mathbf{v} = (u, v, w)$ is the velocity vector, pressure $p = \bar{p} + p'$, density $\rho = \bar{\rho} + \rho'$, $\nabla = \frac{\partial}{\partial x}\mathbf{i} + \frac{\partial}{\partial y}\mathbf{j} + \frac{\partial}{\partial z}\mathbf{k}$, \mathbf{F} is turbulent diffusion, and B is buoyancy, defined as

$$B \equiv -g\frac{\rho'}{\bar{\rho}}. \quad (\text{B.2})$$

Liquid and ice particles in the air quickly achieve their terminal fall speeds; therefore, the frictional drag of the air on the particles can be regarded as being balanced by the downward gravitational force acting on the particles (Houze 1993). Thus, the drag of the particles on the unit mass of air is $-gq_t - gq_i$, where q_t and

q_l are the mixing ratios of liquid water and ice, respectively (mass of liquid water and ice per unit mass of air). Instead of adding these additional accelerations to the righthand side of (B.1), it probably is easier to incorporate these effects by redefining ρ as

$$\rho = \bar{\rho}(1 + q_l + q_i), \quad (\text{B.3})$$

where $\bar{\rho}$ is the density of the air (including water vapor effects). In other words, the hydrometeor weighting automatically becomes a negative contribution to the buoyancy. Substitution of (B.3) into the equation of state,

$$p = \bar{\rho}R_dT_v, \quad (\text{B.4})$$

where R_d is the gas constant of dry air and $T_v \approx T(1 + 0.61q_v)$ here, yields

$$(\bar{p} + p')R_d(\bar{T}_v + T'_v) = (\bar{p} + p')(1 + q_l + q_i), \quad (\text{B.5})$$

and

$$\bar{p}R_d\bar{T}_v + \bar{p}R_dT'_v + p'R_d\bar{T}_v = \bar{p} + \bar{p}q_l + \bar{p}q_i + p' \quad (\text{B.6})$$

is obtained by neglecting the terms $p'R_dT'_v$, $p'q_l$, and $p'q_i$ because it is assumed that products of fluctuations are small in size. Assuming $\bar{p} = \bar{p}R_d\bar{T}_v$ and rearranging terms, we obtain

$$-\frac{p'}{\bar{p}} = \frac{T'_v}{\bar{T}_v} - \frac{p'}{\bar{p}} - q_l - q_i, \quad (\text{B.7})$$

and, using (B.2), buoyancy can be written as

$$B = g \left(\frac{T'_v}{\bar{T}_v} - \frac{p'}{\bar{p}} - q_l - q_i \right). \quad (\text{B.8})$$

The base state atmosphere is assumed to contain no hydrometeors; therefore the mixing ratios q_l and q_i are the total hydrometeor content of the air, and the variables do not contain primes.

Alternatively, buoyancy can be written in terms of a virtual potential temperature, θ_v (the potential temperature that a sample of dry air would have if its density was the same as moist air, without condensate in this case, at the same pressure),

$$\theta_v = T_v \left(\frac{p_o}{p} \right)^\kappa. \quad (\text{B.9})$$

where p_o is a (constant) reference pressure and $\kappa = R_d/c_p$, where c_p is the specific heat of air at constant pressure. Thus,

$$T'_v = (\bar{\theta}_v + \theta'_v) \left(\frac{\bar{p} + p'}{p_o} \right)^\kappa - \bar{\theta}_v \left(\frac{\bar{p}}{p_o} \right)^\kappa, \quad (\text{B.10})$$

assuming $\bar{\theta}_v = \bar{T}_v (p_o/\bar{p})^\kappa$. Therefore

$$T'_v = \bar{\theta}_v \left[\left(\frac{\bar{p} + p'}{p_o} \right)^\kappa - \left(\frac{\bar{p}}{p_o} \right)^\kappa \right] + \theta'_v \left(\frac{\bar{p} + p'}{p_o} \right)^\kappa. \quad (\text{B.11})$$

and

$$\begin{aligned} \frac{T'_v}{\bar{T}_v} &= \left(\frac{\bar{p} + p'}{p_o} \right)^\kappa \left(\frac{\bar{p}}{p_o} \right)^{-\kappa} - 1 + \frac{\theta'_v}{\bar{\theta}_v} \left(\frac{\bar{p} + p'}{p_o} \right)^\kappa \left(\frac{\bar{p}}{p_o} \right)^{-\kappa} \\ &= \frac{(\bar{p} + p')^\kappa}{\bar{p}^\kappa} - 1 + \frac{\theta'_v (\bar{p} + p')^\kappa}{\bar{\theta}_v \bar{p}^\kappa} \\ &= \left(1 + \frac{p'}{\bar{p}} \right)^\kappa - 1 + \frac{\theta'_v}{\bar{\theta}_v} \left(1 + \frac{p'}{\bar{p}} \right)^\kappa, \end{aligned} \quad (\text{B.12})$$

and assuming $\left(1 + \frac{p'}{\bar{p}} \right)^\kappa \approx 1 + \frac{\kappa p'}{\bar{p}}$,

$$\frac{T'_v}{\bar{T}_v} = \frac{\theta'_v}{\bar{\theta}_v} + \frac{\kappa p'}{\bar{p}}, \quad (\text{B.13})$$

if $\theta'_v \kappa p' / \bar{\theta}_v \bar{p}$, assumed to be small, is neglected. Therefore, buoyancy can be written as

$$B = g \left[\frac{\theta'_v}{\bar{\theta}_v} + (\kappa - 1) \frac{p'}{\bar{p}} - q_l - q_i \right]. \quad (\text{B.14})$$

A virtual potential temperature also can be defined to include the effects of hydrometeors on density [i.e., θ_v can now be redefined to be the potential temperature of a sample of dry air that has the same density as a sample of moist, *cloudy* air at the same pressure; see appendix in Stull (1988)], i.e.,

$$\theta_v = \theta(1 + 0.61q_v - q_l - q_i), \quad (\text{B.15})$$

where $\theta = T(p_o/p)^\kappa$. Using the above expression, we can rewrite the buoyancy as

$$B = g \left[\frac{\theta'_v}{\bar{\theta}_v} + (\kappa - 1) \frac{p'}{\bar{p}} \right]. \quad (\text{B.16})$$

Often the momentum equation defined by (B.1) is written more conveniently as

$$\frac{d\mathbf{v}}{dt} = -c_p \bar{\theta}_v \nabla \pi' + g \frac{\theta'_v}{\bar{\theta}_v} \mathbf{k} + \mathbf{F}, \quad (\text{B.17})$$

where $\pi = \bar{\pi} + \pi' = (p/p_o)^\kappa$. In this form of the momentum equation, the pressure perturbation term $[(\kappa - 1)p'/\bar{p}]$ disappears from the buoyancy force (it is contained in $-c_p \bar{\theta}_v \nabla \pi'$, or more precisely, in $-c_p \bar{\theta}_v \frac{\partial \pi'}{\partial z}$):

$$\pi' = \left(\frac{\bar{p} + p'}{p_o} \right)^\kappa - \left(\frac{\bar{p}}{p_o} \right)^\kappa, \quad (\text{B.18})$$

assuming $\bar{\pi} = (\bar{p}/p_o)^\kappa$. Then

$$\begin{aligned} -c_p \bar{\theta}_v \frac{\partial \pi'}{\partial z} &= -c_p \bar{\theta}_v \frac{\partial}{\partial z} \left(\frac{\bar{p} + p'}{p_o} \right)^\kappa + c_p \bar{\theta}_v \frac{\partial}{\partial z} \left(\frac{\bar{p}}{p_o} \right)^\kappa \\ &= \frac{-c_p \bar{\theta}_v \kappa}{p_o^\kappa} (\bar{p} + p')^{\kappa-1} \frac{\partial}{\partial z} (\bar{p} + p') + \frac{c_p \bar{\theta}_v \kappa \bar{p}^{\kappa-1}}{p_o^\kappa} \frac{\partial \bar{p}}{\partial z}. \end{aligned} \quad (\text{B.19})$$

But if we assume that $\bar{\theta}_v = \bar{T}_v (\bar{p}/p_o)^{-\kappa}$, $\partial \bar{p}/\partial z = -\bar{\rho}g$, and $\bar{p} = \bar{\rho}R_d \bar{T}_v$, then

$$\begin{aligned}
-c_p \bar{\theta}_v \frac{\partial \pi'}{\partial z} &= -\frac{R_d \bar{T}_v}{\bar{p}^\kappa} (\bar{p} + p')^{\kappa-1} \frac{\partial \bar{p}}{\partial z} - \frac{R_d \bar{T}_v (\bar{p} + p')^{\kappa-1}}{\bar{p}^\kappa} \frac{\partial p'}{\partial z} - g \\
&= g \bar{p} R_d \bar{T}_v \left(1 + \frac{p'}{\bar{p}}\right)^\kappa (\bar{p} + p')^{-1} - \frac{R_d \bar{T}_v}{\bar{p}} \left(1 + \frac{p'}{\bar{p}}\right)^\kappa \left(1 + \frac{p'}{\bar{p}}\right)^{-1} \frac{\partial p'}{\partial z} - g.
\end{aligned} \tag{B.20}$$

and, assuming $\left(1 + \frac{p'}{\bar{p}}\right)^\kappa \approx 1 + \frac{\kappa p'}{\bar{p}}$, then

$$-c_p \bar{\theta}_v \frac{\partial \pi'}{\partial z} = \frac{\bar{p}g}{\bar{p} + p'} \left(1 + \frac{p'}{\bar{p}}\right)^\kappa - \frac{R_d \bar{T}_v}{\bar{p}} \left(1 + \frac{\kappa p'}{\bar{p}}\right) \left(1 - \frac{p'}{\bar{p}}\right) \frac{\partial p'}{\partial z} - g, \tag{B.21}$$

and after rearranging terms and neglecting products of perturbation variables, we obtain

$$-c_p \bar{\theta}_v \frac{\partial \pi'}{\partial z} = g(\kappa - 1) \frac{p'}{\bar{p}} - \frac{1}{\bar{p}} \frac{\partial p'}{\partial z}, \tag{B.22}$$

thus, the pressure fluctuation term in (B.16) does not appear in the buoyancy term of (B.17), because it is contained in the pressure gradient force when $\nabla p'$ is written in terms of $\nabla \pi'$. Therefore buoyancy can be written simply as

$$B = g \frac{\theta'_v}{\bar{\theta}_v} = g \left(\frac{\theta'}{\bar{\theta}} + 0.61 q'_v - q_l - q_i \right), \tag{B.23}$$

where

$$\theta_v = \theta(1 + 0.61 q_v - q_l - q_i) \tag{B.24}$$

and it has been assumed that

$$\bar{\theta}_v = \bar{\theta}(1 + 0.61 \bar{q}_v). \tag{B.25}$$

Summarizing, if the momentum equations are written in terms of π' , then θ'_v [$= \theta(1 + 0.61q_v - q_l - q_s) - \bar{\theta}_v$] is directly proportional to B ($= g \frac{\theta'_x}{\theta'_v}$). If the momentum equations are written in terms of p' , then B is defined slightly differently $\{ B = g \left[\frac{\theta'_x}{\theta'_v} + (\kappa - 1) \frac{p'}{p} \right] \}$ and θ'_v is very nearly directly proportional to B , with the exception that a small $(\kappa - 1) \frac{p'}{p}$ contribution is not included.

Appendix C

Axisymmetric model validation

The axisymmetric model was tested by imposing a stationary body force identical to that used by Howells et al. (1988). It has the form

$$F(r, z) = g (\Delta\theta/\theta_a) R(r) Z(z),$$

$$R(r) = \begin{cases} 1 - (r/r_1)^2 & 0 \leq r \leq r_1 \\ 0 & \text{otherwise} \end{cases}$$

$$Z(z) = \begin{cases} 0 & 0 \leq z \leq z_1 \\ 2(z - z_1) & z_1 < z \leq z_2 \\ 1 & \text{otherwise} \end{cases}$$

where $\Delta\theta$ is a constant excess temperature perturbation of 5 K and θ_a is the ambient potential temperature defined as

$$\theta_a(z) = \begin{cases} 300 & z \leq z_2 \\ 300 + 2(z - z_2) & z > z_2 \end{cases}$$

where $r_1 = 1.5$ km, $z_1 = 1.0$ km, and $z_2 = 1.5$ km. The forcing is zero below 1 km, increases linearly with height to 1.5 km, and is constant above 1.5 km. The body force decreases quadratically to zero in the radial direction at 1.5 km. A cylindrical domain with a 2 km radius and 3 km depth was used for the series of validation experiments, as used by Howells et al. A swirling wind velocity is applied to air entering the domain through the lateral boundary, and a vortex is generated by stretching associated with the imposed updraft.

A uniform grid with a horizontal and vertical grid spacing of 50 m was used. Several experiments were conducted with various (constant) eddy viscosities and imposed swirling wind components. All results agreed reasonably well with those obtained by Howells et al.

In the example presented in Fig. C.1, $K_m = 20 \text{ m}^2 \text{ s}^{-1}$, a tangential wind speed of 4 m s^{-1} has been applied to inflow parcels, and the lower boundary is free-slip. The vortex has a steady-state maximum tangential velocity $>30 \text{ m s}^{-1}$ beneath the region of forcing. An adverse axial pressure gradient is associated with axial downflow of approximately 2 m s^{-1} in the core. An maximum updraft exceeding 18 m s^{-1} is achieved just outside of the region of largest tangential wind speed. [Compare Fig. C.1 with Fig. 5 (p. 808) in the Howells et al. manuscript.]

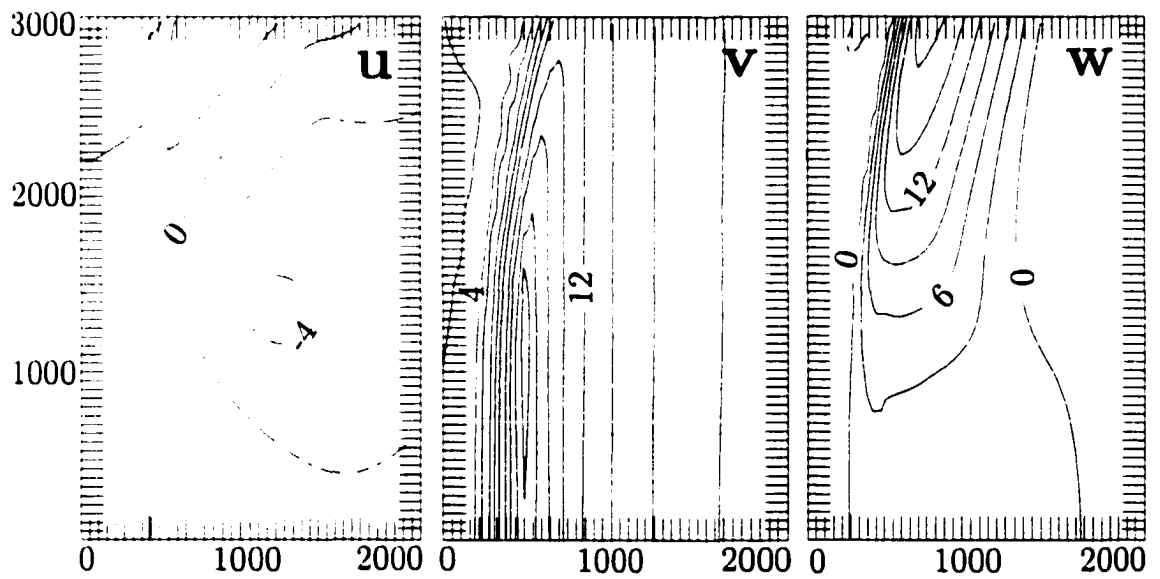


Figure C.1: Steady-state ($t=25$ min) meridional cross-sections of radial, tangential, and vertical velocity components when a body force is imposed as by Howells et al. (1988). In the above example, the lower boundary is free-slip, $K_m=20 \text{ m}^2 \text{ s}^{-1}$, and a swirling wind component of 4 m s^{-1} has been specified on the inflow lateral boundary [cf. Fig. 5 in Howells et al. (1988)].